Intelligent Traction Motor Control Techniques for Hybrid and Electric Vehicles

By

Scott Cash

A thesis submitted to the University of Birmingham for the degree of

Doctor of Philosophy

Department of Mechanical Engineering

The University of Birmingham

September 2018

Abstract

This thesis presents the research undertaken by the author within the field of intelligent traction motor control for Hybrid Electric Vehicle (HEV) and Electric Vehicle (EV) applications.

A robust Fuzzy Logic (FL) based traction motor field-orientated control scheme is developed which can control multiple motor topologies and HEV/EV powertrain architectures without the need for re-tuning. This control scheme can aid in the development of an HEV/EV and for continuous control of the traction motor/s in the final production vehicle.

An overcurrent-tolerant traction motor sizing strategy is developed to gauge if a prospective motor's torque and thermal characteristics can fulfil a vehicle's target dynamic and electrical objectives during the early development stages of an HEV/EV. An industrial case study is presented.

An on-line reduced switching multilevel inverter control scheme is investigated which increases the inverter's efficiency while maintaining acceptable levels of output waveform harmonic distortion.

A FL based vehicle stability control system is developed that improves the controllability and stability of an HEV/EV during an emergency braking manoeuvre. This system requires minimal vehicle parameters to be used within the control system, is insensitive to variable vehicle parameters and can be tuned to meet a vehicle's target dynamic objectives.

To Mom and Dad

Acknowledgements

I would firstly like to thank Dr. Oluremi Olatunbosun for his guidance and advice during my Masters project and my PhD. What I have learned from working with him will prove to be invaluable in the future. I would also like to thank Prof. Hongming Xu for taking over as my lead supervisor and guiding me towards the finish line. His expertise, experience and support has enabled me to conclude my PhD and research to a high level.

I also appreciate Dr. Richard Hood taking over as my co-supervisor at a late stage and on short notice. I would also like to thank Quan Zhou and my other colleges for their technical knowledge and providing a good working environment at the university.

But most of all, I thank my parents for their continual encouragement and support throughout my time at university. Without them I may not have gotten through the difficult and strenuous times to have reached this point. To my Mom for continuously pushing me forward, listening to my complaints and endless cups of tea. To my Dad for his support and the never ending hours of proof reading that I brought him.

Contents

Contents ..... **iv**

List of Figures ..... **x**

List of Tables ..... **xvi**

List of Abbreviations ..... **xviii**

Publications ..... **xx**

1. Chapter One - Introduction **1**

1.1 Purpose of the Research 1

1.1.1 Environmental Protection 1

1.1.2 Energy and Fuel Scenario 3

1.1.3 Vehicle Safety 4

1.2 Vehicle Development Trends and Challenges 5

1.3 Research Objectives and Approach 6

1.4 Key Contributions 7

1.5 Thesis Outline 8

2. Chapter Two – Literature Review **11**

2.1 The HEV and EV 11

2.1.1 HEV Powertrain Architectures 12

2.1.2 EV Powertrain Architectures 14

2.2 Traction Motors for HEV/EV Applications 16

2.2.1 Background into Electric Motors 16

2.2.2 Traction Motor Topology Characteristics 16

2.2.3 Traction Motor Modelling Techniques 19

2.2.4 Advanced Traction Motor Control Schemes 19
2.2.5 Optimised FOC Strategies 21
2.2.6 Real World Motor Control 22
2.2.7 Controller Types for FOC 23
2.2.8 PI vs Fuzzy Logic for FOC 24
2.2.8.1 Speed Control using FOC 24
2.2.8.2 Current Control using FOC 25
2.2.9 Research Gaps in the Field of Traction Motor Modelling and Control 26
2.3 DC-AC Inverters for Traction Motors 27
2.3.1 Inverter Topologies for HEV/EVs 28
2.3.2 Inverter Modulation Methods 29
2.3.3 Space Vector Pulse Width Modulation (SVPWM) 32
2.3.4 Optimising SVPWM 34
2.3.5 On-line SVPWM Methods 35
2.3.6 Research Gaps in the Field of DC-AC Inverter Control 37
2.4 Vehicle Stability Control for HEV/EVs 38
2.4.1 Vehicle Stability Control Techniques 38
2.4.2 Vehicle Yaw Rate Control Methods 41
2.4.2.1 Implementing Yaw Rate Control 41
2.4.2.2 Yaw Rate Controller Types 42
2.4.3 Wheel Slip Controller Schemes 44
2.4.3.1 Wheel Slip Control for an HEV/EV 44
2.4.3.2 Wheel Slip Controller Types 44
2.4.4 Vehicle Yaw Control during Braking Manoeuvres 45

2.4.5 Research Gaps in the Field of Vehicle Stability Control for HEV/EVs 49

2.5 Summary of Literature Gaps and Specific Research Objectives 50

3. Chapter Three – Research Methodology and Model Verification Procedures 53

3.1 Research Methodology 53

3.2 Component Modelling of the HEV/EV 54

3.2.1 Traction Motor Models 54

3.2.1.1 Voltage Vector Transformations 55

3.2.1.2 FOC Architecture 57

3.2.1.3 Analytical Model of an IM 59

3.2.1.4 Analytical Model of a PMSM 62

3.2.1.5 Voltage Constraints 64

3.2.2 DC-AC Inverter Models 65

3.2.2.1 Inverter Switch Control 66

3.2.2.2 Inverter Operating Limits 67

3.2.2.3 Inverter Control for Traction Motor Four-Quadrant Operation 71

3.2.3 Battery Pack Model 71

3.2.4 Vehicle Dynamics 72

3.2.4.1 CarSim Vehicle Modelling 72

3.2.4.2 The Tyre Model 74

3.2.5 Simplified HEV/EV Modelling techniques 77

3.2.5.1 Simplified Traction Motor Model 77

3.2.5.2 Simplified ICE Model 77

3.2.5.3 Simplified APU Model 78

3.2.5.4 Simplified Vehicle Dynamics 78

3.3 Statistical Analysis Methods 80
3.3.1 Controller Error Analysis 80
3.3.2 Waveform Harmonic Distortion 81
3.3.3 Vehicle Dynamic Performance Indices 81
3.4 Model Verification Procedure 83
3.4.1 Traction Motor Model Verification 83
3.4.2 DC-AC Inverter Model Verification 87
3.4.3 Tyre Model Verification 89
3.4.4 Control System Verification 91
3.5 Summary 95

4. Chapter Four – Fuzzy Logic Field-Oriented Control for Traction Motors 96
4.1 Fuzzy Logic Controllers within the FL-FOC Scheme 97
4.1.1 Fuzzy Logic Speed Controller 97
4.1.2 Fuzzy Logic Current Controller 99
4.1.3 Fuzzy Logic Flux Controller 101
4.2 FL-FOC Verification 103
4.3 Performance Evaluation of the FL-FOC System 107
4.3.1 FOC Driving Scenario 1 108
4.3.2 FOC Driving Scenario 2 113
4.4 Robustness Analysis using Variable Motor Parameters 116
4.5 Summary 120

5. Chapter Five – Overcurrent-Tolerant Traction Motor Sizing Strategy 121
5.1 The Overcurrent-Tolerant Temperature Prediction Motor Model 122
5.2 Aircraft Pushback HEV Conversion: A Case Study 126

5.2.1 ICE Pushback Vehicle Parameters 127
5.2.2 Duty Cycle of the Aircraft Pushback Vehicle 129
5.2.3 Battery Pack Constraints and APU Control 131
5.2.4 HEV Pushback Vehicle Feasibility and Efficiency Analysis 132
5.2.4.1 Torque Characteristics for HEV Configuration 1 135
5.2.4.2 Torque Characteristics for HEV Configuration 2 136
5.2.4.3 HEV Electrical Performance Comparison 137
5.2.5 Pushback HEV Final Outcome 141
5.3 Summary 142

6. Chapter Six – Reduced Switching Inverter Control for Traction Motors 143
6.1 The RIS-SVPWM scheme 143
6.1.1 The D-SVPWM method 143
6.1.2 Advancement to the RIS-SVPWM method 146
6.1.3 Inverter Switching Device Control 149
6.2 Performance evaluation of the RIS-SVPWM method 151
6.2.1 Simulation setup procedure 151
6.2.2 Switch Count Analysis 153
6.2.3 Waveform Harmonic Analysis 155
6.2.4 Inverter Output Waveform Analysis 157
6.3 Summary 164

7. Chapter Seven – Fuzzy Logic HEV/EV Stability Control 165
7.1 Operating principles of the FL-VSC 166
7.2 Fuzzy Logic Controllers for the FL-VSC 168
7.2.1 Fuzzy Logic YMC 168

7.2.2 Fuzzy Logic Gradient Command Controller 170
7.2.3 Fuzzy Logic Wheel Slip Controller 172
7.3 FL-VSC Performance Evaluation 175
7.3.1 Simulation Setup and Evaluation Criteria 175
7.3.2 Scenario 1 – Straight Line Braking 176
7.3.3 Scenario 2 – Split μ Braking 180
7.3.4 Scenario 3 – Double Lane Change on a Low μ Surface 185
7.3.5 Scenario 4 – Distracted Driver Accident Avoidance 191
7.4 Summary 196

8. Chapter Eight – Summary and Conclusions 197
8.1 Summary of the Main Outcomes 197
8.1.1 Summary of Chapter Four 197
8.1.2 Summary of Chapter Five 198
8.1.3 Summary of Chapter Six 199
8.1.4 Summary of Chapter Seven 200
8.2 Further Discussion and Future Work 202
8.2.1 Further Discussion for Chapter Four 202
8.2.2 Further Discussion for Chapter Five 203
8.2.3 Further Discussion for Chapter Six 203
8.2.4 Further Discussion for Chapter Seven 204

Appendix: Nomenclature 205

List of References 210

List of Figures

Figure 1.1 Global CO_2 emissions from fuel combustions by sector in 2015 [5] 2

Figure 1.2 Passenger transportation energy consumption estimates up to the year 2040 between **(a)** Organization for Economic Cooperation and Development (OECD) countries and **(b)** Non-OECD countries, scale in quadrillion Btu [22] 4

Figure 1.3 Global HEV/EV Sales forecast up to 2040 [33] 6

Figure 2.1 HEV powertrain architecture, **(a)** Series-HEV, **(b)** Parallel-HEV, **(c)** Power Split-HEV 13

Figure 2.2 EV Powertrain Architecture, **(a)** Single motor with single/multi speed gearbox, **(b)** Dual motors with single speed transmissions, **(c)** Four independent in-wheel motors with single speed gearboxes 15

Figure 2.3 Traction motor constructional topologies cross-section view, **(a)** IM, **(b)** S-PMSM, **(c)** I-PMSM, **(d)** RM 17

Figure 2.4 Five -Level inverter topologies, **(a)** Neutral-Point Clamped, **(b)** Cascaded H-Bridge, **(c)** Isolated Neutral load 28

Figure 2.5 3 phase waveforms from an inverter operating using 6-step operation 30

Figure 2.6 One pole voltage waveform of a 3-phase voltage waveform generated by an inverter using Carrier-based SPWM 31

Figure 2.7 Inverter Space Vector Diagrams [178, 180], **(a)** 5-Level, **(b)** 3-Level, **(c)** 2-Level 33

Figure 2.8 How intermediate switches are generated when transitioning between SVM cycles, **(a)** No intermediate switching, **(b)** One intermediate switch on A2 35

Figure 2.9 Oversteer, Understeer and Target yaw rate trajectory graphical view 39

Figure 2.10 Diagrammatical view of the tyre dynamics, **(a)** Wheel slip ratio, **(b)** Wheel side-slip angle and velocity components, **(c)** Tyre contact patch distortion 39

Figure 2.11 COF curves for one tyre and road combination over different wheel slip and sideslip angles, **(a)** μ_X curves, **(b)** μ_Y curves [277] 40

Figure 2.12 How varying asymmetrical braking forces can produce an external yaw moment, **(a)** Symmetrical Braking forces, **(b)** Asymmetrical braking forces 46

Figure 3.1 Vector transformations, **(a)** 2D visual representation of the transformation process, **(b)** Original 3-phase AC waveforms, **(c)** Clarke transformation, **(d)** Park transformation 56

Figure 3.2 FOC flowchart architecture between the MATLAB/Simulink and CarSim environments 57

Figure 3.3 IM analytical equivalent circuits, **(a)** q-axis **(b)** d-axis 59

Figure 3.4 I-PMSM analytical equivalent circuits, **(a)** d-axis, **(b)** q-axis 62

Figure 3.5 I-PMSM MTPA i_{ds}^{*} flow chart 64

Figure 3.6 Fundamental component of an inverter operating in 6-step square wave control . 68

Figure 3.7 Modulation modes diagrammatical analysis [177, 204], **(a)** Sinusoidal, **(b)** Overmodulation mode I, (**c)** Overmodulation mode II..... 69

Figure 3.8 Modulation mode modifier [172, 178] **(a)** Crossover Angle, **(b)** Holding Angle . 71

Figure 3.9 14 Degree of Freedom vehicle model [239, 240]..... 73

Figure 3.10 Wheel dynamics, **(a)** Wheel Slip, **(b)** Wheel sideslip angles..... 75

Figure 3.11 IM model verification simulation **(a)** ω_m comparison, **(b)** τ_e comparison, **(c)** i_{ds} comparison, **(d)** v_{ds} voltage comparison, **(e)** i_{qs} comparison, **(f)** v_{qs} comparison, **(g)** ω_e comparison 85

Figure 3.12 I-PMSM model verification simulation **(a)** ω_m comparison, **(b)** τ_e comparison, **(c)** i_{ds} comparison, **(d)** v_{ds} voltage comparison, **(e)** i_{qs} comparison, **(f)** v_{qs} comparison, **(g)** ω_e comparison 86

Figure 3.13 DC-AC inverter model comparison, **(a)** v_{aN} at $m = 0.2$, **(b)** v_{ab} at $m = 0.2$, **(c)** v_{aN} at $m = 0.7$, **(d)** v_{ab} at $m = 0.7$, **(e)** v_{aN} at $m = 0.9$, **(f)** v_{ab} at $m = 0.9$, **(g)** v_{aN} at $m = 1$, **(h)** v_{ab} at $m = 1$ 88

Figure 3.14 Tyre model verification, **(a)** Applied axle torque, **(b)** F_t, **(c)** σ_{wh}, **(d)** u_{wh} 90

Figure 3.15 PIL control flowchart using Matlab/Simulink, CarSim and an Arduino Mega 2560 microcontroller 93

Figure 4.1 FL speed controller membership functions, **(a)** Input 1 - ΔV_x, **(b)** Input 2 – $d(\Delta V_x)/dt$, **(c)** Output - Pedal movement 98

Figure 4.2 FL Current controller membership functions, **(a)** Input 1 - $\Delta i_{ds,qs}$, **(b)** Input 2 – $\zeta_{ds,qs}$, **(c)** Output – $v_{d0,q0}$ 100

Figure 4.3 FL Flux controller membership functions, **(a)** Input 1 – $\Delta\varphi_r$, **(b)** Input 2 – $d(\Delta\varphi_r)/dt$, **(c)** Output – i_{ds}^{*} 102

Figure 4.4 PIL simulations for a C-Class hatchback vehicle using dual IMs following a short section of the US Federal Drive Cycle, **(a)** V_x, **(b)** Pedal movement, **(c)** i_{qs} current, **(d)** v_{qs} votlage, **(e)** i_{ds} current, **(f)** v_{ds} voltage, **(g)** Flux wave magnitude φ_r 105

Figure 4.5 PIL simulations for an E-Class saloon vehicle using a single I-PMSM following a short seciton of the Extra Urban Drive Cycle, **(a)** V_x, **(b)** Pedal movement, **(c)** i_{qs} current, **(d)** v_{qs} votlage, **(e)** i_{ds} current, **(f)** v_{ds} voltage, ... 106

Figure 4.6 PI and FL speed control for driving scenario 1, **(a)** V_x comparison, **(b)** Pedal movement, **(c)** ΔV_x comparison 109

Figure 4.7 PI and FL i_{qs} current control for driving scenario 1, **(a)** i_{qs} comparison, **(b)** v_{qs} comparison, **(c)** i_{qs} error comparison 110

Figure 4.8 PI and FL i_{ds} current control for driving scenario 1, **(a)** i_{ds} comparison, **(b)** v_{ds} comparison, **(c)** i_{ds} error 111

Figure 4.9 PI and FL φ_r control for driving scenario 1, **(a)** φ_r comparison, **(b)** i_{ds}^* comparison, **(c)** φ_r error comparison 112

Figure 4.10 PI and FL speed control for driving scenario 2, **(a)** V_x comparison, **(b)** Pedal movement, **(c)** ΔV_x comparison 113

Figure 4.11 PI and FL i_{qs} current control for driving scenario 2, **(a)** i_{qs} comparison, **(b)** v_{qs} comparison, **(c)** i_{qs} comparison 114

Figure 4.12 PI and FL i_{ds} current control for driving scenario 2, **(a)** i_{ds} comparison, **(b)** v_{ds} comparison, **(c)** i_{ds} error comparison 115

Figure 4.13 Stator resistance $r_s = 0.04\Omega$ simulation for the FOC-2 and FL-FOC, **(a)** V_x comparison, **(b)** Pedal movement, **(c)** i_{qs} comparison 118

Figure 4.14 Stator resistance $r_s = 0.16\Omega$ simulation for the FOC-2 and FL-FOC, **(a)** V_x comparison, **(b)** Pedal movement, **(c)** i_{qs} comparison 119

Figure 5.1 Diagrammatical view of how δ_τ is generated 123

Figure 5.2 Overcurrent-tolerant prediction model torque control flowchart 125

Figure 5.3 Conventional ICE powered pushback vehicle torque-speed curve and fuel map (L/hr) 128

Figure 5.4 Conventional ICE powered pushback vehicle emissions maps, **(a)** Hydrocarbons (HC) (g/s), **(b)** Carbon Monoxide (CO) (g/s), **(c)** Nitrous Oxides (NOx) (g/s), **(d)** Particulate Matter (g/s) 128

Figure 5.5 Towing tractive force requirements for a Boeing 737-7 aeroplane over numerous runway conditions [320] 129

Figure 5.6 Genset control flowchart for the pushback HEV 132

Figure 5.7 Torque Speed curves and efficiency map (%) for the traction motors used in HEV configuration 1 134

Figure 5.8 Torque Speed curves and efficiency map (%) for the traction motor used in HEV configuration 2 134

Figure 5.9 Motor usage for the HEV with configuration 1 over the daily duty cycle 135

Figure 5.10 Theoretical temperature profile of the traction motors for configuration 1 over a section of the daily duty cycle; 1 maintenance operation, 1 pushback operation and 2 solo runs 136

Figure 5.11 Motor usage for the HEV with configuration 2 over the daily duty cycle 137

Figure 5.12 Velocity profile and battery pack SOE over the complete duty cycle for the HEV using configuration 1 139

Figure 5.13 Velocity profile and battery pack SOE over the complete duty cycle for the HEV using configuration 2 139

Figure 5.14 Final HEV aeroplane pushback vehicle prototype [323] 141

Figure 6.1 5L-SVM diagram separated into the 6 sectors for the D-SVPWM method and an example V_{ref} in Sector 2 [208, 209] 145

Figure 6.2 5L-SVM mapping process example for the D-SVPWM method [208, 209] 146

Figure 6.3 Example 2-level optimised dwell vector mapping options 147

Figure 6.4 2L-SVM diagram inverter reference points 147

Figure 6.5 Null vector mapping state value example for 5L-SVM diagram with V_{ref} in Figure 6.2 149

Figure 6.6 Switch count reduction over a range of modulation indices $m \in [0.2\ 1]$ and output voltage frequencies $f \in [20\ 150] Hz$ for a 5L-CHB inverter $f_s = 10\ kHz$, **(a)** Intermediate switch decrease, **(b)** Total switch decrease 153

Figure 6.7 WTHD comparison for v_a over a range of modulation indices and output voltage frequencies for a 5L-CHB inverter using $f_s = 5\ kHz$, **(a)** D-SVPWM, **(b)** RIS-SVPWM, **(c)** Percentage Difference 155

Figure 6.8 THD comparison for i_{ab} over a range of modulation indices and output voltage frequencies for a 5L-CHB inverter using $f_s = 5\ kHz$, **(a)** D-SVPWM, **(b)** RIS-SVPWM, **(c)** Percentage Difference 156

Figure 6.9 5L-CHB inverter simulation waveform results *m = 0.2*, **(a)** v_a, **(b)** v_{ab}, **(c)** i_{ab} 158

Figure 6.10 5L-CHB inverter simulation harmonic analysis results *m = 0.2*, **(a)** v_a, **(b)** i_{ab} 158

Figure 6.11 5L-CHB inverter simulation waveform results *m = 0.45*, **(a)** v_a, **(b)** v_{ab}, **(c)** i_{ab} 159

Figure 6.12 5L-CHB inverter simulation harmonic analysis results *m = 0.45*, **(a)** v_a, **(b)** i_{ab} 159

Figure 6.13 5L-CHB inverter simulation waveform results *m = 0.7*, **(a)** v_a, **(b)** v_{ab}, **(c)** i_{ab} 160

Figure 6.14 5L-CHB inverter simulation harmonic analysis results *m = 0.7*, **(a)** v_a, **(b)** i_{ab} 160

Figure 6.15 5L-CHB inverter simulation waveform results *m = 0.907,* **(a)** v_a, **(b)** v_{ab}, **(c)** i_{ab} 161

Figure 6.16 5L-CHB inverter simulation harmonic analysis results *m = 0.907,* **(a)** v_a, **(b)** i_{ab} 161

Figure 6.17 5L-CHB inverter simulation waveform results *m = 0.955,* **(a)** v_a, **(b)** v_{ab}, **(c)** i_{ab} 162

Figure 6.18 5L-CHB inverter simulation harmonic analysis results *m = 0.955,* **(a)** v_a, **(b)** i_{ab} 162

Figure 6.19 5L-CHB inverter simulation waveform results *m = 1,* **(a)** v_a, **(b)** v_{ab}, **(c)** i_{ab} .. 163

Figure 6.20 5L-CHB inverter simulation harmonic analysis results *m = 1,* **(a)** v_a, **(b)** i_{ab} .. 163

Figure 7.1 Top level FL-VSC control flow architecture 166

Figure 7.2 YMC and Gradient Command control flowcharts 167

Figure 7.3 Gradient Controller with the Braking and Tyre Model control flowchart 167

Figure 7.4 FL YMC membership functions [239, 240], **(a)** Input 1 - Δr, **(b)** Input 2 - $\Delta\beta_{ss}$, **(c)** Output - M_Z 169

Figure 7.5 FL Gradient control, **(a)** Input 1 - M_Z, **(b)** Input 2 - $d(M_Z)/dt$, **(c)** Output - G^*. 171

Figure 7.6 Gradient based wheel slip controller membership functions, **(a)** Input 1 – ΔG_{wh} **(b)** Input 2 – γ, **(c)** Output – τ_{Bwh} 173

Figure 7.7 Longitudinal braking forces for scenario 1, **(a)** *rl*, **(b)** *fl*, **(c)** *rr*, **(d)** *fr*..... 177

Figure 7.8 Vehicle dynamics for scenario 1, **(a)** V_x, **(b)** X_g 178

Figure 7.9 Animation preview for the accident avoidance braking manoeuvre scenario 4, **(a)** $t = 1\ s$ (start), **(b)** $t = 3.5\ s$, **(c)** $t = 4.7\ s$ final resting position..... 179

Figure 7.10 Independent gradient control for the FL-VSC vehicle during braking scenario 2, **(a)** *rl*, **(b)** *fl*, **(c)** *rr*, **(d)** *fr*..... 180

Figure 7.11 Longitudinal braking forces for scenario 2, **(a)** *rl*, **(b)** *fl*, **(c)** *rr*, **(d)** *fr*..... 181

Figure 7.12 Vehicle Dynamics comparison for braking scenario 2, **(a)** V_x, **(b)** X_g, **(c)** β_{ss}, **(d)** Steering wheel angle..... 182

Figure 7.13 Animation preview for the accident avoidance braking manoeuvre scenario 2, **(a)** $t = 2\ s$ C-ABS greatest positive sideslip, **(b)** $t = 2.7\ s$ Z-GR greatest positive sideslip, **(c)** $t = 3\ s$ C-ABS greatest negative sideslip, **(d)** $t = 3.6\ s$ Z-GR greatest negative sideslip, **(e)** $t = 6.2\ s$ final resting position..... 184

Figure 7.14 Independent wheel gradient control for FL-VSC vehicle during scenario 3, **(a)** *rl*, **(b)** *fl*, **(c)** *rr*, **(d)** *fr* 185

Figure 7.15 Longitudinal braking forces for scenario 3, **(a)** *rl*, **(b)** *fl*, **(c)** *rr*, **(d)** *fr*.....186

Figure 7.16 Vehicle dynamics comparison for braking scenario 3, **(a)** Global co-ordinates, **(b)** Steering wheel angle, **(c)** V_x.....188

Figure 7.17 Vehicle yaw and stability control variables for braking scenario 3, **(a)** r, **(b)** β_{ss} 189

Figure 7.18 Animation preview for the accident avoidance braking manoeuvre scenario 3, **(a)** $t = 2.7\ s$ FL-VSC greatest negative sideslip, **(b)** $t = 3.2\ s$ C-ABS greatest negative sideslip, **(c)** $t = 4.3\ s$ C-ABS and FL-VSC greatest corrective sideslip, **(d)** $t = 5.9\ s$ final resting position.....190

Figure 7.19 Vehicle controllability and stability variables for braking scenario 4, **(a)** r, **(b)** β_{ss} 192

Figure 7.20 Longitudinal braking forces for scenario 4, **(a)** *rl*, **(b)** *fl*, **(c)** *rr*, **(d)** *fr*.....193

Figure 7.21 Vehicle dynamics comparison for braking scenario 4, **(a)** Global co-ordinates, **(b)** Steering wheel angle, **(c)** V_x.....194

Figure 7.22 Animation preview for the accident avoidance braking manoeuvre scenario 4, **(a)** $t = 1\ s$ Brake pedal activation, **(b)** $t = 1.7\ s$ FL-VSC crosses the target lateral position, **(c)** $t = 2.3\ s$, **(d)** $t = 3\ s$ greatest FL-VSC lateral position, **(e)** $t = 3.8\ s$ Greatest Z-GR lateral position, **(f)** $t = 5.28\ s$ final resting position 195

List of Tables

Table 3.1 Per-phase switching table for a 5L-NPC inverter [164, 166] 67

Table 3.2 Per-phase switching table for a 5L-CHB inverter [157, 178] 67

Table 3.3 Input-output parameters between CarSim and MATLAB/Simulink. 74

Table 3.4 IM and I-PMSM parameters [146, 301] 84

Table 3.5 PI controller gains for IM and I-PMSM model comparison investigation 84

Table 3.6 SMAPE analysis between the MATLAB and Commercial IM and I-PMSM models. 87

Table 3.7 Simscape DC-AC inverter model parameters 88

Table 3.8 Longitudinal tyre parameters for commercial and Simulink tyre models 90

Table 3.9 SMAPE evaluation between the Simulink tyre model and commercial tyre model. 91

Table 3.10 Arduino Mega 2560 microcontroller technical specification [310] 92

Table 3.11 Arduino PIL controller input-output parameters 94

Table 4.1 FL Speed Controller rule base 97

Table 4.2 FL current controller rule base 101

Table 4.3 FL Flux Controller rule base 103

Table 4.4 Vehicle parameters used for this simulation investigation [312] 104

Table 4.5 IM and I-PMSM parameters used for the simulation investigation [146, 301] 104

Table 4.6 A-Class compact vehicle with a 50 kW IM PI-FOC controller gains 107

Table 4.7 PI-FOC and FL-FOC SMAPE performance evaluation. 108

Table 4.8 PI-FOC and FL-FOC SMAPE performance evaluation for the original and variable stator resistance simulations. 117

Table 5.1 ICE Speed-Torque characteristics for the conventional aeroplane pushback vehicle 127

Table 5.2 Vehicle parameters of the typical ICE powered pushback vehicle to be converted into an HEV 127

Table 5.3 Pushback operation descriptions for the typical ICE vehicle and the HEV equivalent 130

Table 5.4 HEV parameters for configuration 1 and configuration 2 133

Table 5.5 Battery pack parameters used in the pushback HEV for both configuration 1 and configuration 2 138

Table 5.6 Aeroplane pushback vehicle powertrain configuration energy requirement and fuel consumption comparison 141

Table 6.1 Null vector modifications [206, 207] 146

Table 6.2 2-Level SVPWM duty ratio calculations converts the vector on-times T_0, T_1, T_2 into phase pulses X, Y and Z to be applied to phase A, B and C respectively [195]. 150

Table 6.3 Peak Torque Profile 152

Table 6.4 Load Torque percentage profile 152

Table 6.5 Inverter output waveform harmonic magnitude and quality analysis 164

Table 7.1 FL YMC rule base [237, 238] 169

Table 7.2 FL Gradient controller rule base 172

Table 7.3 Gradient based wheel slip controller rule base 174

Table 7.4 Vehicle parameters for CarSim vehicle model [237, 238] 176

Table 7.5 Performance Indices comparison for braking scenario 1. Units in brackets represent percentage change from the C-ABS vehicle. 178

Table 7.6 Performance Indices comparison for braking scenario 2. Units in brackets represent percentage change from the C-ABS vehicle. 183

Table 7.7 Performance indices comparison for braking scenario 3. Units in brackets represent percentage change from the C-ABS vehicle. 187

Table 7.8 Performance indices comparison for braking scenario 4. Units in brackets represent percentage change from the Z-GR vehicle. 193

List of Abbreviations

ABS	Anti-lock Braking System
AC	Alternating Current
APU	Additional Power Unit
B-EMF	Back-Electromotive Force
BYMC	Brake Yaw Moment Control
C-ABS	Conventional Anti-lock Braking System
CH_4	Methane
CHB	Cascade H-Bridge
CO	Carbon Monoxide
CO_2	Carbon Dioxide
COF	Coefficient of Friction
DC	Direct Current
DLC	Double Lane Change
DTC	Direct Torque Control
EHB	Electrohydraulic Braking
ESS	Energy Storage System
EV	Electric Vehicle
FL	Fuzzy Logic
FLC	Fuzzy Logic Controller
fl	Front Left
FL-FOC	Fuzzy Logic based Field-Oriented Control
FL-VSC	Fuzzy Logic based Vehicle Stability Control
FL-VSC-GR	Fuzzy Logic based Vehicle Stability Control Gradient command controller
FL-VSC-FR	Fuzzy Logic based Vehicle Stability Control Front Right wheel controller
FL-VSC-RL	Fuzzy Logic based Vehicle Stability Control Rear Left wheel controller
FOC	Field-Oriented Control
FOC-2	Field-Oriented Control – Current Proportional-Integral Controller
fr	Front Right
FWD	Front Wheel Drive
FWS	Front Wheel Steering
GA	Genetic Algorithm
HEV	Hybrid Electric Vehicle
HIL	Hardware-in-the-Loop
ICE	Internal Combustion Engine
IM	Induction Motor
I-PMSM	Interior-Permanent Magnet Synchronous Motor
ISC	Integrated Steering Control
ISSE	Integrated Sideslip Error
IYRE	Integrated Yaw Rate Error
MIL	Model-in-the-Loop
MPC	Model Predictive Control
MTPA	Maximum Torque Per Amp

NL	Negative Large
NM	Negative Medium
NO_x	Nitrous Oxides
NPC	Neutral-Point Clamped
NS	Negative Small
OECD	Organization for Economic Cooperation and Development
P-HEV	Plug-in Hybrid Electric Vehicle
PI	Proportional-Integral
PI-FOC	Proportional-Integral based Field Oriented Control
PID	Proportional-Integral-Differential
PIL	Processor-in-the-Loop
PL	Positive Large
PM	Positive Medium
PMSM	Permanent Magnet Synchronous Motor
PS	Positive Small
PSO	Particle Swarm Optimisation
PWM	Pulse Width Modulation
RIS-SVPWM	Reduced Intermediate Switching Space Vector Pulse Width Modulation
rl	Real Left
RM	Reluctance Motor
rr	Rear Right
RWD	Rear Wheel Drive
RWS	Rear Wheel Steer
SIL	Software-in-the-Loop
SMAPE	Symmetrical Mean Absolute Percentage Error
SMC	Sliding Mode Control
SOE	State of Energy
S-PMSM	Surface Permanent Magnet Synchronous Motor
SPWM	Sine Pulse Width Modulation
SVM	Space Vector Modulation
SVPWM	Space Vector Pulse Width Modulation
SYMC	Steer Yaw Moment Control
THD	Total Harmonic Distortion
TCS	Traction Control System
TV	Torque Vectoring
VSC	Vehicle Stability Control
WTHD	Weighted Total Harmonic Distortion
WLTP	Worldwide Harmonized Light Vehicle Test Procedure
YMC	Yaw Moment Control
Z	Zero
Z-GR	Zero-Gradient
4WS	4 Wheel Steer

Publications

Journal Publications:

1. **S. Cash** and O. Olatunbosun, "Fuzzy logic field-oriented control of an induction motor and a permanent magnet synchronous motor for hybrid/electric vehicle traction applications," International Journal of Electric and Hybrid Vehicles, vol. 9, no. 3, pp. 269-284, 2017.
2. **S. Cash**, Q. Zhou, O. Olatunbosun, H. Xu, S. Davis, R. Shaw, "A New Traction Motor Sizing Strategy for a HEV/EV based on an Overcurrent-tolerant Prediction Model," IET Intelligent Transport Systems, - Awaiting publishing

Conference Papers:

1. **S. Cash**, Q. Zhou, O. Olatunbosun and H. Xu, "Development of a Hybrid Tug for Aircraft Pushback," in EAEC 15th Automotive European Congress, Madrid, 2017.
2. **S. Cash**, Q. Zhou, O. Olatunbosun and H. Xu, "A Robust Fuzzy Logic Field-Oriented Control Scheme for Hybrid and Electric Vehicles," in Biennial International Conference on Powertrain Modelling and Control Testing, Mapping and Calibration, Loughborough, 2018.

Co-authored papers:

1. Q. Zhou, W. Zhang, **S. Cash**, O. Olatunbosun, H. Xu and G. Lu, "Intelligent sizing of a series hybrid electric power-train system based on Chaos-enhanced accelerated particle swarm optimization," Applied Energy, vol. 189, no. 1, pp. 588-601, 2017.
2. Q. Zhou, **S. Cash**, B. Shuai, Y. He, J. Li and H. Xu, "Model-based Swarm Intelligent Optimization for Sizing and Energy Management of Hybrid Electric Vehicles," in Biennial International Conference on Powertrain Modelling and Control Testing, Mapping and Calibration, Loughborough, 2018.

3. Q. Zhou, **S. Cash**, B. Shuai, Y. He, J. Li and H. Xu, "Model-Based Swarm Intelligent Optimization for Sizing and Energy Management of Hybrid Electric Vehicles," in Biennial International Conference on Powertrain Modelling and Control Testing, Mapping and Calibration, Loughborough, 2018.

Chapter One
Introduction

This thesis outlines the research conducted by the author surrounding intelligent traction motor control methods for Hybrid Electric Vehicle (HEV) and Electric Vehicle (EV) applications. These control systems aim to simplify the development of an HEV/EV, increase the energy efficiency of the traction motor/inverter and improve the vehicle's safety. This is achieved by investigating various control technologies for the traction motors, Direct Current (DC) to Alternating Current (AC) inverters – also known as DC-AC inverters - and Vehicle Stability Control (VSC) systems. This chapter presents the purpose for this research in Section 1.1, vehicle development trends and challenges in Section 1.2, the research objectives in Section 1.3 and the thesis structure in Section 1.5.

1.1 Purpose of the Research

The main purposes for the research conducted in this thesis include; Environmental protection on a global and local platform; reducing tensions surrounding the dwindling energy and fuel supply crisis; and improving vehicle safety during emergency braking scenarios.

1.1.1 Environmental Protection

Climate change threatens the future of our survival on this planet. Mankind's impact from the burning of fossil fuels and the production of greenhouse gasses is undeniably the main perpetrator to the rising irreversible global climate [1, 2].

"No challenge poses a greater threat to our future and future generations than a change in climate"

- *Barack Obama, 2015*

Carbon Dioxide (CO_2) is the leading greenhouse gas contributing to climate change [3]. The breakdown of CO_2 emissions by sector in Figure 1.1 shows that 18% of the total CO_2 emissions produced globally comes from the burning of fossil fuels within an Internal Combustion Engine (ICE) in the road transportation sector alone [4, 5]. In addition, an ICE produces large quantities of other greenhouse gasses such as Methane (CH_4) and Nitrous Oxides (NO_x) [6]. Forecasts of the total emissions produced from the transport sector are predicted to increase over the next few decades [7, 8]. The greenhouse gasses produced by an HEV/EV are a fraction of those generated by a purely ICE powered vehicle [9].

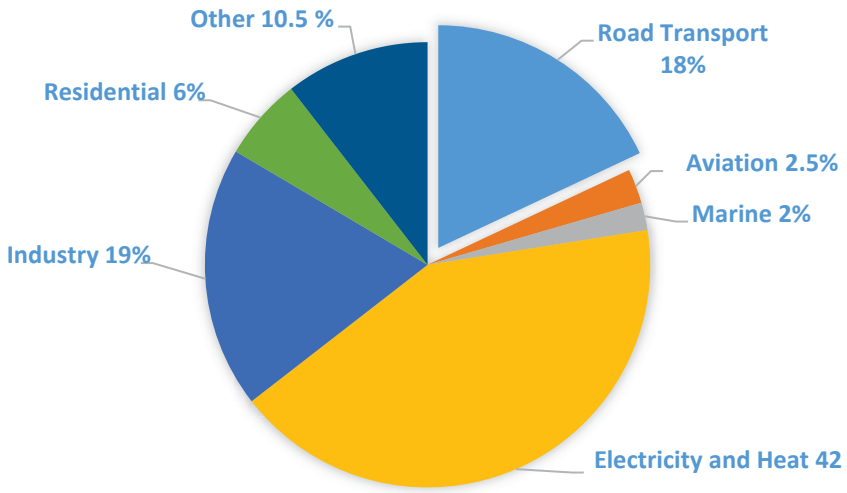

Figure 1.1 Global CO_2 emissions from fuel combustions by sector in 2015 [5]

Particulate matter emissions produced by an ICE pose the greatest threat to human health within urban environments [10]. In the UK alone, nearly 29,000 deaths are attributed to exposure with fine particulate matter each year [11]. Vehicle emissions in urban areas account for nearly 30% of the NO_x and 54% of the Carbon Monoxide (CO) emissions produced globally [12]. NO_x emissions are converted into photochemical smog when exposed to ultraviolet light, extended exposure to this causes eye irritation and deteriorates respiratory functions [13, 14].

Both HEVs and EVs use electric traction motors to drive the vehicle (see Section 2.1). Optimising the traction motor and powertrain components enable the motor to operate in the high efficiency regions for longer and dissipate less energy as heat. For HEVs, this can lead to an increase in fuel economy and possibly a reduction in output emissions [15, 16]. For both Plug-in HEVs (and pure EVs, this would enable the vehicle to drive longer distances between recharging and consequently reduce the burden upon the electrical grid - reducing the emissions from the Electricity and Heat generation sector (see Figure 1.1) [17, 18]. Tools that aid in the development of an HEV/EV by correctly sizing a traction motor can influence the total emissions produced by the vehicle. Development of an HEV/EV can be difficult, time consuming and expensive [17, 18]. Intelligent traction motor control techniques that can be applied to multiple motors and vehicles would enable a vehicle manufacturer to easily optimise their HEV/EV design to improve efficiency and reduce emissions. The more tools available to vehicle manufacturers that reduce the development time and cost might increase the number of HEV/EVs produced and therefore reduce the overall global emissions produced by the transportation sector.

1.1.2 Energy and Fuel Scenario

The current World Energy Outlook forecasts higher and an ever-growing need for more energy and fuel over the next few decades [19]. The New Policies Scenario is expected to require an additional 20% increase in energy and a 32% increase in oil over the Sustainability Development Scenario. Figure 1.2 shows that from the total energy demand, nearly 50% of the global energy consumption by end-user is expected to come from the transportation sector [20].

An HEV consumes less fuel than a purely ICE powered vehicle, an EV consumes none (directly). As popularity with these vehicles increase, the burden on the current fuel stocks used

within the transport sector reduces. However, it is thought that a full EV society would merely shift the energy demand onto the power generation sector. Therefore, an equal effort in the move towards renewable energy is also required to fully exploit the benefits HEV/EVs and alleviate the fuel and energy crisis

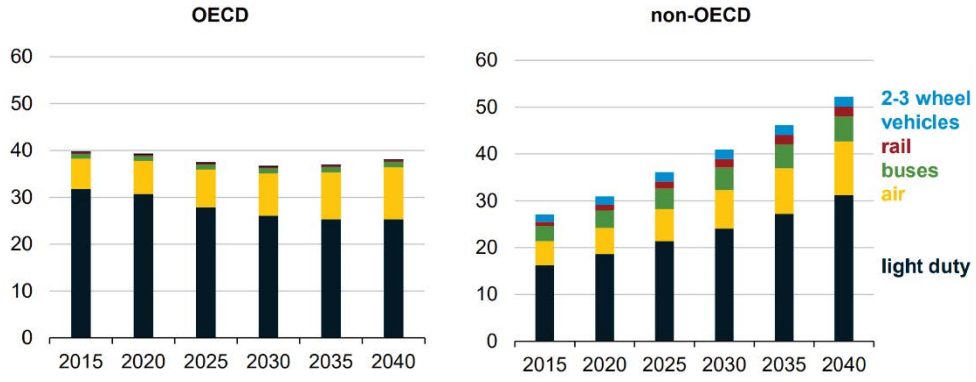

(a) (b)

Figure 1.2 Passenger transportation energy consumption estimates up to the year 2040 between **(a)** Organization for Economic Cooperation and Development (OECD) countries and **(b)** Non-OECD countries, scale in quadrillion Btu [22]

As with Section 1.1.1, if the efficiency of these vehicles can be improved by optimally sizing the powertrain components and efficiently controlling the traction motors, then it may elevate some of the foreseen energy and fuel demand as HEVs will have increased fuel economy and EVs will be able to drive for longer between charging.

1.1.3 Vehicle Safety

Road traffic incidents are the result of; excessive speed, driving in poor weather conditions, driver error or distracted drivers and component failure. There were nearly 2,000 deaths on UK roads in 2017 and a further 28,000 serious injuries, of which 57% of total casualties involved passenger vehicles [21]. In 2016, excessive speed in harsh conditions accounted for nearly 24% of fatal incidents [22].

Safety is one of the highest priorities in vehicle design. HEV/EVs have exceptional dynamic performance and stability control because the electric traction motor/s offer high frequency and instant torque modulation, simple feedback to the control system and easy estimation of the current driving conditions [23, 24, 25]. Intelligent control over the traction motor/s therefore allow an HEV/EV to have a shorter breaking distances and superior steering controllability over an ICE counterpart [26, 27, 28]. These improved safety features ensure that there is a greater chance that a driver would be able to remain in control of their vehicle during an emergency manoeuvre and reducing the total number accidents and fatalities.

1.2 Vehicle Development Trends and Challenges

It is generally considered by the general public and researchers within the automotive industry that the HEV/EV is the next technological paradigm for the transport sector for personnel, public and fleet vehicles [29, 30]. Figure 1.3 shows that an estimated 55% of all new car sales are expected to be electrified by 2040, this accounts for 33% of the total global fleet [31]. The growth in HEV/EVs has been attributed to both the public's concern over the issues (discussed in Section 1.1), but also due to planned legislation requiring vehicle manufactures to move towards an EV future [32].

The reason for the growing popularity of electrified vehicles is that they consume less fuel and emit lower emissions when compared to pure ICE powered vehicles [33]. The current challenges in reaching an all-electric vehicle market from the consumers' point of view include; limited driving range [34], long charging times, the upfront cost and lifetime of the battery packs [35, 36].

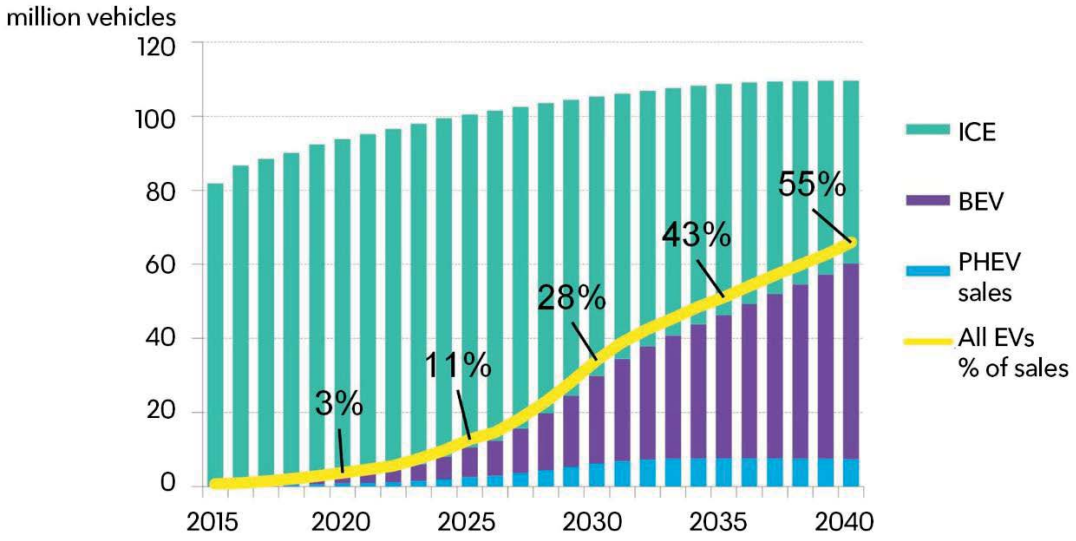

Figure 1.3 Global HEV/EV Sales forecast up to 2040 [33]

Other technological issues include; the impact on the electrical grid [37], material acquirement for batteries [38] and battery recyclability [39, 40]. These issues are being addressed through research and development in their respective fields. No single solution solves all the current challenges, but it requires the collective effort in all areas of science and engineering [41, 42]. This thesis aims to contribute to the current trend in HEV/EV development and tackle some of the major challenges facing their development, the key objectives undertaken as explained in Section 1.3.

1.3 Research Objectives and Approach

The original research objective of this thesis was to investigate intelligent control systems for an HEV/EV. This was separated into the following objectives as follows:

1) To understand the key technical milestones and the current state of the art literature for traction motor modelling, power delivery and intelligent control techniques for HEV/EV applications.

2) To develop tools which simplify the control system of a traction motor system in order to speed up and reduce the development cost of an HEV/EV.
3) To develop tools which optimise the powertrain components of an HEV/EV in order to increase the energy efficiency, reduce fuel consumption and reduce output emissions.
4) To investigate and develop energy efficient methods of powering a traction motor for HEV/EV applications.
5) To develop methods of controlling an HEV/EV's traction motor based powertrain to improve the vehicle's safety during an emergency manoeuvre.

The general approach to the research conducted in this thesis will follow a similar pattern; First, simulate the control system using pre-existing established control methods. Secondly, develop new control techniques based on the gaps in the current literature. Thirdly, verify the new control technique's ability for hardware implementation. Finally, evaluate and compare the new control method to the pre-existing method. This research approach will be achieved largely through detailed simulation studies in MATLAB/Simulink utilising CarSim vehicle models and an intensive series of Processor-in-the-loop (PIL) verification experiments. This is explained in more detail in Section 3.1.

1.4 Key Contributions

The main contributions and novel ideas investigated within this thesis include:

1. A new traction motor Field-Orientated Control (FOC) scheme that can control multiple motor topologies and HEV/EV powertrain architectures without the need for re-tuning. A further investigation into controller robustness under the effects of variable motor parameters is conducted, this type of investigation is rarely done in literature and has never been done for HEV/EV applications.

2. A new empirical data based traction motor model is developed and its application as a traction motor sizing tool is shown. The effects of early stage traction motor sizing on the final vehicle's powertrain design, energy usage and fuel economy is then explored with a real-world case study.
3. An on-line reduced switching inverter control scheme is developed which increases the inverter's efficiency without compromising on the output waveform harmonic distortion. The performance of the inverter control scheme is then investigated over a wide range of traction motor operating regions, unlike other investigations which only investigate a few operating points.
4. A Vehicle Stability Control (VSC) system that improves the controllability and stability of an HEV/EV during emergency braking manoeuvres is developed that requires minimal vehicle parameters within the control system, is insensitive to variable vehicle parameters and is tuneable to meet a vehicle's target dynamic objectives. Whereas other researchers only investigate the a few simple braking manoeuvres, this VSC system is analysed over numerous real-world emergency braking scenarios with a further investigation into the likelihood of if the vehicle could be controlled by real drivers.

1.5 Thesis Outline

Chapter Two reviews the current state of the art control techniques relevant to the research undertaken in this thesis. The limitations and real-world challenges associated with traction motor modelling and control for HEV/EV applications are investigated first. The various control systems and objectives of DC-AC inverters are then explored. Finally, the VSC systems which control the wheel slip and yaw dynamics of an HEV/EV are reviewed.

Chapter Three introduces the general vehicle dynamics, traction motors and inverters modelling and control techniques which are conventionally used in vehicle simulations. An explanation as to how and when they are used in this thesis is given. The experimental PIL procedure adopted within this thesis is then described which is used to verify the control system's readiness to move onto full hardware validation.

Chapter Four develops a Fuzzy Logic (FL) based Field-Orientated Control (FOC) scheme to control any HEV/EV powertrain architecture and multiple motor topologies without the need for re-tuning. A detailed comparison between the simulated FL based FOC scheme and a conventional Proportional-Integral (PI) controller based FOC scheme is given with a further investigation into the controller's robustness.

Chapter Five develops a new HEV/EV traction motor sizing strategy whereby an overcurrent-tolerant prediction model is used to estimate the dynamic and thermal characteristics of a motor operating in the overcurrent region. A case study is explored where this sizing strategy is used to convert an aeroplane pushback vehicle into a series HEV. The feasibility of two possible HEV configurations are then explored further.

Chapter Six develops an on-line Reduced Intermediate Switching Space Vector Pulse Width Modulation (RIS-SVPWM) scheme for multilevel HEV/EV DC-AC inverters. The RIS-SVPWM scheme identifies the switching patterns of the voltage vectors enclosing the reference voltage on-line and controls the switching devices of the inverter with minimal switching. A detailed comparison between the switching count and harmonic quality of the waveforms generated by the RIS-SVPWM scheme against a previous on-line scheme is then given.

Chapter Seven develops a FL based VSC system that has been developed in this thesis which improves the controllability and stability of an HEV/EV during combined emergency braking

and steering manoeuvres. A detailed comparison between the simulated FL based VSC system, a conventional Anti-Lock Braking System and an advanced wheel slip controller is given.

Chapter Eight summarises the major points from the research conducted in this thesis. A critical analysis of this research is given and with recommendations for future work.

Chapter Two
Literature Review

This chapter presents a comprehensive review of the key literature which examines the theoretical concepts, state of the art technology and research trends surrounding; traction motor modelling and control, methods of powering the traction motor and intelligent motor control techniques that improve vehicle safety. Firstly, a broader view of HEV/EV powertrain architectures are discussed in Section 2.1 before moving onto various traction motor characteristics, modelling and control theories in Section 2.2. Popular DC-AC inverter topology and control theories are then presented in Section 2.3. Finally, state of the art Vehicle Stability Control (VSC) systems for HEV/EVs are investigated in Section 2.4. At the end of Section 2.1 - Section 2.4, the research gaps from the literature reviewed will be stated. Section 2.5 will summarise these gaps and present a set of specific research objectives to be investigated in the remainder of this thesis.

2.1 The HEV and EV

The Electric Vehicle (EV) dates back to the mid-1800s, they were rudimentary in comparison to the vehicles of today and their effectiveness in comparison to horse drawn carriages was still under debate [43, 44]. The Hybrid Electric Vehicle (HEV) later utilised an Internal Combustion Engine (ICE) to charge the battery pack and provide additional power when travelling up gradients [45]. The HEV/EVs of today are more refined than their predecessors and because their potential driving range increases are approaching comparable values of a pure ICE vehicles they are becoming more appealing to customers.

2.1.1 HEV Powertrain Architectures

An HEV stores energy on-board in more than one form, most notably as hydrocarbon-based fuel and electricity stored within an Energy Storage System (ESS). An Additional Power Unit (APU) provides power to the vehicle's DC-bus to charge the ESS and/or power the traction motors. Conventional HEV APU systems consists of an ICE, but more research for future HEVs to use fuel cells as an APU is being conducted as they generate no harmful emissions and no noise [46, 47, 48].

Depending on the powertrain architecture, an HEV is able to provide torque to the driven wheels using a traction motor alone and/or be coupled to the ICE to provide additional power. The traction motors are connected to the vehicle's DC-bus which is powered by a battery pack. An ultracapacitor bank may be used if the battery pack cannot provide the peak output power alone [49, 50]. Plug-in HEVs (P-HEV) have grown in popularity because they are able to charge the ESS from an external source [31]. HEV powertrains will normally fall within one of the three following architectures shown in Figure 2.1 [51, 52, 53, 54]:

1) Series HEV – Shown in Figure 2.1(a), this architecture is closely related to a pure EV where only the traction motor/s provide the driving torque to wheels. The ICE is not mechanically connected to the wheels but instead spins the rotor of a generator to charge the ESS. This architecture has the highest efficiency because the ICE runs at its most efficient point, but the vehicle's dynamic performance is limited to the performance of the traction motor/s.
2) Parallel HEV – The traction motor and ICE are mechanically coupled by a gearbox which allows them to provide torque to the driven wheel together or independently from one another as shown in Figure 2.1(b). Typically, the traction motor is used at low speeds or low torque applications and the ICE takes over once a threshold has been reached. The ICE can provide mechanical power to the motor which will act as a generator to charge the ESS.

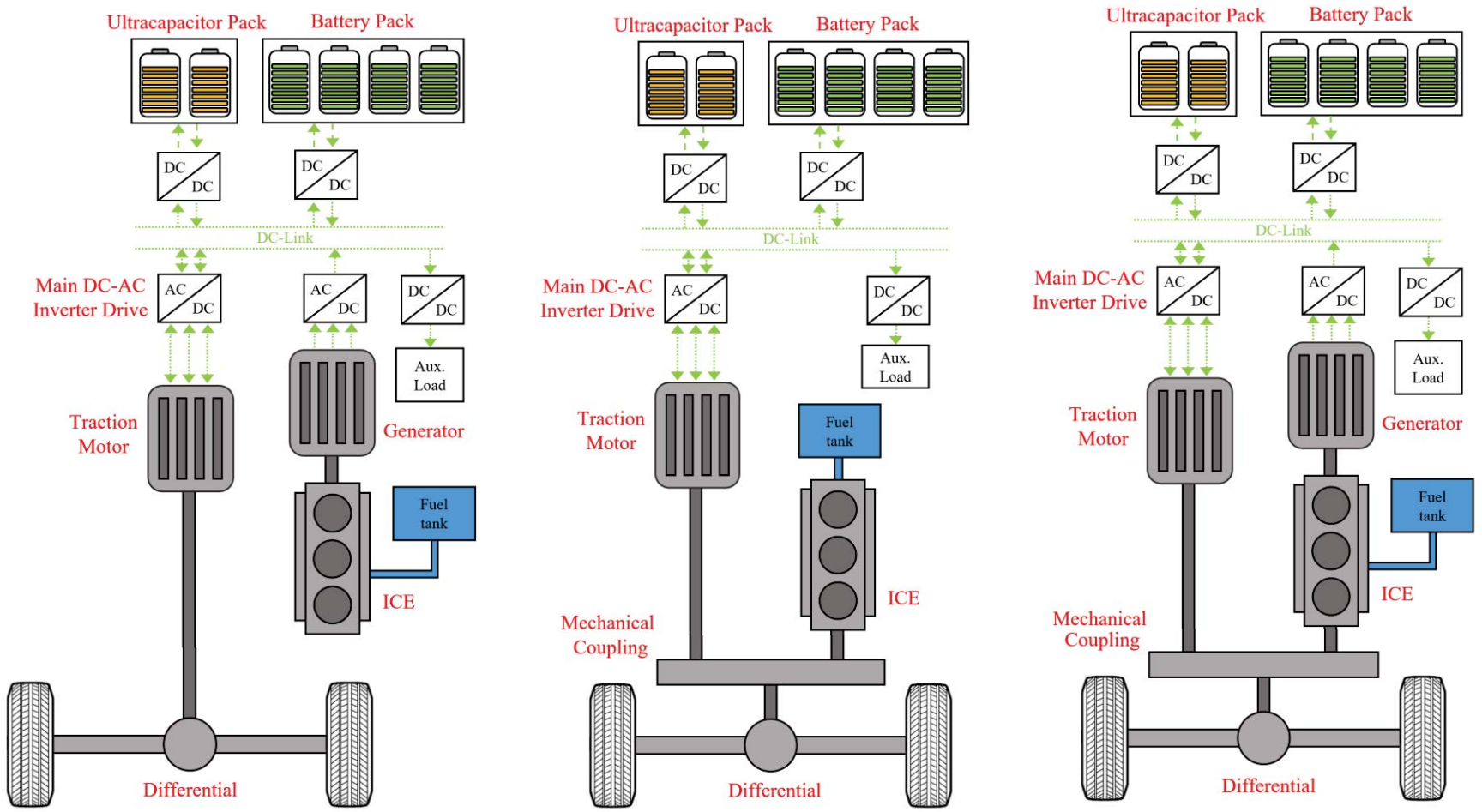

Figure 2.1 HEV powertrain architecture, **(a)** Series-HEV, **(b)** Parallel-HEV, **(c)** Power Split-HEV

3) Power-Split HEV – This behaves similarly to a parallel HEV, but with the inclusion of a dedicated generator the vehicle is also able to act as a series-HEV as shown in Figure 2.1(c). This is a popular powertrain architecture for HEVs because even with the additional costs it allows the greatest control freedom between the two powertrain systems. This was most notably popularised through the Toyota Prius [55, 56].

2.1.2 EV Powertrain Architectures

An EV only uses electric traction motor/s to provide torque to the driven wheels. They do not contain an on-board APU so the ESS must be charged from an external source. The driving range of an EV is limited to the energy stored within the ESS alone (excluding any regenerative braking abilities). There are numerous powertrain architectures for an EV, the following shown in Figure 2.2 are the most common [57, 58]:

1) A single motor with a single/multi speed gearbox as shown in Figure 2.2(a). The power flow of this vehicle is similar to a conventional vehicle utilising a single ICE. The ESS powers the traction motors which provides torque to the driven wheels alone.
2) Dual traction motors with separate gearboxes as shown in Figure 2.2(b). This system allows for greater freedom when choosing between Front-Wheel Drive (FWD), Rear-Wheel Drive (RWD) and All-Wheel Drive. This architecture is adopted by the Tesla Model S P100D which uses a small motor on the front axle while cruising at low speed, and a high-power motor on the rear axle for quick acceleration [59].
3) The use of multiple independent motors as shown in Figure 2.2(c) is able to regulate the torque at any of the driven wheels without the need for complex torque splitting differentials with full freedom of where to apply torque.

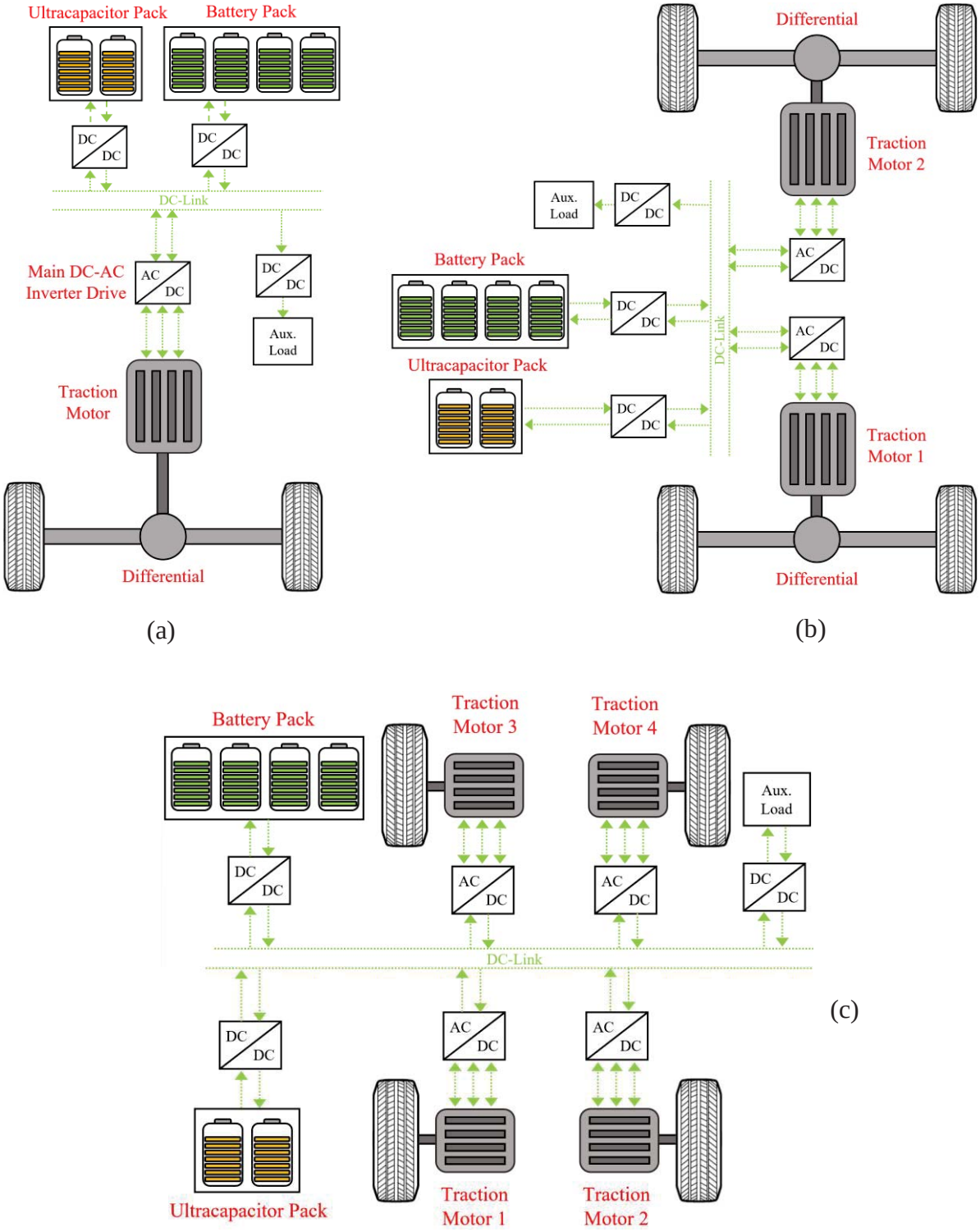

Figure 2.2 EV Powertrain Architecture, **(a)** Single motor with single/multi speed gearbox, **(b)** Dual motors with single speed transmissions, **(c)** Four independent in-wheel motors with single speed gearboxes

2.2 Traction Motors for HEV/EV Applications

2.2.1 Background into Electric Motors

Nikola Tesla's ground-breaking presentation to the American Institute of Electrical Engineers in 1888 introduced his patented Alternating Current (AC) electric motors. He presented three motor topologies; the synchronous motor, the synchronous Reluctance Motor (RM) and the Induction Motor (IM) which became the starting point for future AC motor drives [60]. In 1889, Mikhail Dolivo-Dobrovolsky added a third phase to an IM to reduce the inherent torque ripple problems of Tesla's two-phase motors [61]. Then only three years after Tesla's original paper, General Electric and Westinghouse collaborated on developing an IM for mass production using a squirrel cage rotor in 1891 [62]. Cahill published the complete theory of Permanent Magnet Synchronous Motors (PMSM) in 1962 by attaching permanent magnets to the squirrel cage of an IM [63].

Charles Steinmetz wrote several publications about how equivalent analytical circuits are an effective tool for representing and analysing AC motors [64]. Robert Park's and Edith Clarke's voltage transformations significantly simplified the analysis of AC motors [65, 66]. This allowed the three-phase system to be separated into individual torque and magnetic flux producing current components.

2.2.2 Traction Motor Topology Characteristics

DC motors were a popular choice for transportation applications in the early 20th century because they are relatively simple in construction and produce high torque at low speeds [67]. However, due to their dependence on carbon commutators they were unreliable, generated high friction at high speeds, had a low specific power density and their relatively large volume saw them being overtaken by the AC traction motor.

One factor which determines a motors eligibility for HEV/EVs applications is the output torque ripple from the rotor shaft. This ripple can be generated either by mechanical imbalances (due to uneven wear of rotor shaft bearings, etc.), poor motor design or excessive current distortion (Total Harmonic Distortion $\geq 5\%$). A general rule for motor design and control systems is that a torque ripple magnitude $\leq 1\%$ of the motor's rated torque is *desirable* for most applications including HEV/EVs [68].

Currently, the four common traction motor topologies for HEV/EV applications include the IM, Surface-PMSM (S-PMSM), Interior-PMSM (I-PMSM) and the RM. The cross sectional view of these motors are shown in Figure 2.3 and are characterised as follows [69, 70, 71, 72]:

1) IM – As shown in Figure 2.3(a), the IM has no magnets but instead induces its own magnetic flux within the windings of the rotor on the basis of Lorentz's law. Their simple construction makes them inexpensive, rugged, and reliable. These qualities make them an ideal candidate for HEV/EV traction motors. In addition, they have good dynamic performance and a wide speed range. However, they are susceptible to rotor winding failure due to overheating which means they have a relatively lower efficiency and require the most amount of cooling.

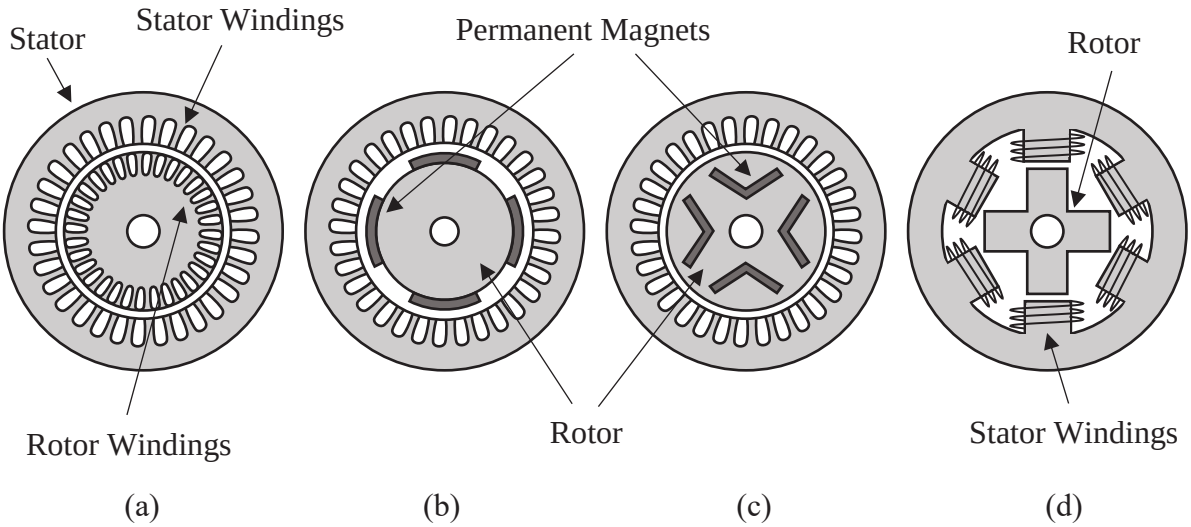

Figure 2.3 Traction motor constructional topologies cross-section view, **(a)** IM, **(b)** S-PMSM, **(c)** I-PMSM, **(d)** RM

2) S-PMSM – This motor uses permanent magnets attached to the outside of the rotor as shown in Figure 2.3(b). Because the permanent magnets produce a constant magnetic flux, no current is required to be induced in the rotor (as with an IM), and therefore have higher efficiency and require less cooling. However, the permanent magnets are brittle, sensitive to temperature changes and because the magnets are on the outside of the rotor, they are vulnerable to demagnetization and create a large air gap between the rotor and stator.
3) I-PMSM – Similarly to the S-PMSM, this motor also uses permanent magnets attached to the rotor, but they are now buried inside as shown in Figure 2.3(c). When placed inside the rotor, the magnets retain themselves without additional fixings, are less prone to demagnetization and reduce the air gap between the rotor and stator. As with the S-PMSM the magnets are expensive and their orientation within the rotor requires careful attention since they induce reluctance torque. The cross-sectional shape of the magnets within the rotor allows for different torque-speed characteristics. These have been the most popular choice for traction motors in modern HEV/EVs [67].
4) RM – These motors have no rotor windings or permanent magnets as shown in Figure 2.3(d). Instead, they use reluctance torque to spin the rotor using a carefully designed rotor core. The large rotor mass makes this motor less susceptible to failure due to overheating. However, they are not currently used for traction applications because they suffer from undesirably large torque ripple, poor noise quality, excessive vibration, low power density and require dedicated inverter circuits [73].

2.2.3 Traction Motor Modelling Techniques

Analytical models provide a good trade-off between computational effort and accurate characterisation of an AC motor, these are often used during the development stages of an HEV/EV [70, 71, 74, 75]. These models represent the motor as equivalent electrical circuits constructed from smaller components (resistors, inductors and voltages) whose currents determine the torque and magnetic flux of the motor. Per-phase analytical models provide useful information about the motor's dynamic performance and power requirements during stead-state conditions, but cannot be used with more advanced control methods (see Section 2.2.4) [76]. Magnetic circuit analysis or Finite-Element Analysis of the motor are extremely detailed and accurate representations of the physical motor, but due to their high computational requirements they are usually confined to AC motor development and not used for HEV/EV simulations [67].

Simple empirical data based torque-speed curves and efficiency maps characterise the traction motor/s of an HEV/EV when a low simulation time is preferred over model accuracy [77, 78]. This is done at the cost of losing some motor control analysis, but fewer motor parameters are required. This approach is used for preliminary vehicle design analysis or where the primary objective of the research is not heavily reliant on the motor's current control (e.g. vehicle stability control).

2.2.4 Advanced Traction Motor Control Schemes

Field-Oriented Control (FOC) is a popular motor control method because it allows for independent control over a motor's torque (q-axis i_{qs}) and magnetic flux (d-axis i_{ds}) producing current components [79, 80, 81]. During the late 60's, Blaschke and Hasse proposed the Indirect-FOC and Direct-FOC schemes as a way of controlling IMs and PMSMs respectively

[82, 83]. The general theory of both FOC schemes are similar to one another, but I-FOC has to estimate the position of the IM's rotor flux wave because it cannot be measured easily or accurately. When compared to the preceding scalar V/Hz motor control, FOC increases the torque responsiveness, improves the overall efficiency by avoiding oversaturation of the magnetic material and improves field-weakening performance at high speeds [84, 85, 86, 87]. However, FOC requires multiple independent controllers for the motor's speed and current components that must be carefully tuned, multiple voltage and current sensors, a rotor speed sensor (if sensorless FOC is not used) and an independent Pulse Width Modulation (PWM) scheme to generate inverter switching patterns.

Direct Torque Control (DTC) in a similar way to FOC tries to minimise the error between the dq-current axes. DTC uses a look-up table to directly control the inverter's switching patterns and achieve the target voltage vector [84]. This negates the need for current controllers and an external PWM module. Generally, DTC offers a greater torque responsiveness over FOC, but generates high current/torque ripples, produces variable-switching behaviour, high noise and offers poor control at low speed [85].

Model Predictive Control (MPC) is another popular control technique for AC motors [86, 87]. An optimisation problem is used to find the optimal inverter switching sequence to meet an objective cost function using a model of the motor within the control scheme. MPC has shown to be more responsive than FOC and more control freedom than DTC [88]. A major drawback of MPC is the large computational effort required to simulate all the possible scenarios for each action [89]. This confined MPC to slow varying processes such as chemical plant and industry process applications for many years [90]. However, with improved modern processors the use of MPC for real-time applications such as motor control schemes have grown in popularity. The accuracy of MPC is greatly affected by model parameters and signal noise

in the feedback loops. These effects can be minimised with improved parameter estimators and filters, but the added computational complexity rises further [91]. The resemblance of MPC based current control to hysteresis current controllers in DTC can require variable inverter switching frequency and can promote higher torque ripple [92]. To reduce the computational burden of MPC, the model used within the control algorithm can be simplified. This then produces a trade-off between controller accuracy and computational effort [93, 94, 95, 96].

MPC for motor control operates either as Predictive Torque Control [97, 98] or Predictive Current Control [99]. Predictive Torque Control aims to minimise the error between the electromagnetic torque and the magnitude of the motor flux by generating appropriate target axis currents. Predictive Current Control aims to minimise the dq-current error by selecting suitable inverter voltage vectors [98]. The computational effort of Predictive Current Control grows exponentially with inverter size as the total number of available switching states grows [100]. Samaranayake [101] reduced the degradation of a traction motor by minimising the power losses. The MPC scheme by Schubert [102] was used to optimise the trade-off between torque and flux producing current control to improve motor efficiency and torque responsiveness, this provides good performance during start-up operations.

2.2.5 Optimised FOC Strategies

Because the magnets of an I-PMSM are buried within the rotor, the magnetic circuit of the motor becomes disturbed and a d-axis reluctance torque is generated. Jahns [103] developed the Maximum-Torque-Per-Amp (MTPA) control for an I-PMSM to exploit the motor's d-axis reluctance torque to produce useful work. Jahns later extended the MTPA theory into the constant-power speed region of the I-PMSM to cover the motor's entire torque-speed range [104]. MTPA allows smaller permanent magnets to be used, increases the power density and

efficiency of the motor and improves the torque responsiveness. Morimoto [105] applied the MTPA theory to both S-PMSMs and I-PMSMs while abiding to current and voltage constraints. Morimoto [106] also explains how the supply voltages must be compensated to account for the cross-coupling between the dq-axis.

A similar MTPA theory was developed by Kim [107] for an IM. Maximum Efficiency Per-Amp control theory by Lemmens [108] searches for the smallest d-axis current which generates the lowest iron and inverter switching losses for the same target torque output using a gradient based optimisation problem. Sergaki [109] showed how the efficiency of an IM increases by reducing the d-axis current when the motor is under light load and use a larger q-axis current instead to produce more useful work.

2.2.6 Real World Motor Control

The physical properties of a motor (electric resistance of the rotor/stator windings, inductance and magnetic flux) vary with temperature [110]. FOC requires accurate representations of these parameters in order to operate optimally and the control parameters representing these properties should also change to reflect their physical counterparts [111].

Matsuo [112] developed an on-line gain scheduling scheme to improve the FOC performance of an IM susceptible to variable rotor resistance. Bose [113] showed how to compensate the B-EMF voltage to account for changes in the permanent magnet's magnetic flux strength. Holtz [114] and Marino [115] developed on-line rotor flux estimation methods to identify the parameters of an IM for direct use within the FOC scheme. Lemmens [108] also provides a temperature control scheme to limit the current without affecting the Maximum Efficiency Per-Amp control of the motor and prolonging the lifetime of the motor. However, this control scheme yields undesirable torque/current ripple and produces audible noise from

running the inverter at a low switching frequency. These publications highlight some of the difficulties that arise from the variable motor parameters and how the control scheme should be modified to ensure optimal control. However, these methods require highly detailed and time-consuming experimentation for each particular motor under investigation.

2.2.7 Controller Types for FOC

Sliding Mode Controllers (SMC) for FOC offer quick responsiveness and great robustness with a well-designed sliding surface. SMC speed [116] and current [117] controllers have superior control over Proportional-Integral (PI) counterparts. However, SMCs suffer from implementation issues due to the chattering nature of the controllers at steady-state if not properly accounted for with adaptive smoothing functions [118, 119]. Also, designing a good sliding surface is not an intuitive process when dealing with complex non-linear systems.

Neural Networks for motor speed and current control are computationally efficient and robust once they are trained [120, 121]. However, these controllers would again require re-tuning and re-training between systems. An artificial neural network speed controller trained via a GA showed superior speed tracking and torque responsiveness over a conventional PI speed controller [122]. The neural network developed by Lftisi [123] is trained on-line for the speed control of an IM with the aim of mimicking an optimally tuned PI controller. This negates the need for time consuming off-line manual PI controller tuning or neural network training, but the effect of variable motor parameters and the on-line training time is not discussed.

FOC schemes commonly use PI controllers to regulate the speed of a vehicle/motor, the independent current components and the magnetic flux because they are simple to use, require little computational effort and operate with minimal steady-state error if tuned correctly [124,

125]. If tuned incorrectly then these controllers may produce unstable or non-optimal vehicle/motor control.

A Fuzzy Logic Controller (FLC) offers an accurate representation of how a vehicle's speed would be controlled by a real driver and therefore a better estimation of how the physical vehicle would perform in the real world. A FLC also offers greater robustness over a PI controller because it is insensitive to variable motor parameters, similar controller designs have appeared for numerous publications using vastly different motors [126, 127, 128, 129, 130, 131].

2.2.8 PI vs Fuzzy Logic for FOC

2.2.8.1 Speed Control using FOC

Numerous heuristic optimisation techniques [85] have been developed in response to PI controller gain tuning including; Particle Swarm Optimisation (PSO) [132, 133], Genetic Algorithms (GA) [125, 134] and Backtracking Search Optimisation [135]. Each of these optimisation methods improve the control performance of the PI controllers without an intensive manual iterative tuning process but require re-tuning for different FOC systems and may still suffer from variable motor parameters.

One inherent characteristic of PI controllers is that they tend to overshoot their control objective if improperly tuned, this is unrealistic and not desirable for vehicle control applications. For example, a PI speed controller that overshoots the target velocity will have to apply the brakes in order to reduce the vehicle's speed. In the real world, a driver would reduce the accelerator pedal ahead of the approaching target velocity. This has been investigated by numerous researchers who have compared the performance of PI vehicle/motor speed controllers against FLCs [136, 137, 138].

An adaptive Fuzzy Logic (FL) controller by Zeb [139] used to control the speed of an IM was shown to not only have greater robustness over a PI speed controller, but to also reduce the steady-state error by on-line updating the input and output gains via an optimisation algorithm. Hybrid PI-FLC speed controllers also reduce some of the overshooting and robustness difficulties that arise from pure PI speed controllers for FOC [140, 141, 142, 143, 144]. These use a PI system to tune the input and output gains of a FLC and combine some of the robustness of a FLC with the small steady-state error of a Proportional-Integral-Differential (PID) controller. Alonge [145] presented a PI-FLC system to control a motor's speed, command flux and dq-axis current components. This has good variable tracking performance, but Alonge offered no robustness analysis with variable motor parameters. A PI-FLC speed controller by Masiala [146] uses a PI controller to change the input/output gains, membership function and rule base of a Takagi-Sugeno type FLC. The PID elements of these hybrid controllers still require an iterative tuning process for each independent system being controlled. The FL-PID speed controller presented by Rohan [147] uses a FLC to change the proportional and integral gains of a PI controller and reduces the overshooting characteristics. However, this does not use any current control so the performance of this system cannot be fully validated.

2.2.8.2 Current Control using FOC

The output from a PI or FL speed controller in an FOC system is either a target output torque or a target q-axis current. If a FL speed controller is used in conjunction with a PI q-axis current controller, the benefits of the FL speed controller may not be as effective if the motor's torque overshoots its target value or if the current controller is susceptible to parameter changes. FLCs also show superior current control over PI counterparts for both the q-axis i_{qs} [148] and d-axis i_{ds} [149, 150, 151] currents. Lubin [148] compares independent FL speed and i_{qs} current

controllers to a PI based FOC system. The highly robust FLCs proved to be insensitive to variable parameter changes when the rotor resistance was intentionally altered, whereas the PID controllers tuned for the original motor system became unstable and had a sluggish response.

Typically, the target flux producing d-axis current in an IM is not as dynamic as the torque producing q-axis current, it remains constant up to the motor's rated speed and gradually reduces as the motor speed increases in the constant power region. It might be seen that the d-axis current does not require the same attention as the q-axis current and a PI controller is sufficient for most circumstances. But as explained previously in Section 2.2.6, varying parameters may affect the motor's ability to produce flux and the d-axis current tracking may suffer. In an I-PMSM, the d-axis current's reluctance torque requires the regulator be more active. FOC schemes that incorporate FL d-axis current controllers have improved robustness as with the FL q-axis current controllers [149, 150, 151].

2.2.9 Research Gaps in the Field of Traction Motor Modelling and Control

FOC is now thought to be a mature branch of motor control. Generally, the scope of intelligent motor control is moving in the direction of sensorless-FOC to estimate the rotor/flux position without rotary encoders, fault detection mechanisms and control of future motor topologies such as switched and synchronous reluctance motors for HEV/EV applications. However, from the literature reviewed in Section 2.2, the author recognises the following gaps in the literature which aim to be resolved within this thesis:

1) The high robustness of FLCs and their insensitivity to variable motor or vehicle parameters makes them ideal for vehicle control applications. However, it has not been shown how a single FOC system (using FLCs or any other controller type) can be used to control multiple

different motor topologies, powertrain architectures or with variable motor parameters for HEV/EV applications.

2) Only a small handful of the literature examined in this section acknowledges the effects of variable motor parameters and their effect on the control algorithm. This should be taken into account for every control system designed as it will drastically lower the performance of the system.

3) All the FOC algorithms and analytical traction motor models reviewed in this section require detailed motor parameters that are only obtainable from an intensive series of experiments. When multiple motors are under investigation, the time and cost required to conduct multiple experiments on each motor in order to find all the required parameters becomes impractical. However, the author is yet to find an empirical motor model that considers the constraints of operating within the overcurrent region as a simpler and more cost-effective alternative for traction motor sizing during the early development stage of an HEV/EV.

2.3 DC-AC Inverters for Traction Motors

A DC-AC inverter modulates a DC voltage into multiple stepped DC voltage levels so that the fundamental harmonic of the output resembles an AC waveform. An inverter is classified according to its construction and the number of output voltage levels that it can generate. Multilevel inverters can output more than two voltage levels per phase. Richard Baker and Lawrence Bannister developed a multilevel Cascaded H-Bridge (CHB) inverter by stringing together multiple H-Bridge inverters and multiple DC sources [152, 153, 154]. Nabae [155] developed a 3-level (3L) Neutral-Point Clamped (NPC) inverter which required only a single DC source to generate multiple voltage levels. Nabae also showed how a multilevel inverter

increases the combined efficiency of the inverter and motor as well as reduces high frequency harmonics over the 2-Level (2L) predecessors.

2.3.1 Inverter Topologies for HEV/EVs

The inverters used in HEV/EVs convert the DC voltage of the battery pack to 3-phase AC power for the traction motor. Both NPC and CHB inverters are common topologies used in HEV/EVs [156, 157, 158, 159, 160]. The schematic diagrams for a 5-Level (5L) NPC and CHB inverters are shown in Figure 2.4(a)-(b) respectively. The NPC inverter uses a single large DC voltage battery, whereas the CHB inverter uses multiple smaller DC battery packs.

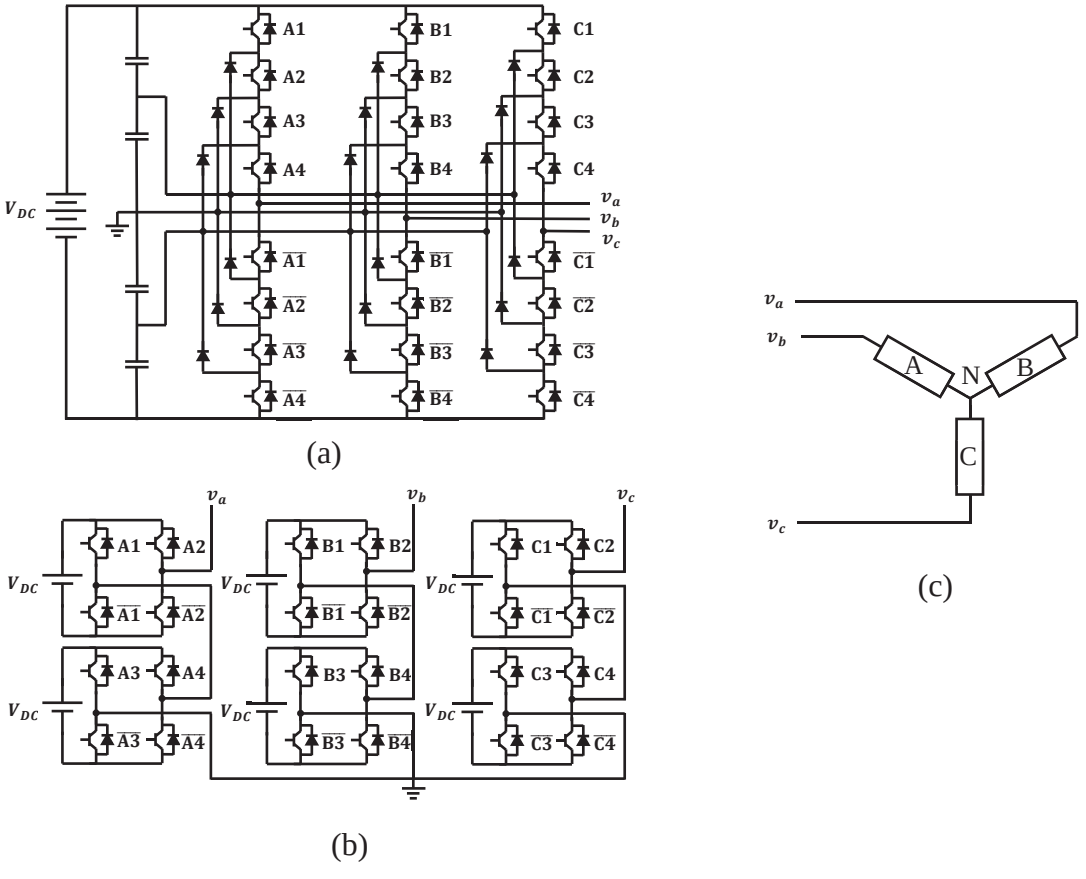

Figure 2.4 Five -Level inverter topologies, **(a)** Neutral-Point Clamped, **(b)** Cascaded H-Bridge, **(c)** Isolated Neutral load

Numerous surveys investigate the control, topology and general applications of multilevel inverters [161, 162, 163] with their application in HEV/EV traction drives. The largest benefits

multilevel inverters have over 2-level inverters include; lower rate of change in output voltages, lower harmonic distortion, smaller common-mode voltages and can operate at lower switching frequencies. Multilevel inverter surveys directed at HEV/EV applications compare Voltage source inverters (NPC and CHB) along with current source inverters and Z-Source inverters [164, 165]. The benefits and shortcomings for each inverter type are given with how the vehicle's performance, efficiency and price is affected. Particularly, Malinowski's [166] survey on multilevel CHB inverters explains how they are more suitable for HEV/EVs because they utilise the numerous individual DC cells within the vehicle effectively.

2.3.2 Inverter Modulation Methods

The simplest method of controlling the switching devices of an inverter is 6-step waveform control [167]. This outputs the maximum phase-pole voltage for 180° for each phase, and then the maximum negative phase-pole voltage for the remaining 180°. This is replicated for the three phase voltages but shifted 120° out of phase as shown in Figure 2.5. This produces 6 distinct phase-neutral voltage levels and generates the maximum fundamental AC waveform possible for an inverter.

Figure 2.6 displays how carrier-based Sine Pulse Width Modulation (SPWM) uses a reference target AC voltage waveform (dotted blue line in Figure 2.6) overlaid by a set of triangular carrier waveforms (green lines in Figure 2.6) for a 3-Level (3L) inverter. The switching devices of the inverter change whenever these waveforms cross. The stepped output pole voltage (red line in Figure 2.6) has a fundamental harmonic that is similar to the target reference voltage waveform. The maximum fundamental voltage using SPWM is only 78.55% of what is generated using 6-step control. SPWM can be adopted into multilevel PWM, phase-

shifted PWM and include harmonic injection by changing the carrier waveforms or the AC reference voltage [168].

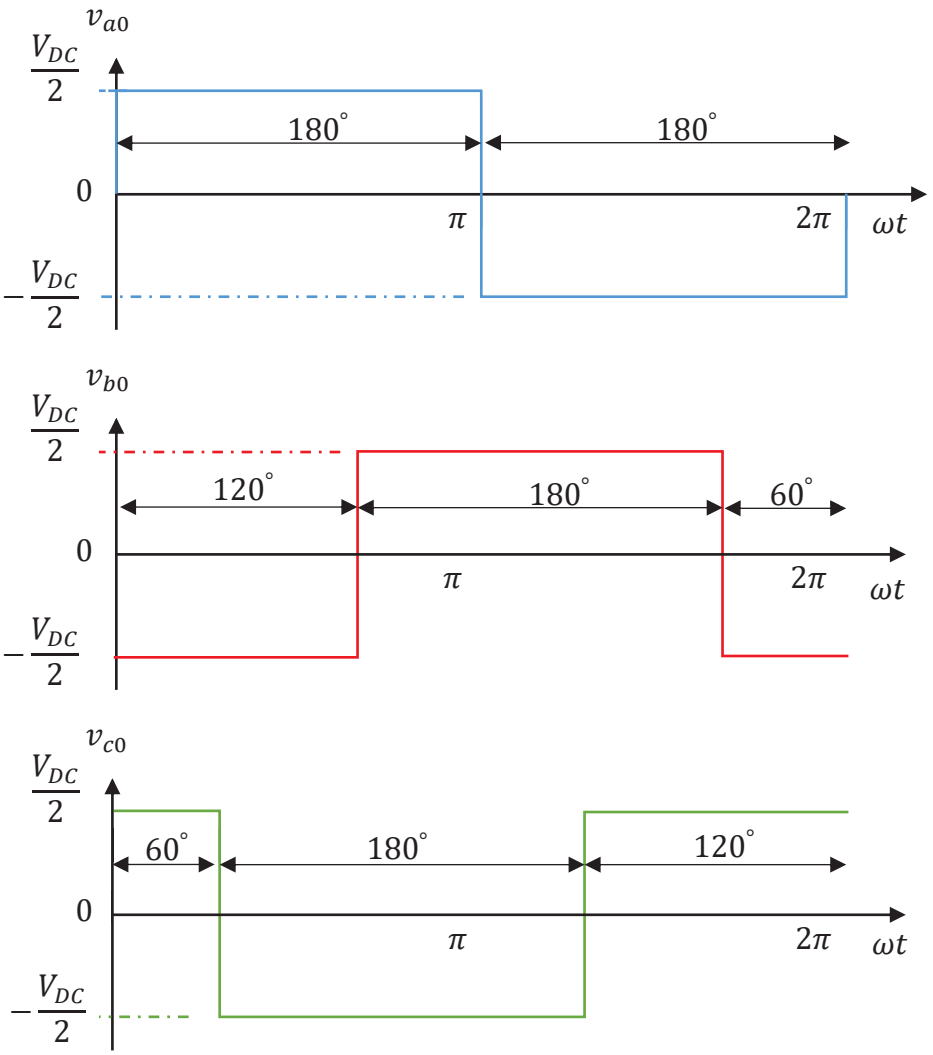

Figure 2.5 3 phase waveforms from an inverter operating using 6-step operation

SVPWM is a popular control method for voltage source inverters as it improves the harmonic quality of the output waveforms, has good DC-link utilisation and is simple to implement [169]. The target input voltage waveforms v_a, v_b and v_c are transformed into v_α and v_β on an $\alpha - \beta$ axis. The magnitude of v_α and v_β creates a rotating reference voltage V_{ref}. Examples of 5L, 3-level (3L) and 2L Space Vector Modulation (SVM) diagrams are shown in

Figure 2.7. Any point within the outer hexagonal SVM diagram is enclosed by a triangular sector. Every triangular vertex represents a voltage vector with unique $\alpha - \beta$ co-ordinates.

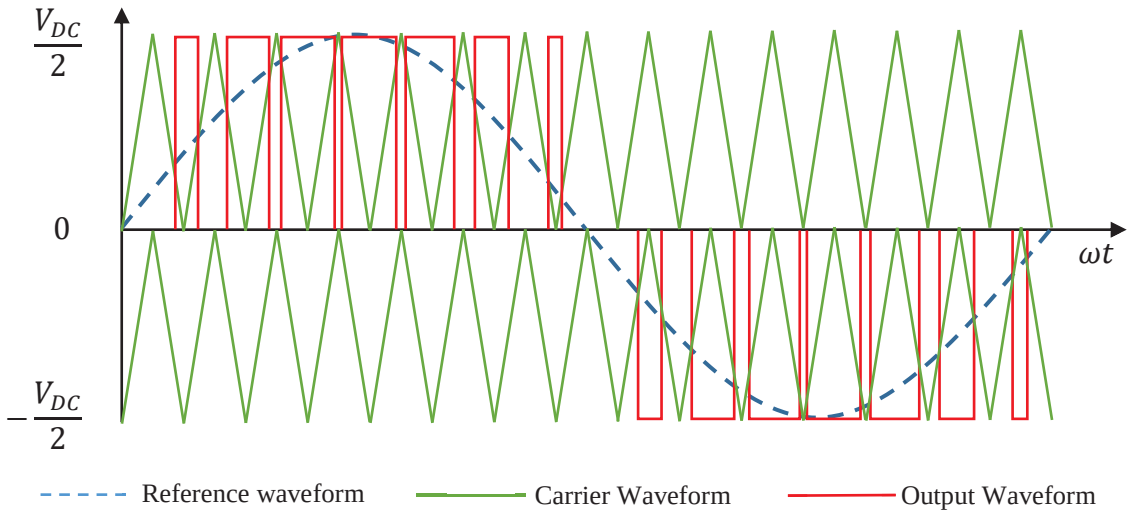

Figure 2.6 One pole voltage waveform of a 3-phase voltage waveform generated by an inverter using Carrier-based SPWM

The switching combinations that generate the same v_α and v_β co-ordinates are assigned to a respective voltage vector. SVPWM calculates how long the inverter must occupy each of the three voltage vectors enclosing the reference voltage so that the average output voltage over the SVM cycle equals V_{ref}. The maximum fundamental voltage of an inverter using SVPWM is 90.7% of that generated using 6-step control in the inverter's linear region of operation. Because the inverter can operate in the overmodulation region it is also able utilise full 6-step control.

Calligaro [170] and Hasan [171] reviewed various PWM strategies for multilevel inverters and compared the indices which quantify their performance including; Neutral point balancing, Total Harmonic Distortion (THD), Weighted THD (WTHD) and switching losses. Through a simulation investigation, SVPWM reduced the total switching count over SPWM and Double-Signal PWM due to one phase of the inverter phases being clamped over a single SVPWM cycle and reduced the output current THD.

2.3.3 Space Vector Pulse Width Modulation (SVPWM)

Holtz [172] extended the operating range of a 2L inverter using SVPWM to fully exploit the voltage capabilities of a DC source. Inverters had previously been confined to the circular trajectory boundaries of a Space Vector Modulation (SVM) diagram, but Holtz showed how to control the inverter all the way up to 6-step operation. The SVM regions were defined as "Continuous", "Overmodulation mode - I", and "Overmodulation mode – II" in relation to how the reference voltage is modified. This was later expanded upon by different authors who applied the theory to 3-level NPC inverters [173, 174, 175].

Celanovic [176] presented a general SVPWM algorithm for three phase inverters of any voltage level which was computationally efficient and suitable for real-time implementation on digital processors. Seo [177] and Zhang [178] developed simplified SVM strategies for a 3L-NPC inverter by reducing the 3L-SVM diagram into multiple 2L-SVM diagrams and enabled simpler 2L-SVM duty ratio calculations to be used.

Jiao [179] investigated the major SVM switching pattern strategies and their effect on neutral point voltage balancing, switching loss reduction, and noise reduction for 3-level NPC inverters. Prabaharan [180] reviewed different performance parameters for multilevel inverters which quantify the power output and efficiency of the different inverter topologies and control algorithms. These investigations highlight the need to give more attention to other aspects of the inverters control other than harmonic quality. In the case of an HEV/EV, the inverter should be controlled efficiently to optimise energy usage and extend the vehicles driving range [181].

Attique [182] reviewed the numerous reference frames for SVPWM and argues that the imaginary axis aligning with the 3-phase voltage waveforms of the inverter offers the simplest control and conceptual understanding over the other widely researched schemes.

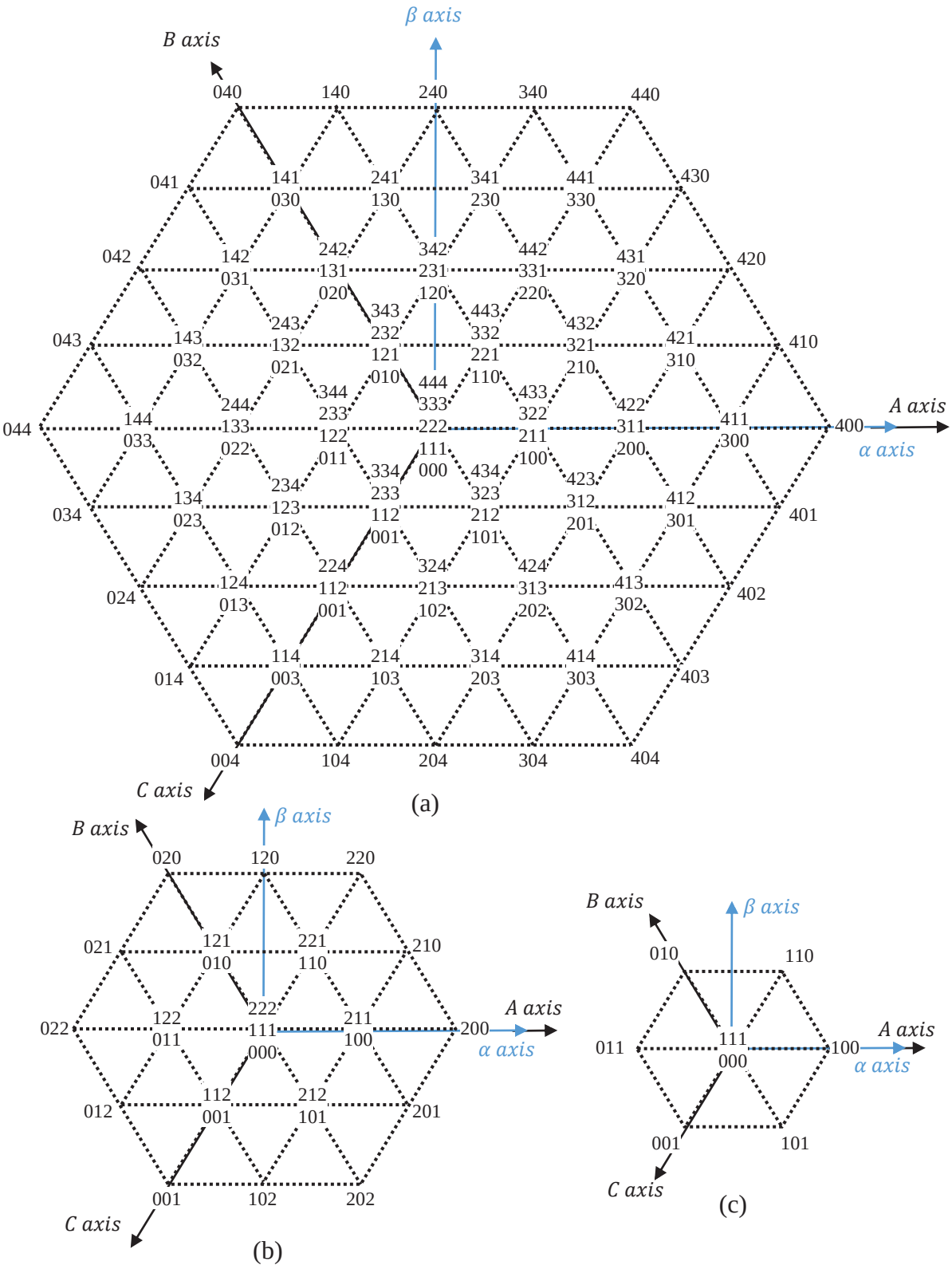

Figure 2.7 Inverter Space Vector Diagrams [178, 180], **(a)** 5-Level, **(b)** 3-Level, **(c)** 2-Level

2.3.4 Optimising SVPWM

Optimisation objectives for SVPWM include zero-voltage reduction [183], neutral point balancing of NPC inverters [184, 185, 186, 187], waveform harmonic distortion reduction [188, 189, 190] and noise reduction [191].

Pinewski [192] converted the voltage vector on-times calculated using SVPWM into switching patterns to control the individual switching devices of a 2L inverter. The alternating-null vector duty ratios reduced the harmonic distortion of the output wave signals, reduced capacitor voltage imbalances and lowered the risk of switching device overheating when compared to other switching patterns.

A direct comparison between different SVPWM switching patterns was carried out by Pahlavani [193]. This review considered the switching losses and harmonic distortion to quantify the overall efficiency of the inverter and quality of the waveforms. It was shown that different starting-ending switching states and the order in which they change over a single SVPWM cycle has a trade-off between switching losses and the harmonic distortion.

An example of how intermediate switching is generated over two SVM cycles is shown in Figure 2.8 for phase A of a 5L-NPC inverter. In Figure 2.8(a), the inverter switching states change between 0-1-2 for SVM cycle-1, then repeat in reverse 2-1-0 for SVM cycle-2. The switching states at the end of SVM cycle-1 are the same as the starting switching state for SVM cycle-2. Therefore, the inverters switching devices can remain in the same position when transitioning between the two SVM cycles and no intermediate switching required.

In Figure 2.8(b), the inverter's switching states change between 0-1-2 for SVM cycle-3, but then decreases 3-2-1 for SVM cycle-4. Although switching devices $A3$ and $A4$ remain in the same switching position, switch $A2$ requires an intermediate switch to put the inverter into the correct position before SVM cycle-4 can begin. In addition, the complimentary switching

device $\overline{A2}$ will also require an intermediate switch. This situation often occurs when the reference voltage vector transitions into a different voltage vector triangle and the switching states for one SVM cycle are not be available for the next SVM cycle.

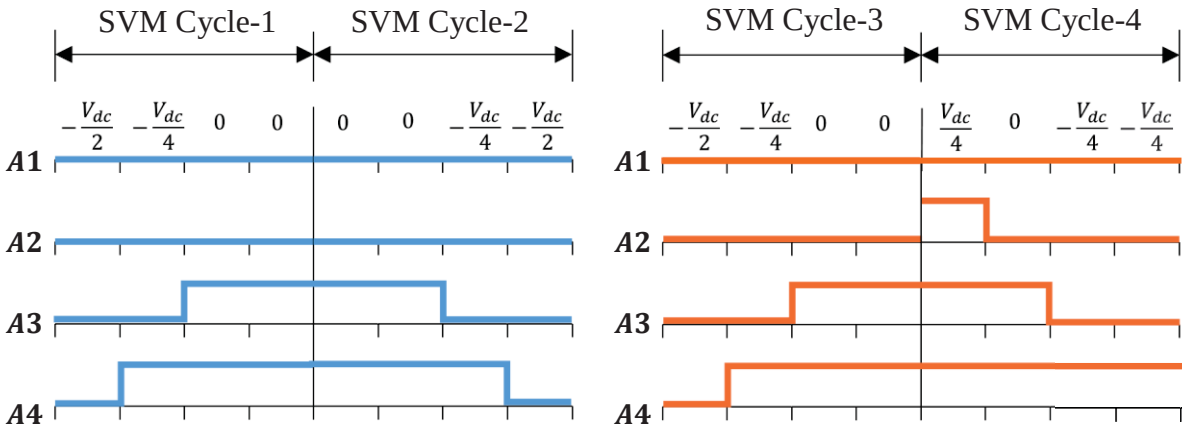

Figure 2.8 How intermediate switches are generated when transitioning between SVM cycles, **(a)** No intermediate switching, **(b)** One intermediate switch on A2

McGrath [194, 195] gave a detailed comparison between a variety of PWM strategies for multilevel NPC and CHB inverters. This emphasised the importance of switching sequences for SVM to reduce the total switching count. By selecting appropriate starting-ending switching patterns (null vector), the intermediary switching losses will be reduced when the reference voltage vector transitions between enclosing SVM triangles. Again, the trade-off between lower switching losses and the harmonic distortion of the waveform was shown to be a limiting factor.

2.3.5 On-line SVPWM Methods

As the inverters voltage level nL increases, the number of enclosing vector triangles within the SVM diagram grows at a rate of $6(nL-1)^2$ and the total number of switching states grows at a rate of $(nL)^3$. Assigning a SVM switching pattern for a particular reference voltage is difficult when there are multiple options to choose between for a single voltage vector. Storing all this information requires large look-up tables and is computationally inefficient. On-line

methods of calculating the available switching patterns remove these problems by directly calculating the switching pattern for each SVM cycle [196, 197].

Mohammed [196] and Susheela [198] separate an nL -SVM diagram into layers as a means of locating the reference voltage V_{ref} and map it on a $2L - SVM$ diagram. Gopinath's [197] fractal approach of identifying the triangle sub-section is mathematically simple, but the total number of iterative calculations increases rapidly with inverter size. These methods do not calculate all the available null switching patterns, nor do they allow for a different enclosing voltage vector to be used.

Neural networks have been used to calculate the on-times of the switching devices and as image processors used to identify the enclosing vector triangle [199, 200, 201, 202]. These are computationally efficient and are implemented easily using dedicated hardware. However, a pre-existing control scheme is required to train the network. This training is time consuming and the performance of the network will only match that of the training scheme.

Deng's [203, 204] on-line SVPWM method gradually reduces the $nL - SVM$ diagram (through $nL - 1$ and $nL - 2$ … diagrams) down to a single 2L-SVM diagram which encloses the reference voltage vector. This calculates all the possible switching patterns for one enclosing voltage vector. The linear time-complexity in proportion to the SVM voltage level is ideal because for every voltage level increase on the SVM diagram only one additional mapping sequence is required. However, this control method does not calculate the switching patterns of the alternative voltage vectors which might contain a better switching pattern to be used for a given SVM cycle.

Off-axis on-line SVPWM schemes identify the triangle sub-sector enclosing V_{ref} and directly computes the time durations for the switching devices [174, 175, 205, 206, 207]. These do not use a Cartesian co-ordinate system but instead opt for one parallel to the triangular edges.

The freedom to choose the switching pattern and control objectives (lower THD, lower switch count etc.) is removed and confined to the single switching pattern generated from the calculations. Jana's [208] on-line SVPWM scheme required minimal iterative calculations, lowered the switch count and improved the harmonic quality simultaneously. This was achieved by finding the triangle sub-sector that encloses the reference voltage in a similar manner to Gupta [174, 175] and Chamarthi [206], but instead opted to directly calculate the switching states of the enclosing voltage vectors.

2.3.6 Research Gaps in the Field of DC-AC Inverter Control

From the literature reviewed in Section 2.3, the author has the following comments about the research trend and the gaps in knowledge within the current literature:

1) The method presented by Deng [203, 204] currently has the lowest computational demand for an on-line SVPWM scheme. However, the optimisation of this control scheme is not analysed further (switch count, harmonic quality, etc.).
2) Jana [208] argues how Cartesian on-line SVPWM methods are more complex, require a greater number of iterative calculations and need more storage to hold switching patterns that have been calculated offline. However, the author of this thesis argues that the numerous logic-based identification methods for finding the enclosing triangle sub-sector, the correct equations to calculate the switching states and switching patterns required for off-axis on-line SVPWM methods can prove to be as computationally inefficient.
3) The general scope of multilevel inverter control seems to be increasingly growing with the invention of more modular and hybrid inverter topologies. As new topologies are created, their corresponding control systems are developed alongside and advance in a similar

progression to NPC and CHB inverters through reduced switching, improved harmonic quality, lower noise, etc.

4) There is only a small handful of inverter control and topology reviews for HEV/EV applications. Nearly all the inverter control schemes investigated within this literature are applicable to isolated inverter-motor applications. While most identify the harmonic quality of the waveforms delivered to the motor, they only consider single points of operation. This is usually taken to be at the end of the linear modulation region and only for a few full or part load applications. For inverter control strategies applicable to HEV/EVs, the full operating regions of the inverter and motor should be considered.

2.4 Vehicle Stability Control for HEV/EVs

2.4.1 Vehicle Stability Control Techniques

The terms oversteer and understeer were first defined for steady-state and transient conditions by Bergman [209] of the Ford Motor Company in the 1960's. The ability to quantify these variables enabled researchers and vehicle manufactures to improve future vehicle design and investigate active control methods. Diagrammatical views of vehicles with oversteer or understeering characteristics are shown in Figure 2.9 in comparison to a vehicle following the ideal target trajectory.

The mid-90s saw the beginning of Yaw Moment Control (YMC) when Bosch developed the yaw stability controller [210, 211]. This controller pulsated the brakes on the appropriate wheels to achieve an extra moment about the vehicle's yaw axis during an emergency steering manoeuvre. Shibahata [212], Motoyama [213] and Ikushima [214] where some of the first researchers to investigate YMC and implementation methods to distribute tractive/braking forces to the wheels of a vehicle. Shibahata [212] developed a new method for analysing YMC

by introducing a parameter derived from the vehicle's side-slip referenced the vehicles centre of gravity. These methods show how YMC transitions from emergency manoeuvres to improving the yaw control in every day driving and increase cornering performance.

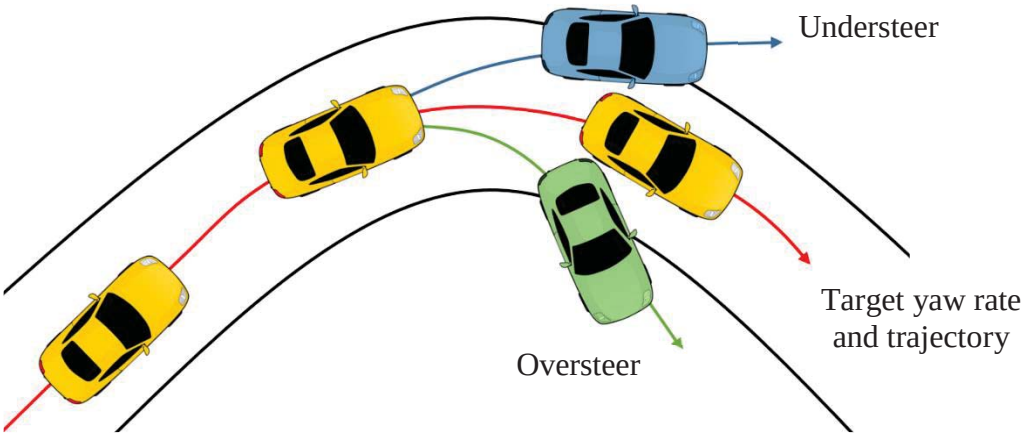

Figure 2.9 Oversteer, Understeer and Target yaw rate trajectory graphical view

The geometry and velocity components of a tyre are shown in Figure 2.10. The wheel slip ratio σ_{wh} compares the velocity of the tyre's outer surface at a radius R with rotational velocity ω_{wh} at the road-tyre interface against the longitudinal velocity at the centre of the tyre u_{wh} shown in Figure 2.10(a). The velocity components of the tyre in Figure 2.10(b) distorts the tyre's contact patch at the road-tyre interface in (shown in Figure 2.10(c)) by side slip angle α_{wh}.

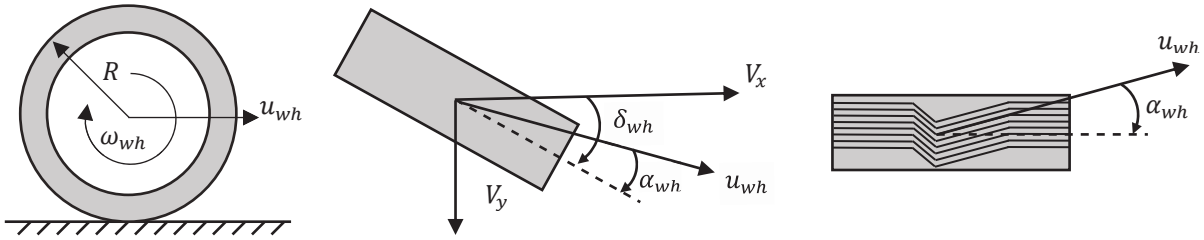

(a) (b) (c)

Figure 2.10 Diagrammatical view of the tyre dynamics, **(a)** Wheel slip ratio, **(b)** Wheel side-slip angle and velocity components, **(c)** Tyre contact patch distortion

Anti-lock Braking Systems (ABS) aim to maximise the Coefficient of Friction (COF) at the road-wheel interface to increase the braking force and reduce the stopping distance. It is shown in Figure 2.11 that the peak longitudinal COF μ_x is generated at a particular wheel slip σ_{wh}, but the actual slip varies for different tyre-road conditions and the tyre's side slip angle α_{wh}. As α_{wh} increases, the lateral COF μ_Y also increases and produces a larger lateral tyre force which aids in steering.

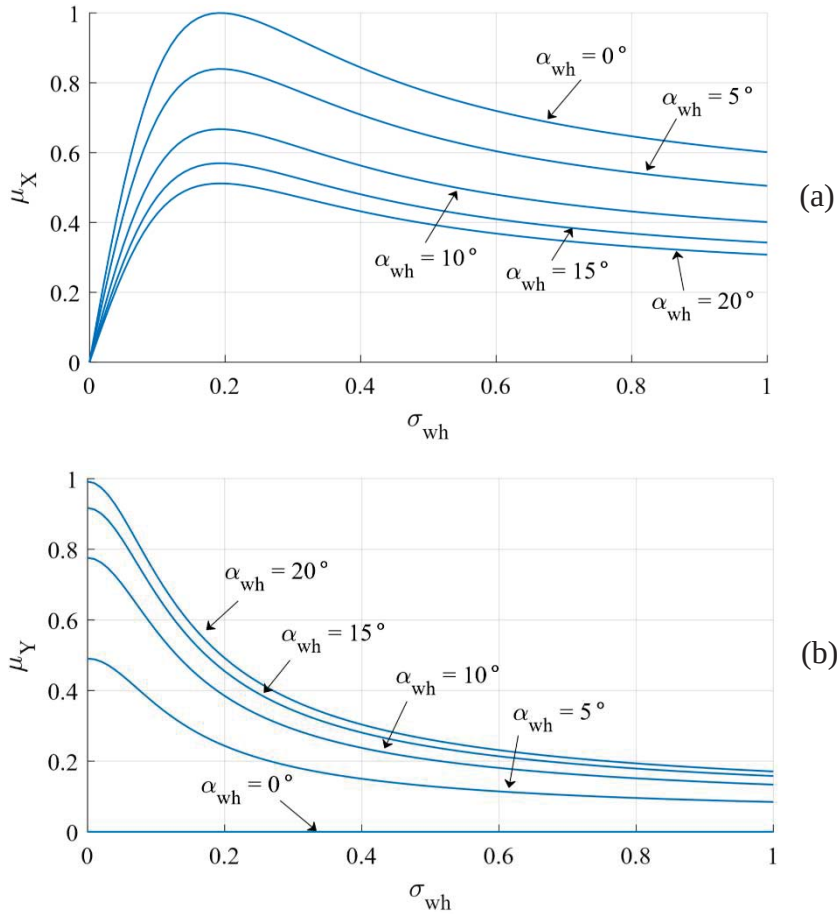

Figure 2.11 COF curves for one tyre and road combination over different wheel slip and sideslip angles, **(a)** μ_X curves, **(b)** μ_Y curves [277]

ABS appeared in the early 1950's within the aviation industry [215]. The high cost of these systems prevented them from crossing into the automotive industry until later that decade. Early adaptations of ABS were purely mechanical, a system of interconnected flywheels and springs would open hydraulic valves and release the brake fluid pressure if the wheel locked up.

Madison [216] patented the first automotive anti-skid system which used electronic sensors and actuators in 1969. Independent ABS control of all four wheels did not arrive until the early 80's where authors such as Satoh [217], Newton [218] and Main [219] showed how ABS improved steering control during emergency braking.

Under the same principles as ABS, Traction Control Systems (TCS) limit wheel slip to improve tractive force and maintain vehicle stability. Buick introduced the Max-Trac system [220] in the early 1970's to control the engine power according to electronic wheel speed sensors to prevent excessive wheel slip.

2.4.2 Vehicle Yaw Rate Control Methods

2.4.2.1 Implementing Yaw Rate Control

There are two popular methods for implementing YMC for road vehicles; varying the braking/tractive forces on either side of the vehicle, also known as Torque Vectoring (TV); and compensation steering angle.

Mokhiamar [221] compared the effect of TV with Front-Wheel Steer (FWS), Rear-Wheel Steer (RWS) and Four-Wheel Steer (4WS). The simulation study showed that a vehicle with TV+RSW has lower yaw rate tracking ability than a TV+FWS vehicle, but a TV+FWS+RWS vehicle has the best responsiveness and stability overall. This concluded that the 4WS vehicle has superior cornering performance over single axle steer vehicles and how the effect of FWS is greater than RWS. The key information from this publication is that the asymmetrical tractive forces alone improved the yaw rate control of these vehicles regardless of what steering system was used. A further comparison between 4WS and TV was conducted by Abe [222] who highlighted that the saturation effects of the tyre forces using steering compensation may limit

the performance in contrast to TV, but a combination of the two methods outperform both independently.

The application of TV in an EV with multiple independent traction motors has shown to be advantageous over ICE vehicles using torque splitting differentials [26, 27]. The traction motors enabled greater control of the tractive/braking force at each wheel and therefore improved the controllability and stability of the vehicle [28].

2.4.2.2 Yaw Rate Controller Types

Control of a vehicle's yaw rate and sideslip angle has been investigated for YMC independent of one another [223, 224], but both methods are required to ensure both controllability and stability of the vehicle.

Sliding-Mode Controllers (SMC) have been a popular method for TV as they allow for smooth and stable control of the vehicle and allocation of tyre forces. Goggia [225] changed the vehicle's driving modes (Normal and Sport) by changing the gain values of an integral sliding mode TV based YMC subject to the vehicle's lateral acceleration. Novellis [226] and Fu [227] later improved the yaw rate and sideslip control using electric traction motors. Novellis [228] compared the performance of the SMC against a PID controller for YMC. The comparison showed that a SMC has a lower yaw rate error than the PID controllers, but suffered from undesirable chattering, an inherent SMC control problem.

Optimisation methods applied to YMC allow for multiple objectives to be monitored and controlled simultaneously [229]. Kampanakis [230], Kasinathan [231] and Wong [232] used the vehicle's yaw rate error and side-slip as control objectives as well as the independent traction motor's temperature. This improved the yaw performance of the vehicle without

overheating the traction motors. Zhai [233] included the regenerative energy capturing ability of the traction motors to maximise the vehicle's driving range.

Boada [234] used the yaw rate error and sideslip angle as inputs to a FLC system to generate an ideal additional yaw moment that would minimise the input errors. Variable braking forces on the front axle generated the additional yaw moment during a detailed simulation study. Because the target speed for these simulations was intended to be constant for the duration of the manoeuvre, an opposing tractive force on the opposite side of the axle should have been included. Boada [235] and Li [236] advanced upon the FLC method by including compensation FWS and RWS respectively, both controllers and implementation methods showed improved vehicle control over [234]. Jin [237] used a genetic algorithm to tune the membership functions of a FLC using the yaw rate error and vehicle side-slip as optimisation parameters. The performance of the final FLC iteration was superior to the initial controller design.

Ghosh [238] attempted to use the vehicle's yaw rate error and steering wheel angle as the inputs to a FLC for YMC instead of the vehicle's sideslip angle because it is difficult to measure or estimate. However, this approach is in danger of stabilisation issues since no stability input was considered. Krishna [239] included the driver steering angle into the FL yaw controller on top of the vehicle yaw rate error and sideslip angle. This improved the dynamic performance over the original vehicle, but it is difficult to determine whether the improvements are due to steering wheel input as no comparison is given without it. Kim [240] used a FL yaw moment controller to maintain the yaw rate and vehicle side-slip angle in conjunction with an optimisation problem to minimise the utilisation of the electrohydraulic braking system and maximise regenerative energy recuperation.

2.4.3 Wheel Slip Controller Schemes

2.4.3.1 Wheel Slip Control for an HEV/EV

Conventional ABS controllers will pulsate the brake torque around a single target wheel slip σ or if the wheel rapidly approaches lockup. Since the target σ changes for various different driving-wheel-road conditions this method may not offer optimal braking performance, but it is simple to implement [241, 242, 243, 244].

Hori [25], Kuruppu [245], and Ivanov [246] all promoted the use of electric vehicles over ICE powered vehicles because of the superior tractive and braking performance only attainable from electric traction motors. The fast, accurate and predictable torque output of the electric motor/s allowed for higher frequency torque modulation [246]. Because it is easier to estimate the torque output from the traction motors than an ICE, MPC and parameter estimation methods are simpler and more accurate for use in ABS/TCS [23, 245].

Spichartz [247] compared the regenerative braking ability of EV's using a single electric motor against four independent in-wheel motors when the ABS is engaged during braking. Because the independent in-wheel motors are not limited by the dynamics of the other wheels in the same way as a single drive EV, greater regenerative energy capturing and braking performance is obtainable.

2.4.3.2 Wheel Slip Controller Types

SMCs for ABS often take on the role of extremum seeking algorithms which search for the peak coefficient of friction, an advantage of these controllers over PI and FL controllers are that if designed correctly they negate the need for knowing the wheel slip or coefficient of friction and opt for other control parameters (e.g. wheel forces) [248, 249, 250, 251].

A FLC's ability to handle the nonlinearities associated with tyre and vehicle dynamics has made them a popular choice for implementing ABS/TCS [241, 252, 253]. The optimal wheel slip for maximum coefficient of friction changes with different road and tyre conditions, Bauer [254] used a FLC to estimate the optimal wheel slip on varying road surfaces and a secondary system of FLCs to regulate the brake torque so the wheels match the target slip value. This method improves over other authors who choose to only operate around a constant σ [255].

Colli's [256, 257] FL wheel slip controller uses the gradient of the longitudinal slip curve (rate of change in friction over the rate of change in wheel slip) and the accelerator pedal movement for a vehicle's TCS. This was achieved by estimating the coefficient of friction and measuring the instantaneous wheel slip for each independently driven wheel. This method changed the control objective of a wheel slip percentage, to the peak gradient of the curve which remains constant for all driving conditions as shown in Figure 2.11. Since this was implemented on a vehicle using electric traction motors, the road conditions are estimated easier than if an ICE vehicle was used.

A comparison between pure PI torque control and a compensated PID-FLC for a vehicle's TCS was given by Li [258]. The torque control of the PI controller regulated the wheel-slip for both control methods, but the inclusion of the FLC to compensate the torque when the road conditions abruptly changed offered a shorter settling time and smaller oscillations around the target wheel-slip.

2.4.4 Vehicle Yaw Control during Braking Manoeuvres

Braking YMC (BYMC) is diagrammatically shown in Figure 2.12 (brake forces for each wheel are represented by green arrows) whereby the brakes on one side of the vehicle are given a lower brake torque, this produces asymmetrical braking forces around the vehicle's centre of gravity and thus an additional yaw moment is generated [259].

Early attempts to improve the poor yaw control of a vehicle while braking during a turn-in manoeuvre was improved by Novel [260] and Heinzl [261] during the early 2000's who reduced the systems down into an optimisation problem and a SMC respectively. Both systems used asymmetrical braking by changing the target wheel slip or additional brake pressures in order to generate the additional yaw moment. However, these systems are used for gradual vehicle braking and use the ABS as a limiting factor instead of controlling the brake forces at the point of maximum braking force.

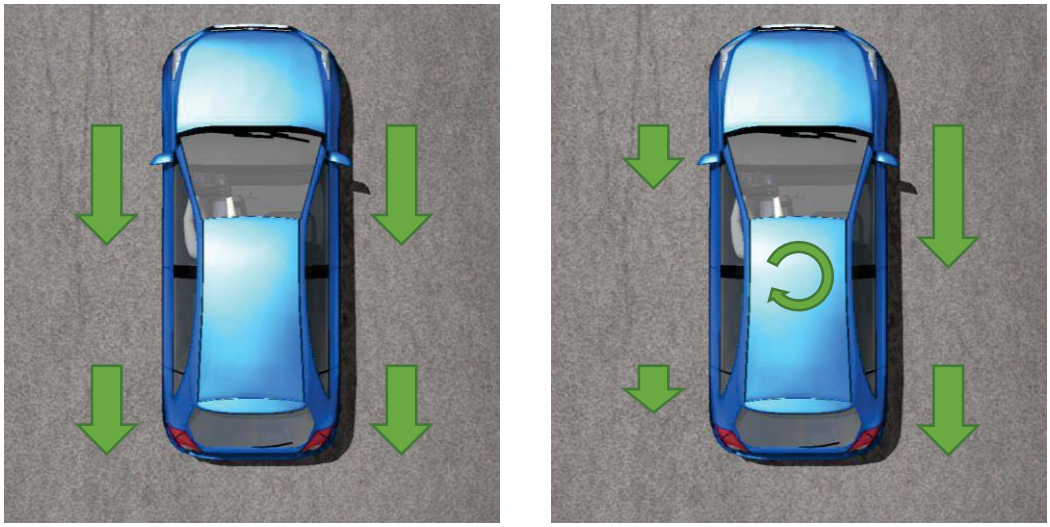

(a) (b)

Figure 2.12 How varying asymmetrical braking forces can produce an external yaw moment, **(a)** Symmetrical Braking forces, **(b)** Asymmetrical braking forces

Cascaded [262] and parallel [263] YMC and ABS/TCS architectures are simple to implement, but the hierarchy of the layout and/or sensitivity of the control parameters may create difficulties in deciding the overruling control method. Kaiser [264] showed how an interconnected architecture of the two control methods reduced the typical layout control problems to either reduce the input torque request or output torque command.

Song [250, 265, 266] provides numerous detailed studies on the effect of YMC under steady state driving and emergency braking/steering manoeuvres. Many of these investigations

compare the performance of BYMC and compensated Steering YMC (SYMC) against a vehicle with only an ABS which achieves peak longitudinal COF on all four wheels. Song shows that both BYMC and SYMC have greater controllability and stability over the original vehicle, with SYMC performing slightly better than BYMC. A problem not addressed by Song is the increased cost associated with additional RWS and if the small increase in controllability over BYMC is justified. Systems which combine asymmetrical brake forces and active front steering [267, 268] for braking and steering manoeuvres have shown better yaw control and stability over systems which use these implementation methods independently.

Mirzaeinejad's [269] optimization problem sought to minimise the yaw rate tracking error with the smallest amount of external yaw moment while maximising total braking force to ensure a short stopping distance. The design of this control algorithm however does limit its use to split-mu surfaces, it also does not directly control the wheel torque but instead applies the ideal tyre force to the road.

The yaw control system given by Mirzaei [268] uses an optimisation problem to minimise the amount of asymmetrical braking forces and slow the vehicle down as fast as possible while preventing compensated steering oversaturation. Mirzaei uses a FLC to control the weighting factors of the optimisation problem depending on the saturation properties of the tyre forces while meeting the required performance of the system.

Naderi's [270] YMC system directly controls the wheel torque of the vehicle under various braking and steering scenarios. A SMC is used to produce the ideal braking torques on either side of the vehicle where a FL wheel slip controller scales these values to ensure the wheel does not lock-up. This is advantageous because the wheel torques are directly calculated instead of target wheel forces as with previous control algorithms. However, an experimental validation

is not provided and SMCs often suffers from a chattering around the target values when implemented in hardware.

Dogruğüven [271] investigated the regenerative ability of an EV during an emergency braking manoeuvre. A major advantage highlighted by this control scheme is the combined hydraulic and traction motor braking system. The traction motors braking torque becomes less effective at high road speeds and the hydraulic brakes must be incorporated into the control. At lower speeds, the fast torque response of the traction motors offers greater control of the torque provided to the wheels and the yaw control becomes more effective.

Dincmen [272] advanced upon the work of Drakunov's [248] extremum seeking algorithm by changing the single sliding-mode curve into a sliding-mode surface to incorporate the changes in the lateral coefficient of friction of the wheels. Dincmen showed that during combined braking and cornering manoeuvres, sacrificing a small amount of longitudinal friction by reducing the target wheel slip operating point increases the tyre's lateral force. The results showed that the vehicle may be able to avoid a collision during an emergency braking scenario because it is able to travel more laterally.

Song [273] compared the performance of a PI, FLC and SMC for compensated FWS controllers for driving scenarios with and without asymmetrical braking forces. Song found that the membership functions and rule base of the FLC that was specifically tuned for braking manoeuvres outperformed the SMC and PI controllers, the FLC thus performed worse during constant velocity scenarios. An additional comparison to a FLC tuned to either constant velocity manoeuvres or a FLC able to accommodate the two scenarios would offer a better comparison of the performance of this type of controller.

The YMC presented by Tahami [274] was designed for use during emergency braking and steering manoeuvres. Tahami used a FL wheel slip and yaw moment controller in conjunction

with a neural network to generate target yaw reference values. However, only a constant target wheel slip was used for this investigation, the performance of the network on other surfaces may suffer if the COF changes and the optimum slip value changes.

2.4.5 Research Gaps in the Field of Vehicle Stability Control for HEV/EVs

From the literature reviewed in Section 2.4, the author has the following comments and has recognised the following gaps in knowledge within the current literature:

1) A gradient based wheel slip control algorithm (like the TCS developed by Colli [256, 257]) has not been applied to braking manoeuvres.
2) The TCS system developed by Colli [256, 257] also only considers straight line manoeuvres. Implementation of a gradient based wheel slip control system has not been investigated in combination with yaw rate control systems.
3) The current trend in VSC research is heading in multiple directions including; combining independent vehicle control algorithms with autonomous and connected vehicle systems, improving system robustness and improving real-time implementation for computationally heavy control systems. In addition, improving estimation methods to find the tyre-road COF, vehicle sideslip angle, wheel slip and tyre forces are also of concern.
4) Most of the VSC control algorithms investigated require numerous detailed vehicle parameters to be used within the control algorithms. However, the nonlinear or time varying parameters (e.g. vehicle mass changing due to passengers, luggage and fuel) often required for vehicle simulation and control might cause the system to perform sub-optimally if the values used within the control system do not accurately represent the corresponding real-world parameters. Values that can be accurately estimated (wheel slip, road COF) offer

better wheel slip and yaw rate control over values that use predetermined estimated values within the control algorithm.

2.5 Summary of Literature Gaps and Specific Research Objectives

An overarching aim for this thesis is to investigate how *intelligent motor modelling and control techniques* can be used to create *new HEV/EV development tools, increase vehicle energy efficiency and improve vehicle safety*. The first original research objective for this thesis in Section 1.3 has been achieved by examining the technological milestones and state of the art literature while exposing gaps in the current research within this chapter.

Research gaps #1 and #2 from Section 2.2.9 detail the lack of a single FOC algorithm that is able to control multiple vehicle systems without the need for re-tuning and the lack of depth of investigations into the effects of variable motor parameters for HEV/EV applications. As discussed in Section 2.2.8, FLCs offer high robustness and excellent control performance for FOC applications. The first specific research objective investigated within this thesis is:

Objective 1 - To develop a single FL based FOC system that can be implemented into multiple different motor topologies and vehicle powertrain architectures without the need for re-tuning to simplify the development of an HEV/EV. The control system's robustness will be examined with the effect of variable motor parameters for HEV/EV applications.

This will fulfil the second original research objective listed in Section 1.3 - to develop a traction motor control system in order to simplify the development process of an HEV/EV. A control system such as this would be a useful tool for vehicle manufacturers as this single FOC scheme could be used for any vehicle prototype under investigation without the risk of unstable or undesirable control.

Research gap #3 from Section 2.2.9 highlights how there are no effective methods to estimate the thermal and torque characteristics of the motor operating in the overcurrent region without detailed motor parameters. The second specific research objective investigated within this thesis is:

Objective 2 - To develop a traction motor model for HEV/EV design applications which uses only readily available empirical motor data to estimate the torque and thermal characteristics of a motor operating in the overcurrent region without any detailed motor parameters.

This will fulfil the third original research objective in Section 1.3 - to develop a traction motor modelling tool to inform a vehicle manufacturer if a motor and powertrain combination offers the greatest total vehicle energy efficiency or lowest output emissions. A modelling tool such as this would show if the traction motor and powertrain combination allow the vehicle to achieve its own dynamic performance quickly and early on in the development process when only empirical data is available.

Observation #1 - #2 into the literature trend surrounding DC-AC inverter control schemes in Section 2.3.6 show how the on-line SVPWM method by Deng [203, 204] has the lowest computational burden in comparison to other on-line methods, but does not extend its control objectives into other quantifiers (low intermediate switching, low THD) used to describe the quality of SVPWM methods as described in literature observation #3. The third specific research objective investigated within this thesis is:

Objective 3 - To advance upon the current state of the art on-line SVPWM schemes with a new reduced intermediate switching algorithm which does not inhibit the computational efficiency of the SVPWM algorithm and improves the energy efficiency of the inverter over the entire driving range of an HEV/EV.

This will fulfil the fourth original research objective in Section 1.3 - to develop an energy efficient method of powering the traction motor of an HEV/EV. By reducing the intermediate switching, there will be lower energy dissipated as heat and therefore a higher energy efficiency, if this can be achieved over the entire driving range of an HEV/EV.

Literature gaps #1 - #2 in Section 2.4.5 show that gradient based wheel slip controllers have not been applied to braking manoeuvres nor do they directly incorporate yaw rate control for steering scenarios. Therefore, the fourth specific research objective investigated within this thesis is:

Objective 4 - To develop a gradient based wheel slip control algorithm for braking manoeuvres which directly incorporates yaw stability into the control algorithm in order to improve the safety of a vehicle during an emergency manoeuvre.

This will fulfil the fifth original research objective in Section 1.3 - to increase a vehicle's safety by intelligently controlling the traction motors during an emergency manoeuvre.

Chapter Three

Research Methodology and Model Verification Procedures

This chapter presents the methodology and experimental procedures used within this thesis. Section 3.2 discusses the general modelling and control techniques commonly used for the vehicle dynamics, traction motors and DC-AC inverters for HEV/EV simulations. How and why these methods are used in this thesis are explained to offer a basic understanding to the reader of how the advanced control methods work in later chapters. The statistical analysis methods in Section 3.3 are used to quantify the performance of the Processor-in-the-Loop (PIL) verification simulations in Section 3.4 and the systems developed in the remainder of this thesis.

3.1 Research Methodology

The following steps describe the main methodology steps used for the research conducted within this thesis:

1) Model the vehicle components under investigation in MATLAB/Simulink. How and why these components are modelled instead of commercially available models is given in Section 3.2. To ensure that these models perform as expected, they are validated against commercially available equivalents. Both models should produce comparable outputs within acceptable margins of error for a set of given inputs (see Section 3.4).
2) Implement the current state of the art control techniques into the validated models. This highlights areas of room for improvement within the control algorithms. These state of the art control schemes then act as a baseline to compare and highlight the advantages of the new control algorithms developed within this thesis.

3) From examination of the current state of the art control algorithms and considering the current literature from Chapter Two, a new control system is developed addressing the major problems of the system and control algorithms under investigation found by the gaps in the current literature explained in Section 2.2.9, Section 2.3.6 and Section 2.4.5.
4) The newly developed control systems ability to be unaffected by hardware limitations and compiler errors are verified using a series of PIL simulation experiments (see Section 3.4).
5) Compare the new control system to the previous state of the art control techniques. Areas of improvement for both control techniques are highlighted and areas for future work to address are discussed.

3.2 Component Modelling of the HEV/EV

3.2.1 Traction Motor Models

The Induction Motor (IM) and Interior Permanent Magnet Synchronous Motor (I-PMSM) are two common traction motor topologies used in HEV/EVs [67, 275]. Chapter Four presents an intelligent FOC scheme and Chapter Six observes the harmonic quality of the motor's current waveforms. As discussed in Section 2.2.3, there are several methods for modelling a motor for HEV/EV applications (analytical models, Finite Element Analysis or empirical data based). The torque-speed characteristics and electrical analysis of the motors in these chapters are represented by the equivalent electrical circuits given in Section 3.2.1.3 - 3.2.1.4. This modelling method has been well documented throughout literature as an acceptable method for both standalone motor applications and HEV/EV applications [71, 75, 276, 277]. It should be noted that there are some limitations to this modelling method as they do not include the effects of eddy currents, local saturation points, skin effects or any end effects [67]. This makes them unsuitable for motor design purposes as the errors may be too high. The trade-off between

relatively high accuracy over the full operating range of the motors torque-speed curve with low computational power does make them suitable for HEV/EV applications.

Chapter Five and Chapter Seven do not examine any motor current or voltage control, simple 2D look-up table representations of the traction motors given in Section 3.2.5.1 are sufficient as they simplify the overall control system and reduce simulation time.

3.2.1.1 Voltage Vector Transformations

In Figure 3.1(a), an arbitrary choice of voltages v_a, v_b and v_c from the 3-phase AC waveforms supplied to the motor windings in Figure 3.1(b) are represented on a 2D plane. These voltages use the $A - B - C$ axis for their respective windings (black dotted lines) whose combined magnitude produces a reference voltage V_{ref} which travels around the origin at synchronous speed ω_e.

Only two co-ordinates are required to represent any point in 2D space. The Clarke transformation (1) converts v_a, v_b and v_c into the voltages v_α and v_β on an $\alpha - \beta$ axis as shown in Figure 3.1(c). The Park transformation (2) then converts the sinusoidal v_α and v_β waveforms into the direct v_{ds} and quadrature v_{qs} voltages on the dq-axis (Figure 3.1(d)) [66]. The dq-axis observes v_{ds} and v_{qs} as DC waveforms on a rotating reference frame with an angular velocity ω_e. The Park transformation requires finding the electrical angle θ_e from (3) by integrating ω_e over a time t from the initial time t_0. The same transformations are used to find the direct i_{qs} and quadrature i_{ds} stator currents which are responsible for the motor's torque and magnetic flux respectively.

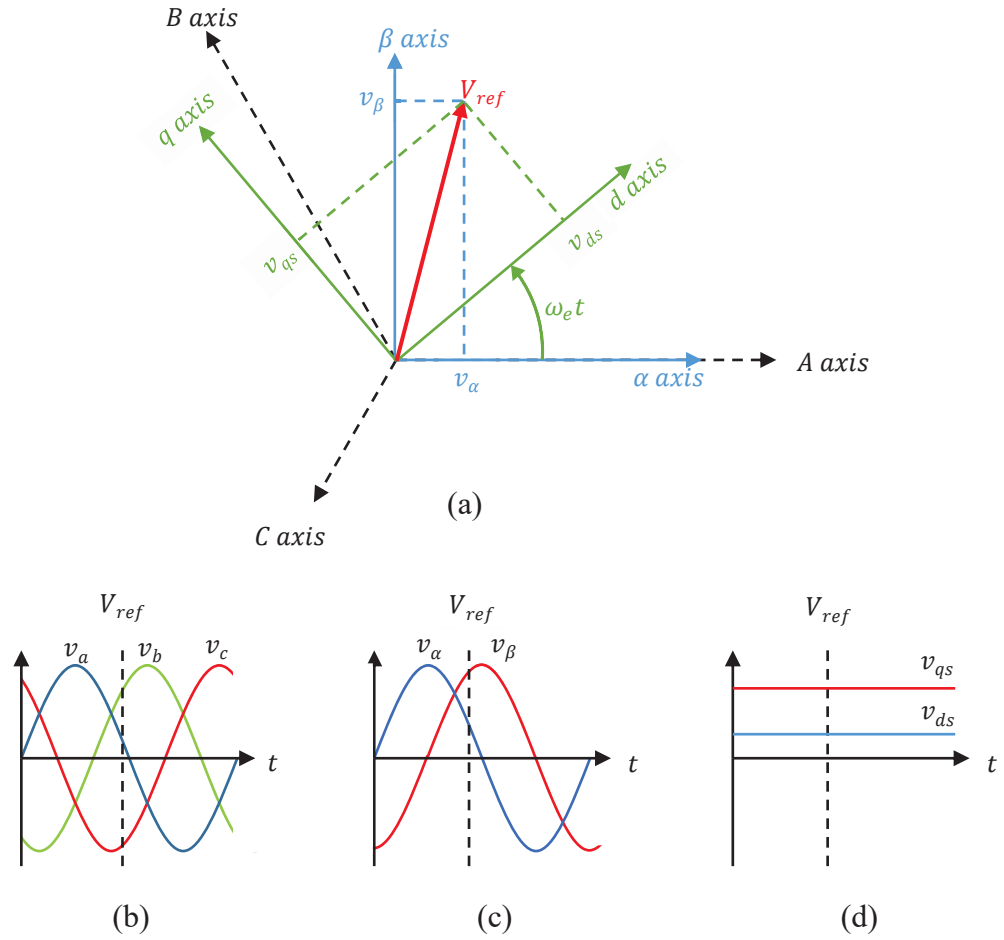

Figure 3.1 Vector transformations, **(a)** 2D visual representation of the transformation process, **(b)** Original 3-phase AC waveforms, **(c)** Clarke transformation, **(d)** Park transformation

$$\begin{bmatrix} v_\alpha \\ v_\beta \end{bmatrix} = \begin{bmatrix} 1 & -\frac{1}{2} & -\frac{1}{2} \\ 0 & \frac{\sqrt{3}}{2} & -\frac{\sqrt{3}}{2} \end{bmatrix} \begin{bmatrix} v_a \\ v_b \\ v_c \end{bmatrix} \tag{1}$$

$$\begin{bmatrix} v_{ds} \\ v_{qs} \end{bmatrix} = \begin{bmatrix} \cos\theta_e & \sin\theta_e \\ -\sin\theta_e & \cos\theta_e \end{bmatrix} \begin{bmatrix} v_\alpha \\ v_\beta \end{bmatrix} \tag{2}$$

$$\theta_e = \theta_e(t_0) + \int_{t_0}^{t} \omega_e \, dt \tag{3}$$

3.2.1.2 FOC Architecture

The FOC flowchart in Figure 3.2 is used to control the direct and quadrature currents of the motor of the analytical traction motor models used throughout this thesis [278]. Using the import and export parameters between CarSim and MATLAB/Simulink in Table 3.3 of Section 3.2.4.1, the FOC architecture is explained as follows:

MATLAB Environment – MATLAB/Simulink imports the vehicle's instantaneous longitudinal velocity V_x and the rotational velocity of the wheels ω_{wheel} from CarSim. The error between V_x and the target velocity V_x^* of the drive cycle is fed to a speed controller which generates suitable accelerator pedal $\gamma_{acc} \in [0\ 1]$ or brake pedal $\gamma_{brk} \in [0\ 1]$ activation levels.

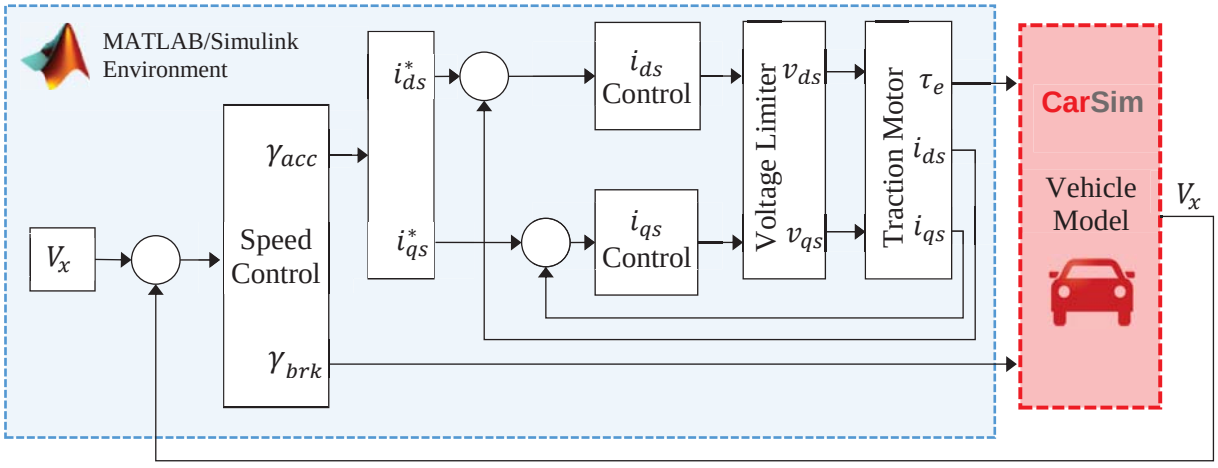

Figure 3.2 FOC flowchart architecture between the MATLAB/Simulink and CarSim environments

If the brake pedal is activated, a brake pedal force proportional to the brake pedal's activation level is exported to CarSim. No traction motor regenerative braking is considered within this FOC scheme. The traction motor model control and verification in Section 3.4.1 show that this FOC architecture and analytical models are able to operate in all four quadrants of the traction motor and regenerative braking is a possible route for future control applications. This was done to simplify the control architecture at this stage of the research to avoid complications with

wheel slip control. Instead, the internal Anti-Lock Braking Systems (ABS) of the CarSim vehicle model will monitor this area by controlling the brake fluid pressure of the pure hydraulic braking system. The wheel slip and regenerative braking systems will be accommodated for in future research by employing the wheel slip control schemes developed in Chapter Seven.

When the accelerator pedal is activated, it signifies that the speed controller is requesting torque from the motors. For motor control and FOC, a torque command corresponds to an increase in torque producing current components. Target q-axis i_{qs}^{*} and d-axis i_{ds}^{*} currents are generated which would satisfy the increase in output torque. The independent current controllers compare i_{qs}^{*} and i_{ds}^{*} against the instantaneous q-axis i_{qs} and d-axis i_{ds} currents being drawn by the motor respectively.

The current controllers produce unit q-axis v_{q0} and d-axis v_{d0} voltages to reduce the current error. These voltages are de-coupled and have the constraints imposed by the motor applied to them (see Section 3.2.1.5). The final d-axis v_{ds} and the q-axis v_{qs} voltages are then supplied to the stator windings. It is assumed that voltage and current waveforms are perfectly generated by an ideal inverter. The traction motor model generates an output torque τ_e which is exported to CarSim.

CarSim Environment – The vehicle model imports τ_e and the brake fluid pressure from MATLAB/Simulink. The vehicle model accounts for the 6 degrees of freedom around the vehicle body, spin dynamics of the tyres and uses steering control to maintain a straight heading. The longitudinal velocity of the vehicle's centre of gravity V_x is then exported back to MATLAB/Simulink.

3.2.1.3 Analytical Model of an IM

The q-axis and d-axis analytical circuits for a squirrel cage IM with magnetic poles *P* are given in Figure 3.3(a)-(b) respectively. Equations (4)-(14) are used to simulate the characteristics of the IM motor [279, 280].

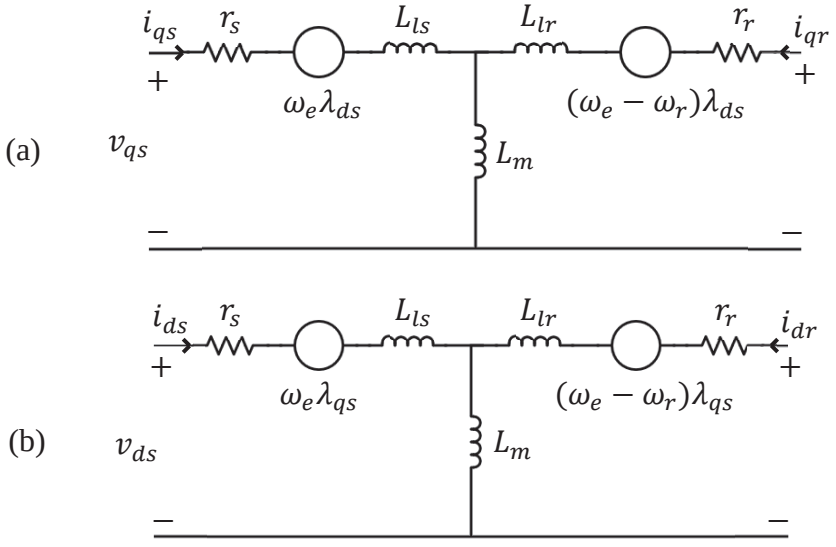

Figure 3.3 IM analytical equivalent circuits, **(a)** q-axis **(b)** d-axis

Equations (4)-(7) represent the voltage drop over the stator winding resistance r_s, rotor winding resistance r_r and the Back Electromotive Force (B-EMF). These are used to find the flux linkages λ of the d-axis and q-axis circuits for both the stator (λ_{ds} and λ_{qs}) and the rotor (λ_{dr} and λ_{qr}). The magnitude of the B-EMF is proportional to difference between the *electrical* angular velocity of the rotor ω_r and ω_e.

$$v_{ds} = r_s i_{ds} + \frac{d\lambda_{ds}}{dt} - \omega_e \lambda_{qs} \tag{4}$$

$$v_{qs} = r_s i_{qs} + \frac{d\lambda_{qs}}{dt} + \omega_e \lambda_{ds} \tag{5}$$

$$0 = r_r i_{dr} + \frac{d\lambda_{dr}}{dt} - (\omega_e - \omega_r)\lambda_{qr} \tag{6}$$

$$0 = r_r i_{qr} + \frac{d\lambda_{qr}}{dt} + (\omega_e - \omega_r)\lambda_{dr} \tag{7}$$

The inductance leakages of the stator L_s and rotor L_r in Equations (8)-(9) require their respective leakage inductances L_{ls} and L_{lr} as well as the magnetising inductance of the motor L_m.

$$L_s = L_m + L_{ls} \tag{8}$$

$$L_r = L_m + L_{lr} \tag{9}$$

The current flow within the d-axis and q-axis circuits for both the stator (i_{ds} and i_{qs}) and rotor (i_{dr} and i_{qr}) are found using Equations (10)-(13). The stator d-axis i_{ds} (10) and q-axis i_{qs} (11) currents are fed back to the current controllers. Equation (14) calculates the output torque τ_e from the IM which is exported to CarSim.

$$i_{ds} = \frac{\lambda_{ds} - L_m i_{dr}}{L_s} \tag{10}$$

$$i_{qs} = \frac{\lambda_{qs} - L_m i_{qr}}{L_s} \tag{11}$$

$$i_{dr} = \frac{\lambda_{dr} - L_m i_{ds}}{L_r} \tag{12}$$

$$i_{qr} = \frac{\lambda_{qr} - L_m i_{qs}}{L_r} \tag{13}$$

$$\tau_e = \frac{3P}{4} L_m \left(i_{qs} i_{dr} - i_{ds} i_{qr}\right) \tag{14}$$

The mechanical rotational velocity of the rotor ω_m is calculated from the wheel's rotational velocity ω_{wheel} imported directly from CarSim. The magnitude of the rotor's magnetic flux wave φ_r is estimated using (15) because it cannot be directly measured [146, 279]. The magnetic flux is induced in the rotor because of the slip between the *electrical* rotational velocity of the rotor ω_r (16) and the rotating magnetic flux wave of the stator travelling at synchronous speed ω_e (17). The supply voltage frequency f is then calculated using (18).

$$\frac{L_r}{r_r}\frac{d\varphi_r}{dt} + \varphi_r = L_m i_{ds} \tag{15}$$

$$\omega_r = \frac{P\omega_m}{2} \tag{16}$$

$$\omega_e = \left(\frac{L_m r_r}{L_r}\right)\left(\frac{i_{qs}}{\varphi_r}\right) + \omega_r \tag{17}$$

$$\omega_e = \frac{120f}{P} \tag{18}$$

The priority for an IM is being able to induce the target magnetic flux φ_r^* (19) in the rotor. The IM uses constant target φ_r^* up to the motor's base speed ω_b [107]. The corresponding target d-axis current i_{ds}^* in Equation (20a) is also constant up to base speed, this is dependent on the rated voltage V_s and the rated supply frequency f_b. At base speed, the B-EMF matches the rated voltage of the motor and restricts the flow of current. To allow the motor to reach higher speeds, the target flux φ_r^* and i_{ds}^* reduce proportionally with the rotor speed in Equation (20b) [71, 276]. A scaling factor ρ is used to control the rate at which i_{ds}^* reduces.

$$\varphi_r^* = L_m i_{ds}^* \tag{19}$$

$$i_{ds}^* = \begin{cases} \dfrac{V_s}{2\pi f_b L_m} & \omega_m \leq \omega_b \quad (20a) \\ \dfrac{V_s}{2\pi f_b L_m}\left[\dfrac{\omega_b}{\omega_m}\right]^{\rho} & \omega_m > \omega_b \quad (20b) \end{cases}$$

Because the maximum motor current is limited to the rated value I_s, the target d-axis current i_{ds}^* is given priority over the target q-axis current [124]. The upper limit of the target q-axis current $i_{qs\,max}^*$ (21) thus varies depending with i_{ds}^*. The target q-axis current i_{qs}^* (22) which goes towards the current controller is linearly proportional to the accelerator pedal activation level $\gamma_{acc} \in [0\ 1]$.

$$i_{qs\,max}^{*} = \sqrt{I_s{}^2 - i_{ds}^{*}{}^2} \tag{21}$$

$$i_{qs}^{*} = \gamma_{acc} i_{qs\,max}^{*} \tag{22}$$

3.2.1.4 Analytical Model of a PMSM

The q-axis and d-axis analytical circuits for an I-PMSM are given in Figure 3.4(a)-(b) respectively [70, 105]. Equations (23)-(27) simulate the electrical and dynamic characteristics of an I-PMSM [281, 282]. Unlike an IM, permanent magnets with constant magnetic flux φ_m are attatched to the rotor of a PMSM. The cross-sectional design of the magnets within the rotor effect the q-axis and the d-axis inductance L_q and L_d respectively [283, 284]. In a surface mounted PMSM (S-PMSM), the magnets are attached to the surface of the rotor and $L_q = L_d$. Whereas in an I-PMSM, the magnets are buried inside the rotor, so disturb the magnetic circuit between rotor and stator, this causes $L_q \neq L_d$ [105]. Since there is no slip between the angular velocity of the rotor and the magnetic flux wave of the stator $\omega_e = \omega_r$ and no estimation methods are required as ω_r is easily measured. The output torque for the I-PMSM is given by Equation (27).

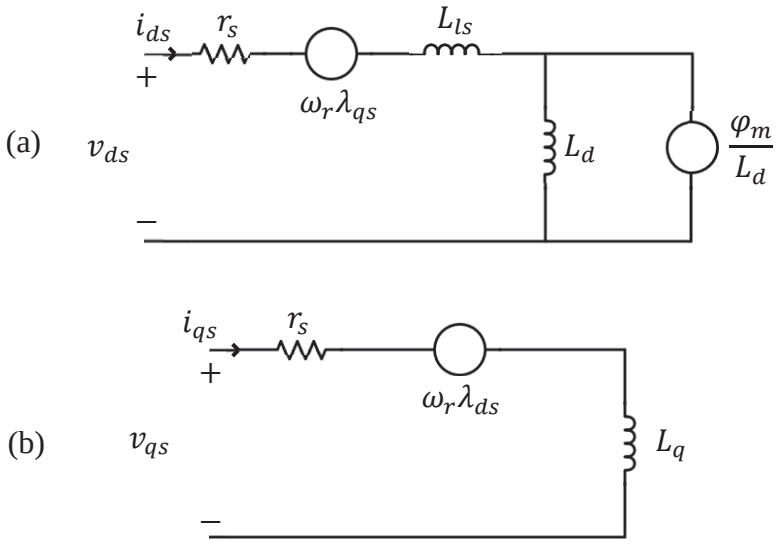

Figure 3.4 I-PMSM analytical equivalent circuits, **(a)** d-axis, **(b)** q-axis

$$v_{qs} = r_s i_{qs} + \frac{d\lambda_{qs}}{dt} + \omega_e \lambda_{ds} \tag{23}$$

$$v_{ds} = r_s i_{ds} + \frac{d\lambda_{ds}}{dt} - \omega_e \lambda_{qs} \tag{24}$$

$$\lambda_{qs} = L_q i_q \tag{25}$$

$$\lambda_{ds} = L_d i_d + \varphi_m \tag{26}$$

$$\tau_e = \frac{3P}{4}\left(i_{qs}\varphi_m - i_{qs} i_{ds}\left(L_q - L_d\right)\right) \tag{27}$$

The difference between L_q and L_d within an I-PMSM creates a reluctance torque, if this did not occur (like in an S-PMSM) the output torque would be proportional to i_{qs} and φ_m. Maximum Torque Per-Amp (MTPA) theory utilises the I-PMSM's saliency ratio ε (28) to have the d-axis reluctance torque produce useful work [104, 285, 286].

$$\varepsilon = \frac{L_q}{L_d} \tag{28}$$

The requested torque by a driver is separated between the d-axis and q-axis currents. As with the IM, the target i_{qs}^* is proportional to the accelerator pedal activation level γ_{acc} (22). Equation (29) first finds a suitable target q-axis limit $i_{qs\,max}^*$ for each rotor speed [287]. The motor's rotational velocity lies within one of three operating regions; below base speed, partial-flux weakening and full-flux weakening [288]. The partial flux weakening region lies between ω_b and the critical speed ω_c (32) [106, 284]. The target d-axis current i_d^* is then found using (30) or (31) according to the flowchart in Figure 3.5 [288].

$$i_{qs\,max}^* = \begin{cases} \dfrac{\varphi_m - \sqrt{{\varphi_m}^2 + 8(L_q - L_d)^2 I_s^2}}{4(L_q - L_d)} & \omega_m \le \omega_b \\ \dfrac{1}{\varepsilon^2 - 1}\left[\dfrac{\varphi_m}{L_d} - \sqrt{\left(\dfrac{\varepsilon\varphi_m}{L_d}\right)^2 + (\varepsilon^2 - 1)\left((\varepsilon I_s)^2 - \left(\dfrac{V_s}{\omega_e L_d}\right)^2\right)}\right] & \omega_m \ge \omega_b \end{cases} \tag{29}$$

$$i_{ds}^{*} = \frac{\varphi_m}{2(L_q - L_d)} - \sqrt{\frac{{\varphi_m}^2}{4(L_q - L_d)^2} + i_{qs}^2} \tag{30}$$

$$i_{ds}^{*} = -\frac{\varphi_m}{L_d} + \frac{1}{L_d}\sqrt{\frac{{V_s}^2}{\omega_e^2} - (L_q i_{qs})^2} \tag{31}$$

$$\omega_c = \frac{V_s}{P\varphi_m} \tag{32}$$

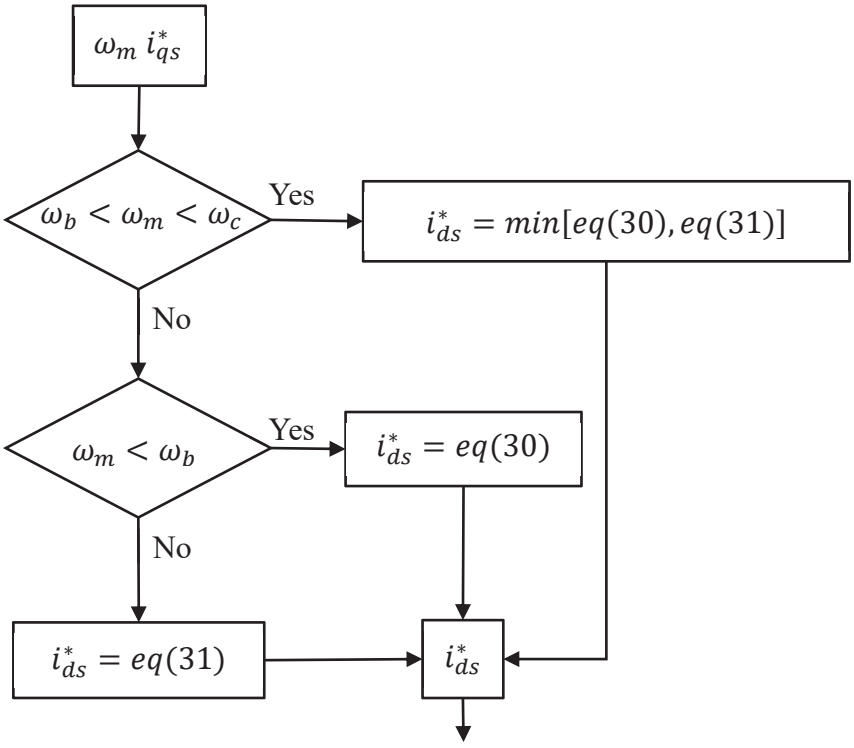

Figure 3.5 I-PMSM MTPA i_{ds}^{*} flow chart

3.2.1.5 Voltage Constraints

The process of generating the d-axis voltage v_{ds} and q-axis voltage v_{qs} is shown in (33)-(34) [105, 108]. The current controllers' output unit value d-axis $v_{d0} \in [-1\ 1]$ and q-axis $v_{q0} \in [-1\ 1]$ stator voltages. These are first multiplied by the stator's rated voltage V_s before the

respective de-coupling terms are added to them depending on whether an IM or I-PMSM is being controlled.

$$v_{ds} = v_{d0}V_s + \begin{cases} -\omega_e L_s i_{qs}\left(1 - \dfrac{L_m^2}{L_s L_r}\right) & IM \\ -\omega_e L_q i_{qs} & PMSM \end{cases} \tag{33}$$

$$v_{qs} = v_{q0}V_s + \begin{cases} \omega_e L_s i_{ds}\left(1 - \dfrac{L_m^2}{L_s L_r}\right) + \omega_e \dfrac{L_m}{L_r}\lambda_{dr} & IM \\ \omega_e L_d i_{ds} + \omega_e \varphi_m & PMSM \end{cases} \tag{34}$$

As the magnitude between v_{ds} and v_{qs} approaches V_s, the d-axis voltage v_{ds} is given priority over v_{qs} by reducing the upper q-axis voltage limit $v_{qs\,max}$ (35). Limiting the q-axis voltage does inhibit the current controller's ability to regulate the q-axis current, but this is required to allow the motor to reach higher speeds.

$$v_{qs\,max} = \sqrt{V_s^2 - {v_{ds}}^2} \tag{35}$$

3.2.2 DC-AC Inverter Models

This section discusses the DC-AC inverter topologies and control methods used within Chapter Six whereby the inverter switching devices are controlled using an advanced Space Vector Pulse Width Modulation (SVPWM) scheme.

The inverter modulates a DC voltage source V_{DC} into 3-phase AC voltage waveforms v_a, v_b and v_c. For the purpose of this investigation, pole voltages v_{aO}, v_{bO} and v_{cO} are measured between the inverter's neutral point and the individual output phases. The voltage level of the inverter is in reference to the number of pole voltages that it is able to generate [173]. The phase voltages v_{aN}, v_{bN} and v_{cN} are the potential difference between the pole voltage and an isolated neutral point N (i.e. a motor) and are calculated using Equation (36). The phase voltages are

used within the voltage vector transformations in Section 3.2.1.1 [167]. The line voltages v_{ab}, v_{bc} and v_{ca} (37)-(39) are the potential difference between two phase voltages.

$$\begin{bmatrix} v_a \\ v_b \\ v_c \end{bmatrix} = \begin{bmatrix} v_{aN} \\ v_{bN} \\ v_{cN} \end{bmatrix} = \begin{bmatrix} \frac{2}{3} & -\frac{1}{3} & -\frac{1}{3} \\ -\frac{1}{3} & \frac{2}{3} & -\frac{1}{3} \\ -\frac{1}{3} & -\frac{1}{3} & \frac{2}{3} \end{bmatrix} \begin{bmatrix} v_{aO} \\ v_{bO} \\ v_{cO} \end{bmatrix} \tag{36}$$

$$v_{ab} = v_{aN} - v_{bN} \tag{37}$$

$$v_{bc} = v_{bN} - v_{cN} \tag{38}$$

$$v_{ca} = v_{cN} - v_{aN} \tag{39}$$

3.2.2.1 Inverter Switch Control

The switching tables for a 5L-NPC and a 5-CHB inverter are given in Table 3.1 and Table 3.2 respectively. These switching tables are used to simulate the pole voltage produced by each phase leg of the inverter. The switching state combination corresponding to a particular switching state is fed into a 2D lookup table which outputs the pole voltage.

Modelling a DC-AC inverter in this manner makes numerous physical assumptions about the system. The switching components act as ideal switches with no resistance, capacitance or inductance, there are no copper or switching losses and the effect of the component temperature on the physical properties are not considered. However, because the purpose of this inverter model is to compare the switching count of different modulation strategies, this modelling technique will be adequate for this investigation. Future investigations with more detailed simulation tools and physical components will incorporate these physical assumptions back into the system at a later date.

Table 3.1 Per-phase switching table for a 5L-NPC inverter [161, 163]

Switching state S	**Pole voltage** (V)	**Switch number for phase leg** A, B **or** C			
		1	**2**	**3**	**4**
4	$\frac{V_{DC}}{2}$	1	1	1	1
3	$\frac{V_{DC}}{4}$	0	1	1	1
2	0	0	0	1	1
1	$-\frac{V_{DC}}{4}$	0	0	0	1
0	$-\frac{V_{DC}}{2}$	0	0	0	0

Table 3.2 Per-phase switching table for a 5L-CHB inverter [154, 175]

Switching state S	**Pole voltage (V)**	**Switch number for phase** A, B **or** C			
		Upper Cell		**Lower Cell**	
		1	**2**	**3**	**4**
4	$2V_{DC}$	1	0	1	0
3	V_{DC}	1	1	1	0
		0	0	1	0
		1	0	1	1
		1	0	0	0
2	0	0	0	0	0
		1	1	0	0
		1	0	0	1
		0	0	1	1
		0	1	1	0
		1	1	1	1
1	$-V_{DC}$	0	1	1	1
		0	1	0	0
		1	1	0	1
		0	0	0	1
0	$-2V_{DC}$	0	1	0	1

3.2.2.2 Inverter Operating Limits

The initial target reference voltage vector $V_{ref-initial}$ must be enclosed by the outer edges of the hexagonal SVM diagram as shown in Figure 2.7. Voltages outside the SVM diagram cannot be generated by an inverter because no voltage vectors or switching states define the

area. The six outermost vertices of the hexagonal SVM diagram represent the $\alpha - \beta$ co-ordinates of the inverter operating under 6-step control. The distance between the centre of the hexagon and the outer vertices represent voltage vectors with magnitude $\frac{2}{3}E$, where E is twice the maximum pole voltage during 6-step control (see Figure 3.6).

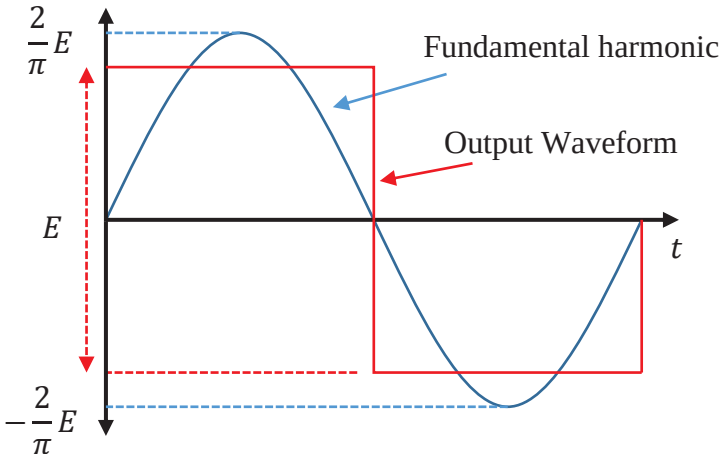

Figure 3.6 Fundamental component of an inverter operating in 6-step square wave control

To begin with, $V_{ref-initial}$ is quantified in terms of a modulation index $m \in [0\ 1]$ using (40). This compares the magnitude of $V_{ref-initial}$ with respect to the magnitude of the fundamental component V_{step} of the voltage waveform using 6-step control [156, 157, 289].

$$m = \frac{|V_{ref-initial}|}{|V_{step}|} = \frac{|V_{ref-initial}|}{\frac{2}{\pi}E} \tag{40}$$

The inverter operates in 6-step control when only the six outermost hexagonal voltage vectors of the SVM diagram are used. A diagrammatical view of the inverter's pole voltage waveform under 6-step control is shown in Figure 3.6. The modulation index classifies what region the inverter operates in (sinusoidal/linear or overmodulation) [156, 175, 177]. Figure 3.7 visually shows how the trajectory of $V_{ref-initial}$ (dotted red line) at an angle α_e against the α axis is modified for sinusoidal mode, overmodulation mode-I, and overmodulation mode-II in one major sector of a 5L-SVM diagram.

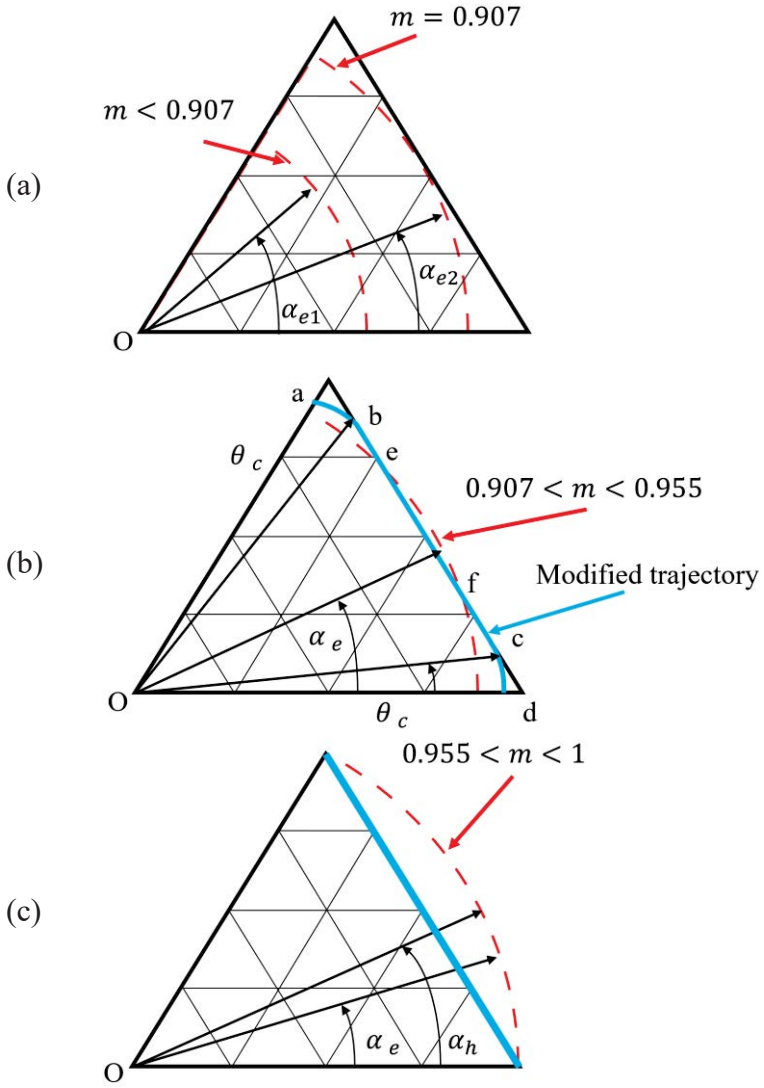

Figure 3.7 Modulation modes diagrammatical analysis [177, 204], **(a)** Sinusoidal, **(b)** Overmodulation mode I, (**c)** Overmodulation mode II

For sinusoidal mode ($0 < m < 0.907$) in Figure 3.7(a), the target trajectory of $V_{ref-initial}$ does not cross any of the outer hexagon boundaries and completes a full circle as it rotates around the SVM diagram. The example reference voltage vectors in Figure 3.7(a) make angles α_{e1} and α_{e2} against the α axis. The reference voltage vector $V_{ref-initial}$ is directly used as V_{ref}. The inverter remains in sinusoidal mode until the reference voltage reaches the edge of the outer hexagonal boundary where $V_{ref-initial} = \frac{\sqrt{3}}{2}\left(\frac{2}{3}E\right)$ and $m = 0.907$ as shown in (41).

$$m = \frac{|V_{ref-initial}|}{|V_{step}|} = \frac{\frac{\sqrt{3}}{2}\left(\frac{2}{3}E\right)}{\frac{2}{\pi}E} = 0.907 \tag{41}$$

For overmodulation mode-I ($0.907 < m < 0.955$), the target trajectory of $V_{ref-initial}$ partially crosses the outer hexagonal boundary as shown in Figure 3.7 (b). The reference voltage $V_{ref-initial}$ is forced to follow the trajectory a-b-c-d. The angular velocity of V_{ref} is the same as $V_{ref-initial}$, but the magnitude V_{ref} follows the linear trajectory b-c when α_e passes the crossover angle θ_c from Figure 3.8(a). To account for the reduction in the fundamental harmonic voltage endured when travelling down the linear trajectory, the magnitude of $V_{ref-initial}$ increases to V_m^* (42) when it re-enters the hexagonal boundaries.

$$V_m^* = \frac{2V_{DC}\left(\frac{\pi}{6} - \theta_c\right)}{\pi \sin\left(\frac{\pi}{6} - \theta_c\right)} \tag{42}$$

As m continues to increase, V_m^* reaches the outer vertices of the hexagonal boundary and the inverter enters overmodulation mode-II ($0.955 \leq m \leq 1$) as shown in Figure 3.7(c) where both the magnitude and angular velocity of $V_{ref-initial}$ are modified (43). The reference voltage V_{ref} is held at one of the hexagon vertices until α_e passes the required holding angle α_h from Figure 3.8(b) before travelling along the linear trajectory to the next hexagonal vertex.

$$\alpha_m^* = \begin{cases} 0 & for\ 0 < \alpha_e < \alpha_h \\ \left(\frac{\alpha_e - \alpha_h}{\frac{\pi}{6} - \alpha_h}\right)\frac{\pi}{6} & for\ \alpha_h < \alpha_e < \left(\frac{\pi}{3} - \alpha_h\right) \\ \frac{\pi}{3} & for\ \left(\frac{\pi}{3} - \alpha_h\right) < \alpha < \frac{\pi}{3} \end{cases} \tag{43}$$

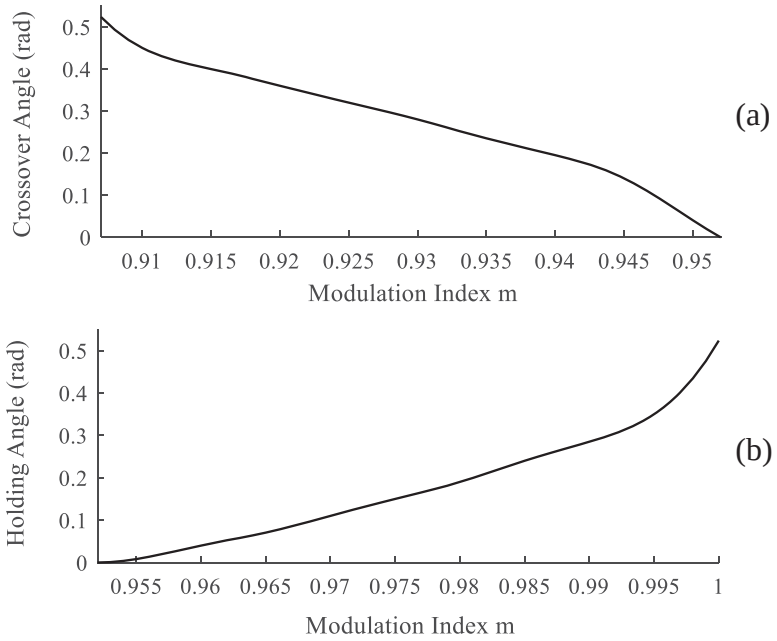

Figure 3.8 Modulation mode modifier [172, 178] **(a)** Crossover Angle, **(b)** Holding Angle

3.2.2.3 Inverter Control for Traction Motor Four-Quadrant Operation

The traction motor of an HEV/EV is required to work in all four-quadrants of the torque-speed curve. These quadrants include; forward tractive, forward braking, reverse tractive and reverse braking. The operating mode is dependent on the direction of rotor spin (forward or reverse) and the directional flow of the motor's supply current to apply either tractive or negative torque. Regardless of the operating quadrant, the reference voltage vector will still be enclosed by a hexagonal SVM diagram. The SVPWM methods examined in this thesis enable the motor to operate in all four quadrants.

3.2.3 Battery Pack Model

The auxiliary power load P_{Aux} of an HEV/EV represents the power consumed by the headlights, heating system, air-conditions pumps, etc. Along with the power consumption of the motor P_m and the charging power of the APU P_{Gen}, the total energy J_{Batt} within the battery

pack is calculated using Equation (44). The State of Energy (SOE) can be calculated using Equation (45) which offers a percentage of the battery pack's energy level with respect to its maximum capacity $J_{Batt-max}$.

$$J_{Batt}(t) = J_{Batt}(t_0) + \int_{t_0}^{t} (-(P_m + P_{Aux}) + P_{Gen})\, dt \tag{44}$$

$$SOE(t)\ \% = 100\left(\frac{J_{Batt}(t)}{J_{Batt-max}}\right) \tag{45}$$

3.2.4 Vehicle Dynamics

3.2.4.1 CarSim Vehicle Modelling

CarSim is a commercial vehicle simulation tool widely used by vehicle manufacturers and researchers around the globe. Figure 3.9 graphically shows the geometry of the vehicle parameters used within CarSim [234, 235].

The vehicle model in Figure 3.9 consists of four 2-degree-of-freedom suspension systems connected by the sprung mass m_s. The components at each corner of the vehicle are denoted by the subscript wh in reference to whether they are on the front right (*fr*), rear right (*rr*), front left (*fl*) or rear left (*rl*) corner of the vehicle, i.e. $wh = fr, rr, fl, rl$. The model accounts for the global longitudinal X_s, lateral Y_s and vertical Z_s positions of the sprung mass as well as its roll φ_s, pitch θ_s and yaw ψ_s angle about its centre of mass at height h_{COG}. The model requires the distance e_s between h_{COG} and the roll axis, the yaw inertia I_{yaw}, roll inertia I_{roll} and pitch inertia I_{pitch} of the sprung mass.

The model requires the basic geometrical parameters of the vehicle including the wheelbase L, the distance between h_{COG} to the front axle a and rear axle b as well as the track width of the front T_f and rear axle T_r. The steer angle δ_{wh} of the wheels are controlled by CarSim's internal closed-loop steering system to follow a predetermined path.

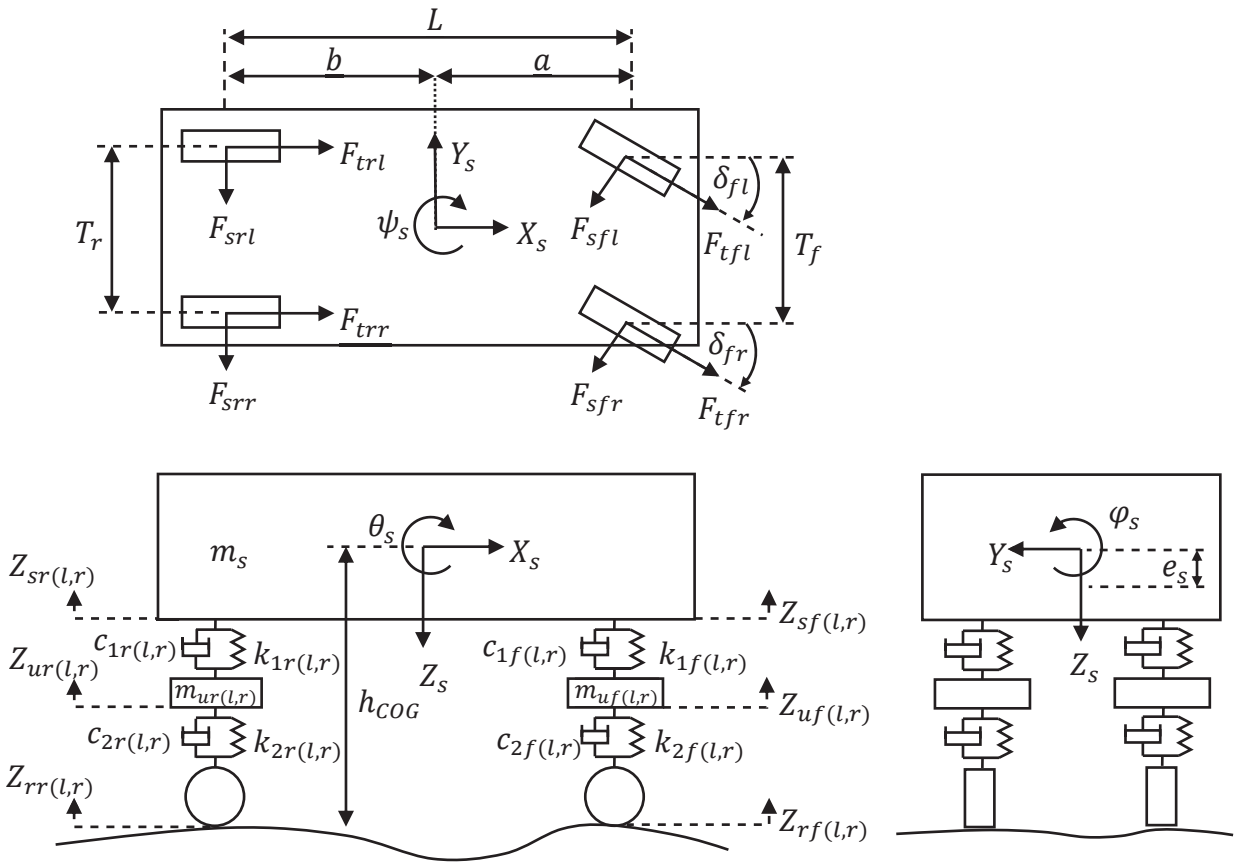

Figure 3.9 14 Degree of Freedom vehicle model [239, 240]

The suspension system consists of unsprung masses on the front axle m_{uwh} at height Z_{uwh} above the road Z_{rwh} with a spring coefficient k_{1wh} and a damping coefficient c_{1wh}. The suspension system from the tyres are represented by spring coefficient k_{2wh} and a damping coefficient c_{2wh}. The front and rear anti-roll bars are represented by torsional springs with coefficients K_{af} and K_{ar} respectively. The torsional characteristics of the chassis are represented by spring coefficient K_{φ} and a damping coefficient C_{φ}.

CarSim offers detailed multiple degree of freedom vehicle body dynamics, tyre rotational dynamics, steering control, suspension response, braking system control and powertrain models. Chapter Four and Chapter Seven use CarSim vehicle models to simulate the dynamics of the vehicle using the control systems developed in their respective chapters. CarSim allows for direct communication between itself and MATLAB via a dedicated CarSim toolbox in

Simulink. Table 3.3 shows the parameters transferred between CarSim and MATLAB/Simulink.

Table 3.3 Input-output parameters between CarSim and MATLAB/Simulink.

Thesis Chapter	CarSim Import		CarSim Export	
	Parameter	**Symbol**	**Parameter**	**Symbol**
4	Motor torque (Nm)	τ_e	Longitudinal velocity (km/h)	V_x
	Brake pedal force (N)	$F_{B-Pedal}$	Wheel rotational velocity (rad/s)	ω_{wh}
7	Longitudinal tyre force (N)	F_{xwh}	Vertical tyre force (N)	F_{zwh}
			Velocity at wheel-road (km/h)	u_{wh}
	Lateral tyre force (N)	F_{ywh}	Longitudinal velocity (km/h)	V_x
			Lateral velocity (km/h)	V_y
			Vehicle Yaw rate (rad/s)	r
			Front right steer angel (deg°)	δ_{fr}
			Front left steer angel (deg°)	δ_{fl}

3.2.4.2 The Tyre Model

Due to integration errors within CarSim, external wheel slip control techniques generate unstable tyre responses. Since Chapter Seven requires direct control of the wheel slip, the tyres and braking system are modelled in MATLAB/Simulink, the longitudinal and lateral tyre forces are then exported back to CarSim to simulate the dynamics of the vehicle body.

The wheel slip ratio σ_{wh} (46) requires the longitudinal velocity at the centre of the wheel u_{wh} and the velocity of the tyre's outer surface at a radius *R* with a rotational velocity ω_{wh}.

$$\sigma_{wh} = \begin{cases} \dfrac{u_{wh} - R\omega_{wh}}{u_{wh}} & R\omega_{wh} < u_{wh} \quad Braking \\ \dfrac{R\omega_{wh} - u_{wh}}{u_{wh}} & R\omega_{wh} \geq u_{wh} \quad Traction \end{cases} \tag{46}$$

The diagrammatical view of the wheel slip velocity components are given in Figure 3.10(a) and the wheel's sideslip angles are shown in Figure 3.10(b). The longitudinal velocity of the wheels u_{wh} (47)-(50) and the individual wheel sideslip angle α_{wh} (51)-(54) are required for the tyre model.

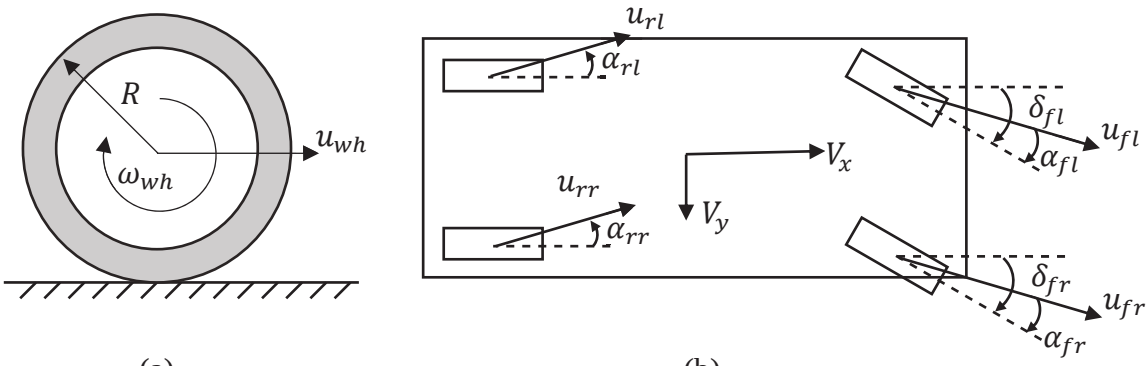

(a) (b)

Figure 3.10 Wheel dynamics, **(a)** Wheel Slip, **(b)** Wheel sideslip angles

$$u_{fl} = \left(V_x + 0.5T_f r\right)\cos\delta_{fl} + \left(V_y + ar\right)\sin\delta_{fl} \tag{47}$$

$$u_{fr} = \left(V_x - 0.5T_f r\right)\cos\delta_{fr} + \left(V_y + ar\right)\sin\delta_{fr} \tag{48}$$

$$u_{rl} = \left(V_x + 0.5T_r r\right)\cos\delta_{rl} + \left(br - V_y\right)\sin\delta_{rl} \tag{49}$$

$$u_{rr} = \left(V_x - 0.5T_r r\right)\cos\delta_{rr} + \left(br - V_y\right)\sin\delta_{rr} \tag{50}$$

$$\alpha_{fl} = \delta_{fl} - \tan^{-1}\left(\frac{V_y + ar}{V_x - 0.5T_f r}\right) \tag{51}$$

$$\alpha_{fr} = \delta_{fr} - \tan^{-1}\left(\frac{V_y + ar}{V_x + 0.5T_f r}\right) \tag{52}$$

$$\alpha_{rl} = \tan^{-1}\left(\frac{br - V_y}{V_x - 0.5T_r r}\right) \tag{53}$$

$$\alpha_{rr} = \tan^{-1}\left(\frac{br - V_y}{V_x + 0.5T_r r}\right) \tag{54}$$

The Pacejka Magic Formula produces accurate results for both steady-state and small slip angle transients (the points of concern within this thesis) in both longitudinal and lateral directions [290]. For larger slip angles beyond stable wheel slip control (past peak friction), a transient tyre model which accounts for the larger contact patch time delay would be required, but these models need more parameters and have a higher computational burden [291]. The over parameterisation of the Magic Formula model requires an extensive series of experimental tests to find all the required parameters if they are not provided. Even with these limitations, the high accuracy and low computational effort of the Magic Formula has made it used throughout literature for vehicle simulation and VSC research [235, 271, 272, 292].

The tractive force F_{twh} (55) and side forces F_{swh} (56) of the wheels from the Pacejka magic formula are split into the longitudinal forces F_{xwh} (57) and lateral forces F_{ywh} (58). The tyre-road force characteristics are represented by a peak value D_x, shape factor C_x, stiffness factor B_x and a curvature factor E_x. The effect of the wheels sideslip angle on the stiffness and shape factors are accounted for with parameters B_α and C_α respectively.

$$F_{twh} = F_{zwh}\cos(C_\alpha \tan^{-1}(B_\alpha \alpha_{wh}))\, D_x \sin\left[C_x \tan^{-1}\left(B_x\sigma_{wh} - E_x(B_x\sigma_{wh} - \tan^{-1}(B_x\sigma_{wh}))\right)\right] \quad (55)$$

$$F_{swh} = F_{zwh}\cos(C_a \tan^{-1}(B_a \sigma_{wh}))\, D_x \sin\left[C_x \tan^{-1}\left(B_x\alpha_{wh} - E_x(B_x\alpha_{wh} - \tan^{-1}(B_x\alpha_{wh}))\right)\right] \quad (56)$$

$$F_{xwh} = F_{twh}\cos\delta_{wh} - F_{swh}\sin\delta_{wh} \quad (57)$$

$$F_{ywh} = F_{twh}\sin\delta_{wh} + F_{swh}\cos\delta_{wh} \quad (58)$$

The rotational velocity of the wheel ω_{wh} (59) depends on the rotational inertia of the wheel $I_{w\,wh}$, longitudinal tractive force of the tyre F_{twh} as well as the brake torque τ_{Bwh} and drive torque τ_{Dwh} supplied to the wheel.

$$\omega_{wh} = \omega_{wh}(t_0) + \frac{1}{I_{wh}}\int_{t_0}^{t} -RF_{twh} - \tau_{Bwh} + \tau_{Dwh}\; dt \quad (59)$$

3.2.5 Simplified HEV/EV Modelling techniques

3.2.5.1 Simplified Traction Motor Model

The detailed analytical models of the traction motors offer a good trade-off between accurate modelling of the motor's dynamic and electrical characteristics against the time-space modelling complexity. However, the detailed parameters used to create these models may be difficult to obtain from motor manufacturers and performing a series of experiments to find them is impractical if numerous motors are being considered [293, 294].

Where detailed analytical motor models are not required, the output torque τ_{PM} for a prime mover (traction motor or ICE) is calculated using a 2D look-up table (60). The lookup table requires the full load output torque $\widehat{\tau_{PM}}$ at the current prime mover rotational velocity ω_{PM} and the accelerator activation level $\gamma_{acc} \in [0\ 1]$. The electrical efficiency map $\eta_e(\omega_{m,}\tau_e)$ of the traction motor is used to calculate the electrical power consumption of a traction motor P_m (61)

$$\tau_{PM} = \gamma_{acc}\ \widehat{\tau_{PM}}(\omega_{PM}) \tag{60}$$

$$P_m = \frac{\tau_{PM}\omega_{PM}}{\eta_e(\omega_{PM,}\tau_{PM})} \tag{61}$$

3.2.5.2 Simplified ICE Model

The torque-speed characteristics of an ICE are simulated using a similar manner to the simplified traction motor models using Equation (60) by replacing $PM = ICE$ or via an equivalent throttle map. The full load torque-speed curve of the traction motors are now representative of the ICE peak torque-speed curve $\widehat{\tau_{ICE}}$ and the efficiency maps of Equation (61) are replaced by the ICE's fuel consumption and tailpipe output emissions maps. See Section 5.2.3 for an example of the characteristic curves used for an ICE.

3.2.5.3 Simplified APU Model

The APU is defined by numerous factors including; output power P_{Gen} (kW), fuel consumption (L/hr) and output emissions (g/s). These parameters are integrated over time to calculate the total energy provided to the DC-Link, total fuel consumption and the total output emissions over a duty cycle.

The APU model within this thesis provides power P_{Gen} to the DC-link in one of 3 ways; full power mode, idle mode, and off. During full power mode, the genset provides full power to the DC-Link and consumes fuel at its full rate. The APU is turned on-off to keep the battery pack's SOE within safe upper and lower working limits. During idle mode, the genset provides no power to the DC-Link but consumes fuel at a fraction of the rated value. For the case study in Section 5.2, a value of 10% of the rated fuel is consumed during idle mode to highlight a worst-case scenario. When the genset is off, no power is provided to the DC-Link and no fuel is consumed and the HEV operates in full EV mode.

The manufacturer of the genset used in the case study in Section 5.2 recommends idle mode to be used for 60 seconds before and after full power mode in order to prolong the lifetime of the genset. If the SOE of the battery pack reaches the lower limit during this idling period, the genset switches to full power mode. This overruling control might adversely affect the genset's lifetime if it occurred frequently, but the more expensive battery pack's sensitivity to under-discharging is a higher priority.

3.2.5.4 Simplified Vehicle Dynamics

Chapter Five uses a simplified vehicle model to reduce the computational effort required for long simulations. The vehicle in Chapter Five is only simulating straight line velocity dynamics with no roll, pitch, yaw or wheel spin dynamics considered.

A Fuzzy Logic (FL) speed controller is used to control the vehicle's speed which attempts to follow a target velocity profile by generating appropriate accelerator $\gamma_{acc} \in [0,1]$ and brake pedal $\gamma_{brk} \in [0,1]$ activation levels [128, 295] (see Section 4.1.1).

A vehicle model created in MATLAB/Simulink contains the basic forces acting upon the vehicle. The tractive force $F_{Traction}$ at the road-wheel interface (62), the rolling resistance $F_{Rolling}$ of the tyres (63), the aerodynamic drag F_{Aero} (64) and the brake force F_{Brake} (65) are all included in the model [49, 53, 296]. The tractive force requires the output torque from the prime mover τ_{PM}, gear ratio of the final drive N_{fd}, transmission ratio N_T, their combined efficiency η_{Tfd} and the wheel's rolling radius R. As the vehicle under investigation in Chapter Five is an aeroplane pushback vehicle, the mass of the aeroplane being towed at the current time M_{Aero} is included in (63) to account for the additional rolling resistance from the aeroplane. Removal of M_{Aero} allows this vehicle model to be used for conventional passenger vehicle simulations. The rolling resistance is also dependant on the acceleration of the vehicle under gravity g and the coefficient of rolling resistance f_r between the tyre and road interface. The aerodynamic drag force F_{Aero} requires the frontal area of the vehicle A_f, coefficient of aerodynamic drag C_D and the density of the air ρ_{air}. The combined brake force F_{Brake} uses a linear relationship between the brake pedal activation level γ_{brk} and the maximum brake force available to the road-wheel conditions F_{B-max}.

The effective additional towing mass of the vehicle M_r (66) is dependent on the rotational inertias of the prime mover I_{PM}, transmission I_T, final drive I_{Fd} and the wheels I_{Wh}. The longitudinal acceleration a_x of the vehicle is then calculated using (67). The rotational speed of the prime mover ω_{PM} is then calculated using (68).

$$F_{Traction} = \frac{\tau_{PM} N_{fd} N_T \eta_{fd}}{R} \tag{62}$$

$$F_{Rolling} = (M_{Veh} + M_{Aero}) g f_r \tag{63}$$

$$F_{Aero} = \frac{1}{2} C_D \rho_{air} A_f {V_x}^2 \tag{64}$$

$$F_{Brake} = \gamma_{brk} F_{B-max} \tag{65}$$

$$M_r = \left(I_{PM} N_{fd}^2 + I_T N_{fd}^2 + I_{Fd} N_{fd}^2 + I_{Wh}\right) \frac{1}{R^2} \tag{66}$$

$$F_{Traction} - F_{Brake} - F_{Aero} - F_{Rolling} = (M_{Veh} + M_{Aero} + M_r) a_x \tag{67}$$

$$\omega_{PM} = \frac{V_x N_{fd} N_T}{R} \tag{68}$$

3.3 Statistical Analysis Methods

This section presents the statistical analysis tools used to evaluate the accuracy of the modelling techniques described in Section 3.2 and the performance of the control methods developed in this thesis against pre-existing control schemes.

3.3.1 Controller Error Analysis

The Symmetrical Mean Absolute Percentage Error (SMAPE) (69) quantifies the accuracy of a control system with an average percentage error. This is done by comparing the target (forecast) values F_n and the actual values A_n at the time interval n in a time series with n_max data points. The smaller the SMAPE, the greater the accuracy of the control system. Throughout this thesis, SMAPE values below 5% are deemed acceptable error percentages to state that the control system is sucessfully able to regulate its control variables.

$$SMAPE\ (\%) = \frac{100}{n\_max} \sum_{n=1}^{n\_max} \frac{|F_n - A_n|}{|A_n| + |F_n|} \tag{69}$$

The advantage this version of the SMAPE over other average percentage error quantifiers for time series data is that this SMAPE equation will still work when $A_n = 0$. However, this version of the SMAPE is slightly sensitive to percentage value variances between overestimation and underestimation, but it is still commonly used in practice as this variance is usually small enough to be negligible [297].

3.3.2 Waveform Harmonic Distortion

The Total Harmonic Distortion (THD) (70) is a measure of how much a waveform has distorted from its fundamental component $|V|_{fund}$ due to other harmonics Hf between the second harmonic ($Hf = 2$) and an upper limit Hf_max. The Weighted-THD (WTHD) (71) places more emphasis on low order harmonic distortion by giving high frequency harmonics a lower weighting factor [163]. Minimising these values is a key objective for DC-AC inverters as they attempt to produce pure sinusoidal voltage and current waveforms.

$$THD = \frac{1}{|V|_{fund}} \sqrt{\sum_{Hf=2,3\ldots}^{Hf\_max} |V|_{Hf}^2} \tag{70}$$

$$WTHD = \frac{1}{|V|_{fund}} \sqrt{\sum_{Hf=2,3\ldots}^{Hf\_max} \left(\frac{|V|_{Hf}}{Hf}\right)^2} \tag{71}$$

3.3.3 Vehicle Dynamic Performance Indices

The performance indices (72)-(75) are used to evaluate dynamic and braking performance of a vehicle during an emergency braking scenario. The total braking time (t_{bk}) and longitudinal braking distance (X_{bk}) are primarily used for straight line braking scenarios, but these do not account for any steering or yaw rate control.

The performance index J (72) compares the braking severity and steering controllability between the start of the braking scenario at time t_1 until the vehicle comes to a complete stop at time t_2 [259]. This index relies on the peak COF between the road and wheel interface μ, the initial velocity entering the braking manoeuvre V_{x0} and a weighting factor ρ_w ($\rho_w = 0.7$). The weighting factor is used to place more emphasis on the braking severity or the yaw rate control.

The Integrated Yaw Rate Error (IYRE) (73) integrates the error between the vehicle's target yaw rate r^* and the actual yaw rate r over time. Low IYRE values show that the vehicle has good steering responsiveness. The Integrated Sideslip Error (ISSE) (74) integrates the vehicle sideslip angle β_{ss} over time. Low values of the ISSE show that the vehicle has good stability.

The Integrated Steering Control (ISC) (75) shows how much driver steering intervention is needed to maintain control by integrating the steer angle δ over time. Inexperienced drivers may be unable to control the vehicle if excessive steering input is required.

$$J = \rho_w \left(\frac{2\mu g X_{bk}}{{V_{x0}}^2} - 1 \right)^2 + (1 - \rho_w) \left(\frac{\int_{t_1}^{t_2} (r - r^*)^2 \, dt}{\int_{t_1}^{t_2} (r^*)^2 \, dt} \right) \tag{72}$$

$$IYRE = \int_{t_1}^{t_2} |r - r^*| \, dt \tag{73}$$

$$ISSE = \int_{t_1}^{t_2} |\Delta\beta_{ss}| \, dt \tag{74}$$

$$ISC = \int_{t_1}^{t_2} |\delta| \, dt \tag{75}$$

3.4 Model Verification Procedure

3.4.1 Traction Motor Model Verification

The traction motor models are constructed in MATLAB/Simulink using the equations described in Section 3.2.1 using basic components (integrators, multipliers, etc.). To ensure that the motor models are constructed correctly, their dynamic and electrical performance are compared to the commercial Powertrain Blockset™ motor models. The models within this Blockset were chosen over other commercial MATLAB/Simulink models because they are based on the same analytical equations and the same assumptions described in Section 3.2.1. This makes them not suitable for motor design application, but acceptable for HEV/EV and standalone motor control applications. The commercial models include additional features such as viscous damping, power loss considerations and bandwidth current control. The additional complexity of the commercial models increase the simulation time during parallel simulations and these commercial models cannot be easily deconstructed to examine the internal control signals and do not permit exporting the internal control variables required for the flux wave estimation (see Section 3.2.1.3). The commercial motor models are therefore not used for the main investigation of this thesis but confined to this verification investigation and act as a sensibility check of the newly constructed MATLAB/Simulink models to ensure that they produce similar magnitude results.

The motor models for this verification investigations are modelled independently from a vehicle and instead have a load torque τ_L providing resistance applied to the rotor with rotational inertia J_r. An IM and an I-PMSM motor with parameters given in Table 3.4 are used in both MATLAB/Simulink and within the Powertrain Blockset™ models [143, 298]. These motors are controlled using identical FOC architectures as shown in Figure 3.2 of Section 3.2.1.2 and follow the same target speed-torque profile. The PI controllers for the IM and I-

PMSM motor were tuned for the specific motors using the controller gains in Table 3.5. Data used for the SMAPE results in Table 3.6 were taken at $5x10^{-4}$s discrete time steps, data points lower than 1% of the peak control variable are negated.

Table 3.4 IM and I-PMSM parameters [143, 298]

Parameter	Symbol	Motor	
		IM	**I-PMSM**
Number of poles	P_m	4	8
Rated power (kW)	P_{max}	37.5	100
Base speed (rpm)	ω_b	1675	3000
Rated Voltage (V)	V_s	380	155
Rated Current (A)	I_s	78	450
Stator resistance (Ω)	r_s	0.087	0.0083
Rotor resistance (Ω)	r_r	0.228	-
Magnetising inductance (mH)	L_m	34.7	-
Leakage stator inductance (mH)	L_{ls}	0.8	-
Leakage rotor inductance (mH)	L_{lr}	0.8	-
Rotor flux max (Wb)	φ_r	0.97	-
Magnet flux (Wb)	φ_m	-	0.071
D-axis inductance (mH)	L_d	-	0.174
Q-axis inductance (mH)	L_q	-	0.293
Rotor Inertia (kg.m^2)	J_r	0.2	0.5

Table 3.5 PI controller gains for IM and I-PMSM model comparison investigation

Motor	Controller	Proportional gain	Integral gain
IM	V_x	1	0.2
	i_{qs}	10	10
	i_{ds}	10	10
	φ_r	1000	100
I-PMSM	V_x	0.1	0.1
	i_{qs}	1	0.2
	i_{ds}	1	0.2

The comparison between the IM and I-PMSM motor models are given in Figure 3.11 and Figure 3.12 respectively.

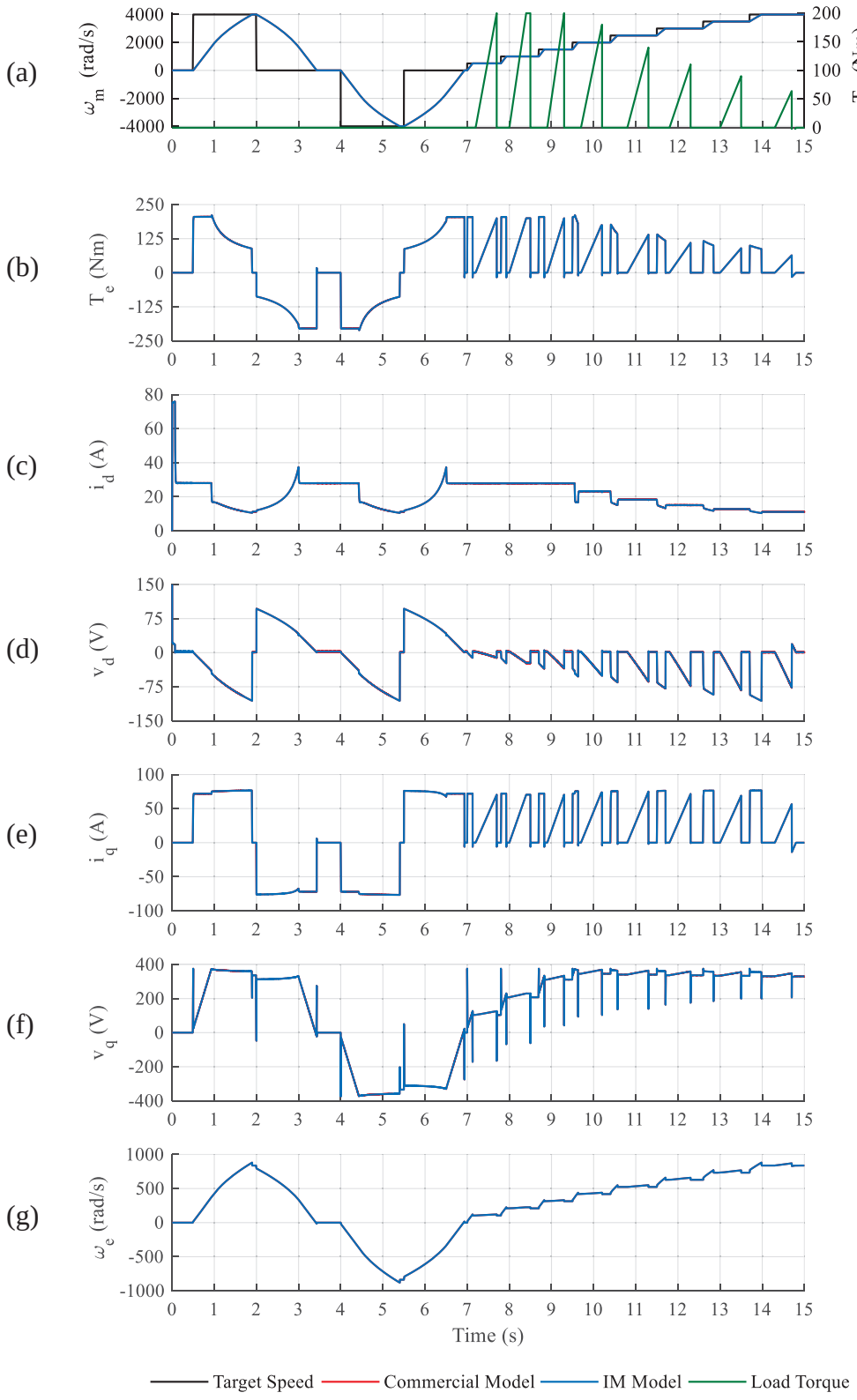

Figure 3.11 IM model verification simulation **(a)** ω_m comparison, **(b)** τ_e comparison, **(c)** i_{ds} comparison, **(d)** v_{ds} voltage comparison, **(e)** i_{qs} comparison, **(f)** v_{qs} comparison, **(g)** ω_e comparison

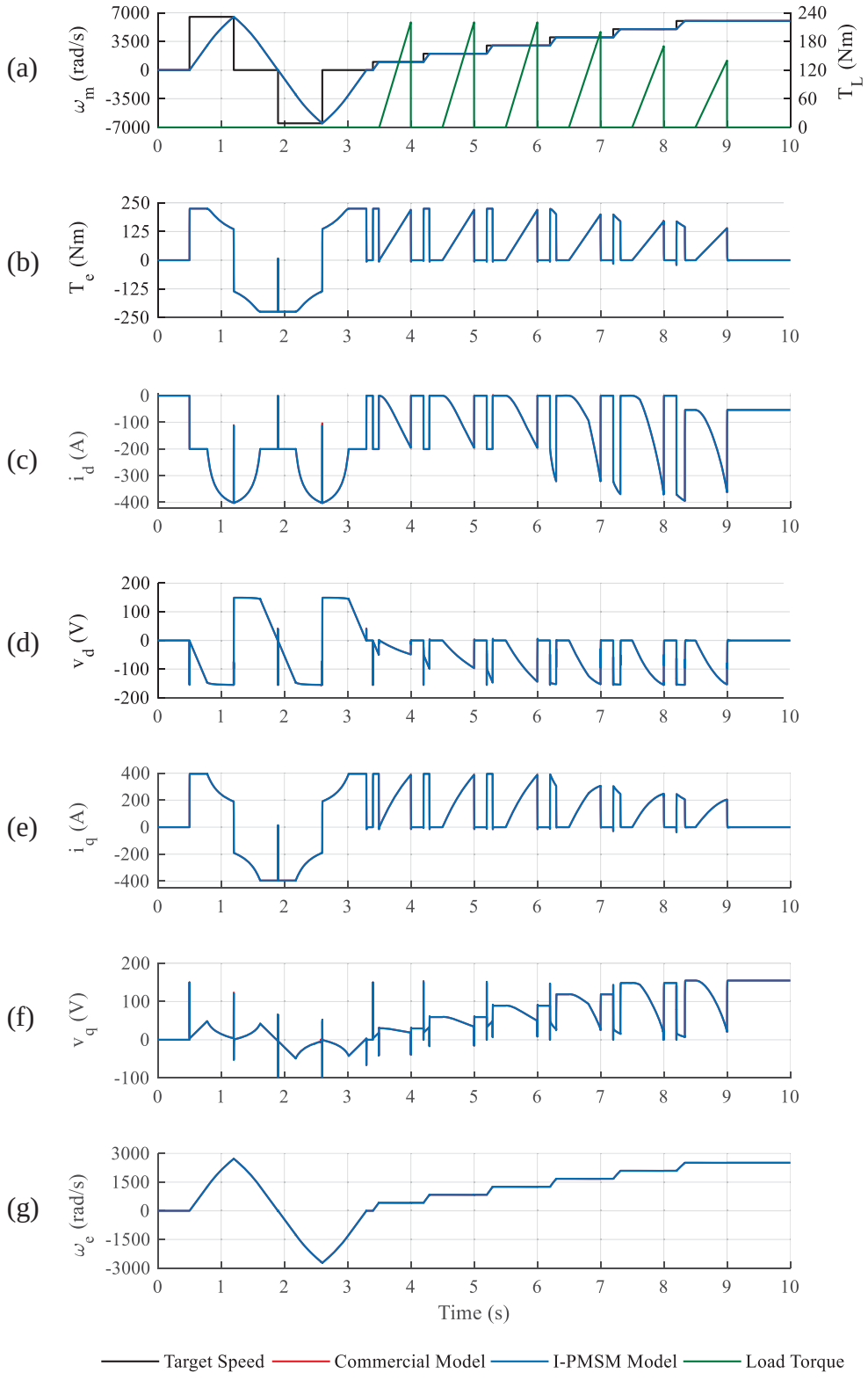

Figure 3.12 I-PMSM model verification simulation **(a)** ω_m comparison, **(b)** τ_e comparison, **(c)** i_{ds} comparison, **(d)** v_{ds} voltage comparison, **(e)** i_{qs} comparison, **(f)** v_{qs} comparison, **(g)** ω_e comparison

The dynamic and electrical performance of the motors constructed from basic MATLAB/Simulink components perform comparably to the commercially available models. In addition, the FOC schemes are able to suitably maintain the control variables while conforming to the systems current and voltage limits.

The SMAPE analysis between the MATLAB and commercial motor models given in Table 3.6 show that the error percentage between the two models are within acceptable levels. Therefore, the analytical motor models and FOC scheme architecture produce comparable results to the commercial models (accounting for similar limitations and simplifications as discussed) and deemed suitable for use within the main investigation of this thesis.

Table 3.6 SMAPE analysis between the MATLAB and Commercial IM and I-PMSM models.

Control Variable	SMAPE (%)	
	IM	I-PMSM
ω_m	9.6×10^{-6}	0.0051
τ_e	0.0152	2.77
i_d	0.0115	1.37
v_d	0.825	3.41
i_q	0.015	3.65
v_q	0.067	2.83
ω_e	0.0012	0.0049

3.4.2 DC-AC Inverter Model Verification

To ensure that the inverter model described in Section 3.2.2 is constructed correctly, the output voltage for this model is compared to the output voltage of a CHB inverter modelled in the Simscape environment of MATLAB/Simulink. This is to verify that both models output the correct voltage level for a given combination of command signals. The Simscape CHB inverter is constructed using the 5L-CHB architecture as shown in Figure 2.4(b) using 32 ideal switches and 8 ideal DC voltage sources with parameters given in Table 3.7. Simscape models are widely used throughout literature for DC-AC inverter modelling and control applications [160, 299,

300, 301]. Because ideal components are being used for the Simscape model, they will have the same simplifying physical assumptions to the inverter model described in Section 3.2.2, but the justification remains the same in that only the output voltage is being checked for this inverter topology and control signals.

Table 3.7 Simscape DC-AC inverter model parameters

Parameter	Value
DC Source	
Voltage (V)	100
Internal Resistance (Ω)	0.1
Charge Capacity	Infinite
Switches	
Closed Resistance (Ω)	0.01
Open Resistance (Ω)	$1x10^8$

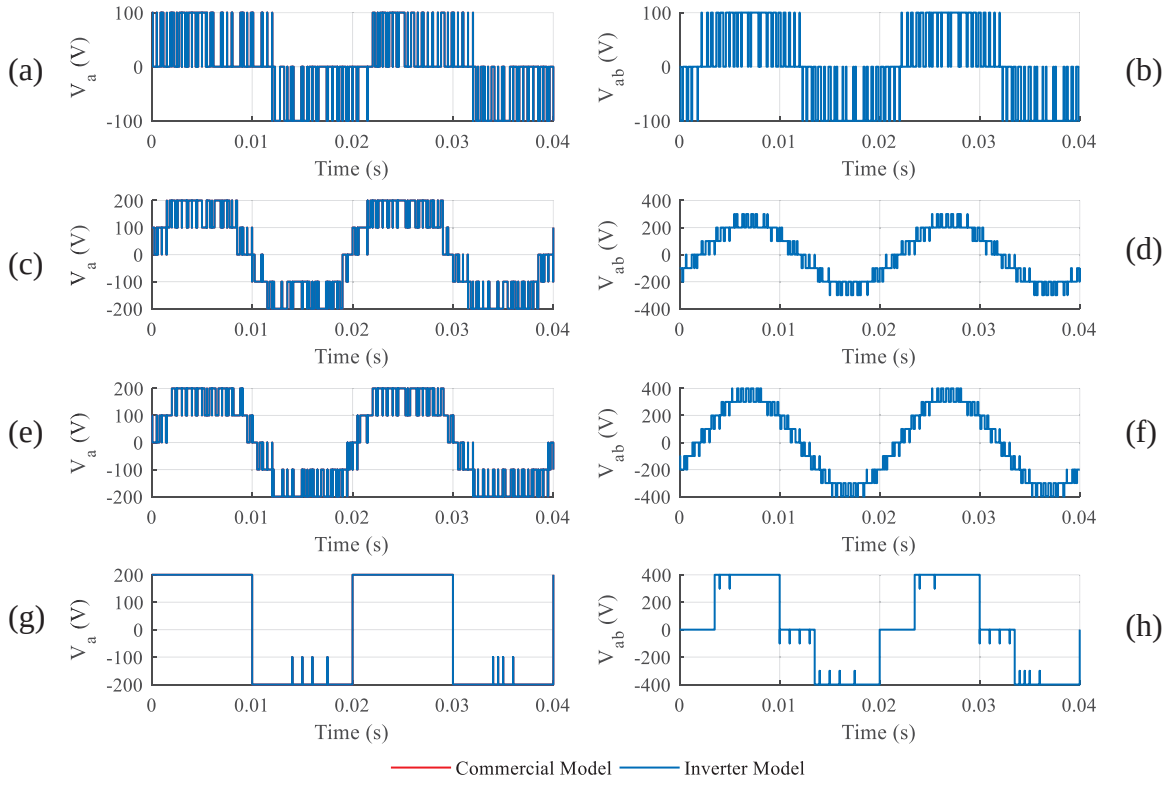

Figure 3.13 DC-AC inverter model comparison, **(a)** v_{aN} at $m = 0.2$, **(b)** v_{ab} at $m = 0.2$, **(c)** v_{aN} at $m = 0.7$, **(d)** v_{ab} at $m = 0.7$, **(e)** v_{aN} at $m = 0.9$, **(f)** v_{ab} at $m = 0.9$, **(g)** v_{aN} at $m = 1$, **(h)** v_{ab} at $m = 1$

The inverter switching devices are controlled using the SVPWM scheme described in Section 6.1. The inverter uses a switching frequency of $f_s = 2$ kHz to create a voltage waveform with a fundamental harmonic of 50 Hz over a range of modulation indexes. The comparison between the two inverter models is shown in Figure 3.13. Both models produce identical voltage waveforms to one another over the range of output waveform modulation indices. However, due to the large number of parallel simulations required for the investigation in Section 6.2, the simpler 2D look-up tables will be used for the simulation investigation in this thesis instead of the Simscape model to reduce simulation time.

3.4.3 Tyre Model Verification

To ensure that the tyre models are constructed correctly in MATLAB/Simulink, their tractive force and dynamic performance is compared to the commercial Powertrain Blockset™ tyre model. The models within this Blockset were chosen over other commercial MATLAB/Simulink models because they are based on the same Pacejka Magic Formula equations described in Section 3.2.4.2. The commercial models will therefore also suffer with the limitations discussed in Section 3.2.4.2 but still act as a suitable verification tool and act as a sensibility check of the newly constructed MATLAB/Simulink models to ensure that they produce similar magnitude results.

The Powertrain Blockset™ tyre model is more detailed as it includes greater detail about the tyre's relaxation length, contact patch and damping coefficient. However, this model does not consider the sideslip angle or lateral tyre forces and therefore cannot be used for the VSC vehicle model in Chapter Seven, it will therefore be confined to the comparison simulations for the longitudinal tractive forces using the parameters in Table 3.8. The applied axle torque, longitudinal speed profile and wheel dynamics for both models are given in Figure 3.14.

Table 3.8 Longitudinal tyre parameters for commercial and Simulink tyre models

Parameter	**Value**
I_{Wh} (Kg.m^2)	0.8
Relaxation length (m)	0.05
R (m)	0.3
Inflation pressure (kPa)	220
D_X	1
C_X	2.7
B_X	4
E_X	1
F_z (N)	1000
m_s (kg)	100

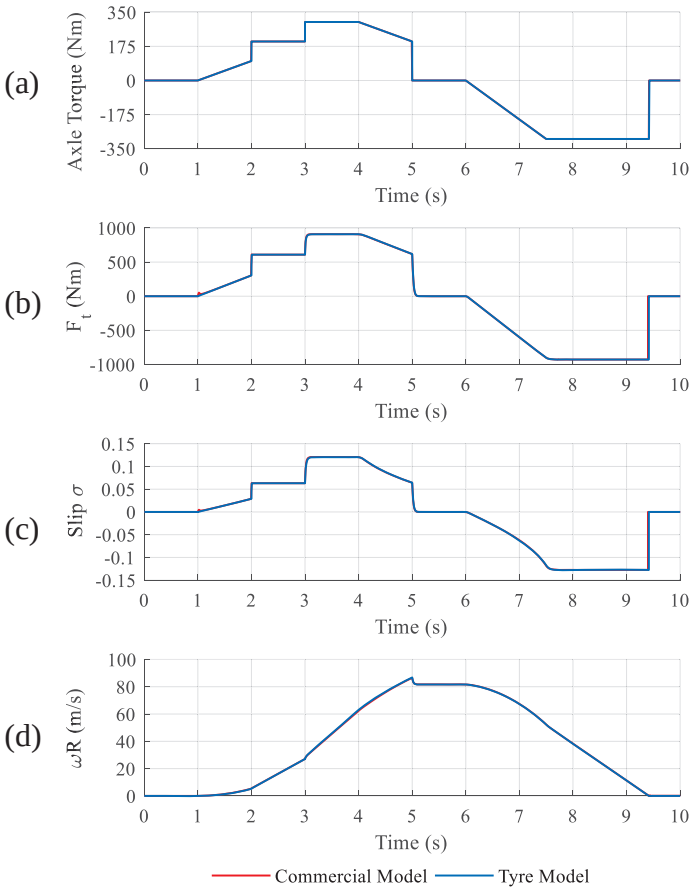

Figure 3.14 Tyre model verification, **(a)** Applied axle torque, **(b)** F_t, **(c)** σ_{wh}, **(d)** u_{wh}

From the results in Figure 3.14 and the SMAPE comparison values in Table 3.9, both the commercial and Simulink tyre models have comparable longitudinal performance to one another validating the use of the MATLAB tyres for the main investigation within this thesis.

Data for the SMAPE values in Table 3.9 used at $1x10^{-6}$s discrete time steps. Data points lower than 1% of the peak control variable are negated.

Table 3.9 SMAPE evaluation between the Simulink tyre model and commercial tyre model.

Control Variable	SMAPE (%)
$\boldsymbol{F_t}$	1.43
$\boldsymbol{\sigma_{wh}}$	1.41
$\boldsymbol{\omega_{wh}R}$	1.37

3.4.4 Control System Verification

There are numerous levels of controller verification, each method progresses upon the previous and increasing the amount of verification. The different methods should be applied at different times of the controller development process as follows:

- Model-in-the-Loop (MIL) – The control system is first designed with a plant model in a fully simulated environment [302]. The parameters of the control system can be initialised, tested and adjusted quickly to obtain a first iteration of the controller design which will operate as intended.
- Software-in-the-Loop (SIL) - The controller designed using the MIL simulations now runs on a simulated version of the hardware which the controller is intended to be implemented into [303]. During the SIL stage, any limitations or undesirable characteristics of the physical hardware will be replicated in the simulation. As both MIL and SIL still operate in a fully simulation-based environment, adjustments to the control system can be made and re-tested quickly.
- Processor-in-the-Loop (PIL) – Here, the MIL controller is compiled into code that enables it to run on physical hardware [302, 304, 305]. As a precursor to the final hardware verification, the key objectives for PIL simulations are to ensure that the compiled code performs numerically identical to the MIL counterparts, check for compiler optimisation

flags and the memory footprint of the compiled code [306]. PIL is able to run the controller in pseudo-time on physical hardware with a simulated plant environment.

- Hardware-in-the-Loop (HIL) – This is the final stage of the verification process before the controller is implemented on a physical plant. The controller must run successfully in real-time with a simulated plant environment.

A control system that can successfully run in real-time for a HIL simulation can be classed as validated and ready for full scale implementation with a physical control plant. PIL however acts an ideal bridge between MIL/SIL and HIL. In the absence of real-time simulation tools, the pseudo-time PIL simulation can be used to verify the controller code and compiler methods ahead of the HIL simulation. PIL simulations will be carried out throughout this thesis as a method of verifying that the compiled control systems behave numerically identical to their MIL counterparts. The HIL validation procedure will be conducted in the future when real-time simulation and hardware tools become available.

An Arduino Mega 2560 with specifications given in Table 3.10 acts as the physical hardware for the PIL simulations. The open source Arduino toolbox for MATLAB/Simulink enables code generation which directly converts the controllers designed in Simulink into code and directly implements it onto the Arduino.

Table 3.10 Arduino Mega 2560 microcontroller technical specification [307]

Information	**Specification**
Microcontroller	ATmega2560
Connection Type	USB
Operating Voltage	5 V
DC Current per I/O Pin	20 mA
Flash Memory	256 kb
SRAM	8 kb
EEPROM	4 kb
Clock Speed	16 MHz

A USB connection between the Arduino and the computer running the software-based simulations enable the two environments to communicate with one another. The flowchart of controller inputs and outputs between MATLAB/Simulink, CarSim and the Arduino is shown in Figure 3.15. The communication between MATLAB/Simulink and CarSim is confined to the software environment, only during the PIL simulations is the Arduino required.

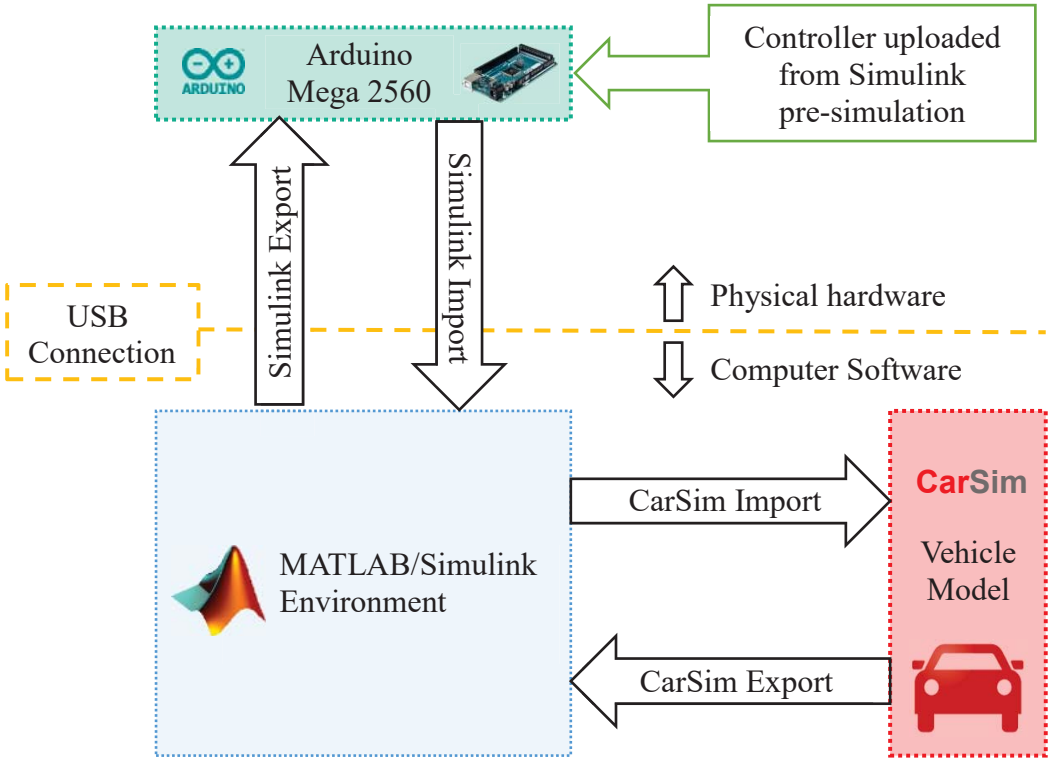

Figure 3.15 PIL control flowchart using Matlab/Simulink, CarSim and an Arduino Mega 2560 microcontroller

Only one controller (Fuzzy Logic, PI etc) from each system is able to run on the Arduino when communicating with MATLAB/Simulink at a single time. Therefore, numerous PIL simulations are conducted for each process or scenario investigated within this thesis. The individual control system variables for each PIL simulation which are exported to the Arduino and imported back into Simulink are given in Table 3.11, the reader should refer to the corresponding chapters for further detail on the control variables under investigation. All the

controllers in Table 3.11 ran at a discrete time step of 0.001s. However, due to the high computational load on the computer running the simulations and use of serial connection between the Arduino and the computer, the PIL simulations do not run in real time. Therefore, the PIL simulations are conducted before the main simulation study to verify that the compiled controller code acts identically to the MIL simulations which then take over for the remainder of the investigation.

Chapter Four and Chapter Seven each develop new control systems. The results of the PIL simulations are presented in their respective chapters before the simulation investigation begins to ensure that the controllers are unaffected by the code compiler methods. Because Chapter Five introduces a new traction motor sizing strategy which uses no controllers, no PIL simulations are required. Even though Chapter Six does develop a DC-AC inverter control methodology, no controllers (PI, FLC SMC) are used, instead a series of algebraic functions simply generate appropriate switch controls. Future efforts will be undertaken to validate the control methodology in Chapter Six by controlling the physical switches of an inverter, but no PIL simulations are conducted at this stage.

Table 3.11 Arduino PIL controller input-output parameters

Thesis Chapter	Controller Name	Simulink Export		Simulink Import
4	FL-Speed	ΔV_x	$\frac{\Delta V_x}{dt}$	γ_{acc} , γ_{brk}
	FL-Current	$\Delta i_{ds,qs}$	$\zeta_{ds,qs}$	$v_{ds,qs}$
	FL-Flux	$\Delta \varphi_r$	$\frac{\Delta \varphi_r}{dt}$	i_{ds}^*
7	FL-VSC-GR	M_Z	$\frac{M_Z}{dt}$	G^*
	FL-VSC-FR	ΔG	γ	τ_B
	FL-VSC RL	ΔG	γ	τ_B

3.5 Summary

This chapter has presented the modelling and control techniques used to represent the traction motor, DC-AC inverter and vehicle dynamics required for the research conducted within the remainder of this thesis. The suitability of the models created in MATLAB/Simulink for use within HEV/EV simulations have been verified by comparing their outputs against commercially available equivalent simulation tools. How and why these models are used for the various research activities within this thesis is given and why they were chosen over the commercially available methods has also been explained.

The statistical analysis methods used to verify the modelling techniques and analyse the control algorithms in the remainder of this thesis have also been introduced. The explanations as to how and why they are used accompany their explanation. These statistical methods are used to quantify the performance of the control systems developed within this thesis against the state-of-the-art predecessors.

The PIL experimental procedures used to verify the intelligent control algorithms have been presented. These are used to confirm that the control systems can perform numerically identical to their software-based counterparts once they have been compiled for use on embedded hardware.

Chapter Four

Fuzzy Logic Field-Oriented Control for Traction Motors

The robustness of Fuzzy Logic (FL) controllers in previous literature have shown them to be insensitive to system and parameter changes, making them a suitable candidate for Field-Oriented Control (FOC) [140, 141, 142]. The author proposes a FL controller based FOC (FL-FOC) system consisting of independent FL; vehicle speed, traction motor i_{qs}, traction motor i_{ds} and IM φ_r controllers developed in Section 4.1. These controllers take place in the FOC architecture in Figure 3.2 of Section 3.2.1.2. The aim of the FL-FOC scheme is to stably control the FOC objectives within acceptable error tolerances with any HEV/EV powertrain architecture system and multiple traction motor topologies without the need for re-tuning.

Although this chapter only investigates vehicles powered purely by traction motors, as is the case with series-HEVs and pure EVs, it is possible to extrapolate this system to control the electric motors of other HEV powertrain architectures (parallel, power-split) with minimal changes to the control architecture. This is explained where necessary within this chapter.

Section 4.1 presents the FL controllers used within the FL-FOC system whereby the PIL simulations are then given in Section 4.2. The performance of the FL-FOC system in comparison to a PI based FOC scheme is given in Section 4.3 with an investigation into the systems robustness in Section 4.4.

The contents of this chapter have been published in a journal article which presented the FL-FOC scheme [295] and at a conference which analysed its robustness in further detail [308].

4.1 Fuzzy Logic Controllers within the FL-FOC Scheme

The FL-FOC scheme consists of independent FL speed, i_{qs}, i_{ds} and φ_r (in an IM) controllers. These controllers use the linguistic terms Positive Large (PL), Positive Medium (PM), Positive Small (PS), Zero (Z), Negative Small (NS), Negative Medium (NM) and Negative Large (NL).

4.1.1 Fuzzy Logic Speed Controller

The membership functions for the FL speed controller are given in Figure 4.1 and the rule base is given in Table 4.1. This controller uses the longitudinal velocity error ΔV_x (76) at time t as the first input and its time derivative as the second input to generate a suitable pedal activation level.

$$\Delta V_x(t) = V_x^*(t) - V_x(t) \tag{76}$$

Table 4.1 FL Speed Controller rule base

		ΔV_x						
		NL	**NM**	**NS**	**Z**	**PS**	**PM**	**PL**
$\frac{d(\Delta V_x)}{dt}$	**NL**	NS	Z	Z	PS	PM	PM	PL
	NM	NM	NS	Z	Z	PS	PM	PL
	NS	NM	NM	NS	Z	PS	PM	PL
	Z	NL	NM	NS	Z	PS	PS	PM
	PS	NL	NM	NS	Z	PS	PS	PM
	PM	NL	NM	NS	Z	Z	PS	PM
	PL	NL	NM	NM	NS	Z	Z	PS

An input range of ± 5 km/h in Figure 4.1(a) is used for the controller's first input ΔV_x because this offers the best trade-off between a low steady-state velocity error and control realism. Reducing this input range improves the steady-state error of the vehicle, but it also resulted in erratic pedal control. For this investigation, pulsating the accelerator or brake pedal more than 2 times per second (>2 Hz) with >20% activation level is considered to be *erratic* pedal control. Larger pedal activation levels at this frequency (or higher frequencies) are

deemed to be beyond *typical* achievable vehicle speed control by a real driver. Higher pedal activation levels ($> 20\%$) at a lower frequency (< 2 Hz) are permitted. The second input range ± 20 km/h/s in Figure 4.1(b) for the time derivative of ΔV_x is used because 20 km/h/s approaches the acceleration ability of high performance sports vehicles (0-60 mph time ≈ 4.8 s). Most typical drivers would accept ± 20 km/h/s to be a *large* acceleration value.

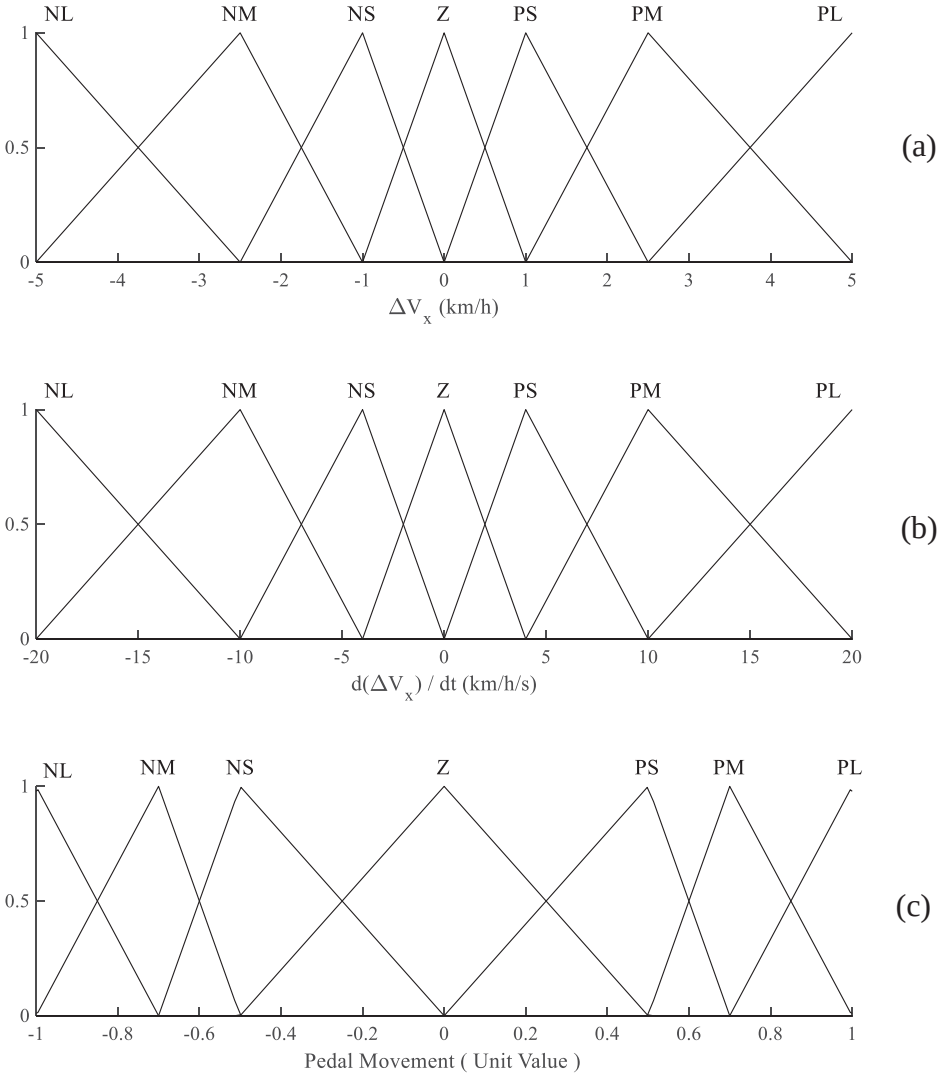

Figure 4.1 FL speed controller membership functions, **(a)** Input 1 - ΔV_x, **(b)** Input 2 – $\frac{d(\Delta V_x)}{dt}$, **(c)** Output - Pedal movement

A controller output with a magnitude 1 shows that the accelerator or brake pedal is fully activated. Positive speed controller outputs represent accelerator pedal activation levels and

negative outputs represent brake pedal activation levels. An accelerator pedal activation level corresponds to the driver requesting a motor torque output to either accelerate the vehicle or maintain a steady cruising speed. For series-HEVs and pure EVs, the positive unit value output from the controller is multiplied by the motors rated current I_s and separated into d and q axis currents for the respective motor topologies to generate the required output torque (see Section 3.2.1.3-3.2.1.4). For other HEV powertrain architectures (parallel, power-split, etc.), the positive unit value output is first separated between the individual torque sources (ICE and traction motor). The fraction of the total torque required to be produced by the traction motor/s then follow a similar process as for a pure EV. Brake pedal activation levels correspond to the driver requesting brake torques to decelerate the vehicle.

Some examples of the rule base for the for the FL speed controller are explained as follows:

- If $\Delta \boldsymbol{V_x}$ is (Z) and $\frac{\Delta \boldsymbol{V_x}}{\boldsymbol{dt}}$ is (Z) then **Pedal Movement** is (Z). If the vehicle is travelling at its target velocity and is not accelerating or decelerating, then no accelerator or brake pedal is required.
- If $\Delta \boldsymbol{V_x}$ is (NL) and $\frac{\Delta \boldsymbol{V_x}}{\boldsymbol{dt}}$ is (NS) then **Pedal Movement** is (NM). Even though the vehicle is travelling much faster that its target velocity, the brake pedal does not need to be fully applied because the vehicle is already decelerating towards the target velocity.
- If $\Delta \boldsymbol{V_x}$ is (PL) and $\frac{\Delta \boldsymbol{V_x}}{\boldsymbol{dt}}$ is (NS) then **Pedal Movement** is (PL). If the vehicle is travelling much slower than the target velocity and decelerating, the accelerator pedal is fully applied to bring the vehicle back up to the target velocity.

4.1.2 Fuzzy Logic Current Controller

Both i_{qs} and i_{ds} current are controlled using identicle indpendent FL current controllers. The FL current controllers use the membership functions given in Figure 4.2 and the rule base Table 4.2. These controllers use the instantaneous current error $\Delta i_{ds,qs}$ (77) as the first input

and the change in current error from the previous discrete time step $\zeta_{ds,qs}$ (78) as the second input [148, 287].

$$\Delta i_{ds,qs}(t) = i^{*}_{ds,qs}(t) - i_{ds,qs}(t) \tag{77}$$

$$\zeta_{ds,qs} = \Delta i_{ds,qs}(t) - \Delta i_{ds,qs}(t-1) \tag{78}$$

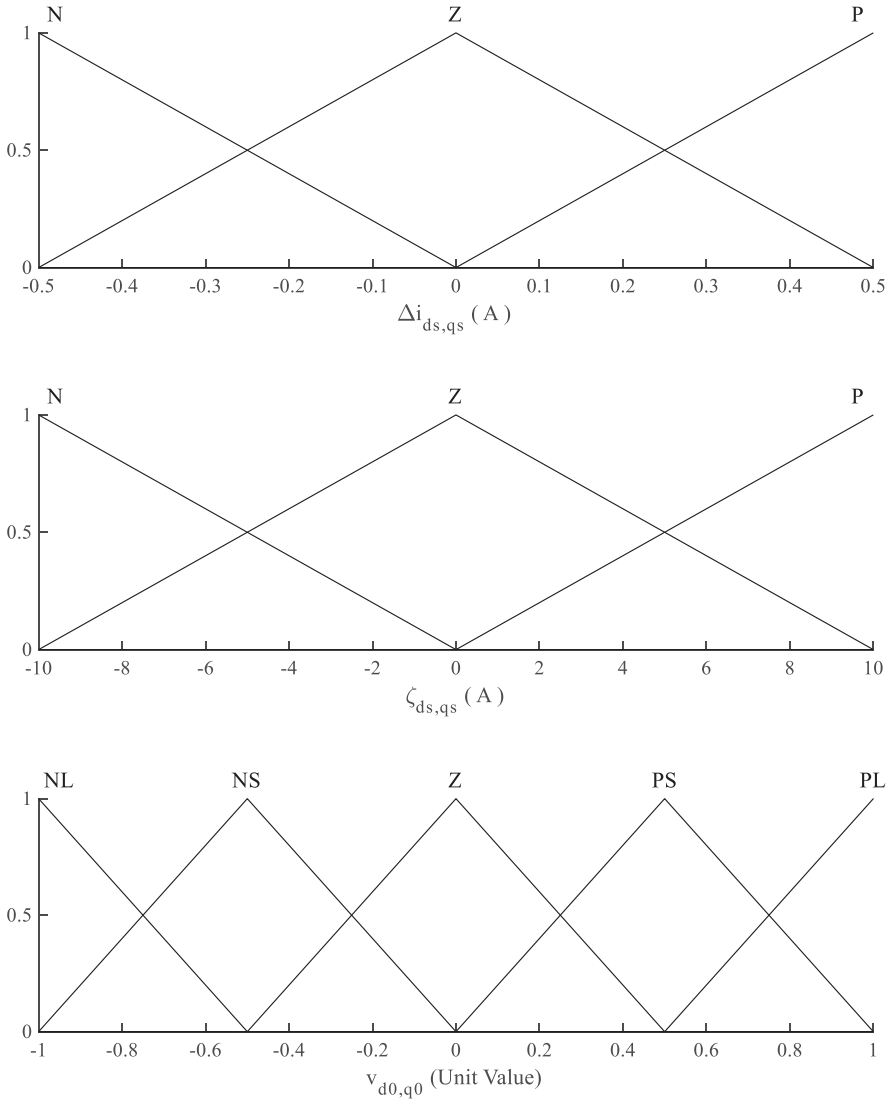

Figure 4.2 FL Current controller membership functions, **(a)** Input 1 - $\Delta i_{ds,qs}$, **(b)** Input 2 – $\zeta_{ds,qs}$, **(c)** Output – $v_{d0,q0}$

In the same way as the FL speed controller, the input ranges for $\Delta i_{ds,qs}$ (Figure 4.2(a)) and $\zeta_{ds,qs}$ (Figure 4.2(b)) were chosen as they offered the best steady-state performance while

remaining stable. The FL current controllers output the voltage $v_{d0,q0}$ (Figure 4.2(c)) as a unit value, these are then multiplied by the rated stator voltage (see Section 3.2.1.5).

Table 4.2 FL current controller rule base

		$\Delta i_{ds,qs}$		
		N	**Z**	**P**
$\zeta_{ds,qs}$	**N**	Z	PS	PL
	Z	NS	Z	PS
	P	NL	NS	Z

Some examples of the rule base for the FL current controllers are explained as followed:

- If $\Delta \boldsymbol{i_{ds,qs}}$ is (Z) and $\boldsymbol{\zeta_{ds,qs}}$ is (Z) then $\boldsymbol{v_{d0,q0}}$ is (Z). When the current error is zero and the error has not changed since the previous time step, the voltage output is zero. The only time this condition occurs is when the target voltage is zero, otherwise the (Z) membership functions is used to scale down the applied voltage from the other rules.
- If $\Delta \boldsymbol{i_{ds,qs}}$ is (N) and $\boldsymbol{\zeta_{ds,qs}}$ is (P) then $\boldsymbol{v_{d0,q0}}$ is (NL). When the instantaneous current is much larger than the target value and is increasing, then a large negative voltage is used to prevent overshooting the target current.
- If $\Delta \boldsymbol{i_{ds,qs}}$ is (N) and $\boldsymbol{\zeta_{ds,qs}}$is (N) then $\boldsymbol{v_{d0,q0}}$is (Z). When the instantaneous current is much larger than the target value, but the error is reducing, then zero voltage is used because the current is going to reach the target value without any intervention.

4.1.3 Fuzzy Logic Flux Controller

The same FL speed and current controllers are used in both the I-PMSM and IM FOC systems, but a third FLC is used to control the magnitude of the magnetic flux wave φ_r (by outputting i_{ds}^*) for an IM. The FL flux controller uses the error of the rotor's magnetic flux $\Delta\varphi_r$ (79) and its time derivative as the two inputs in Figure 4.3(a)-(b) respectively. The controller then outputs a target d-axis current i_{ds}^* in Figure 4.3(c) as a unit value, this is then multiplied

by the motor's rated current I_s. The membership functions and rule base for the FL flux controller are given in Figure 4.3 and Table 4.3 respectively. The rules and membership function input ranges were chosen in a similar manner to the FL speed controller in order to prevent overshooting the target objectives.

$$\Delta\varphi_r(t) = \varphi_r^*(t) - \varphi_r(t) \tag{79}$$

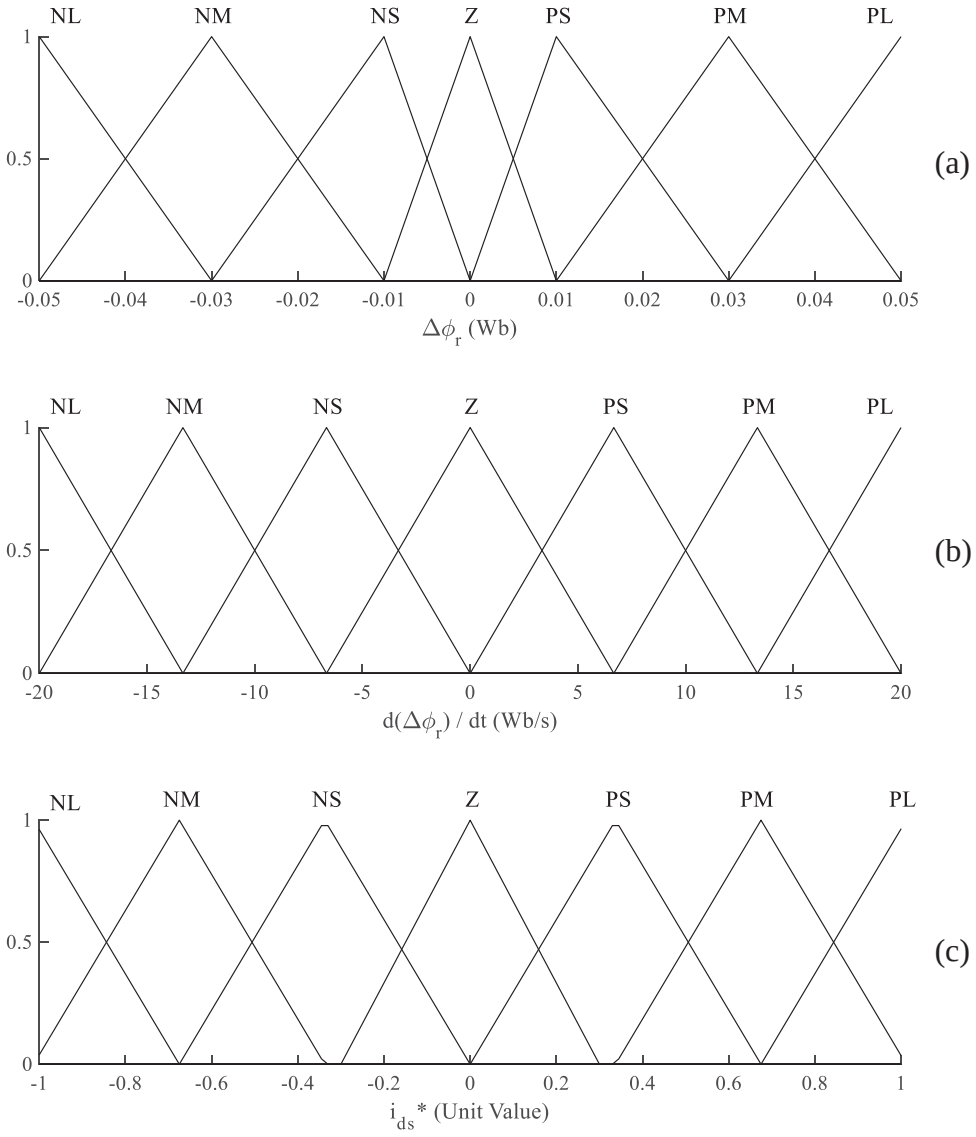

Figure 4.3 FL Flux controller membership functions, **(a)** Input 1 – $\Delta\varphi_r$, **(b)** Input 2 – $\frac{d(\Delta\varphi_r)}{dt}$, **(c)** Output – i_{ds}^*

Table 4.3 FL Flux Controller rule base

$\frac{d(\Delta\varphi_r)}{dt}$	$\Delta\varphi_r$						
	NL	**NM**	**NS**	**Z**	**PS**	**PM**	**PL**
NL	NS	Z	PS	PM	PL	PL	PL
NM	NM	NS	Z	PS	PM	PL	PL
NS	NM	NM	NS	Z	PS	PM	PL
Z	NL	NM	NS	Z	PS	PM	PL
PS	NL	NM	NS	Z	PS	PM	PM
PM	NL	NL	NM	NS	Z	PS	PM
PL	NL	NL	NL	NM	NS	Z	PS

The role of i_{ds} is to induce a magnetic flux wave within the IM's rotor. However, if the properties of the IM changes, causing the target magnetic flux φ_r^* to no longer be represented by a previously defined i_{ds} (e.g. due to temperature changes), then the performance of the IM becomes compromised. Directly controlling φ_r avoids this scenario so long as it is estimated accurately. In addition, permitting a larger i_{ds}^* current for start-up operations in order for φ_r to reach its target value quicker is useful for motors that have large φ_r time constants.

4.2 FL-FOC Verification

Two separate driving cycles using two different vehicles are used within the PIL simulations to examine how the FL-FOC scheme interacts with different vehicle systems. The first PIL driving scenario uses a FWD C-class hatchback (vehicle B in Table 4.4) using two independent 37.5 kW in-wheel IMs (IM#1 in Table 4.5) following the US Federal Drive Cycle. This drive cycle is a close representation to real-world driving scenarios and tests the controller's ability to handle aggressive acceleration and decelerations. The second PIL driving scenario involves a RWD E-Class sedan (vehicle A in Table 4.4) using a single 100 kW I-PMSM (I-PMSM in Table 4.5) following a short section of the Extra Urban Driving Cycle Drive Cycle. This drive cycle examines the controller's ability to control the vehicle at high speed and how the control system approaches a constant target velocity.

Table 4.4 Vehicle parameters used for this simulation investigation [309]

Parameter	Symbol	Vehicle			
		A	**B**	**C**	**D**
Chassis type		Sedan	Hatchback	Compact	Compact SUV
Sprung mass (kg)	m_s	1650	1270	750	1430
Unsprung mass Front (kg)	m_{uf}	90	71	41.5	80
Unsprung mass Rear (kg)	m_{ur}	90	71	41.5	100
Roll inertia (kg.m^2)	I_{roll}	928	535	270	700
Pitch inertia (kg.m^2)	I_{pitch}	2788	1535	750	2060
Yaw inertia (kg.m^2)	I_{yaw}	3234	1536	750	2060
Wheelbase (m)	L	3.05	2.91	2.35	2.66
Centre of mass height (m)	h_{COG}	0.53	0.54	0.54	0.65
Front axle to centre of mass (m)	a	1.4	1.015	1.1	1.05
Aerodynamic coefficient of drag	C_D	0.3	0.3	0.35	0.33
Frontal Area (m^2)	A_f	2.8	2.2	1.6	2.8
Transmission and final drive ratio	N_{FT}	4.7	4.7	3.7	6
Wheel radius – loaded (mm)	R	353	329	284	347

Table 4.5 IM and I-PMSM parameters used for the simulation investigation [143, 298]

Parameter	Symbol	Motor		
		IM #1	**IM #2**	**I-PMSM**
Number of poles	P	4	4	8
Rated power (kW)	p_{max}	35	50	100
Rated speed (rpm)	ω_m	1675	1470	3000
Rated Voltage (V)	V_s	380	380	155
Rated Current (A)	I_s	78	138	450
Stator resistance (Ω)	R_s	0.087	0.04	0.0083
Rotor resistance (Ω)	R_r	0.228	0.15	-
Magnetising inductance (mH)	L_m	34.7	25	-
Leakage stator inductance (mH)	L_{ls}	0.8	1.5	-
Leakage rotor inductance (mH)	L_{lr}	0.8	1.5	-
Rotor flux max (Wb)	φ_r	0.97	0.9	-
Magnet flux (Wb)	φ_m	-	-	0.071
D-axis inductance (mH)	L_d	-	-	0.174
Q-axis inductance (mH)	L_q	-	-	0.293

The PIL results for driving scenarios 1 and 2 are given in Figure 4.4 and Figure 4.5 respectively.

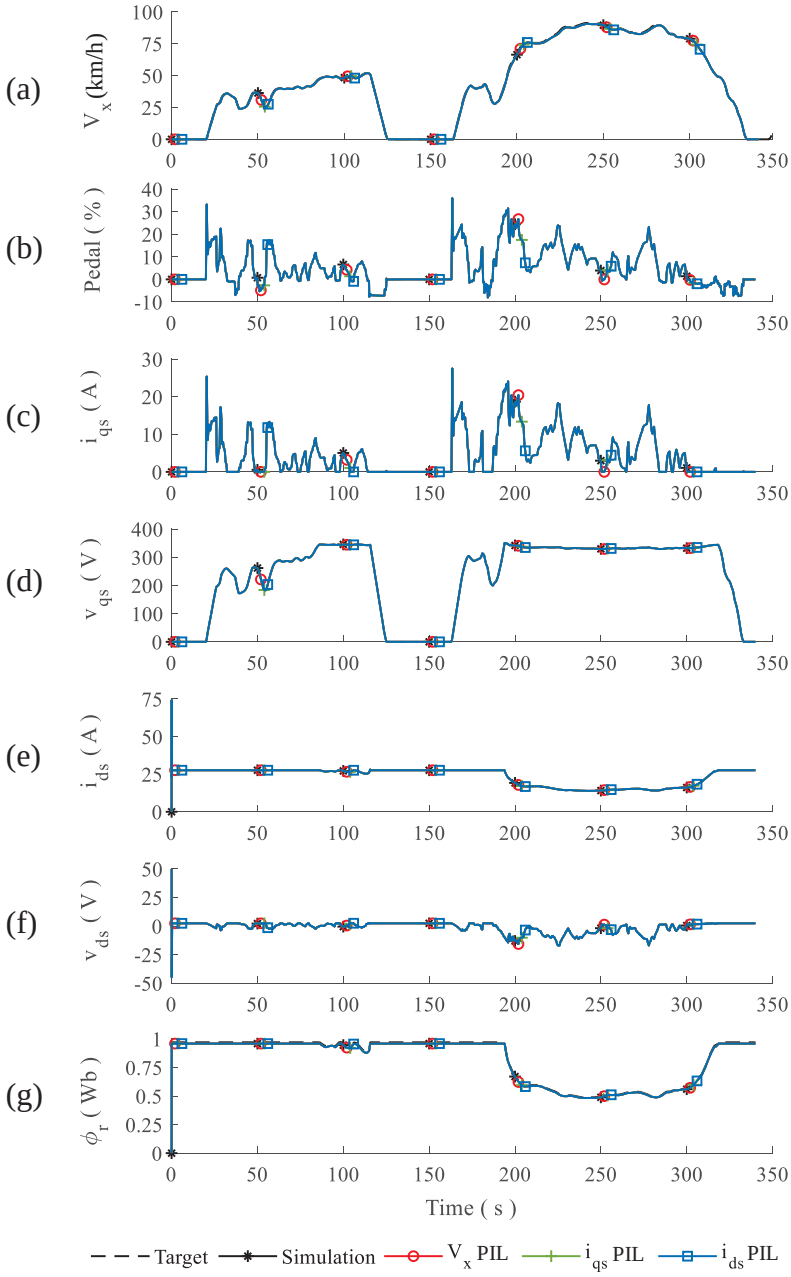

Figure 4.4 PIL simulations for a C-Class hatchback vehicle using dual IMs following a short section of the US Federal Drive Cycle, **(a)** V_x, **(b)** Pedal movement, **(c)** i_{qs} current, **(d)** v_{qs} votlage, **(e)** i_{ds} current, **(f)** v_{ds} voltage, **(g)** Flux wave magnitude φ_r

Figure 4.4(a) and Figure 4.5(a) show that the vehicles are able to follow their respective drive cycles with minimal error. The pedal activation levels for both vehicles in Figure 4.4(b) and Figure 4.5(b) are stable with no erratic movements.

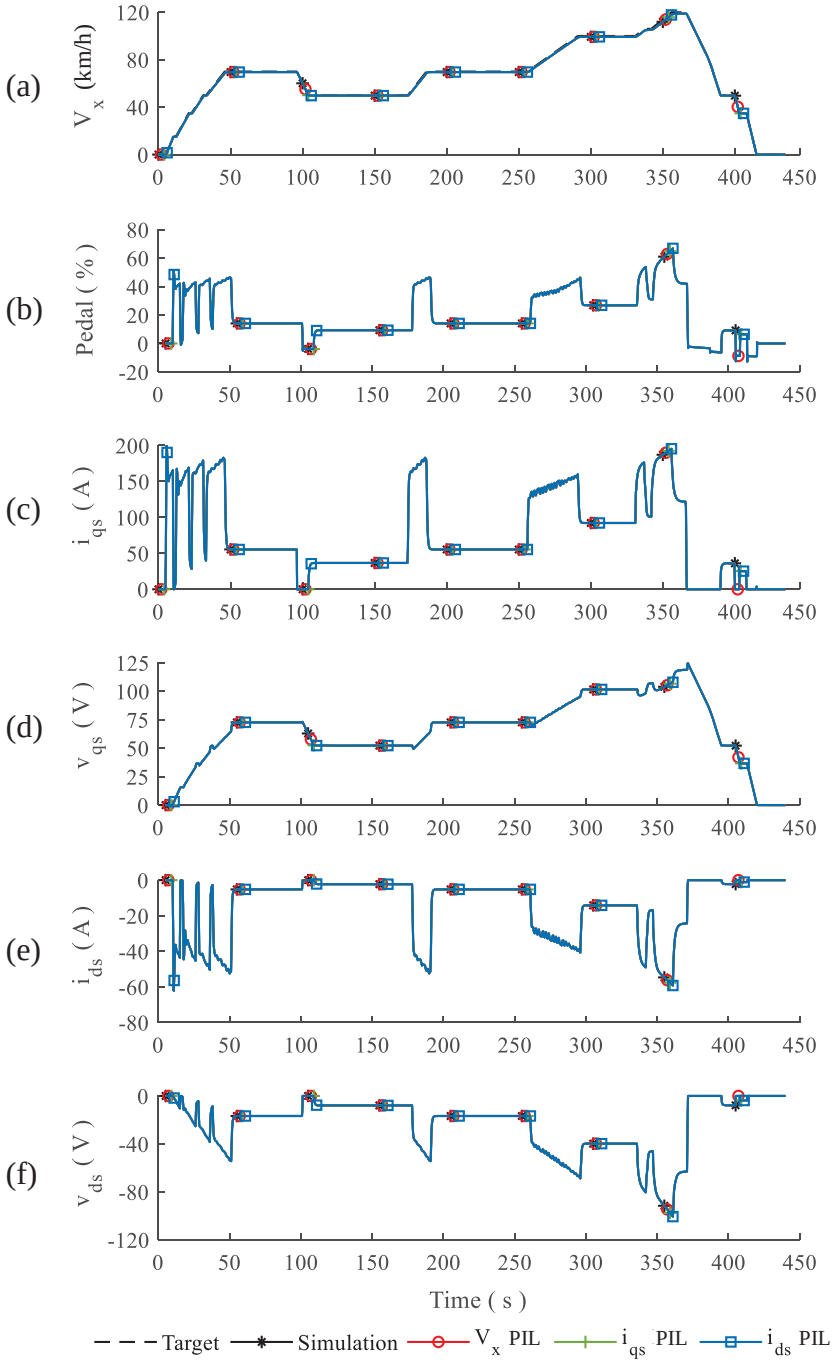

Figure 4.5 PIL simulations for an E-Class saloon vehicle using a single I-PMSM following a short seciton of the Extra Urban Drive Cycle, **(a)** V_x, **(b)** Pedal movement, **(c)** i_{qs}, **(d)** v_{qs}, **(e)** i_{ds}, **(f)** v_{ds}

Both the i_{qs} and i_{ds} currents in Figure 4.4(c) and Figure 4.4(e) for the first driving scenario are well regulated and use suitably stable v_{qs} and v_{ds} voltages in Figure 4.4(d) and Figure 4.4(f) respectively. Similar conclusions are drawn from the current control for driving scenario 2.

Finally, the FL flux control in Figure 4.4(g) shows that the IM's rotor magnetic flux is well maintained over the drive cycle and reduces as the vehicle's velocity increases.

These results show that the FLC PIL simulations act identically to their software-based counterparts. Due to the time-consuming effort of running multiple PIL simulations, the remainder of this chapter investigates the performance of the FL-FOC system using the software-based controllers.

4.3 Performance Evaluation of the FL-FOC System

This section directly compares the performance of a vehicle and traction motors controlled by the FL-FOC system against a PI based FOC (PI-FOC) counterpart. This comparison is conducted using two different vehicles with different motor topologies to further examine how the FL-FOC scheme interacts with different vehicle systems. The FL-FOC system does not change between simulations but the PI-FOC is tuned for the specific vehicle it is implemented. The PI-FOC controller gains for both driving scenarios, given in Table 4.6, offer the greatest trade-off between system responsiveness, low steady-state error and remain stable for the duration of the simulation. The FOC system must be able to maintain the control objectives stably with minimal error throughout the drive cycle. The control actuation must be achievable by physical real-world counterparts (i.e. no erratic control of accelerator/brake pedals).

Table 4.6 A-Class compact vehicle with a 50 kW IM PI-FOC controller gains

Driving scenario	Controller	Proportional gain	Integral gain
1	Speed	0.14	0.16
	i_{qs}	1	2
	i_{ds}	1	2
	Flux	2	10
2	Speed	0.4	1
	i_{qs}	0.05	0.2
	i_{ds}	0.05	0.1

The first driving scenario uses a FWD A-Class compact vehicle (vehicle C in Table 4.4) using a single 50 kW IM (IM#2 in Table 4.5) following a short section of the Japan 10-15 drive cycle. The second driving scenario uses a RWD D-Class SUV (vehicle D in Table 4.4) with a single 100 kW I-PMSM (I-PMSM in Table 4.5) following a short section of the Worldwide Harmonized Light vehicle Test Procedure (WLTP).

The SMAPE values in Table 4.7 show that the FL-FOC system overall has a slightly larger average percentage error than the PI-FOC system due to having a larger steady-state error, but still well within acceptable error tolerances. The SMAPE values in Table 4.7 use data used at $5x10^{-4}$s discrete time steps. Data points lower than 1% of the peak control variable are negated.

Table 4.7 PI-FOC and FL-FOC SMAPE performance evaluation.

Driving scenario	Control Variable	SMAPE (%) for the control system	
		PI-FOC	**FL-FOC**
1	$\boldsymbol{V_x}$	1.67	2.64
	$\boldsymbol{i_{qs}}$	0.35	0.73
	$\boldsymbol{i_{ds}}$	0.02	0.72
	$\boldsymbol{\varphi_r}$	0.04	0.42
2	$\boldsymbol{V_x}$	0.63	1.06
	$\boldsymbol{i_{qs}}$	2.20	1.18
	$\boldsymbol{i_{ds}}$	2.02	1.19

4.3.1 FOC Driving Scenario 1

The comparison using the FL-FOC and PI-FOC systems for the vehicle's velocity (Figure 4.6), i_{qs} current (Figure 4.7), i_{ds} current (Figure 4.8) and flux magnitude (Figure 4.9) for the first driving scenario shows that all control objectives remain stable throughout the drive cycle.

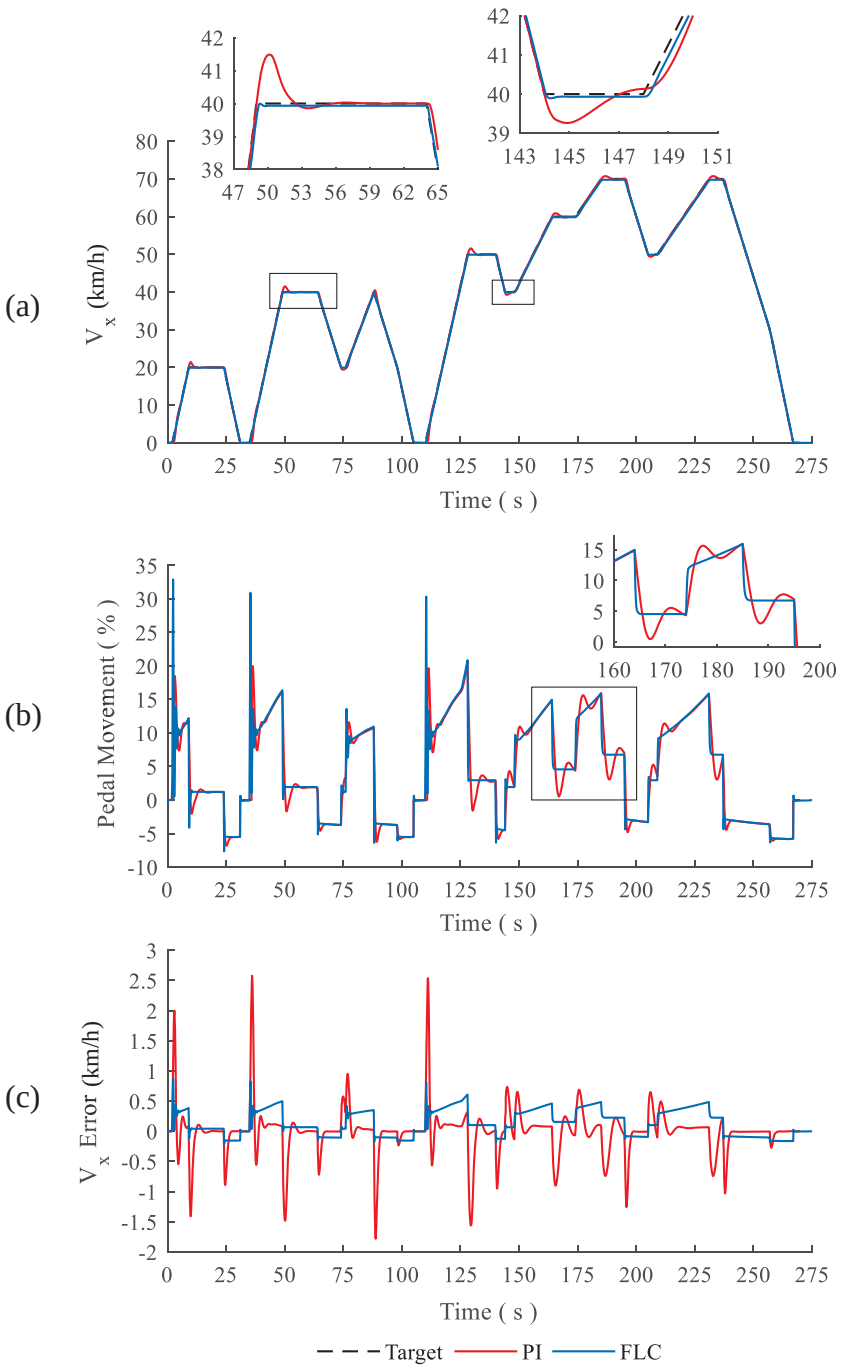

Figure 4.6 PI and FL speed control for driving scenario 1, **(a)** V_x comparison, **(b)** Pedal movement, **(c)** ΔV_x comparison

The i_{qs} and i_{ds} current control shows that both FOC systems regulate the motors current to meet their respective target values over the drive cycle using stable and adequately controlled axis voltages.

Figure 4.6(a) shows that the vehicle's velocity using the PI-FOC system overshoots the target speed whereas Figure 4.6(b) shows that the FL-FOC system reduces the amount of applied accelerator and brake pedal ahead of the approaching target velocity. This makes the FL-FOC system a closer representation to how a vehicle would be controlled by a real driver.

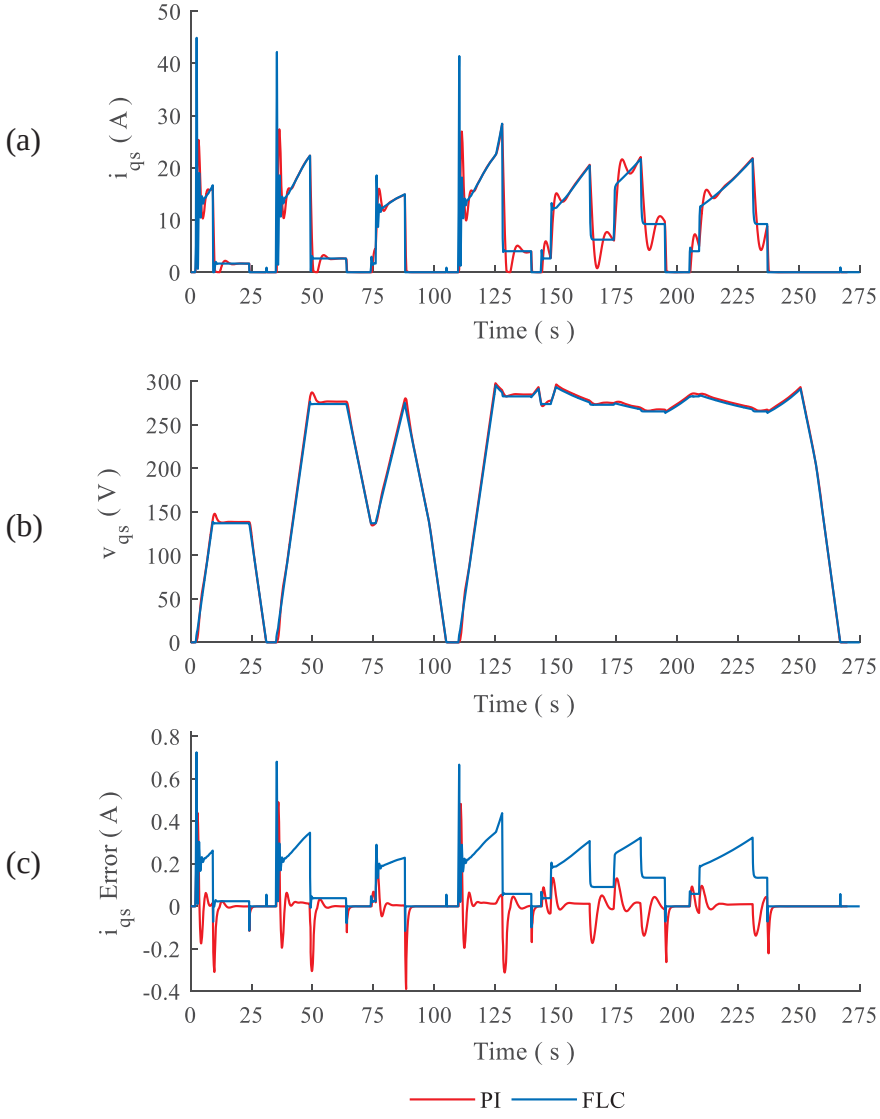

Figure 4.7 PI and FL i_{qs} current control for driving scenario 1, **(a)** i_{qs} comparison, **(b)** v_{qs} comparison, **(c)** i_{qs} error comparison

The FL-FOC scheme responds to the initial acceleration from standstill quicker by applying a larger acceleration pedal angle and generating a larger peak i_{qs} current sooner as shown in

Figure 4.7. Further adjustments to the current control could be made to the FL-FOC scheme to limit the current output and achieve a similar velocity profile to the PI-FOC scheme.

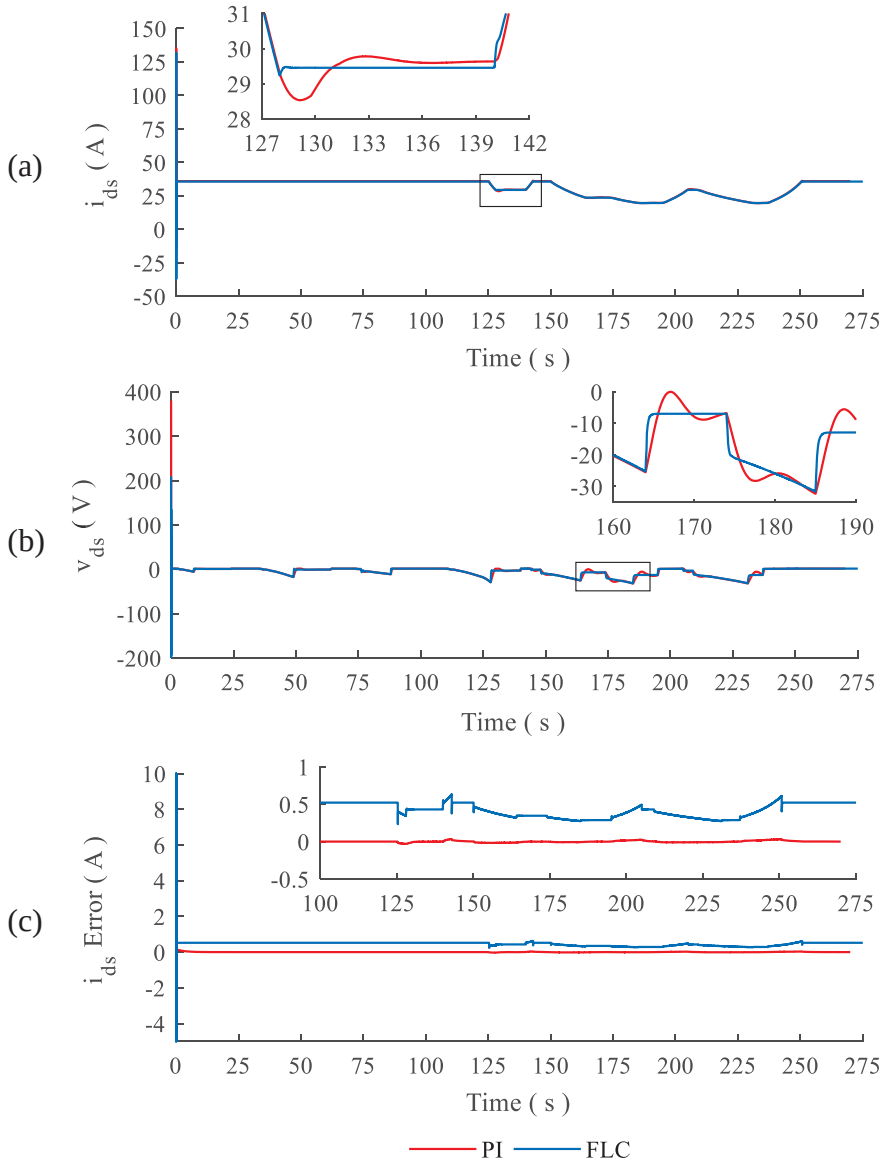

Figure 4.8 PI and FL i_{ds} current control for driving scenario 1, **(a)** i_{ds} comparison, **(b)** v_{ds} comparison, **(c)** i_{ds} error

Because of the longer time response and the overshooting tendency of the PI-FOC scheme, the current controllers apply a greater voltage than what is required once steady-state conditions have been met. Therefore by analysing the electrical requirements in Figure 4.7-Figure 4.9, it

might appear that the PI-FOC vehicle requires a higher voltage rated battery packs and inverter over the FL-FOC system.

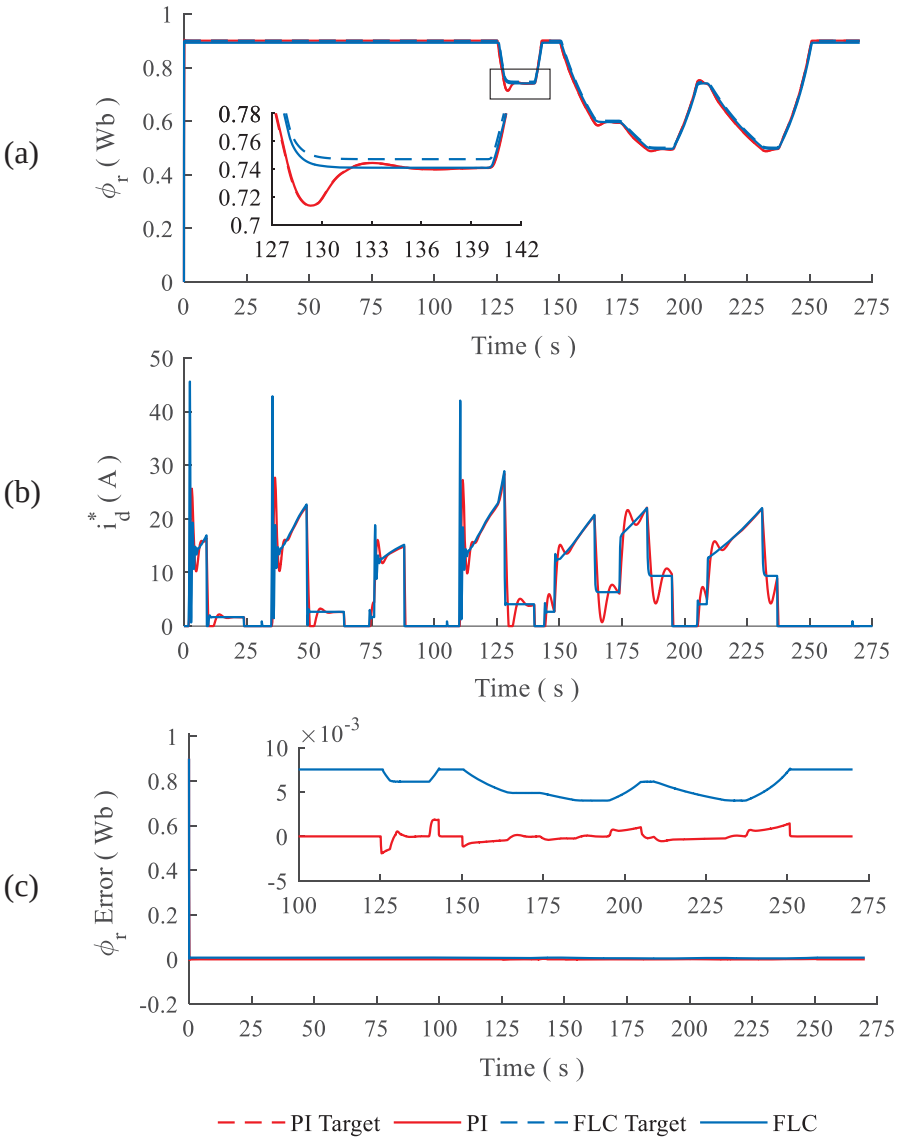

Figure 4.9 PI and FL φ_r control for driving scenario 1, **(a)** φ_r comparison, **(b)** i_{ds}^* comparison, **(c)** φ_r error comparison

Figure 4.9 shows that both FOC systems permit a large i_{ds} current to flow at the beginning of the simulation to allow the rotor's magnetic flux to increase at a faster rate to that achievable using a constant current. The rotor's magnetic flux controlled by the PI-FOC system in Figure 4.9(a) also overshoots its target objective. If it attempts to apply too much rotor flux, then the

motors magnetic material might saturate and lower the electrical efficiency. If the rotor flux goes too low, then the motor might not be able to output the required torque.

4.3.2 FOC Driving Scenario 2

The comparison using the FL-FOC and PI-FOC systems for the vehicle's velocity (Figure 4.10), i_{qs} current (Figure 4.11) and i_{ds} current (Figure 4.12) for the second driving scenario shows that all control objectives remain stable throughout the drive cycle for both FOC system.

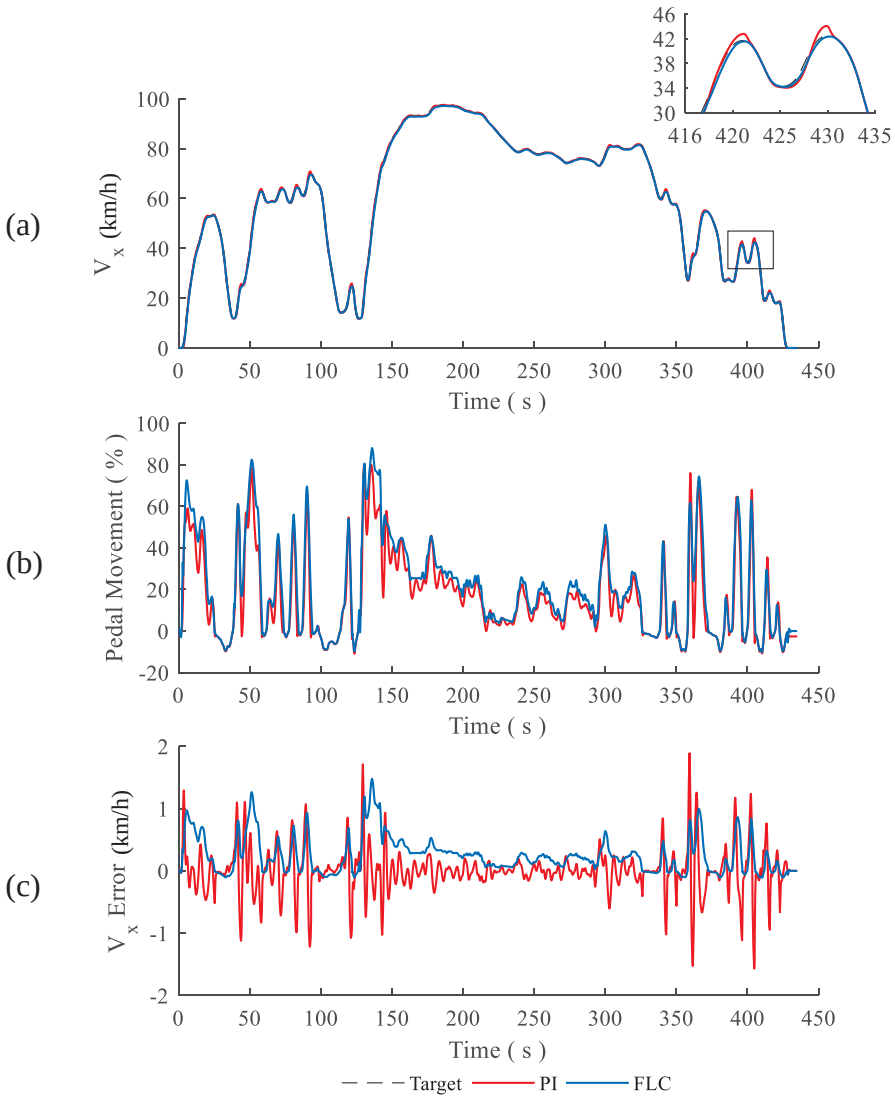

Figure 4.10 PI and FL speed control for driving scenario 2, **(a)** V_x comparison, **(b)** Pedal movement, **(c)** ΔV_x comparison

The pedal control in Figure 4.10(b) causes the i_{qs} and i_{ds} PI current controllers some difficulty as seen by the SMAPE values in Table 4.7. The FL-FOC system appears to outperform the PI-FOC current controllers. This may be due to the FL speed controller using a much smoother pedal actuation and thus enabling the FL current controller to follow smoother targets. Alternatively, it might be possible to tune the PI controllers better to achieve a lower SMAPE, but this further highlights the difficulties that arise with a PI controller based FOC system.

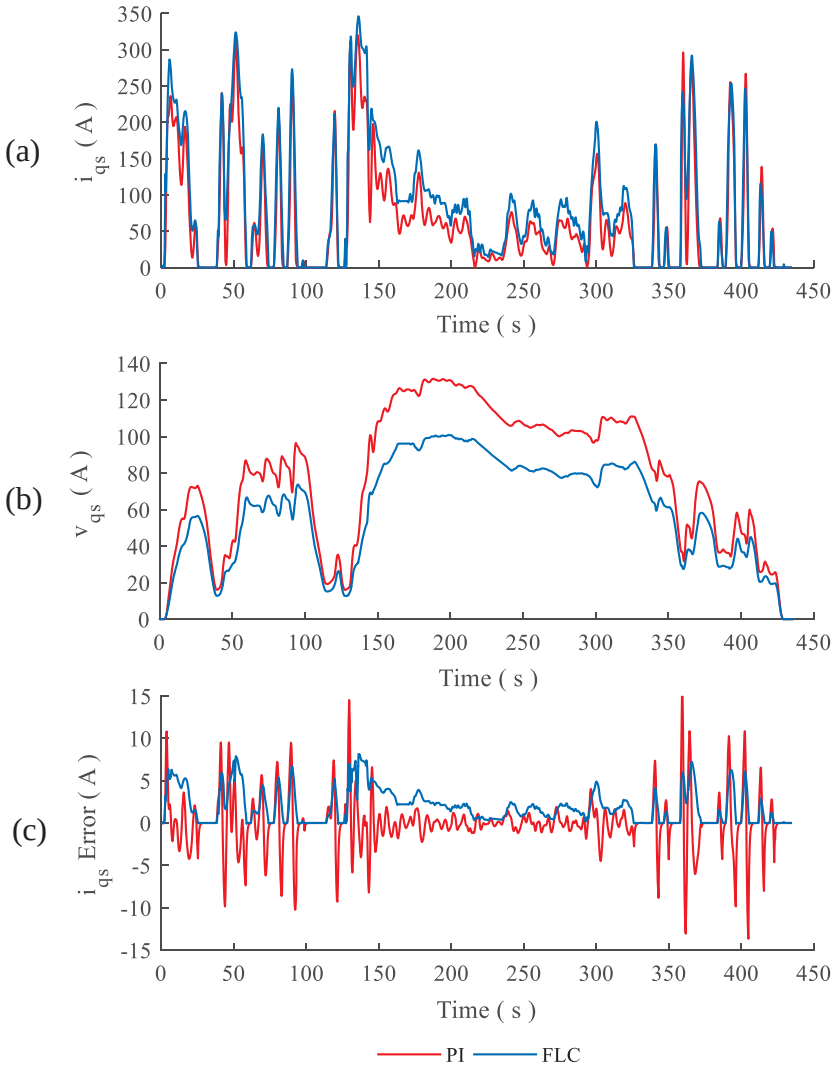

Figure 4.11 PI and FL i_{qs} current control for driving scenario 2, **(a)** i_{qs} comparison, **(b)** v_{qs} comparison, **(c)** i_{qs} comparison

The WLTP drive cycle doesn't have any constant target velocities and thus is a much smoother velocity profile. The overshooting characteristics of the PI speed controller and its effect on the vehicle's velocity in Figure 4.10(a) are not as pronounced as those in Figure 4.6(a). However, it must be noted that the pedal actuation for the FL-FOC system in Figure 4.10(b) is much smoother than the PI-FOC system. This produces a greater reflection on real-world vehicle speed control.

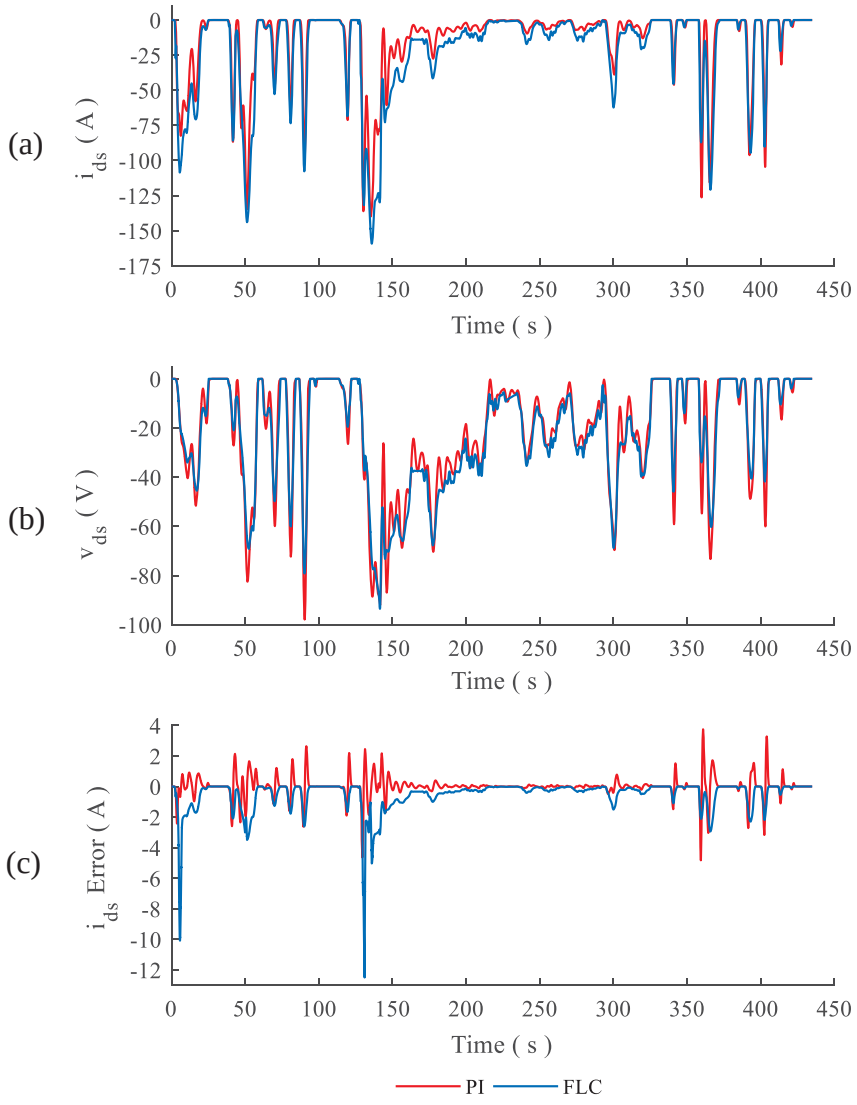

Figure 4.12 PI and FL i_{ds} current control for driving scenario 2, **(a)** i_{ds} comparison, **(b)** v_{ds} comparison, **(c)** i_{ds} error comparison

4.4 Robustness Analysis using Variable Motor Parameters

In part, the robustness of the FL-FOC system has already been established due to its ability to control multiple different vehicle systems and traction motors without the need for any re-tuning between simulations. But now, the performance of the FL-FOC is investigated under scenarios which may affect the control system in the real world. This is achieved by varying the stator resistance of an IM (IM#1 in Table 4.5) in Equations (4)-(5) from their original value of $r_s = 0.04\,\Omega$ to $r_s = 0.16\,\Omega$. Lubin [148] used a similar methodology to examine the robustness of his FL speed and i_{ds} controllers.

A FWD C-class hatchback (vehicle B in Table 4.4) using two independent 37.5 kW in-wheel IMs follows a short section of the NEDC drive cycle and accelerate the vehicle up to 30 km/h. The FL-FOC system is compared against another FOC system (FOC-2) which uses a FL speed, FL i_{ds} and FL flux controller with a PI i_{qs} current controller. This removes any coupling effects in the PI-FOC system that may arise between two PI controllers. Firstly, the performance of both FOC systems are compared using the original stator resistance of $r_s = 0.04\,\Omega$. These simulations are repeated using a stator resistance of $r_s = 0.16\,\Omega$. The PI controller in FOC-2 uses the same gains as the i_{qs} controller during driving scenario 1 in Table 4.6 and are not re-tuned between the two simulations.

Table 4.8 shows that the SMAPE values for both FOC systems remain within acceptable error tolerances over the drive cycle. The values in brackets ( ) next to the variable stator resistance SMAPE represent the percentage change from the original SMAPE.

Figure 4.13 shows the vehicle's velocity (Figure 4.13(a)), pedal actuation (Figure 4.13(b)) and i_{qs} current control (Figure 4.13(c)) for both FL-FOC and FOC-2 using the original stator resistance. Both FOC systems are able to adequately and stably meet the target velocity profile and maintain control over their respective target i_{qs} currents with minimal error. The pedal

actuation in Figure 4.13(b) for the FOC-2 system is different to the FL-FOC system, this is due to a slightly slower response time in the i_{qs} current control. The data used for the SMAPE values are in Table 4.8 and were taken at $5x10^{-4}$s discrete time steps, data points lower than 1% of the peak control variable are negated.

Table 4.8 PI-FOC and FL-FOC SMAPE performance evaluation for the original and variable stator resistance simulations.

Control Variable	FOC-2		FL-FOC	
	$r_s = 0.04\ \Omega$	$r_s = 0.16\ \Omega$	$r_s = 0.04\ \Omega$	$r_s = 0.16\ \Omega$
$\boldsymbol{V_x}$	2.40	2.77 (15.4 %)	2.26	2.40 (6.2 %)
$\boldsymbol{i_{qs}}$	5.04	13.85 (174.8 %)	1.99	1.98 (-0.5 %)
$\boldsymbol{i_{ds}}$	0.71	2.79 (292.9 %)	0.71	0.72 (1.4 %)
$\boldsymbol{\varphi_r}$	0.41	0.43 (4.9 %)	0.41	0.42 (2.4 %)

Both FOC systems in Figure 4.14(a) are still able to maintain the target velocity as with Figure 4.13(a). The pedal actuation and i_{qs} current control for the FL-FOC in Figure 4.14(b) and Figure 4.14(c) respectively are comparable to those in Figure 4.13. Table 4.8 shows that the error for the FL-FOC i_{qs} current control and vehicle's velocity is slightly larger than the original conditions, but still within acceptable error tolerances. The error difference is so small that it doesn't influence the pedal actuation between the two simulations.

For HEV/EV design purposes, it might appear that a vehicle using the PI-FOC scheme requires a larger target i_{qs}^* current over the FL-FOC scheme. This may lead the vehicle designer to believe that a battery pack with a larger current output or larger current rated traction motor would be required for this vehicle to achieve this velocity profile.

The PI controller in Figure 4.14(b) for the FOC-2 scheme is unable to maintain the target i_{qs} current when the stator resistance varies. The speed controller of the FOC-2 scheme has to apply the accelerator pedal more (and thus increase the target i_{qs}) in order for the motor's actual i_{qs} current (and thus output torque) to be large enough for the vehicle to follow the target drive

cycle. Furthermore, when the FOC-2 reduces the target i_{qs} current, the *momentum* of the PI current controller (due to the large integral error) means that the i_{qs} current overshoots the target value. The speed controller of the FOC-2 system has to then apply the brake pedal in Figure 4.14(b).

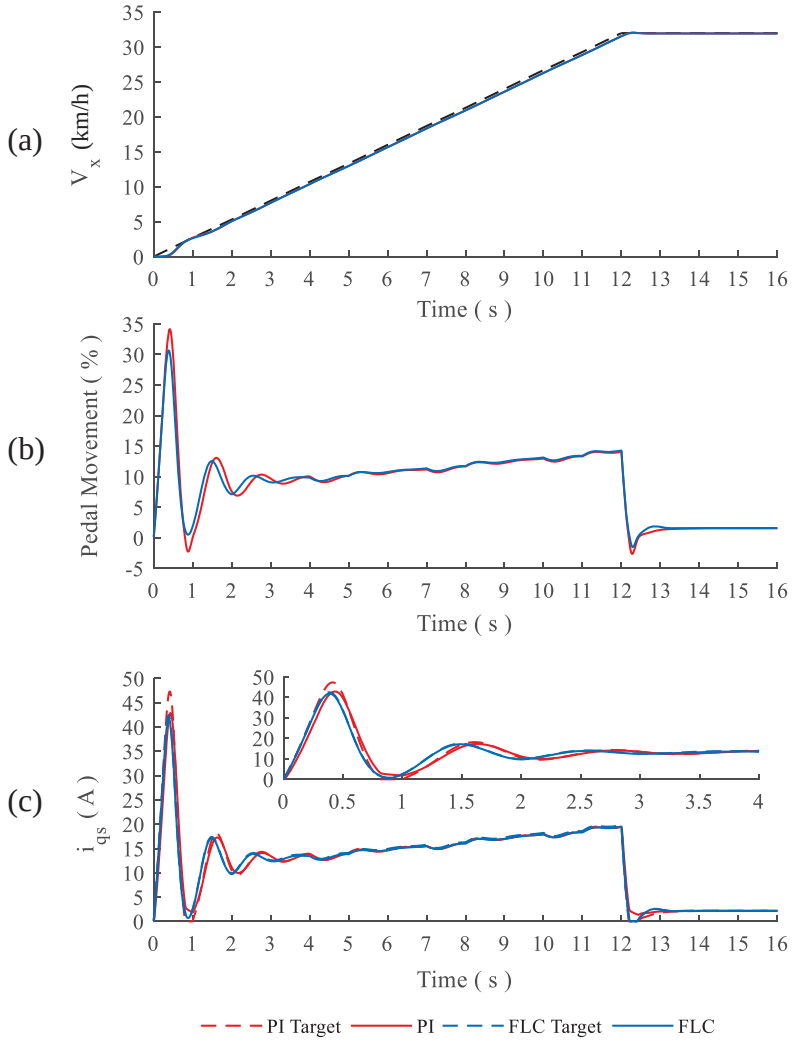

Figure 4.13 Stator resistance $r_s = 0.04\Omega$ simulation for the FOC-2 and FL-FOC, **(a)** V_x comparison, **(b)** Pedal movement, **(c)** i_{qs} comparison

The SMAPE values in Table 4.8 show that the i_{qs} error during the variable stator resistance simulation is much higher than the original stator resistance simulation. Due to the coupling effects of the two axes, the SMAPE value for the i_{ds} also increases, however the robustness of

the FL i_{ds} controller in the FOC-2 scheme ensures that the i_{ds} SMAPE value remains within acceptable error tolerances.

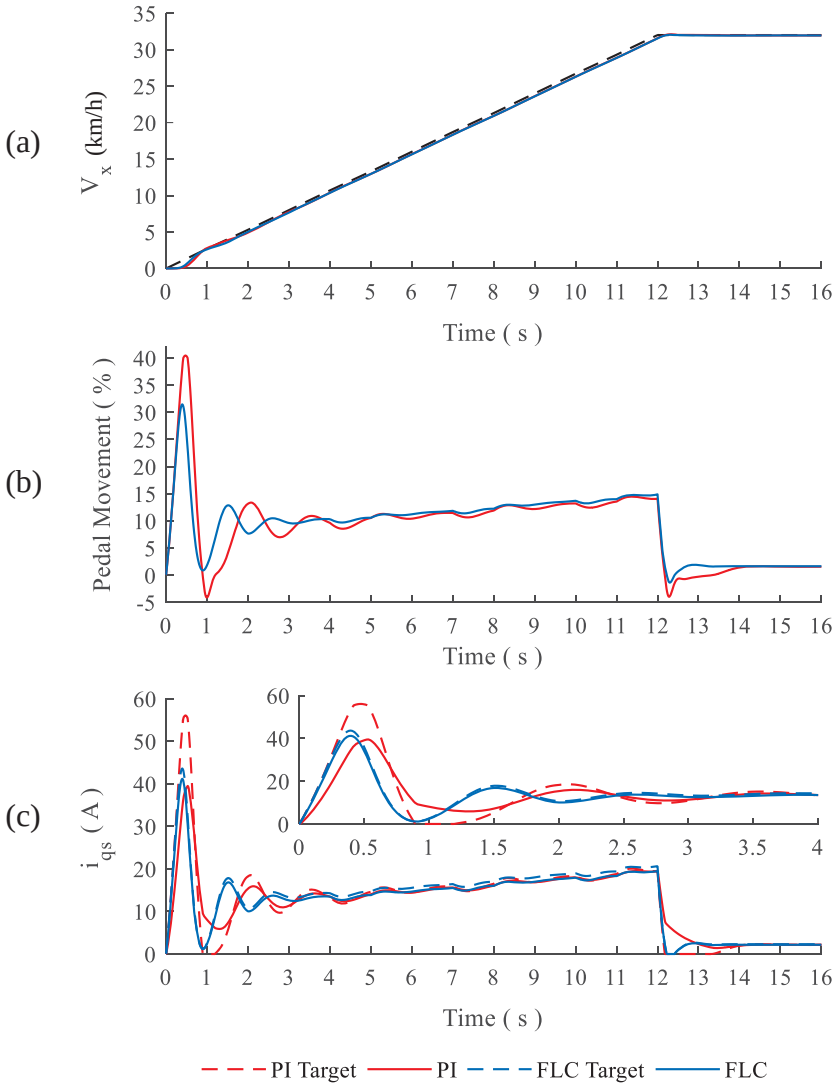

Figure 4.14 Stator resistance $r_s = 0.16\Omega$ simulation for the FOC-2 and FL-FOC, **(a)** V_x comparison, **(b)** Pedal movement, **(c)** i_{qs} comparison

This investigation has shown that the FL-FOC system is more robust than a PI based FOC system by means of the FOC-2 scheme for variable motor parameters. This is due to the PI controller gains which were intended for the original motor parameters no longer being the optimal choice for the new motor parameters.

4.5 Summary

A FLC based FOC (FL-FOC) scheme for the traction motor of an HEV/EV was developed which consists of independent vehicle speed, traction motor current and magnetic flux FLCs. The FLCs were verified ready for use in a HIL experiment via a series of PIL simulations and showed comparable control to their simulated counterparts after compiling. The FL-FOC scheme showed to be able to control multiple motor topologies and HEV/EV powertrain architectures without the need for re-tuning.

The FL-FOC scheme managed to regulate the FOC variables (speed, current, flux) within acceptable error tolerances (of below 5% error) for a wide range of vehicle systems. In comparison to a PI controller based FOC (PI-FOC) scheme, the FL-FOC showed more realistic vehicle control and thus a better representation of how a physical vehicle would behave. A more detailed robustness analysis showed that the FL-FOC scheme performs significantly better than PI-FOC scheme when variable motor parameters were introduced.

Chapter Five

Overcurrent-Tolerant Traction Motor Sizing Strategy

This chapter presents a new traction motor sizing strategy proposed by the author by utilising an overcurrent-tolerant prediction motor model to estimate the dynamic and thermal characteristic of the motor operating in the overcurrent region. This control scheme only uses basic motor torque-speed characteristics as they are easily obtained from a motor manufacturer. The prediction model quickly shows if a prospective traction motor operating in the overcurrent region and the powertrain configuration would enable the vehicle to achieve its required dynamic and electrical objectives. Similarly, to Chapter Four, only a vehicle powered purely by a traction motor is investigated (series-HEV), but again it is possible to extrapolate this sizing strategy for use on various HEV powertrain architectures (parallel or power-split). It will be denoted where these changes would occur within this chapter. The work presented in this chapter has been accepted by IET Intelligent Transport Systems awaiting online publication and at a conference [310].

The motor's rate of change in temperature and its output torque are both proportional to the magnitude of the supply current. The safe torque-speed operating region where the motor is able to run for its entire lifetime is referred to as the *continuous* region. Here, the supply current is limited to a rated value to prevent the motor from overheating, but this also has the effect of limiting the output torque. A motor's *overcurrent* region temporarily permits a higher supply current to produce a larger output torque. Motor manufacturers represent the overcurrent region by one or more torque-speed curves which are assigned time limits to show how long the peak overcurrent torque can be used before the motor begins to overheat. Operating in the overcurrent region is desirable for HEV/EVs because a smaller, cheaper and more efficient

motor operating in its overcurrent region might be able to achieve the same output torque as a larger motor confined to its continuous torque-speed region.

This chapter is structured as followed; Section 5.1 introduces the overcurrent-tolerant prediction model, Section 5.2 presents a case study where an aeroplane pushback is converted into a series HEV utilising this sizing strategy.

5.1 The Overcurrent-Tolerant Temperature Prediction Motor Model

The role of the overcurrent-tolerant prediction model is to decide if the continuous (where $PM = C$ in (80)) or overcurrent (where $P\,M = O$ in (80)) torque-speed curves should be used in (80) at any given time at the respective traction motor speed ω_m. The choice of torque-speed curve is dependent on the estimated temperature of the motor.

The torque-speed characteristics of a traction motor in this investigation are modelled using 2D look-up tables in MATLAB/Simulink as described in Section 3.2.5.1. A control flowchart for the overcurrent-tolerant prediction model is shown in Figure 5.2. The following steps describe the decision making process within the overcurrent tolerant prediction model:

1) When the driver of the vehicle model (see Section 4.1.1) requests a torque output by activating the accelerator pedal $\gamma_{acc} \in [0,1]$, the motor model initially attempts to access the overcurrent torque curve, where $PM = O$ in (80). For a series-HEV or pure EV, the torque will be fully accommodated by the traction motor. For a parallel or power-split HEV, the fraction of the command torque required to be supplied by the traction motor will take the role of the required output torque in (80).

$$\tau_{PM}(\omega_m, \gamma_{acc}) = \gamma_{acc}\, \widehat{\tau_{PM}}(\omega_m) \quad \text{Where } PM = O, C \tag{80}$$

2) The rate of change in temperature is dependent on the position of the relative output torque $\delta_\tau \in [0,1]$ from (81). This is relative to the peak continuous torque $\widehat{\tau_C}(\omega_m)$ and the peak overcurrent torque $\widehat{\tau_O}(\omega_m)$. A diagrammatical view of how δ_τ is calculated in proportion to the torque-speed curves is shown in Figure 5.1 where $\delta_\tau(\omega_{m1}) > \delta_\tau(\omega_{m2})$.

$$\delta_\tau(\omega_m) = \frac{\tau_O(\omega_m) - \widehat{\tau_C}(\omega_m)}{\widehat{\tau_O}(\omega_m) - \widehat{\tau_C}(\omega_m)} \tag{81}$$

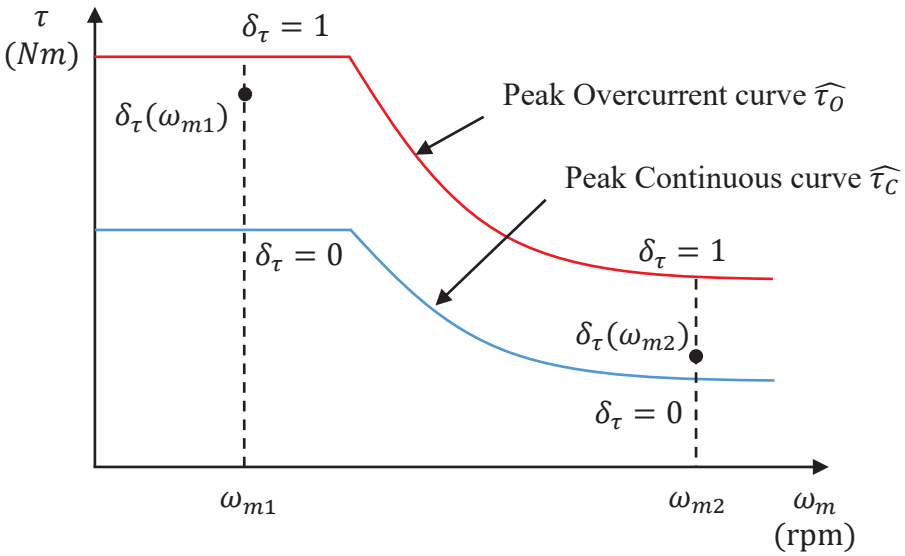

Figure 5.1 Diagrammatical view of how δ_τ is generated

3) The rate of change in temperature is represented by a Temperature Factor T_F from (82a-b).

$$T_F = \begin{cases} \dfrac{100\ \delta_\tau(\omega_m)}{t_{Lim}} & 0 < \delta_\tau(\omega_m) \leq 1 \quad (82a) \\ \dfrac{-100}{t_{Stop}} & \delta_\tau(\omega_m) \leq 0 \quad (82b) \end{cases}$$

The time limits t_{Lim} and t_{Stop} accompany the overcurrent torque-speed curves provided by the motor manufacturer. The estimated temperature from operating in the overcurrent region increases at a rate according to (82a). If $\widehat{\tau_O}$ were to be used at an initial motor

temperature $T = 0$, then the estimated temperature reaches the upper temperature limit T_{High} over a time period t_{Lim}.

4) The motor's estimated temperature T (83) is calculated by integrating T_F over time t from the beginning of the simulation at time t_0.

$$T(t) = T(t_0) + \int_{t_0}^{t} T_F \, dt \tag{83}$$

Where

$$0 \leq T \leq 100$$

5) If the estimated temperature reaches T_{High}, the motor enters a cool-down phase, where $PM = C$ in (80). The maximum output torque is restricted to the peak torque of the continuous region $\widehat{\tau_C}(\omega_m)$.

6) During the cool-down phase, the estimated temperature must reduce to the lower limit T_{Low} over a pre-determined cool-down time t_{stop} before the overcurrent region is allowed to be used again. The estimated temperature reduces at a rate according to (82b) during the cool-down phase or whenever the motor returns to the continuous region.

If only a single overcurrent torque-speed curve is given from the motor manufacturer, then δ_τ is a linear function. If numerous overcurrent curves and time limits are provided, δ_τ becomes a quadratic function and offers a better estimation of the motor's thermal characteristics.

The overcurrent-tolerant prediction model observes the motor's temperature T as a percentage between T_{High} and T_{Low}. For this investigation, these limits are represented as a percentage. For example, T_{High} and T_{Low} are 100% and 50% of the maximum temperature limit respectively.

If δ_τ is linear and $\delta_\tau = 1$, the motor outputs $\widehat{\tau_O}(\omega_m)$ and increase the motor's estimated temperature at a rate where T reachs 100% over the time period t_{Lim}. If $\delta_\tau = 0.5$, the output

torque is half way between $\widehat{\tau_C}(\omega_m)$ and $\widehat{\tau_O}(\omega_m)$. The rate of change in temperature is half that of when $\delta_\tau = 1$, the motor is now able to operate in this region for twice as long, or $2t_{Lim}$.

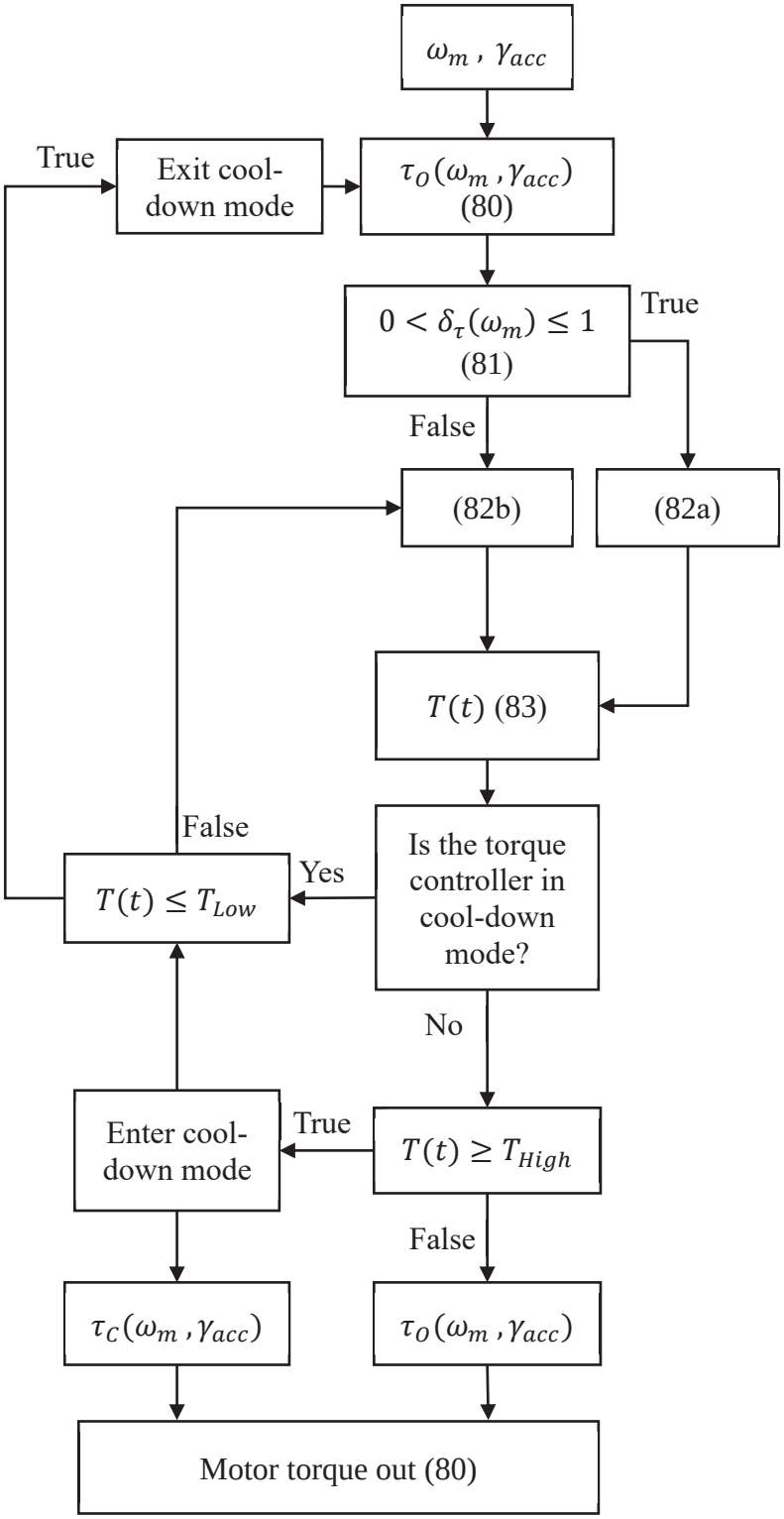

Figure 5.2 Overcurrent-tolerant prediction model torque control flowchart

During the cool-down phase, the vehicle's towing and acceleration ability is limited, this is necessary to prevent overheating and premature component failure. Ideally, the overcurrent region would only be used for a short time period to accelerate the vehicle to a cruising speed where a lower motor torque would be required to maintain a constant steady-state velocity.

5.2 Aircraft Pushback HEV Conversion: A Case Study

A case study is now investigated to show how the overcurrent-tolerant prediction model developed in this chapter should be applied in a real-world case-study to convert an aeroplane pushback vehicle into a series-HEV. Relating back to the Purpose of the Research for this thesis in Section 1.1, the benefits of correctly sizing the traction motor using the newly developed overcurrent motor model will be discussed in relation to fuel consumption, a possible reduction in output emissions and the energy usage.

Effective HEV/EV design requires optimising the choice of electrical storage/generation systems and powertrain components to meet the vehicle's target driving range and dynamic performance [53, 311, 312]. The development process of an HEV/EV must also compromise between other constraints such as price and legislative requirements [313, 314]. Therefore, a vehicle manufacturer might deliberate between numerous vehicle iterations before the final design is confirmed. Quick estimation of the motors dynamic and thermal performance is key in selecting the appropriate motor without wasting crucial time and resources.

Conventional pushback vehicles use high capacity ICEs as their prime mover with several transmission ratios. Between pushback operations, the vehicle might rest for long periods until it is needed again. The ICE remains idling whenever the vehicle is resting to avoid any technical difficulties when turning the ICE on (particularly during cold weather). These long idle times significantly increase the total fuel consumption and output emissions over the working day.

5.2.1 ICE Pushback Vehicle Parameters

The torque-speed curve for the 185 kW ICE used in the conventional pushback vehicle is given in Table 5.1. Further chassis and powertrain information for the former ICE powered vehicle is shown in Table 5.2, the same chassis information (vehicle mass, wheel radius etc.) is used for the HEV in Section 5.2. The torque-speed curve overlays the fuel consumption map in Figure 5.3 and the output emissions maps in Figure 5.4. The ICE engine of the original pushback vehicle is simulated using the simplified model in Section 3.2.5.2. The longitudinal dynamics of the pushback vehicle are modelled using the simplified vehicle model in 3.2.5.4.

Table 5.1 ICE Speed-Torque characteristics for the conventional aeroplane pushback vehicle

Speed (rpm)	600	700	900	1100	1300	1500	1900	2300	2500
Torque (Nm)	595	630	741	864	987	990	932	915	830

Table 5.2 Vehicle parameters of the typical ICE powered pushback vehicle to be converted into an HEV

Parameter	**Symbol**	**Value**
ICE only		
Transmission ratios [1,2,3]	N_T	[5.8,2.5,0.98]
Transmission inertia (kg m^2) [1,2,3]	I_T	[0.14, 0.1, 0.08]
Final drive ratio	N_{fd}	13
Final drive inertia (kg m^2)	I_{Fd}	0.2
Final drive efficiency	η_{fd}	0.98
Driveshaft inertia (kg m^2)	I_{Fd}	0.17
ICE inertia (kg m^2)	I_{ICE}	0.08
ICE and HEV shared		
Vehicle Mass (kg)	M_{Veh}	16000
Coefficient of Drag	C_D	0.8
Frontal Area (m^2)	A_f	6.8
Wheel Radius (m)	R	0.575
Coefficient of rolling resistance (%)	f_r	2
Max Brake Force (N)	F_{B-max}	800
Air density (kg m^{-3})	ρ_{air}	1.22
Wheel Inertia (kg m^2)	I_{Wh}	2.4

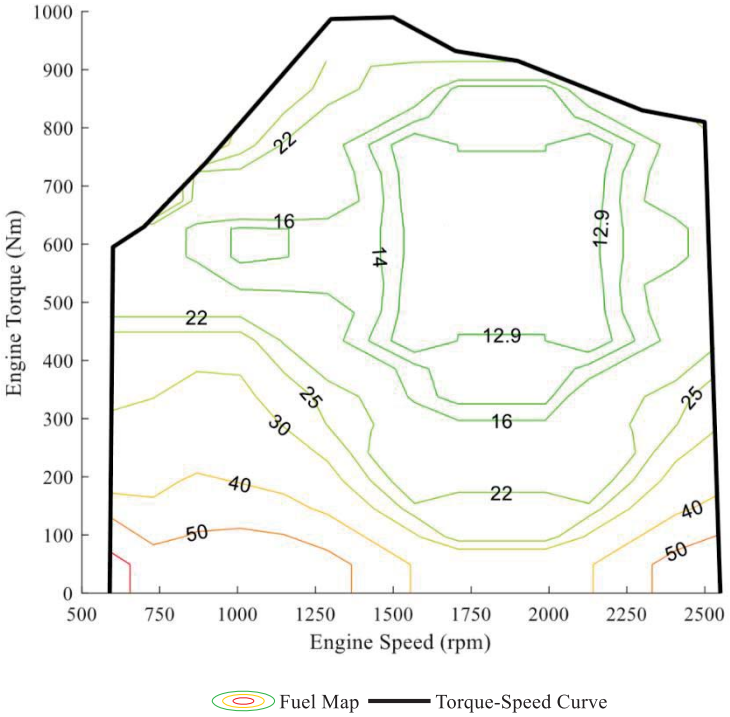

Figure 5.3 Conventional ICE powered pushback vehicle torque-speed curve and fuel map (L/hr)

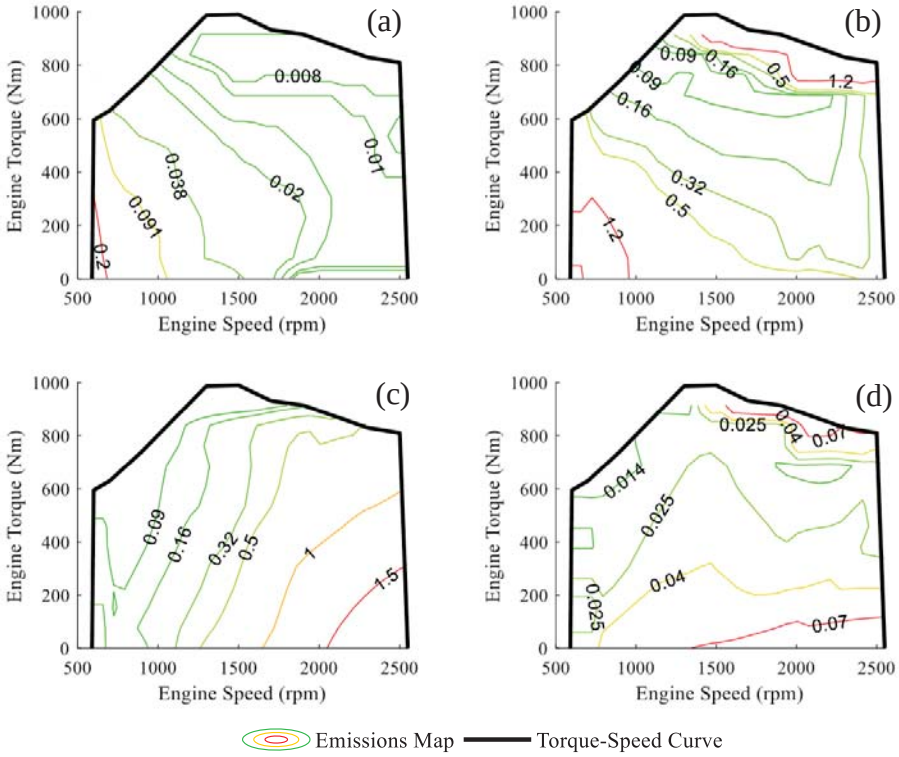

Figure 5.4 Conventional ICE powered pushback vehicle emissions maps, **(a)** Hydrocarbons (HC) (g/s), **(b)** Carbon Monoxide (CO) (g/s), **(c)** Nitrous Oxides (NOx) (g/s), **(d)** Particulate Matter (g/s)

5.2.2 Duty Cycle of the Aircraft Pushback Vehicle

An aeroplane pushback vehicle is required to move aeroplanes away from airport terminals and occasionally tow them across an airfield to receive routine maintenance. Therefore, the pushback vehicle must be able to generate a large towing force, but also have a relatively high-top speed to travel quickly between pushback operations (~30 km/h unloaded).

Airport regulations require all pushback vehicles to have the capacity to generate a theoretical minimum tractive force for each aeroplane weight class that the vehicle is registered to move. An example of the tractive force requirements to move a Boeing 737-7 aeroplane over various runway surface conditions is shown in Figure 5.5 [315], these are supplied for each aeroplane and must be adhered to by the pushback vehicle manufacturers. An HEV aeroplane pushback vehicle must also comply with these regulations in order to be a viable product.

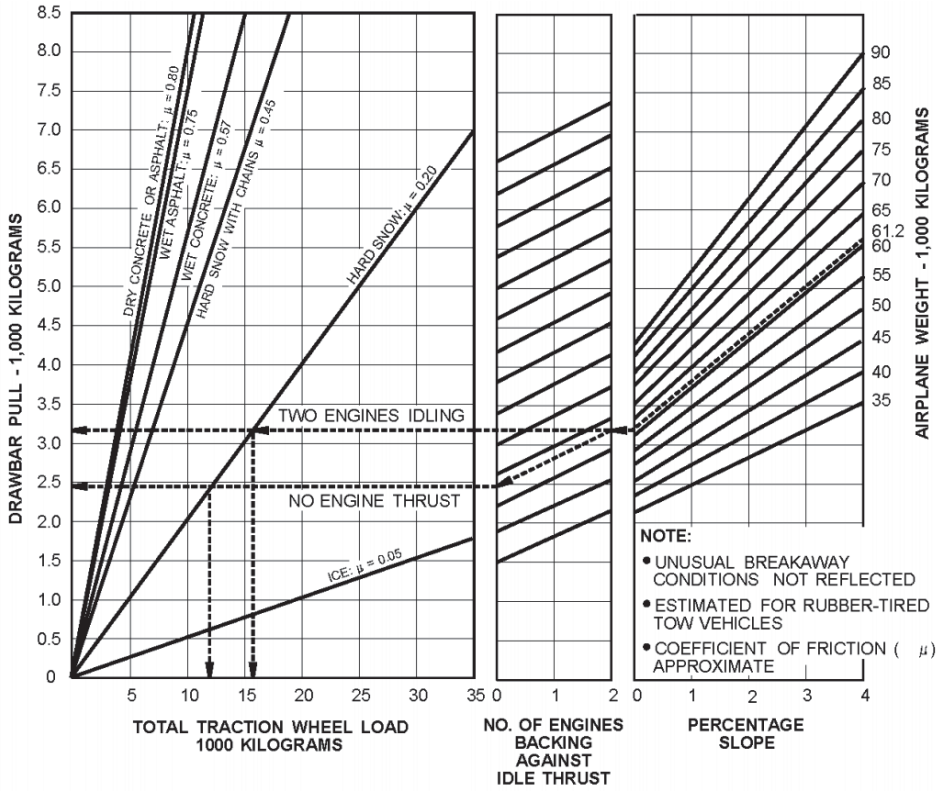

Figure 5.5 Towing tractive force requirements for a Boeing 737-7 aeroplane over numerous runway conditions [320]

A datalogger connected to the pre-existing ICE powered pushback vehicle via CAN bus recorded the vehicle's engine speed, output torque, output power and longitudinal velocity. This was used to construct a target duty cycle for the HEV to follow. The pushback vehicle's duty cycle is broken down into four major areas as shown in Table 5.3 and explained as followed:

- Low velocity pushback operations of heavy aircraft. This scenario occurs when the pushback vehicle is required to move aeroplanes away from the airport terminal
- Medium velocity towing operations of medium weight aircraft. This represents a maintenance run where the pushback vehicle tows an aeroplane for a longer duration across an airfield to receive routine maintenance.
- High velocity unloaded solo runs. Here the pushback vehicle is travelling back and forth between resting areas where it must wait until the next operation.
- Stationary resting periods. Here the vehicle is waiting for its next pushback operation. All hazard warning lights must remain on as the vehicle is still on the operating airfield.

Table 5.3 Pushback operation descriptions for the typical ICE vehicle and the HEV equivalent

Operation	**No. of operations**	M_{Aero} **(Tonne)**	**Target Speed (km/h)**	**Time (s)**
Solo	14	0	27	170
Tow	14	250	5	385
Maintenance	2	160	10	1870
Standby	-	0	0	-

The conventional ICE powered pushback vehicle uses three transmission ratios N_T for the various pushback operations. Gear ratio 1 is used for the towing operation, gear ratio 2 is used for the maintenance runs, and gear ratio 3 is used for the unloaded solo runs. These gears cannot change while the vehicle is moving and must be set before the operation begins.

The pushback HEV would not be held to conventional passenger vehicle development criteria, i.e. fast 0-60 mph acceleration times or able to reach motorway cruising speeds. This

is because aeroplane manufacturers impose low acceleration limits for towing operations to prevent damage to the landing gear and there are speed limits enforced on working airfields for the safety of ground support vehicles.

5.2.3 Battery Pack Constraints and APU Control

As well as having to power the traction motors, the pushback vehicle must also provide power its own heating/air-conditioning unit, external warning lights and various systems on the aeroplane. On the conventional ICE vehicle, these systems are either electrically or hydraulically powered, they are replaced with fully electrical systems on the HEV. In the real vehicle, this load varies throughout the day, but a high constant load contributes to the worst-case scenario duty cycle.

The price of the battery pack grows as its energy storage capacity and peak output power increases. During pushback and towing operations, the peak power demand from the traction motor is substantial. A battery pack capable of solely supplying the necessary power for these towing operations would therefore be large and expensive. To reduce the total price of the HEV, a battery pack with a smaller peak output power is used with supplemented power from the genset P_{Gen} to the DC-Link during towing operations. A flowchart for the genset control is shown in Figure 5.6.

For the HEV to be truly comparable to the ICE counterpart, the SOE of the battery pack must be full at the end of the duty cycle. This would be similar to the ICE vehicle having its fuel tank filled at the end of a working day. Once the final pushback operation has been completed, the genset enters full power mode (with the necessary start-up phase) and begins charging the battery pack while the HEV returns to the overnight storage area. The genset turns off once the SOE of the battery pack has reached its upper limit.

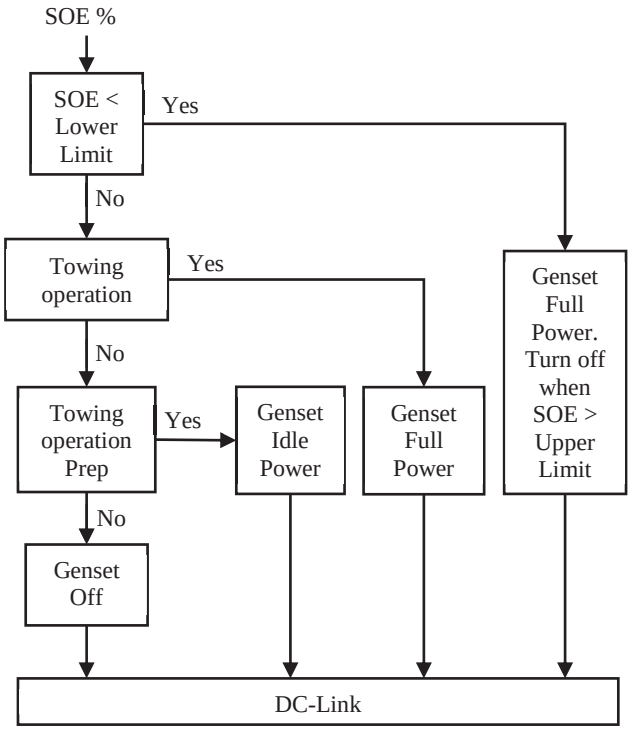

Figure 5.6 Genset control flowchart for the pushback HEV

5.2.4 HEV Pushback Vehicle Feasibility and Efficiency Analysis

The feasibility of two HEV powertrain configurations are considered for the final vehicle prototype, the parameters for both are given in Table 5.4. Suitable powertrain components that would enable the vehicle to achieve the desired duty cycle are investigated first, including; the traction motor torque-speed characteristics, final drive ratio and transmission ratios. The electrical storage and generation components of the HEV are then explored. The vehicle must have the capacity to complete a full duty cycle using only the energy stored or generated internally. The electrical system requires specifying the minimum capacity and peak output power of the battery pack, as well as the output power of the genset.

Configuration 1 uses two relatively low torque and high speed in-wheel traction motors with a single gear ratio $N_{T-fd\,1}$. The torque-speed curves for these motors and the efficiency map is shown in Figure 5.7. This motor is based on a de-rated 3-phase 170 kW PMSM produced by

Zytek [316]. Configuration 1 was developed to fully exploit the traction motors' overcurrent region. A single gear ratio $N_{T-fd\,1}$ enables the HEV to tow the aeroplanes to their target speed for the required duration while also allowing the vehicle to reach its maximum unloaded speed.

Table 5.4 HEV parameters for configuration 1 and configuration 2

Parameter	**Configuration 1**	**Configuration 2**
Continuous power (kW)	128	245
Continuous torque (Nm)	290	2200
Overcurrent power 60 sec (kW)	200	250
Overcurrent torque 60 sec (Nm)	500	2700
Maximum motor speed (rpm)	8000	3252
$N_{T-fd\,1}$	50	50.28
$N_{T-fd\,2}$	-	28

Configuration 2 uses a single high torque and low speed traction motor connected to a transmission with 2 gear ratios and a final drive. The torque-speed curves for this motor and an efficiency map is shown in Figure 5.8. This motor is based on a 9-phase 245 kW IM produced by TM4 [317]. Configuration 2 was developed to meet the minimum tractive force requirements imposed by the airport regulations for the aeroplane weight classes within this duty cycle. A high gear ratio $N_{T-fd\,1}$ is used during towing and maintenance operations as it achieves the minimum tractive force requirement. A low gear ratio $N_{T-fd\,2}$ was chosen for unloaded solo runs that allows the vehicle to reach its top unloaded speed.

The two vehicle configurations follow the target duty cycle with minimal velocity error. Therefore, both powertrain configurations could theoretically be used for the final HEV as they achieve the target dynamic objectives. However, the price of incorrectly/oversized components increases the final vehicle price and the electrical energy usage differs as shown.

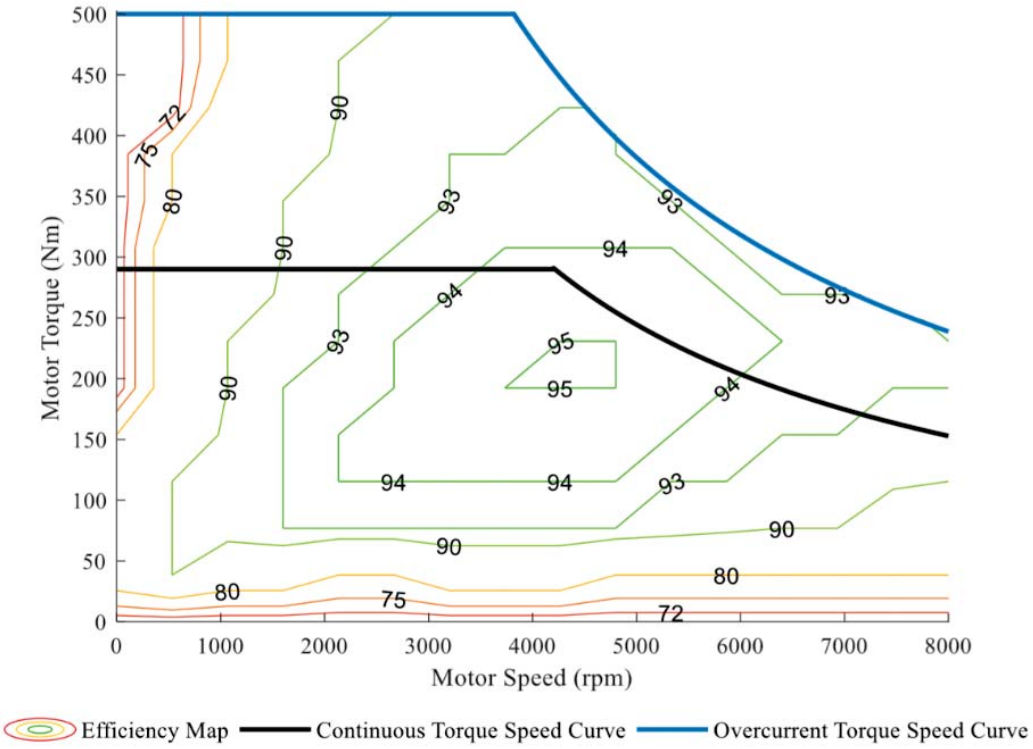

Figure 5.7 Torque Speed curves and efficiency map (%) for the traction motors used in HEV configuration 1

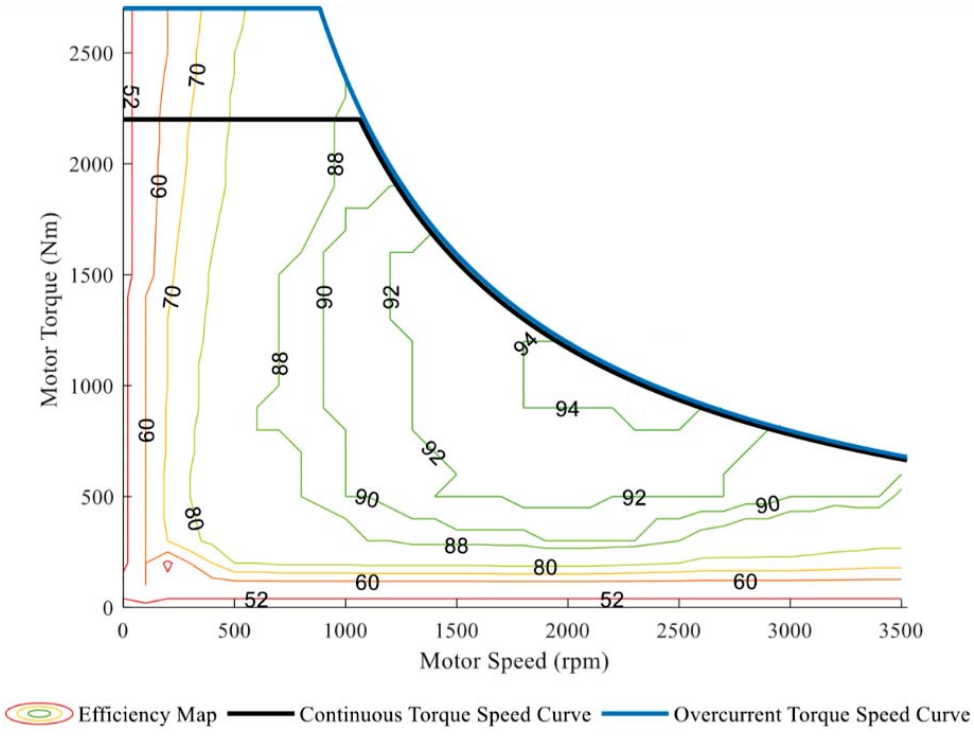

Figure 5.8 Torque Speed curves and efficiency map (%) for the traction motor used in HEV configuration 2

5.2.4.1 Torque Characteristics for HEV Configuration 1

Figure 5.9 shows the traction motor's torque-speed curve usage for the vehicle with configuration 1 over the duty cycle. The overcurrent and constant power regions are fully exploited. The theoretical temperature profile of the motors in Figure 5.10 increases at a greater rate while the HEV is accelerating during a towing operation than when the vehicle reaches its cruising speed.

During the maintenance operations, the command torque also enters the overcurrent region to accelerate the vehicle to its target velocity. However, the rate of change in temperature is smaller than the pushback operations. The motor only stays in the overcurrent region for a short time before the command torque returns to the continuous region to maintain cruising velocity. During solo operations, the command torque remains within the boundaries of the continuous torque region.

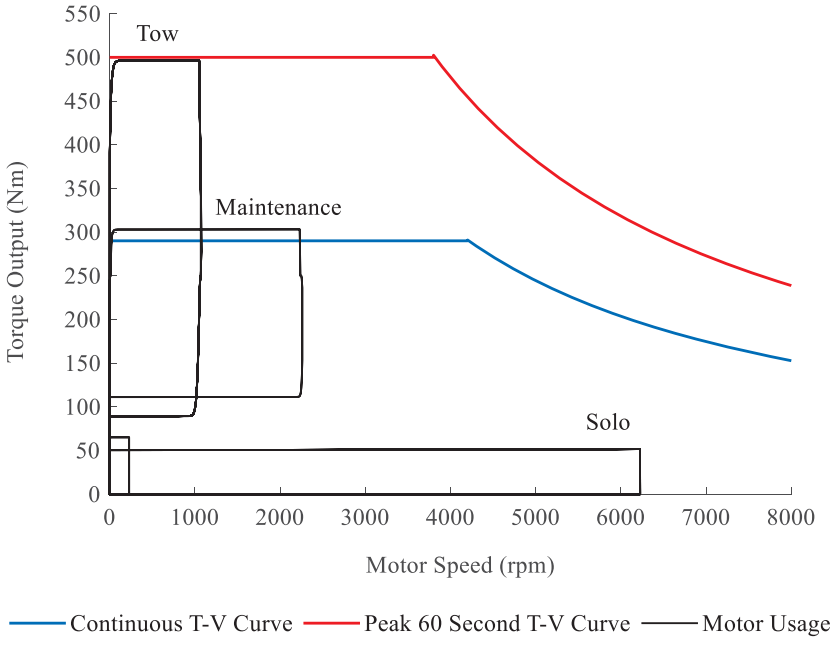

Figure 5.9 Motor usage for the HEV with configuration 1 over the daily duty cycle

The torque-speed characteristics and theoretical temperature profiles for configuration 1 are only obtainable for simulation purposes using the overcurrent tolerant prediction model. The prediction model shows how the traction motor's cool-down time differs depending on how long it operates within the overcurrent region. Without this prediction model, it would be much more difficult to verify that this choice of traction motor and gear ratio allows the vehicle to reach both its unloaded velocity and the maximum tow weights for the required times without overheating.

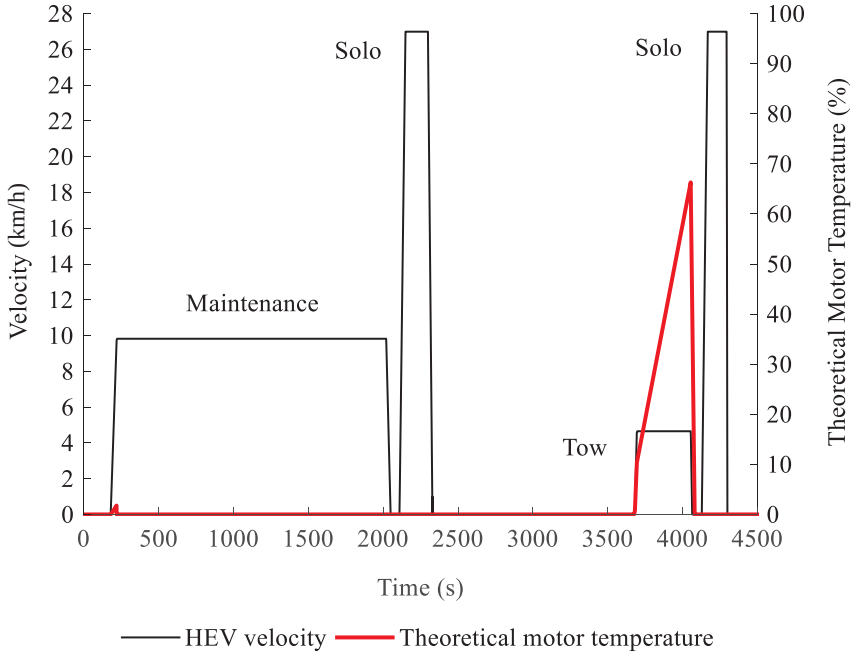

Figure 5.10 Theoretical temperature profile of the traction motors for configuration 1 over a section of the daily duty cycle; 1 maintenance operation, 1 pushback operation and 2 solo runs

5.2.4.2 Torque Characteristics for HEV Configuration 2

Figure 5.11 shows that the motor usage throughout the duty cycle for the vehicle using configuration 2 remains within the boundaries of the continuous torque-speed curve. The large headroom between the torque usage and the continuous torque-speed curve shows that the traction motor is oversized for this application. The traction motor operates in an inefficient

region for a large percentage of the duty cycle. Oversized components also increase the price of the HEV where smaller and cheaper components (Configuration 1) prove to be sufficient.

The overcurrent tolerant prediction model is not fully utilised for this traction motor as the output torque does not enter the overcurrent region. The model acts similarly to a conventional empirical data based model confined to the continuous region. This traction motor is not fully exercised and the advantages of operating in the overcurrent region are not revealed.

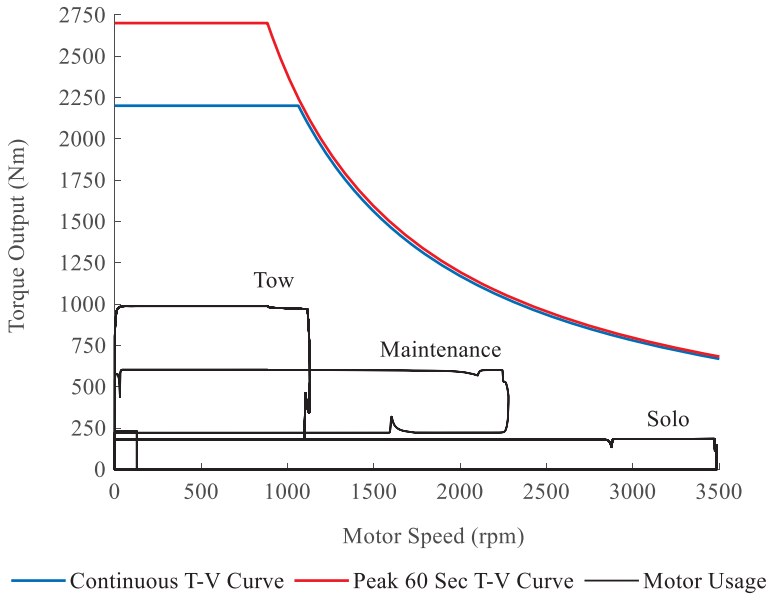

Figure 5.11 Motor usage for the HEV with configuration 2 over the daily duty cycle

5.2.4.3 HEV Electrical Performance Comparison

Because both HEV configurations accurately follow the target duty cycle, their peak power requirements are similar enough that they are able to use the same battery pack and genset configuration with parameters given in Table 5.5.

Figure 5.12-Figure 5.13 shows the SOE of the battery pack, vehicle velocity and the genset operation for Configuration 1 and Configuration 2 respectively over the duty cycle.

The blue shaded areas of Figure 5.12-Figure 5.13 show that the genset is providing full power to the DC-Link and that the traction motors are fully utilising this power during towing

operations. Where the genset power does not meet the output power requirements, the remaining power is provided by the battery pack. The yellow shaded regions show that the genset provides full power to the DC-Link and the battery pack is being charged.

Table 5.5 Battery pack parameters used in the pushback HEV for both configuration 1 and configuration 2

Parameter	**Value**
Per cell	
Rated energy capacity (kWh)	3.5
Rated current (A)	66
Nominal voltage (V)	52
Continuous power output (kW)	6.5
Peak power output (kW)	12.5
Pack configuration and parameters	
Cells in series per string	12
Strings of series in parallel	2
Upper SOE limit (%)	95
Lower SOE limit (%)	40
Battery pack capacity (kWh)	82
Genset parameters	
Genset power (kW)	86
Genset fuel consumption (L/h)	24

It might seem at first glance that the SOE for configuration 1 does not meet the SOE requirements since it drops below the lower SOE limit. Because the in-wheel traction motors in configuration 1 operates in a higher efficiency region than the single traction motor used in configuration 2, the HEV using configuration 1 enters and exits the first maintenance run with a higher SOE. Whereas configuration 2 reaches the lower SOE limit before the end of the first maintenance run, the genset turns on to begin charging the battery pack earlier than in configuration 1. Because configuration 1 SOE does not reach the lower limit during the rest period after the first maintenance run, it enters the second maintenance run with a much lower SOE than configuration 2.

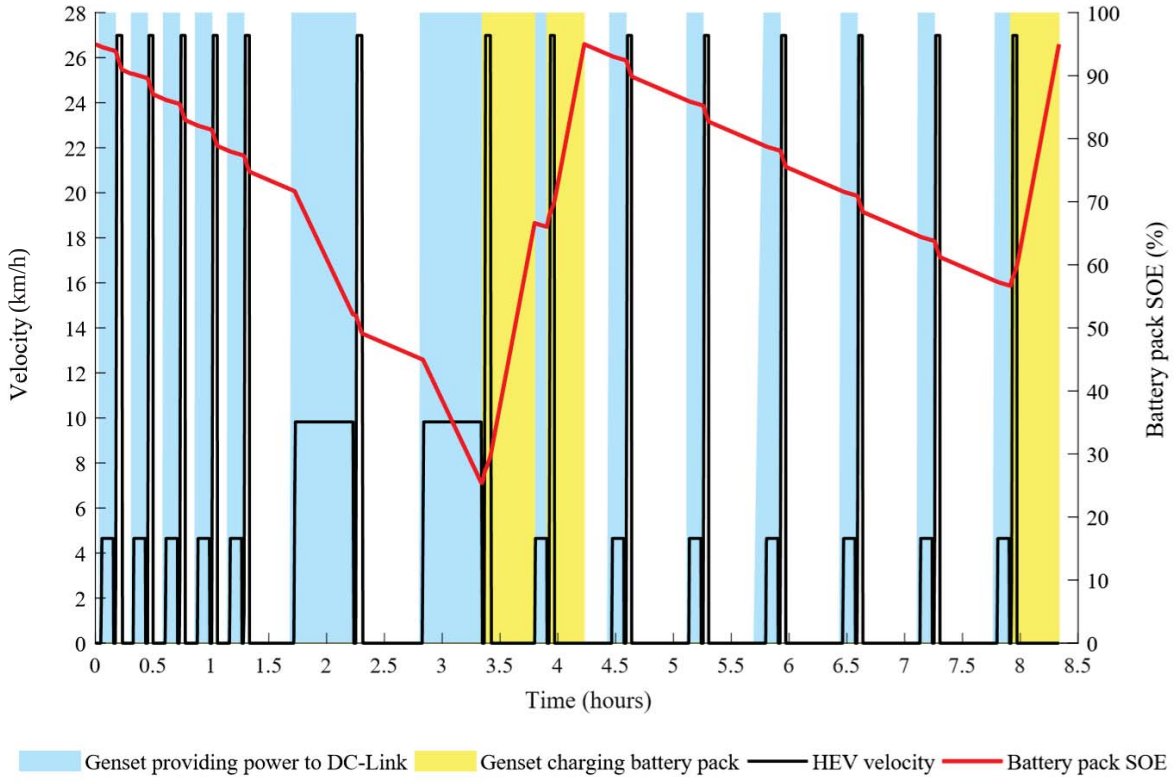

Figure 5.12 Velocity profile and battery pack SOE over the complete duty cycle for the HEV using configuration 1

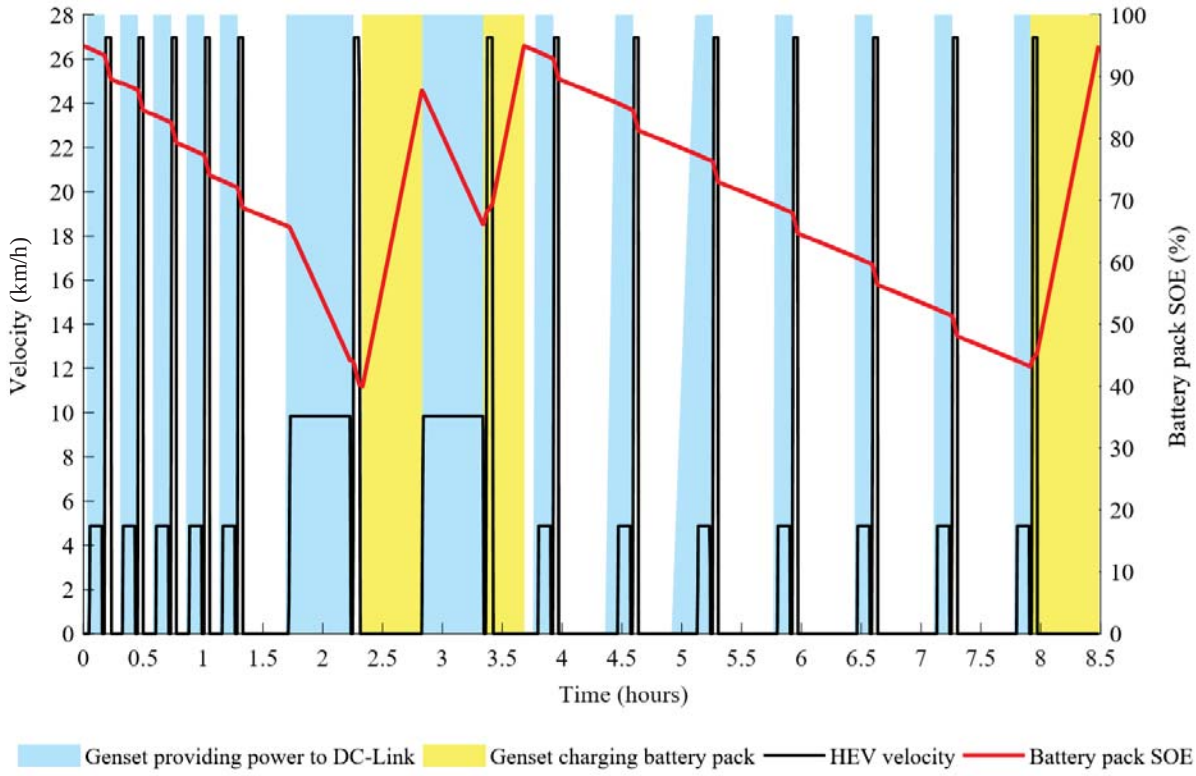

Figure 5.13 Velocity profile and battery pack SOE over the complete duty cycle for the HEV using configuration 2

Since the duty cycle used for this investigation is a rigorous worst-case scenario, the SOE profile for configuration 1 is deemed acceptable. If the duty cycle was designed differently by slightly shifting the maintenance runs, then the SOE for configuration 1 would remain within the upper and lower limits. In the real world, a driver would be able to decline a maintenance run if they think the SOE of the battery pack is insufficient or manually control the genset if they are expected to have long breaks.

A comparison between the electrical energy required and the fuel consumed by the genset for both HEV configurations against the original ICE powered vehicle is shown in Table 5.6. Configuration 2 requires 6.97% more energy and consumes 5.7% more fuel than configuration 1. This is because the dual hub traction motors of configuration 1 operate in the higher efficiency overcurrent region for large portions of the duty cycle. The increase in efficiency and improved energy usage of configuration 1 could only have been revealed by the overcurrent tolerant prediction model. If an empirical data-based traction motor model confined to the continuous torque region was used, the traction motors and powertrain in configuration 1 would not have been able to achieve the target duty cycle and therefore could not have shown an improvement over configuration 2. However, since configuration 1 does not meet the minimum tractive force regulations, configuration 2 is used as the final design for the HEV pushback vehicle. This legislative constriction further verifies the use of the overcurrent prediction model for vehicle design as there might be various other design limitations other than dynamic performance and require a larger number of traction motors to be investigated. Table 5.6 shows that configuration 2 reduced fuel consumption by 52% from the original ICE powered pushback vehicle over the duty cycle.

Throughout different ICE working conditions (e.g. start-up, cold running, hot running etc.), different emissions are produced at different rates. This makes it difficult to assess the change

in output emissions between the two HEV configurations and the original ICE vehicle. However, there is a consensus that significant reductions in fuel consumption correlates to a reduction in engine emissions [9, 15, 16]. In addition, for HEV/EVs there is a similar conclusion drawn between electrical efficiency and output emissions. From the results in Table 5.6, we can assume at this point in the vehicle's development there is a reduction in engine emissions for both HEV configurations over the ICE vehicle and the overcurrent prediction model produced a vehicle design that was more fuel economic and reduced the total output emissions further.

Table 5.6 Aeroplane pushback vehicle powertrain configuration energy requirement and fuel consumption comparison

Powertrain Configuration	**Energy required (kWh)**	**Fuel consumed (L)**
ICE	-	190
HEV Configuration 1	244	86.3
HEV Configuration 2	261	91.22

5.2.5 Pushback HEV Final Outcome

The prototype HEV aeroplane pushback vehicle is shown in Figure 5.14 using configuration 2 [318]. The vehicle is currently being challenged with following similar duty cycle operations to the ones investigated in this chapter to validate the choice of powertrain components.

Figure 5.14 Final HEV aeroplane pushback vehicle prototype [323]

5.3 Summary

A new HEV/EV traction motor sizing strategy was developed based on an overcurrent-tolerant prediction model of a traction motor operating in the overcurrent region. Using minimal motor parameters, this model is able to gauge if a motor's torque and thermal characteristics are able to fulfil the vehicle's target dynamic and electrical objectives. Using the motor's overcurrent torque-speed curve time constraints, the motor's temperature was estimated between safe upper and lower working boundaries. The rate of change in temperature was dependent on the position of the motor's output torque between the continuous and overcurrent torque-speed curves to represent the supply current magnitude.

Chapter Six

Reduced Switching Inverter Control for Traction Motors

This chapter aims to increase the efficiency of a DC-AC inverter for HEV/EV applications. The author proposes an extension to the on-line D-SVPWM method developed by Deng [203, 204] by introducing a Reduced Intermediate Switching SVPWM (RIS-SVPWM) scheme. The RIS-SVPWM method advances upon a previous on-line SVPWM method to find all possible available null switching states enclosing the reference voltage vector. The RIS-SVPWM scheme assigns inverter switching patterns which require the minimal amount of intermediate switching to reduce the power losses. The available null voltage vectors are generated on-line which negates the need for large and complicated look-up tables. This inverter control scheme is applicable to any HEV or EV that utilises traction motors without modifications.

This chapter is structured as follows; Section 6.1 presents the RIS-SVPWM method. Section 6.2 then analyses the intermediate switching losses and the harmonic quality of the generated waveforms when controlling a 5L-CHB inverter while powering a traction motor.

6.1 The RIS-SVPWM scheme

6.1.1 The D-SVPWM method

The D-SVPWM method developed by Deng [203, 204] is able to calculate all the switching states for one of the voltage vectors enclosing V_{ref}. The original SVM diagram with nL voltage levels (nL-SVM) is slowly reduced (e.g. ($nL-1, nL-2$ …) until only a $2L$-SVM diagram remains enclosing V_{ref}. The switching states S of the voltage vector representing the origin of the nL-SVM diagram $V_{nL-\mathrm{SVM}}(S_a, S_b, S_c)$ are modified with each mapping iteration. Any

invalid switching states are then removed at the end of the mapping process. The remaining switching states corresponding to one of the voltage vectors enclosing V_{ref} are then assigned to the inverter. The co-ordinates of V_{ref} are also mapped to the remaining voltage vector so the $2L$-SVM duty cycle equations to be used. The preliminary steps required for the D-SVPWM and the RIS-SVPWM methods are as followed:

1) The nL-SVM diagram is scaled so the distance between any two voltage vectors have a unit length of 1. Label the outermost hexagon boundary H_1.
2) The co-ordinates of the reference voltage vector V_{ref} are also made proportional to the new SVM diagram. The maximum length of V_{ref} is $(nL-1)$ of unit length.
3) The $nL-SVM$ diagram is labelled H_1 and has an origin at V_i with coordinates $V_{nL-\mathrm{SVM}}(\alpha,\beta)=(0,0)$.

To complete the mapping process, a total of $(nL-2)$ mapping iterations are required, each iteration is denoted by $h=1,2\ldots(nL-2)$. The following steps explain the D-SVPWM iterative mapping process:

1) Set the mapping iteration number h.
2) Separate the $(nL-h+1)$L-SVM diagram into 6 mapping sectors separated by 60° (an example is shown in Figure 6.1 for the first mapping iteration of a $5L$-SVM diagram).
3) Label the voltage vectors closest to the origin in each sector Q_{hq}. The sector q that V_{ref} lies in is calculated using Equation (84), where $\vartheta_\alpha \in [0\ 2\pi]$ is the angle V_{ref} makes with the α axis.

$$q = int\left\{mod\left(\vartheta_\alpha + \frac{\pi}{6}, 2\pi\right)\cdot\frac{3}{\pi}\right\}+1 \tag{84}$$

4) Place the origin of an $(nL-h)$L-SVM diagram (labelled H_{1+h}) on the vector Q_{hq}

5) Modify all the switching states of $V_{nL-\mathrm{SVM}}$ according to the switching state modifier q in Table 6.1.

6) Subtract the α modifier and the β modifier for sector q from the $V_{ref}(\alpha, \beta)$ co-ordinates. This maps V_{ref} to the origin of the $(nL - h + 1)$L-SVM diagram.

7) If $nL - h \neq 2$, go back to step 1 using $h + 1$. If $nL - h = 2$, the iterative mapping process is now complete.

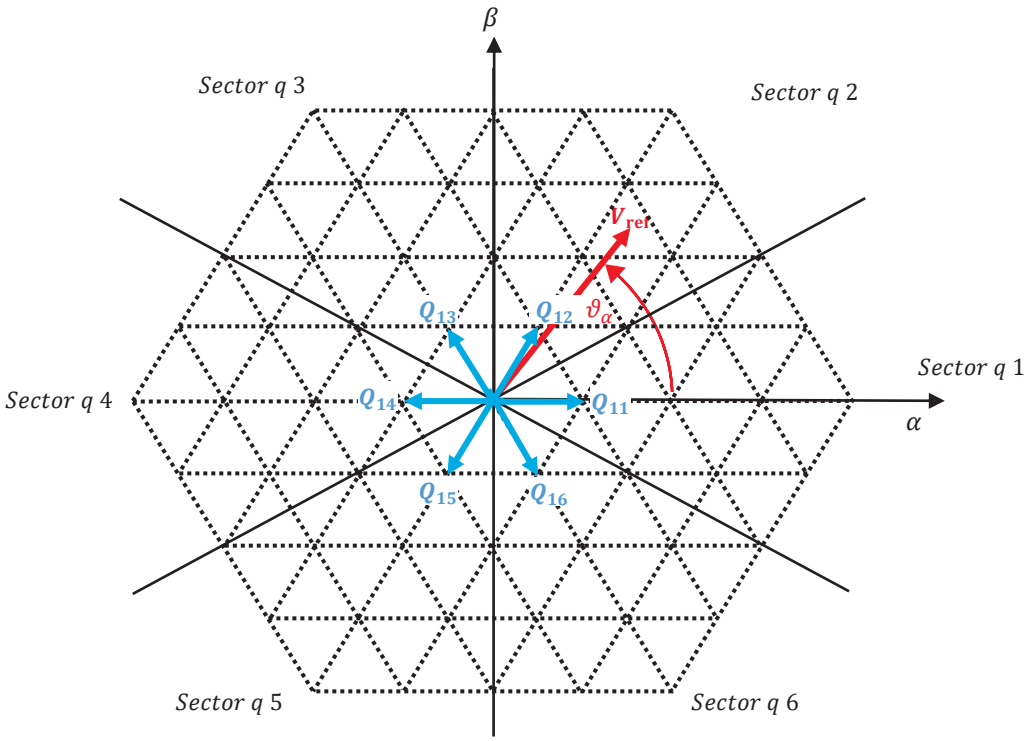

Figure 6.1 5L-SVM diagram separated into the 6 sectors for the D-SVPWM method and an example V_{ref} in Sector 2 [208, 209]

At this point, the D-SVPWM method is complete, the mapping vector and switching patterns from the final mapping iteration would be used to control the switching devices of the inverter. However, the switching states at this stage may require multiple intermediate switching before starting the next SVPWM cycle. An example of the iterative mapping process in Figure 6.2 graphically demonstrates how the D-SVPWM reduces the SVM diagram from a 5L-SVM diagram down to a 2L-SVM diagram.

Table 6.1 Null vector modifications [203, 204]

Sector q	State Modifier	α Modifier	β Modifier
1	$(S_a+1)S_bS_c$	1	0
2	$S_aS_b(S_c-1)$	0.5	$\frac{\sqrt{3}}{2}$
3	$S_a(S_b+1)S_c$	-0.5	$\frac{\sqrt{3}}{2}$
4	$(S_a-1)S_bS_c$	-1	0
5	$S_aS_b(S_c+1)$	-0.5	$-\frac{\sqrt{3}}{2}$
6	$S_a(S_b-1)S_c$	0.5	$-\frac{\sqrt{3}}{2}$

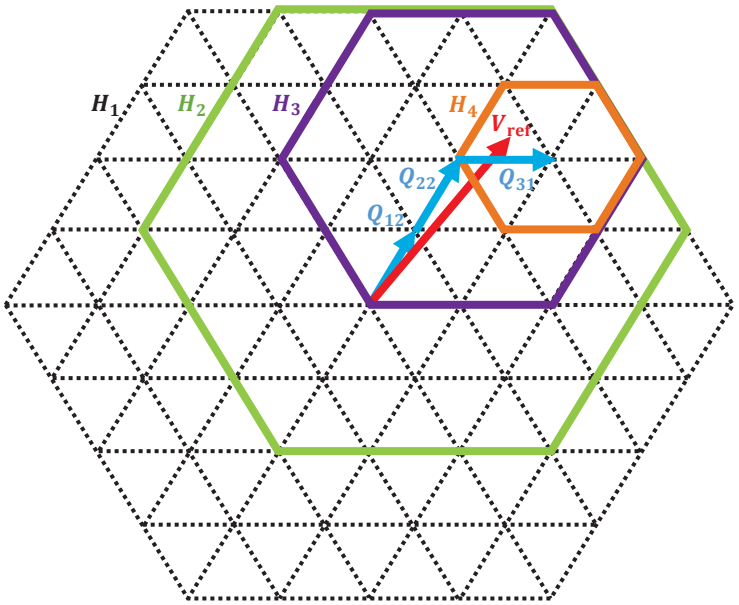

Figure 6.2 5L-SVM mapping process example for the D-SVPWM method [208, 209]

6.1.2 Advancement to the RIS-SVPWM method

It is now the role of the RIS-SVPWM to find the switching states of the other enclosing vectors to determine if they would be more appropriate null voltage vectors. An example V_{ref} enclosed by the voltage vectors $V_G[442,331,220]$, $V_J[431,320]$ and $V_K[441,330]$ is shown in Figure 6.3. The D-SVPWM method would map V_{ref} against V_J. Mapping V_{ref} against V_G, V_J or

V_K to create $V_{ref\,G}$, $V_{ref\,J}$ or $V_{ref\,K}$ respectively allows for simpler $2L$-SVM duty cycle. The reference voltage vector with respect to the origin of a 2LTS is labelled V_{ref-2L}.

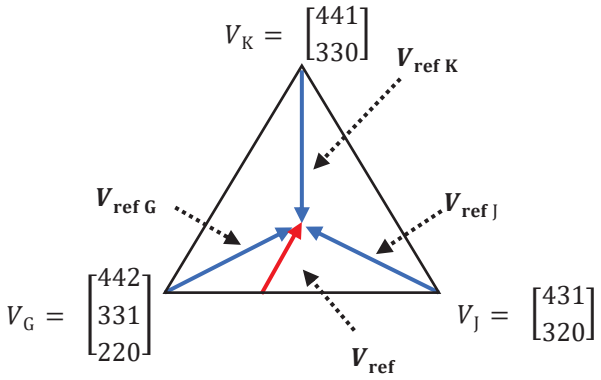

Figure 6.3 Example 2-level optimised dwell vector mapping options

The RIS-SVPWM mapping process is explained as followed:

1) Locate the current 2-Level triangular sector $2LTS$ that V_{ref-2L} lies in with respect to the final mapped voltage vector from the D-SVPWM method ($2LTS = 1,2 \ldots 6$). The example in Figure 6.3 attempts to map V_{ref} to V_J, this means V_{ref-2L}lies within a $2LTS = 3$ sector. Figure 6.4 shows two more examples, the red V_{ref-2L} lies in $2LTS = 1$ and the blue V_{ref-2L} lies in $2LTS = 4$ with respect to the origin V_0.

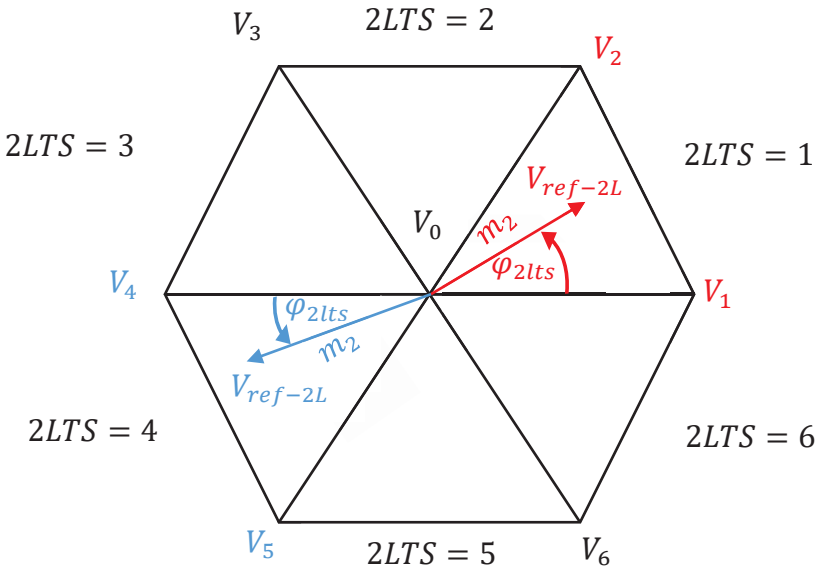

Figure 6.4 2L-SVM diagram inverter reference points

2) In a similar manner to steps 5 and 6 for the D-SVPWM method, apply two more mapping iterations to the origin vector of the current 2L-SVM diagram. Independently apply the mapping modifier $q = 2LTS$ and $q = 2LTS + 1$ $(if\ q > 6, then\ q = 1)$.
3) There are now three separate lists of switching state options, one list for each voltage vector enclosing V_{ref-2L}.
4) Any switching state combinations (S_a, S_b, S_c) that contain invalid switching states are removed. Invalid switching states include values $S < 0$ or $S > (nL - 1)$.
5) Calculate which vector requires the lowest total number of intermediate switching to start the next SVM cycle.
6) If multiple combinations of switching states have the same minimum number of intermediate switches from the previous SVM cycle, the switching combination on the voltage vector ahead of V_{ref} in the direction of travel is used. This is because the next voltage vector triangle that V_{ref} enters will share this null voltage vector, this reduces future intermediate switching losses ahead of time.
7) Label the optimal voltage vector V_0.
8) Subtract the α modifier and the β modifier from the $V_{ref}(\alpha, \beta)$ co-ordinates using the state modifier for the optimal voltage vector. If the original voltage vector using D-SVPWM holds V_0, no modifications are required.

The RIS-SVPWM scheme is now complete. The optimal null voltage vector which requires the minimum total number of intermediate switching has been found and the reference voltage vector has been mapped to it. The complete null switching state mapping process under the RIS-SVPWM scheme for the example given in Figure 6.2 is shown in Figure 6.5.

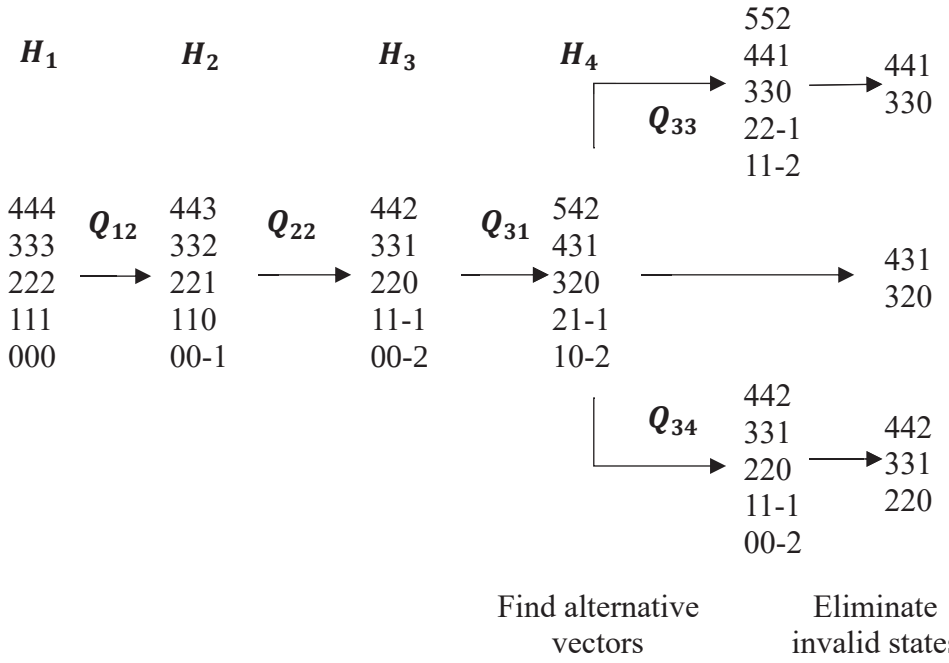

Figure 6.5 Null vector mapping state value example for 5L-SVM diagram with V_{ref} in Figure 6.2

6.1.3 Inverter Switching Device Control

Timing pulses X, Y and Z delivered to the switching devices of phase A, B and C respectively ensure only one complimentary pair of switching devices change over the SVPWM cycle for each phase. The timing pulses are calculated using the following steps:

1) Find the magnitude of $V_{ref-2L}(\alpha, \beta)$ with respect to the optimal choice of 2L voltage vector in the range $m_2 \in [0\ 1]$.
2) Find the $2LTS$ sector V_{ref-2L} lies in with respect to the optimal V_0.
3) V_{ref-2L} makes an angle $\varphi_{2LTS} \in \left[0\ \frac{\pi}{3}\right]$ with respect to the vector V_{2LTS}. Two examples are given in Figure 6.4 for the correct voltage vector that φ is measured against.
4) The reference voltage vector V_{ref-2L} is generated over a SVM switching cycle of length T_s using (85). The required on-times T_0, T_1 and T_2 for the enclosing vectors V_0, V_{2LTS}, and

V_{2LTS+1} respectively must be calculated using the 2L-SVM diagram Equations (86)-(88) [154, 175, 319, 320].

$$V_{ref-2L} = T_0V_0{+}T_1V_{2LTS} + T_2V_{2LTS+1} \tag{85}$$

$$(if\ 2LTS + 1 > 6\ then\ V_{2LTS+1} = V_1)$$

$$T_1 = \frac{Tm_2 \sin\left(\frac{\pi}{3} - \varphi\right)}{\sin\left(\frac{\pi}{3}\right)} \tag{86}$$

$$T_2 = \frac{Tm_2 \sin(\varphi)}{\sin\left(\frac{\pi}{3}\right)} \tag{87}$$

$$T_0 = T_s - T_1 - T_2 \tag{88}$$

5) Table 6.2 converts the vector on-times T_0, T_1 and T_2 into phase pulses X, Y and Z depending on $2LTS$ [192]

Table 6.2 2-Level SVPWM duty ratio calculations converts the vector on-times T_0, T_1, T_2 into phase pulses X, Y and Z to be applied to phase A, B and C respectively [192].

$2LTS$	Phase A	Phase B	Phase C
1	$X = T_1 + T_2 + \frac{T_0}{2}$	$Y = T_2 + \frac{T_0}{2}$	$Z = \frac{T_0}{2}$
2	$X = T_1 + \frac{T_0}{2}$	$Y = T_1 + T_2 + \frac{T_0}{2}$	$Z = \frac{T_0}{2}$
3	$X = \frac{T_0}{2}$	$Y = T_1 + T_2 + \frac{T_0}{2}$	$Z = T_2 + \frac{T_0}{2}$
4	$X = \frac{T_0}{2}$	$Y = T_1 + \frac{T_0}{2}$	$Z = T_1 + T_2 + \frac{T_0}{2}$
5	$X = T_2 + \frac{T_0}{2}$	$Y = \frac{T_0}{2}$	$Z = T_1 + T_2 + \frac{T_0}{2}$
6	$X = T_1 + T_2 + \frac{T_0}{2}$	$Y = \frac{T_0}{2}$	$Z = T_1 + \frac{T_0}{2}$

The switching table for a 5L-NPC inverter in Table 3.1 consists of 4 pairs of complimentary power electronic switching devices on each phase leg. The switch control is simplified by only observing the top 4 switches and acknowledging that the bottom 4 switches have complimentary switch positions. For phase-A to change from switching state 2 to 3, switch $A2$ in phase-A remains off for $(T_s - X)$s, and then remains on for the remainder of the SVPWM cycle (refer to Figure 2.4 for switch labels). During this time, all of the switches above switch $A2$ are off, and all the switches below $A2$ remain on for the entire of the SVPWM cycle. For phase-A to change from switching state 3 to 2, switch $A2$ in phase-A remains on for Xs and is then turned off for the remainder of the SVM cycle.

The switching table for a 5L-CHB inverter in Table 3.2 shows that multiple combinations of inverter switching patterns are able to output the same switching state [154]. Keeping with the objective of reducing intermediate switching losses, the switching pattern that requires the minimum number of intermediate switching has the phase pulse assigned to it.

6.2 Performance evaluation of the RIS-SVPWM method

6.2.1 Simulation setup procedure

For HEV/EV applications, an inverter must be able to generate voltage waveforms of varying magnitude and frequency that enable a traction motor to operate in its entire torque-speed region. A C-Class Hatchback (Vehicle B in Table 4.4) using an IM (IM# 1 in Table 4.5) covering a velocity range of 15-75 mph or 25-115 km/h would require the motor and inverter to operate with a voltage supply frequency range of $f \in [30\ 150]$ Hz according to the synchronous speed. Therefore, supply voltage waveforms within this frequency range are explored covering a wide range of modulations indices $m \in [0.2\ 1]$. The 5L-CHB inverter model discussed in Section 3.2.2 generates voltage waveforms and feeds them to a traction

motor model (IM# 1) presented in Section 3.2.1. The 5L-CHB inverter for these simulations uses a switching frequency f_s of 10 kHz (i.e. $T_s = 1/f_s$). To compare the switching count and harmonic quality when using the D-SVPWM and the RIS-SVPWM modulation schemes, both methods are used to control the individual switching devices of the inverter.

The following steps describe the process of determining appropriate load torques applied to the rotor during the simulations, this process is repeated for each supply frequency f:

1) An output voltage waveform of f Hz with a modulation index of $m = 0.9$ is supplied to the motor windings.
2) The load torque is steadily increased until the line current meets the rated supply current of the motor.
3) Because no speed or current control is implemented for this investigation, the motor's speed decreases. The speed at which the motor dropped down to is recorded as ω_f.
4) The peak load torque for each supply frequency is shown in Table 6.3. This waveform matches the expected speed-torque profile for IM# 1.

Table 6.3 Peak Torque Profile

f **(Hz)**	**30**	**40**	**50**	**60**	**70**	**80**	**90**	**100**	**110**	**120**	**130**	**140**	**150**
Load (N)	200	200	200	170	150	130	115	105	95	87	80	70	65

5) This was repeated for a range of modulation indices $m \in [0.2\ \ 0.9]$. The load torque was steadily increased until the motors speed reached ω_f.
6) The percentages of the load torque for each modulation indices with respect to the peak torque is shown in Table 6.4. The investigation showed that the same load torque percentages in Table 6.4 is used for every supply frequency investigated.

Table 6.4 Load Torque percentage profile

m	**0.2**	**0.3**	**0.4**	**0.5**	**0.6**	**0.7**	**0.8**	**0.9**
Load %	5	10	20	30	40	60	80	1

6.2.2 Switch Count Analysis

At the start of each SVM cycle, both modulation methods are allowed to select a starting null voltage vector which would minimise the intermediate switching count from the previous SVM cycle from the options made available to them from their respective control schemes.

The percentage decrease in intermediate switching using the RIS-SVPWM method over the D-SVPWM method is given in Figure 6.6(a) for a range of modulation indices and output waveform frequencies. The total switching count percentage decrease is shown in Figure 6.6(b).

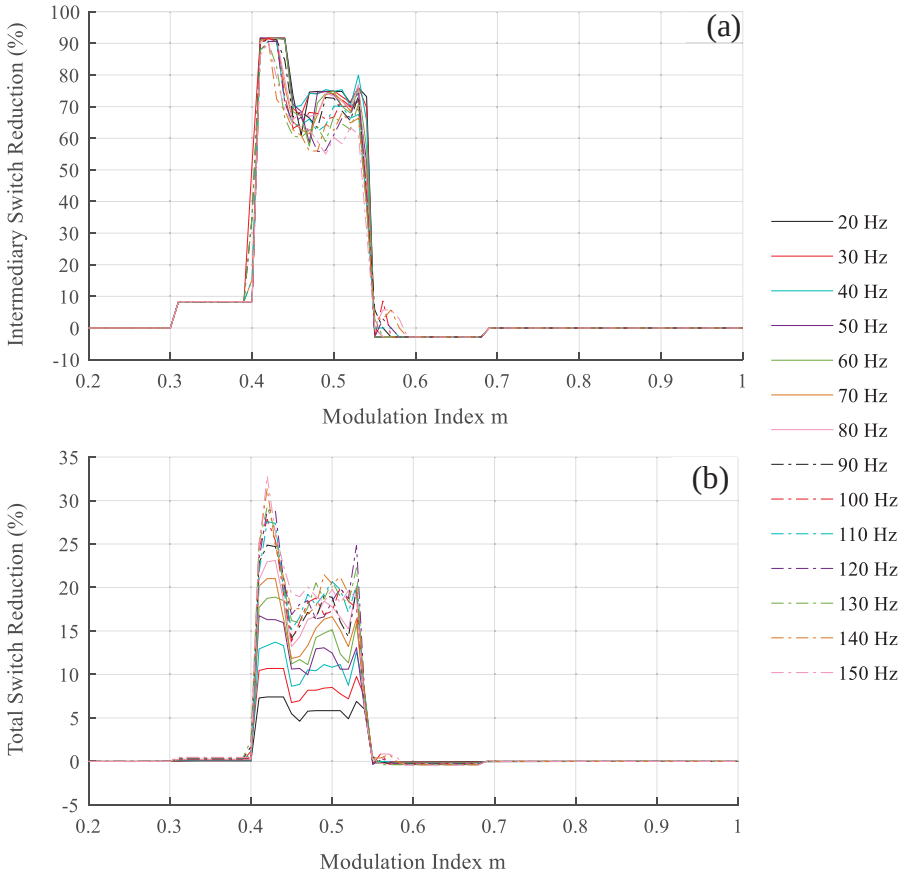

Figure 6.6 Switch count reduction over a range of modulation indices $m \in [0.2\ 1]$ and output voltage frequencies $f \in [20\ 150] Hz$ for a 5L-CHB inverter $f_s = 10\ kHz$, **(a)** Intermediate switch decrease, **(b)** Total switch decrease

The reduction in intermediate switching over the range of waveform frequencies remain somewhat comparable when using the RIS-SVPWM scheme. This is because over a single

voltage waveform cycle (or one rotation of the V_{ref}) the same number of enclosing vector triangles are crossed. However, the total reduction in switching count increases as the output waveform frequency increases. This is because V_{ref} completes a full rotation faster for high output waveform frequencies, the total number of SVM cycles inside an enclosing voltage vector is lower and thus there is a lower total switching count.

The RIS-SVPWM method significantly reduces the amount of intermediate switching for modulation indices $m \in [0.35\ 0.55]$ by up to 90%. This is because V_{ref} crosses the highest number of enclosing voltage vector triangles for a 5L inverter in this range with a high number of possible null voltage vectors.

Due to the linear trend between the energy lost during the turn on-off phases of the power electronics and the switching losses for this inverter, it is assumed that the switching losses also reduce in proportion to the reduction in switching count [321]. For modulation indices $m \in [0.55\ 1]$, the RIS-SVPWM method shows little improvement over the D-SVPWM method since the number of available switching vectors suitable for SVPWM decreases in this modulation range.

It must be noted that as part of this investigation the vector $V_{n\mathrm{L-SVM}}$ (the origin of the nL-SVM diagram) was not included in the RIS-SVPWM scheme. This was done to avoid adversely affecting the THD or DC-voltage balancing. If this vector was included, there would be no intermediate switching losses for the RIS-SVPWM method when V_{ref} if fully contained within the 6 innermost voltage vector triangles of the nL-SVM diagram. The slight increase in switching count from the D-SVPWM in the modulation index range $m \in [0.55\ 0.7]$ is a result of using a constant starting null vector of [2 2 2] at the beginning of all the simulations. The results in Figure 6.6 were created over a time period of $2T_s$ s, if the simulation were to continue running, this increase in switching count would become negligible.

6.2.3 Waveform Harmonic Analysis

The WTHD for the phase voltage v_a is shown in Figure 6.7 for the full range of modulation indices and output waveform frequencies. Figure 6.7(a) shows the WTHD using the D-SVPWM method, Figure 6.7(b) for the RIS-SVPWM method and the percentage difference is shown in Figure 6.7(c). The WTHD for the RIS-SVPWM scheme is higher than the D-SVPWM method but remains within acceptable tolerances during the sinusoidal region below 1% [322].

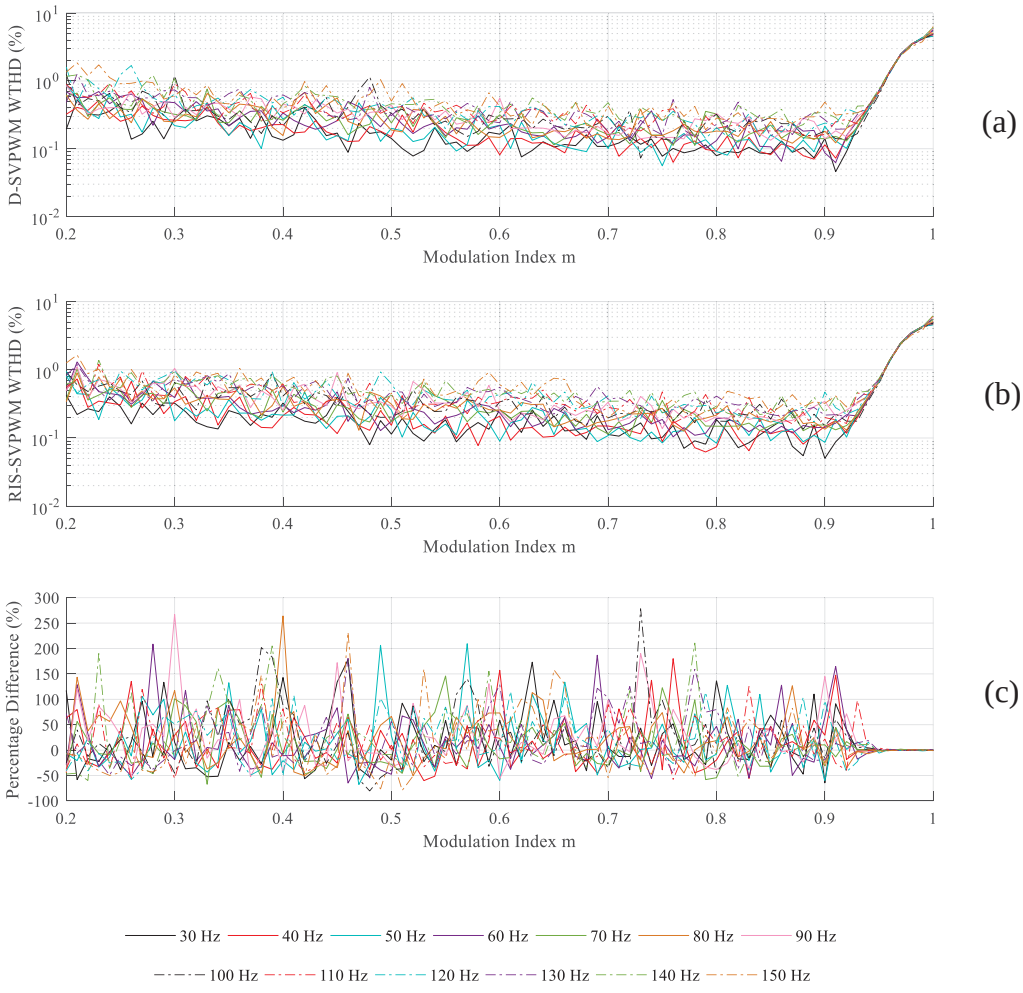

Figure 6.7 WTHD comparison for v_a over a range of modulation indices and output voltage frequencies for a 5L-CHB inverter using $f_s = 5\ kHz$, **(a)** D-SVPWM, **(b)** RIS-SVPWM, **(c)** Percentage Difference

The THD for the line current i_{AB} is shown in Figure 6.8 for a range of modulation indices and output waveform frequencies. Figure 6.8(a) shows the THD using the D-SVPWM method,

Figure 6.8(b) for the RIS-SVPWM method and the percentage difference is shown in Figure 6.8(c). The THD for the RIS-SVPWM scheme is again higher than the D-SVPWM method, but remains well within acceptable tolerances (according to the IEEE Standard 519-92) for large portions of the sinusoidal region of below 5% [322, 323, 324]. This is in part a reflection on the research presented by Pahlavani [193] and McGrath [325] who recognise the trade-off between lower switching counts and an increase in harmonic distortion.

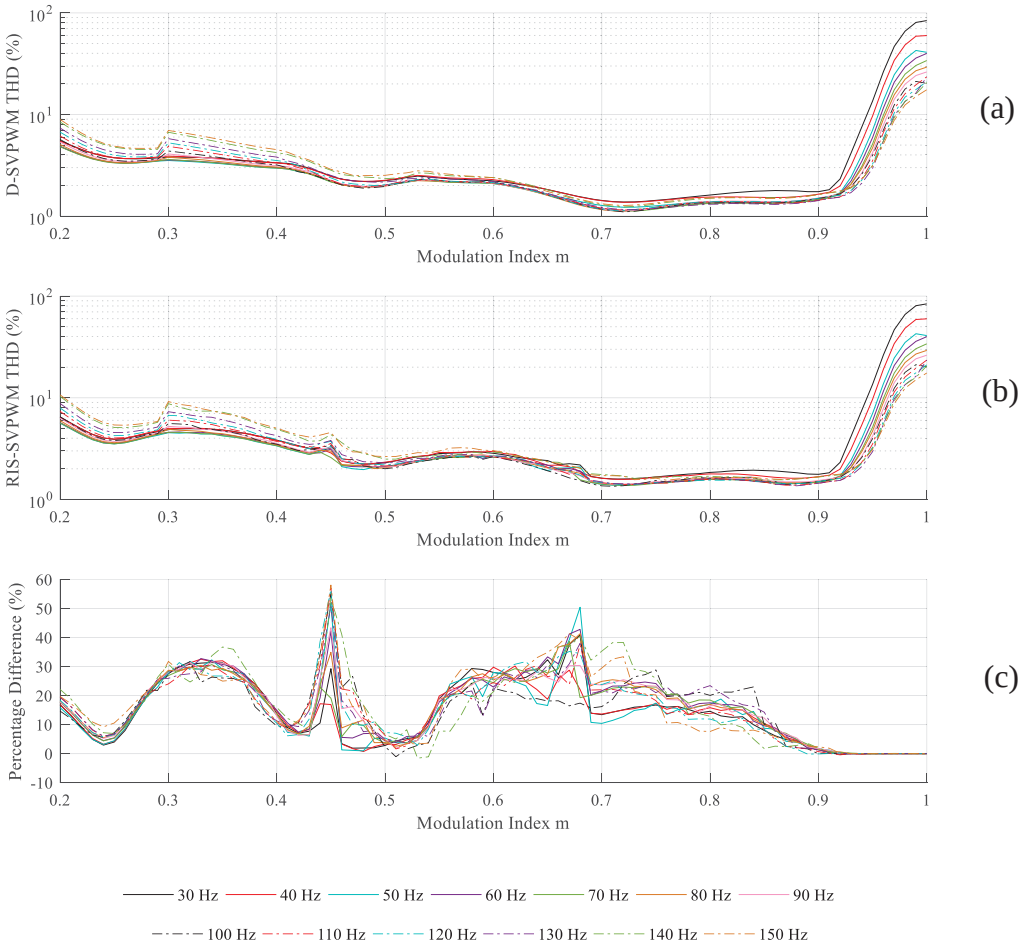

Figure 6.8 THD comparison for i_{ab} over a range of modulation indices and output voltage frequencies for a 5L-CHB inverter using $f_s = 5\ kHz$, **(a)** D-SVPWM, **(b)** RIS-SVPWM, **(c)** Percentage Difference

Once the inverter enters the overmodulation region, the choice of available switching vectors become limited and the modulation methods begin to perform comparably to one another. However, the WTHD and THD values for the phase voltage and line currents respectively reach

unacceptable values. Operation in the overmodulation region has been addressed by previous researchers who suggest restricting SVPWM to the sinusoidal region for low speed operation and permit overmodulation for high speed operation [326, 327, 328]. The THD for 150 Hz line currents in Figure 6.8 are higher in the overmodulation region than the sinusoidal region but reduce for low frequencies (i.e. 30-50 Hz).

6.2.4 Inverter Output Waveform Analysis

The pole voltage v_{a0}, the line voltage v_{ab} and line current i_{ab} for a target waveform frequency of 50 Hz and modulation index $m = 0.2$ is shown in Figure 6.9(a)-(c) respectively. The phase voltage WTHD and line current THD harmonic spectrum for these waveforms are shown in Figure 6.10(a)-(b) respectively. Similar graphs are shown for waveforms of the same output frequency with modulation indices of $m = 0.45$ (Figure 6.11-Figure 6.12), $m = 0.7$ (Figure 6.13-Figure 6.14), $m = 0.907$ (Figure 6.15-Figure 6.16), $m = 0.955$ (Figure 6.17-Figure 6.18) and $m = 1$ (Figure 6.19-Figure 6.20). These graphs show that the inverter is producing the correct number of voltage levels (pole and phase) for a respective modulation index and inverter voltage level (i.e. 5L-CHB).

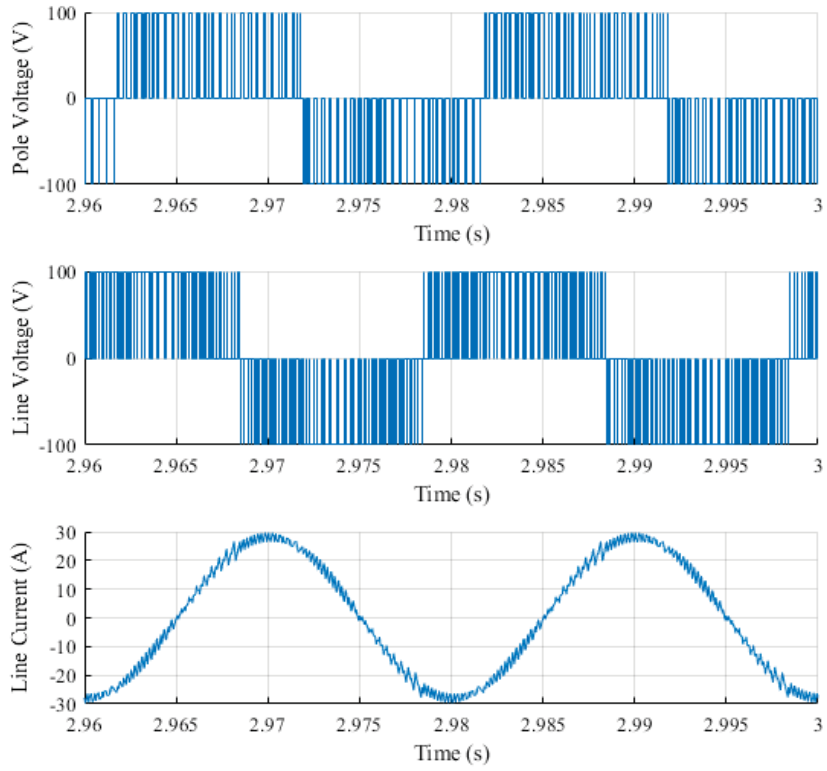

Figure 6.9 5L-CHB inverter simulation waveform results $m = 0.2$, **(a)** v_a, **(b)** v_{ab}, **(c)** i_{ab}

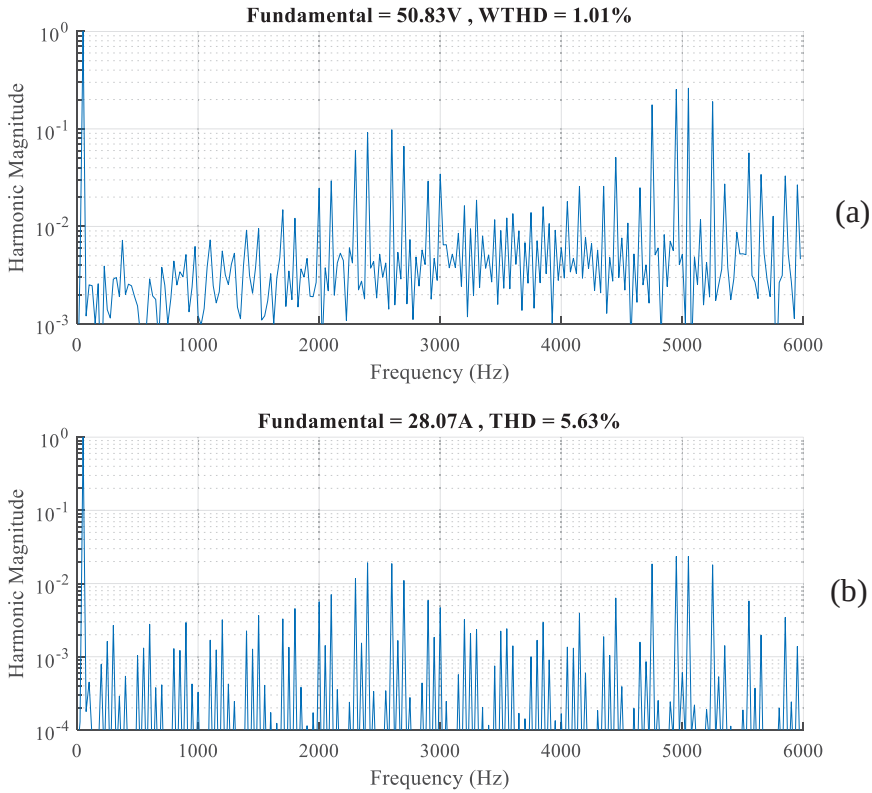

Figure 6.10 5L-CHB inverter simulation harmonic analysis results $m = 0.2$, **(a)** v_a, **(b)** i_{ab}

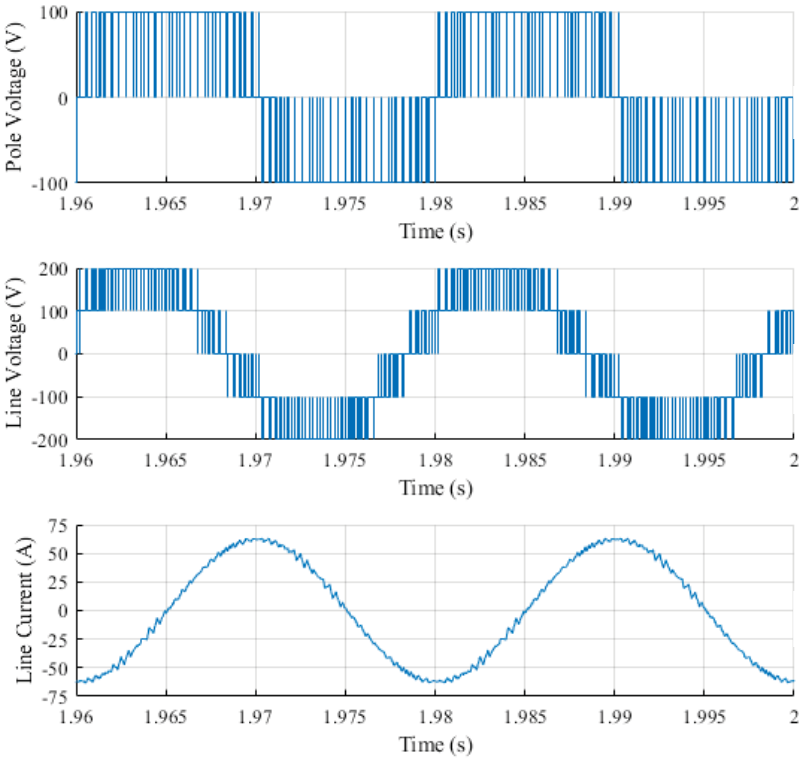

Figure 6.11 5L-CHB inverter simulation waveform results *m = 0.45*, **(a)** v_a, **(b)** v_{ab}, **(c)** i_{ab}

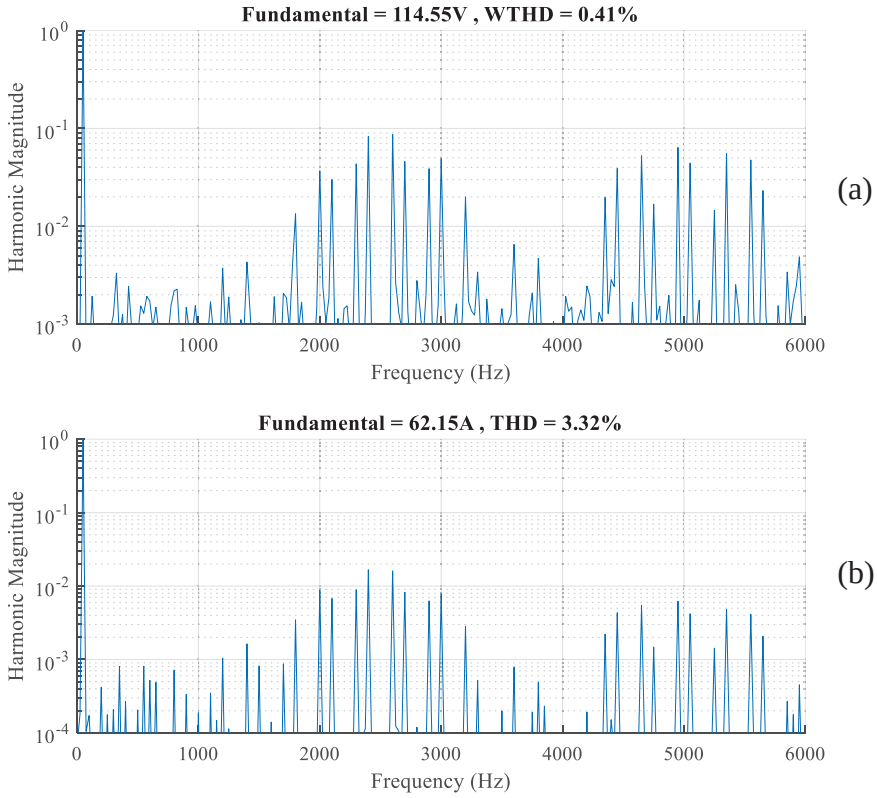

Figure 6.12 5L-CHB inverter simulation harmonic analysis results *m = 0.45*, **(a)** v_a, **(b)** i_{ab}

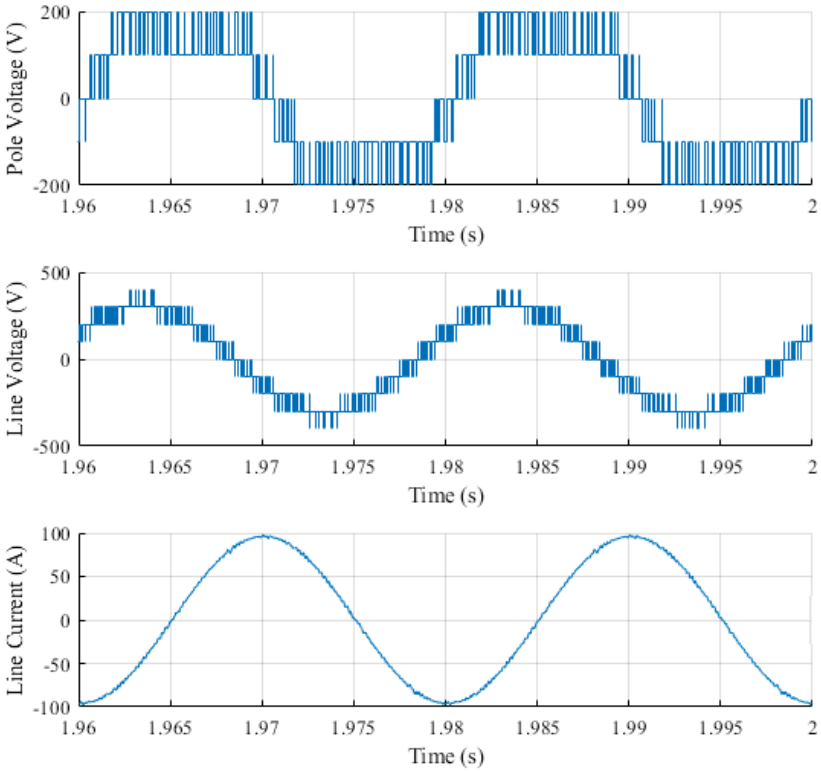

Figure 6.13 5L-CHB inverter simulation waveform results $m = 0.7$, **(a)** v_a, **(b)** v_{ab}, **(c)** i_{ab}

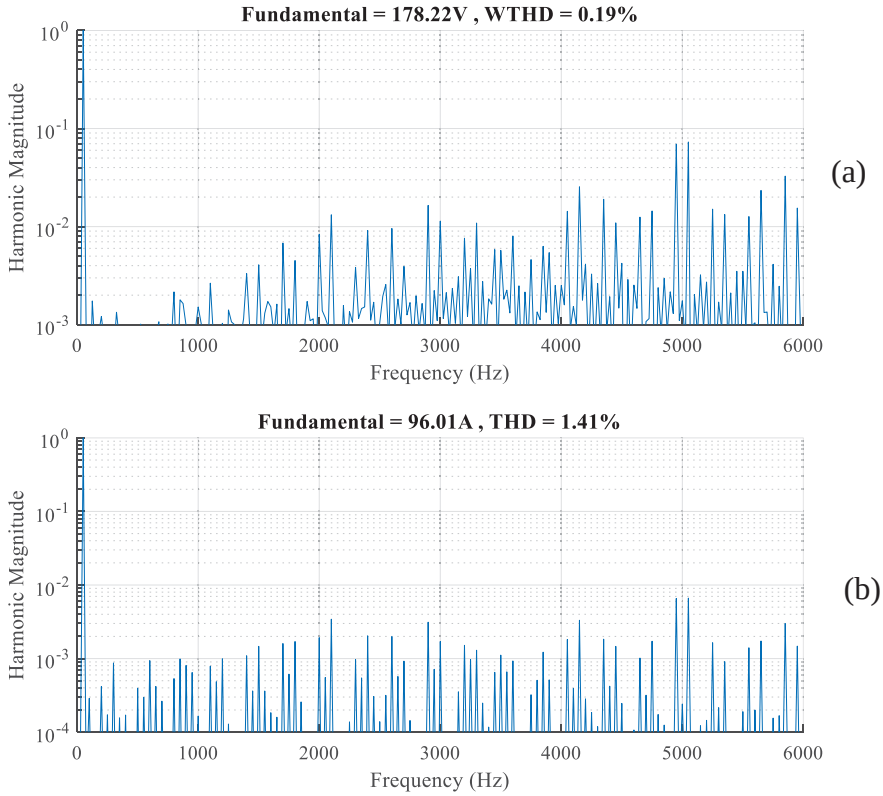

Figure 6.14 5L-CHB inverter simulation harmonic analysis results $m = 0.7$, **(a)** v_a, **(b)** i_{ab}

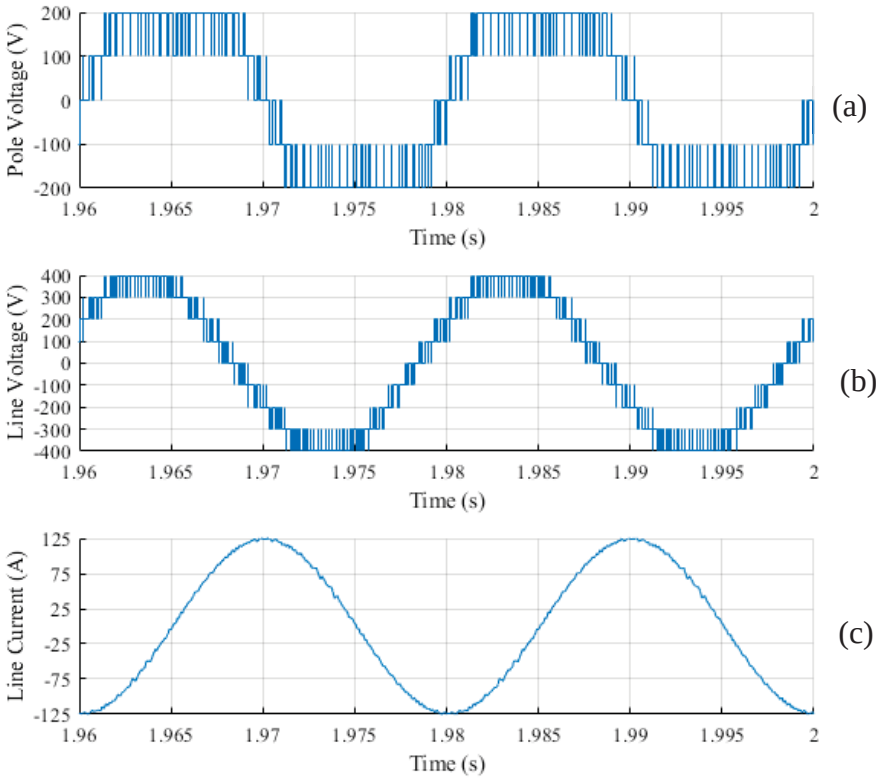

Figure 6.15 5L-CHB inverter simulation waveform results *m = 0.907*, **(a)** v_a, **(b)** v_{ab}, **(c)** i_{ab}

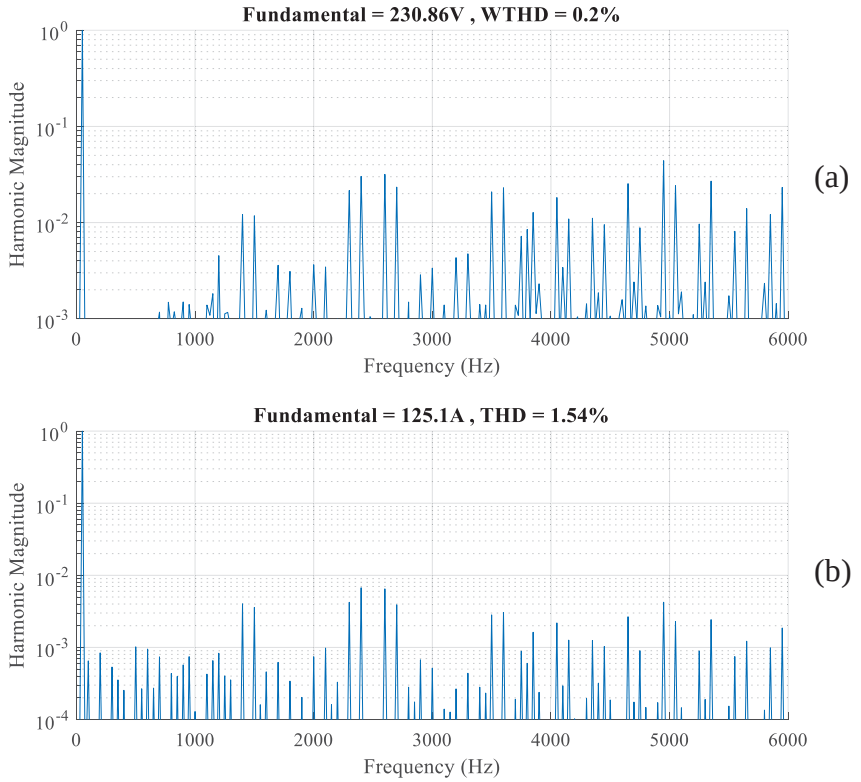

Figure 6.16 5L-CHB inverter simulation harmonic analysis results *m = 0.907*, **(a)** v_a, **(b)** i_{ab}

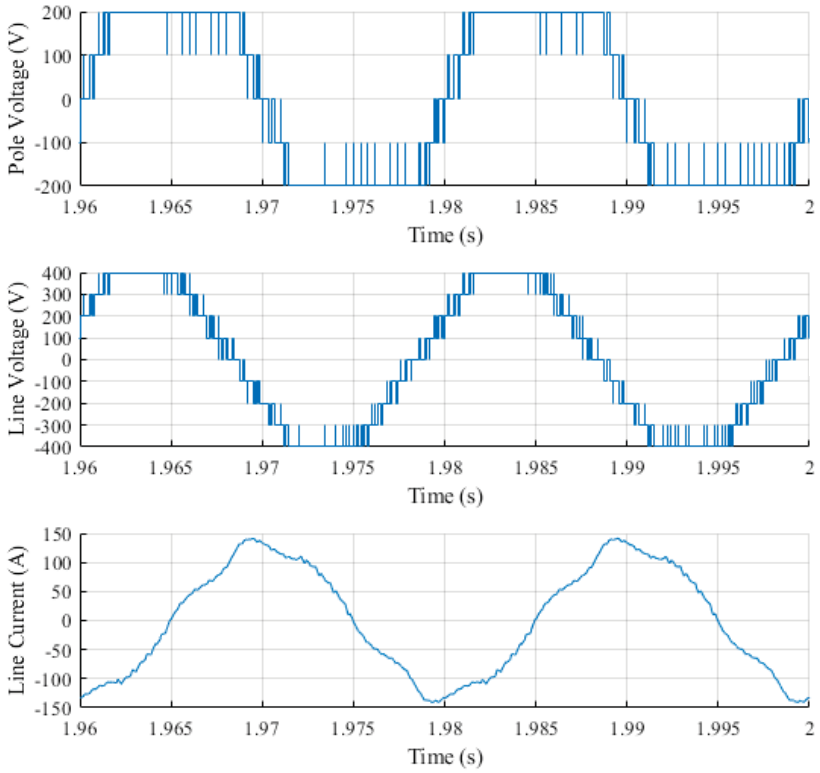

Figure 6.17 5L-CHB inverter simulation waveform results *m = 0.955*, **(a)** v_a, **(b)** v_{ab}, **(c)** i_{ab}

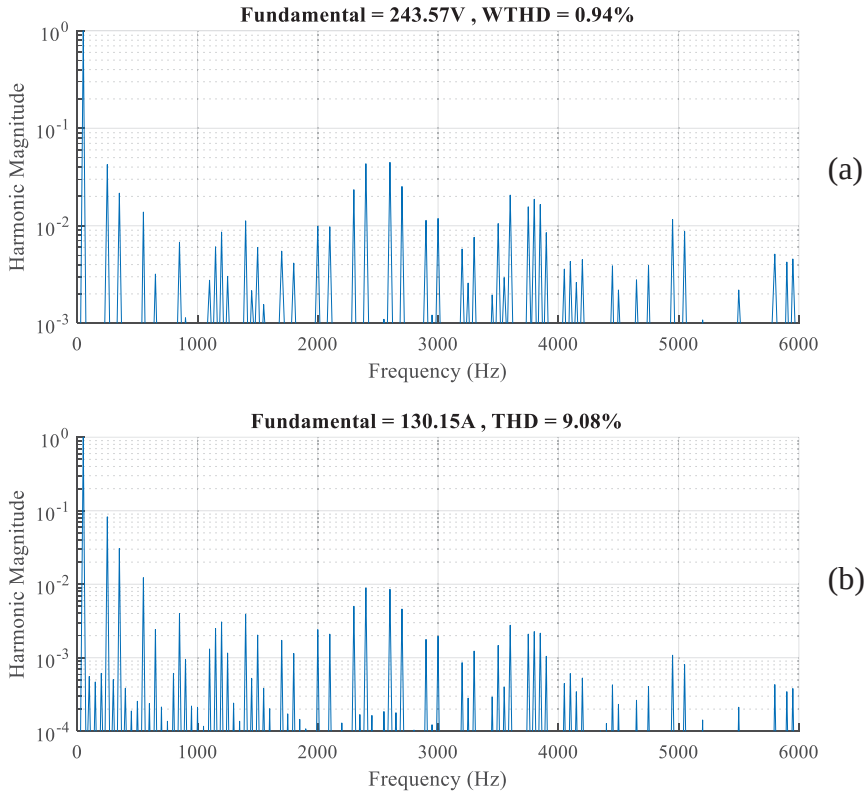

Figure 6.18 5L-CHB inverter simulation harmonic analysis results *m = 0.955*, **(a)** v_a, **(b)** i_{ab}

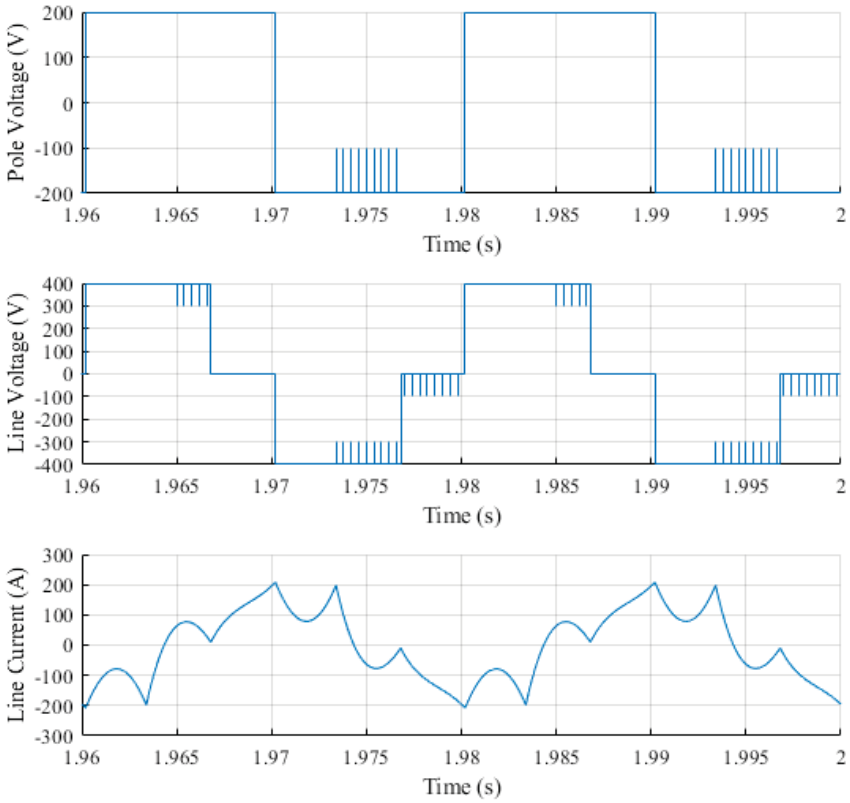

Figure 6.19 5L-CHB inverter simulation waveform results $m = 1$, **(a)** v_a, **(b)** v_{ab}, **(c)** i_{ab}

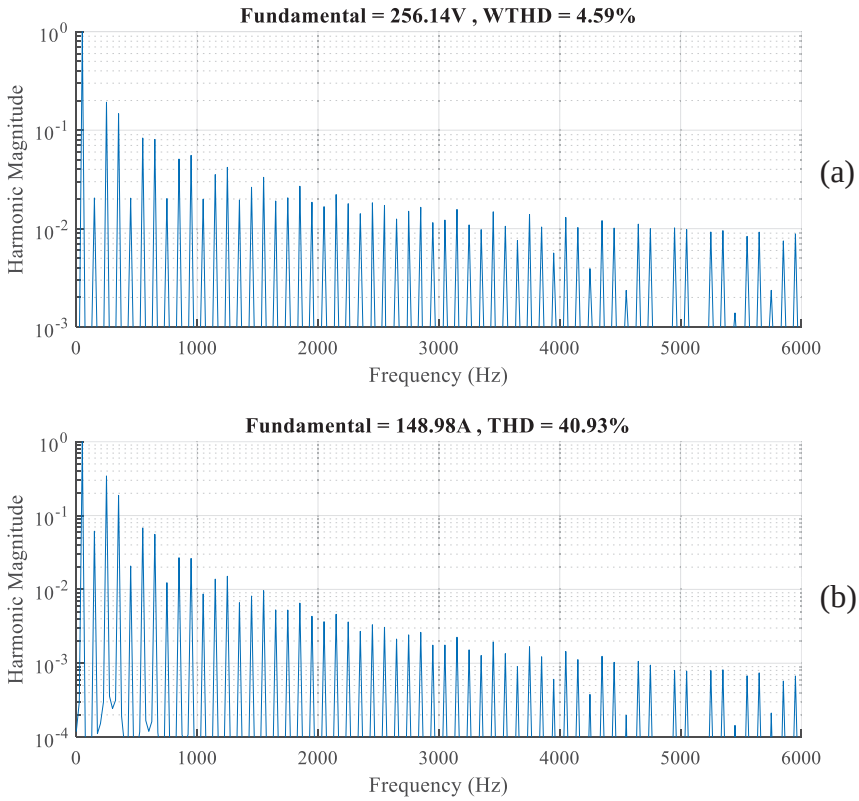

Figure 6.20 5L-CHB inverter simulation harmonic analysis results $m = 1$, **(a)** v_a, **(b)** i_{ab}

The waveform analysis for the voltage waveforms show that the inverter is capable of generating waveforms whose fundamental components meet their target respective modulation indices as shown in Table 6.5. It should be noted that the THD analysis of the current waveforms show that large harmonics are generated at high frequencies. It may be possible to improve the THD of the RIS-SVPWM with additional filters to remove these high harmonic components.

Table 6.5 Inverter output waveform harmonic magnitude and quality analysis

m	Target v_a Harmonic (V)	Actual v_a Harmonic (V)	Error (%)	v_a WTHD (%)	Actual i_{ab} Harmonic (A)	i_{ab} THD (%)
0.2	50.92	50.83	-0.17	1.01	28.07	5.63
0.45	114.59	114.55	-0.03	0.41	62.15	3.32
0.7	178.25	178.22	-0.01	0.19	96.01	1.41
0.907	230.96	230.86	-0.04	0.2	125.1	1.54
0.955	243.18	243.57	0.16	0.94	130.15	9.08
1	254.64	256.14	0.58	4.59	148.98	40.93

6.3 Summary

An on-line Reduced Intermediate Switching Space Vector Pulse Width Modulation (RIS-SVPWM) scheme for multilevel DC-AC inverters for HEV/EV applications was presented. The RIS-SVPWM scheme is applicable to multiple inverter topologies for HEV/EVs of any voltage level. By advancing upon a previous popular on-line SVPWM method, the RIS-SVPWM method included a strategy to reduce the intermediate switching and increase the inverter efficiency. This was achieved by extending the mapping process to calculate alternative switching patterns enclosing the reference voltage vector.

The RIS-SVPWM scheme reduces the intermediate switching by up to 90% and the total switching count by 30% over the previous on-line SVPWM method. This increases the inverter's efficiency while maintaining acceptable levels of voltage and current waveform harmonic distortion. A wide range of voltage and current waveform harmonics was presented and showed that the output waveforms matched their target harmonic component magnitude at the correct frequency

Chapter Seven

Fuzzy Logic HEV/EV Stability Control

In this chapter, the author proposes a Fuzzy Logic (FL) based Vehicle Stability Control (VSC) system which aims to improve the controllability and stability of an HEV/EV during combined emergency braking and steering manoeuvres. A new gradient command controller assigns target operating gradients to a modified wheel slip controller using information obtained from a pre-existing popular FL Yaw Moment Controller (YMC).

In comparison to other VSC systems, the FL based VSC (FL-VSC) system aims to offer; minimal constant vehicle data to be used within the control algorithm, high robustness for superior and stable control over various driving scenarios. The FL-VSC scheme in this work is only implemented into a vehicle utilising four independent traction motors to fully highlight the level of control freedom only obtainable by the traction motors and the FL-VSC scheme. However, future research is planned to investigate this control scheme with various other HEV/EV powertrain architectures. It is expected that minimal changes to the control architecture presented in this chapter would be required.

This chapter is sectioned as follows; Section 7.1-7.2 presents the control architecture and controllers used for the FL-VSC system respectively. Section 7.3 discusses the results of the simulation study by investigating various emergency braking scenarios with a comparison against other VSC systems.

7.1 Operating principles of the FL-VSC

The FL-VSC comprises of a FL YMC, FL gradient command controller and four independent FL gradient based wheel slip controllers. The top-level vehicle control flowchart for the FL-VSC system is shown in Figure 7.1 and is explained as follows:

1) The vehicle's instantaneous longitudinal velocity V_x, lateral velocity V_y, front wheel steer angle δ and the yaw rate r are all exported from the CarSim vehicle model and imported into MATLAB/Simulink (see Section 3.2.4.1 for further CarSim details).

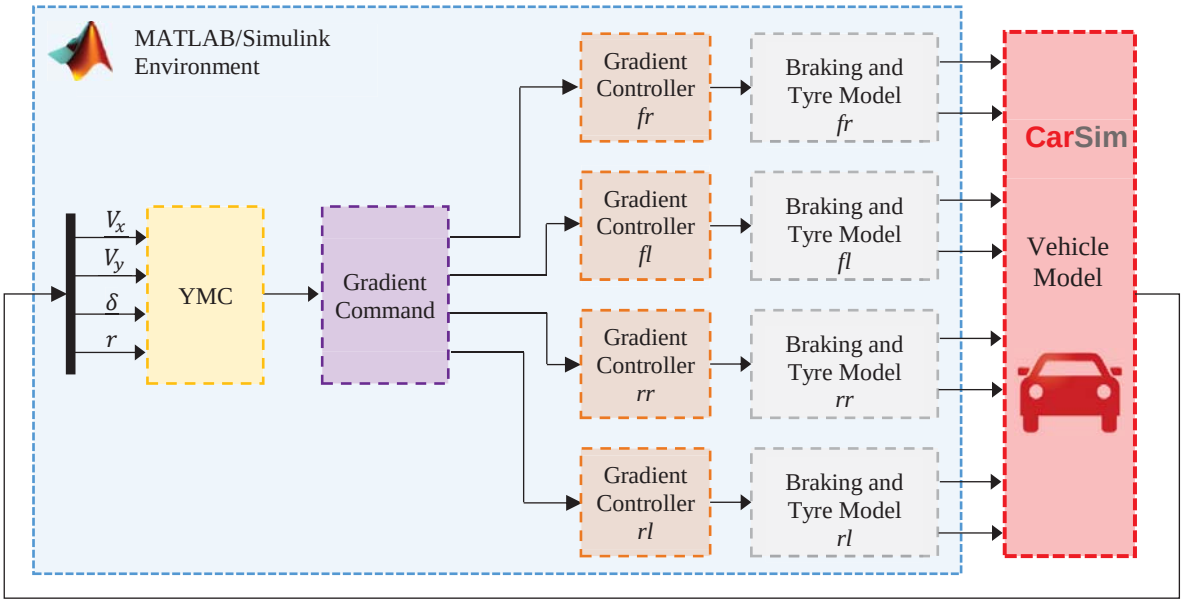

Figure 7.1 Top level FL-VSC control flow architecture

2) The FL YMC subsystem in Figure 7.2 (explained in Section 7.2.1) generates an ideal additional yaw moment M_Z which if applied directly to the vehicle's yaw axis would reduce the yaw rate error and the sideslip angle.

3) A FL gradient command controller (Section 7.2.2) uses the additional yaw moment M_Z to calculate appropriate target operating gradients G^* and assigns them to the independent wheel slip controllers. If G^* is positive, then G^* becomes the new target operating gradient

for both the front right (*fr*) and rear right (*rr*) wheels. If $G^*$is negative, then its magnitude becomes the new target gradient for the front left (*fl*) and rear left (*rl*) wheels.

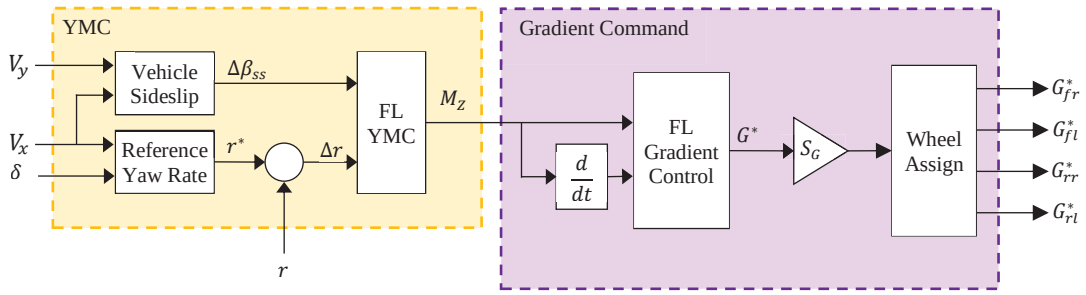

Figure 7.2 YMC and Gradient Command control flowcharts

4) The new target operating gradient is sent to the FL gradient based wheel slip controllers in Figure 7.3 (explained in Section 7.2.3). These controllers calculate appropriate brake torques that would enable the wheels to operate around the target operating gradients.

5) The target brake torque goes to the braking and tyre system in Figure 7.3 (Section 3.2.4.2). The traction motors are modelled using the simplified models described in Section 3.2.5.1. This subsystem calculates the respective tractive and lateral tyre forces for each wheel to export to the CarSim vehicle model.

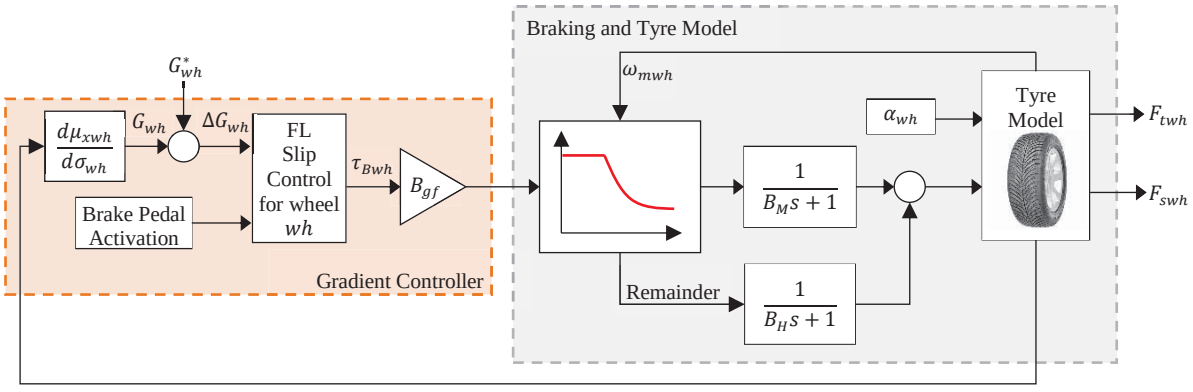

Figure 7.3 Gradient Controller with the Braking and Tyre Model control flowchart

7.2 Fuzzy Logic Controllers for the FL-VSC

The FL membership functions and rules in this investigation use the linguistic terms; Negative Large (NL), Negative Medium (NM), Negative Small (NS), Zero (Z), Positive Small (PS), Positive Medium (PM) and Positive Large (PL).

7.2.1 Fuzzy Logic YMC

The FL YMC developed by Boada [234, 235] uses the yaw rate error Δr (89) and vehicle sideslip error $\Delta\beta_{ss}$ (90) as inputs. The membership functions for this controller are shown in Figure 7.4 and the rule base in Table 7.1.

The target yaw rate r^* is dependent on the vehicle's longitudinal velocity V_x, front wheel steer angle δ, wheelbase L and a stability factor A. The stability factor A allows for the steering responsiveness of the vehicle to be tuned to meet the vehicle's target dynamic objectives. The vehicle's sideslip error β_{ss} is the angle made between the velocity vectors V_x and the lateral velocity V_y. The target value for β_{ss} remains zero for all driving scenarios in this investigation. The FL YMC controller outputs an ideal yaw moment M_Z.

$$\Delta r = r^* - r = \frac{V_x}{L\left(1 + A{V_x}^2\right)}\delta - r \tag{89}$$

$$\Delta\beta_{ss} = \tan^{-1}\frac{V_y}{V_x} \tag{90}$$

The input-output ranges for this controller are used because they offer stable and accurate control of the vehicle throughout the various braking manoeuvres. The output range is a unit value, this is scaled to achieve to the desired sensitivity of the FL YMC system.

Table 7.1 FL YMC rule base [234, 235]

		$\Delta\beta_{ss}$				
		NL	**NS**	**Z**	**PS**	**PL**
	NL	PL	PL	PM	PL	PL
	NS	PL	PM	PS	PM	PL
Δr	**Z**	NS	NS	Z	PS	PS
	PS	NM	NM	NS	NM	NM
	PL	NL	NL	NM	NL	NL

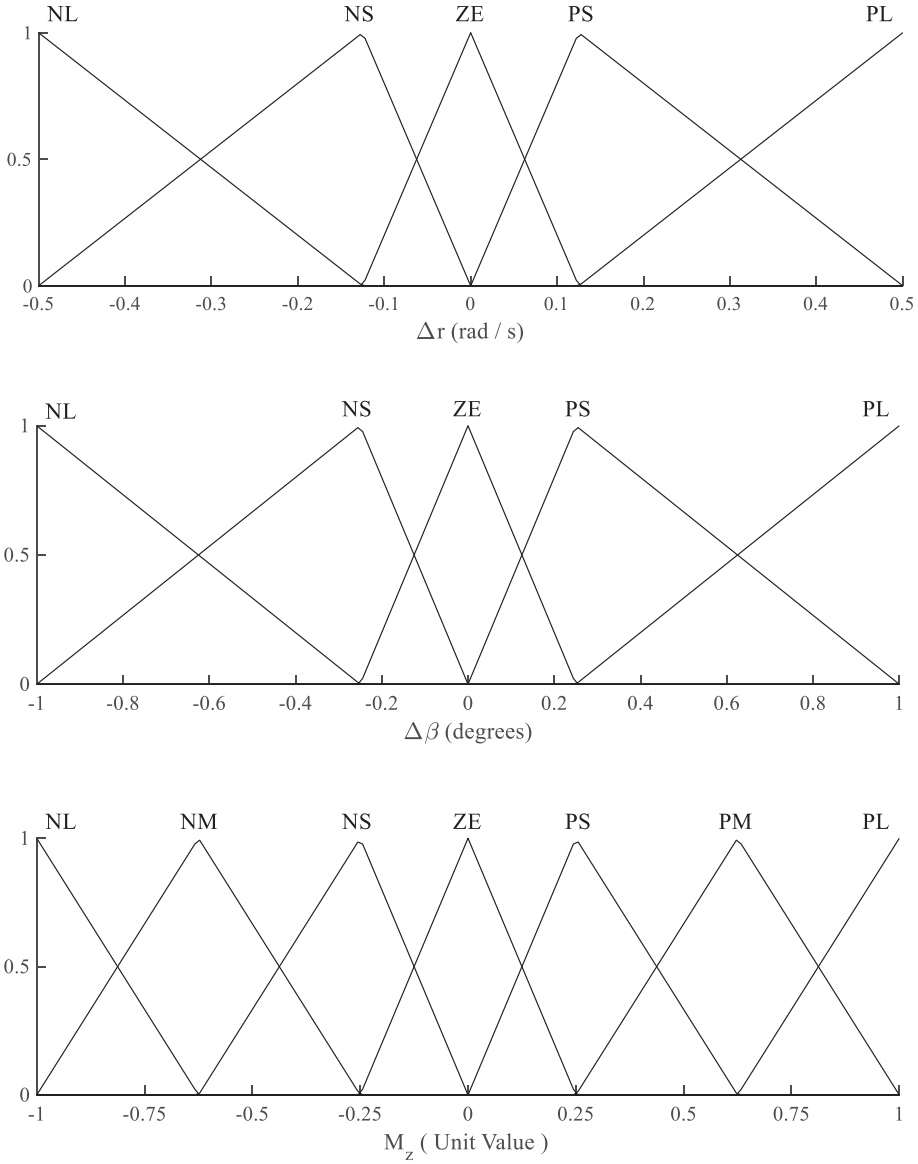

Figure 7.4 FL YMC membership functions [239, 240], **(a)** Input 1 - Δr, **(b)** Input 2 - $\Delta\beta_{ss}$, **(c)** Output - M_Z

Some examples of the rules for the FL YMC in Table 7.1 are explained as follows:

- If $\Delta \boldsymbol{r}$ is (Z) and $\Delta \boldsymbol{\beta_{ss}}$ is (Z) then $\boldsymbol{M_Z}$ is (Z). If there is no yaw rate error and the sideslip angle is zero, then the vehicle is following a target trajectory, no additional yaw moment is required.
- If $\Delta \boldsymbol{r}$ is (PL) and $\Delta \boldsymbol{\beta_{ss}}$ is (PL) then $\boldsymbol{M_Z}$ is (NL). If the vehicle's yaw rate error and the sideslip angle is positive large, then a large negative additional yaw moment is required to reduce these understeering characteristics.
- If $\Delta \boldsymbol{r}$ is (NL) and $\Delta \boldsymbol{\beta_{ss}}$ is (Z) then $\boldsymbol{M_Z}$ is (NM). If the vehicle's yaw rate error is positive large and the sideslip angle is zero, then an additional medium negative yaw moment is required. This is giving priority to the tracking ability of the yaw rate error over the sideslip angle.

7.2.2 Fuzzy Logic Gradient Command Controller

A FL gradient command controller is used to assign the target operating gradient G^* to the individual wheels ${G_{wh}}^*$ $(wh = fl,\ fr,\ rl,\ rr)$. This controller uses the membership functions in Figure 7.5 and the rule base in Table 7.2. This FLC uses the additional yaw moment calculated by the FL YMC in Section 7.2.1 and its time derivative as the two inputs to generate G^*.

The input and output ranges for this controller are of unit value, the yaw moment input M_Z is scaled according to the target yaw performance of the vehicle under control. The output target gradient is also scaled by a factor of S_G. As S_G increases, the wheel's target operating gradient gets closer to the free-rolling condition $\sigma = 0$. To compromise between steering control and braking force a gradient scale of 6 was used in this investigation.

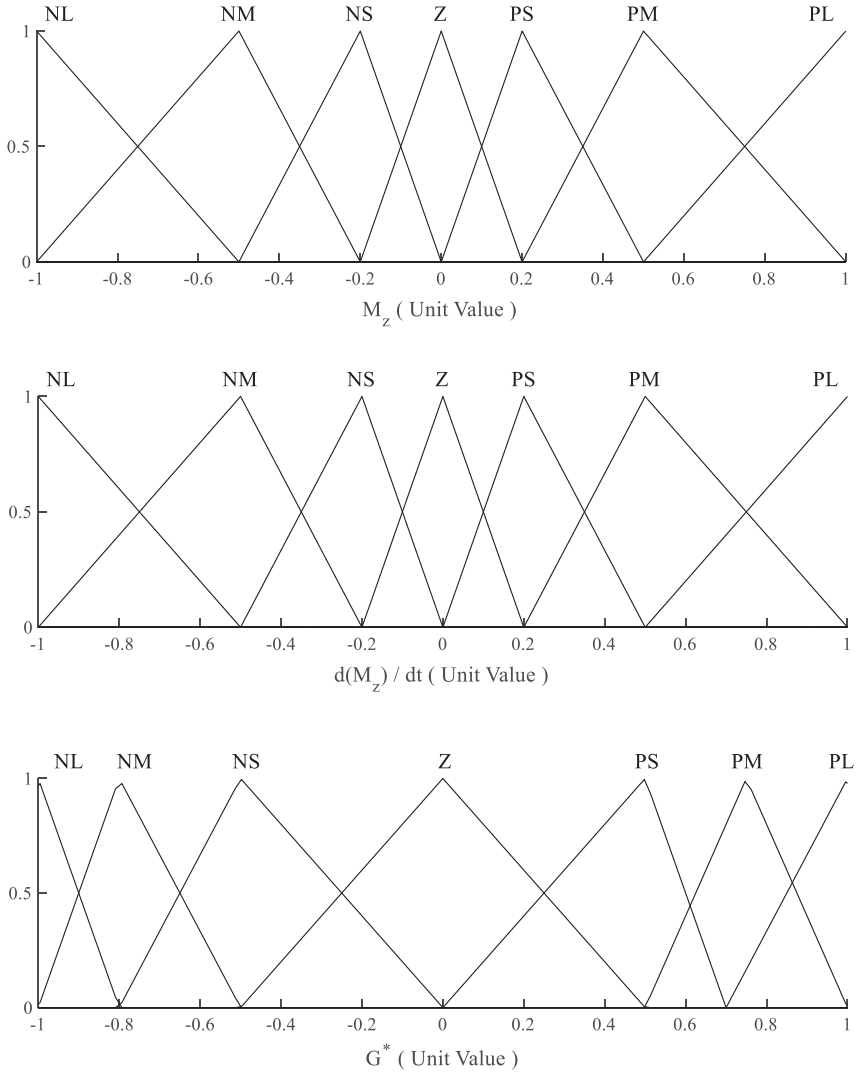

Figure 7.5 FL Gradient control, **(a)** Input 1 - M_Z, **(b)** Input 2 - $\frac{\boldsymbol{d(M_Z)}}{\boldsymbol{dt}}$, **(c)** Output - G^*

Some examples of the rules for the FL gradient command controller in Table 7.2 are explained as follows:

- If $\boldsymbol{M_Z}$ is (Z) and $\frac{\boldsymbol{dM_Z}}{\boldsymbol{dt}}$ is (Z) then $\boldsymbol{G}^*$ is (Z). If no additional yaw moment is required and this value has not changed since the last time step, then the controller outputs a command gradient of zero. This is applied to the four wheel slip controllers.
- If $\boldsymbol{M_Z}$ is (PL) and $\frac{\boldsymbol{dM_Z}}{\boldsymbol{dt}}$ is (Z) then $\boldsymbol{G}^*$ is (NL). The command additional yaw moment is positive large and has not changed since the last time step, the controller outputs a large

negative gradient. The magnitude of this gradient is applied to the wheels on the left of the vehicle.

- If $\boldsymbol{M_Z}$ is (NS) and $\frac{\boldsymbol{dM_Z}}{\boldsymbol{dt}}$ is (PM) then $\boldsymbol{G}^*$ is (NS). Even though the command yaw moment is negative, the rate of change is positive and larger in magnitude. The controller sends a small negative gradient to be used in the wheels on the left of the vehicle.

Table 7.2 FL Gradient controller rule base

		$\boldsymbol{M_Z}$						
		NL	**NM**	**NS**	**Z**	**PS**	**PM**	**PL**
$\frac{\boldsymbol{dM_Z}}{\boldsymbol{dt}}$	**NL**	PL	PL	PL	PL	PM	PS	Z
	NM	PL	PL	PL	PM	PS	Z	NS
	NS	PL	PL	PM	PS	Z	NS	NM
	Z	PL	PM	PS	Z	NS	NM	NL
	PS	PM	PS	Z	NS	NM	NL	NL
	PM	PS	Z	NS	NM	NL	NL	NL
	PL	Z	NS	NM	NL	NL	NL	NL

7.2.3 Fuzzy Logic Wheel Slip Controller

The gradient based FL TCS by Colli [256, 257] is modified for use during braking scenarios. The membership functions for this controller are shown in Figure 7.6 and the rule base in Table 7.3. The brake pedal activation level $\gamma_{brk} \in [0\ 1]$ and the error in operating gradient ΔG_{wh} (91) are used as the two inputs. The controller calculates an ideal brake torque τ_{Bwh} which would reduce the operating gradient error. This brake torque must be generated by the Electrohydraulic Braking (EHB) system.

$$\Delta G_{wh} = {G_{wh}}^* - \frac{d\mu_{Xwh}}{d\sigma_{wh}} \tag{91}$$

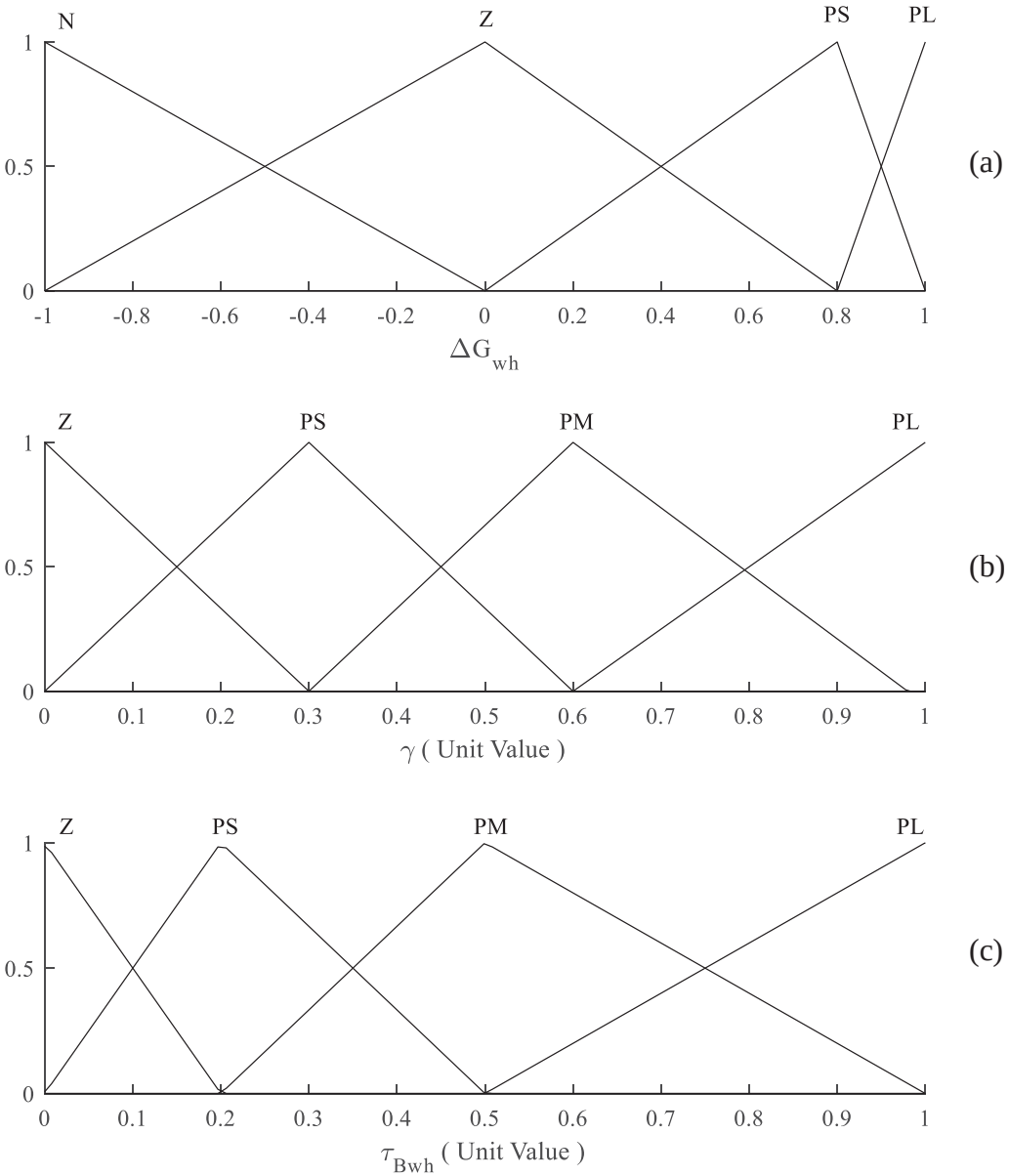

Figure 7.6 Gradient based wheel slip controller membership functions, **(a)** Input 1 – ΔG_{wh} **(b)** Input 2 – γ, **(c)** Output – τ_{Bwh}

The input range for the gradient error offers stable and acceptable control of the wheel operating gradient throughout all the braking manoeuvres. Both the brake pedal input activation level and output brake torque are unit values. The output brake torque is scaled with respect to the maximum brake torque allowed by the vehicle's braking system B_{gf}.

Some examples of the rules in Table 7.3 are explained as follows:

- If $\Delta \boldsymbol{G_{wh}}$ is (Z) and $\boldsymbol{\gamma_{brk}}$ is (Z) then $\boldsymbol{\tau_{Bwh}}$ is (Z). If the operating gradient error is zero and the driver has no intent on decelerating the vehicle, no brake torque is supplied to the wheels.
- If $\Delta \boldsymbol{G_{wh}}$ is (PL) and $\boldsymbol{\gamma_{brk}}$ is (PL) then $\boldsymbol{\tau_{Bwh}}$ is (PL). If the gradient error is positive and large, then the wheel is much closer to the free rolling condition of the wheel and far from the target operating point. Because the brake pedal is also large, the driver aims to decelerate the vehicle quickly. A large brake torque is required to decelerate the wheel and reduce the operating gradient error.

Table 7.3 Gradient based wheel slip controller rule base

		$\Delta \boldsymbol{G_{wh}}$			
		N	**Z**	**PS**	**PL**
$\boldsymbol{\gamma_{brk}}$	**Z**	Z	Z	Z	PS
	PS	Z	Z	PS	PM
	PM	Z	Z	PM	PM
	PL	Z	PS	PM	PL

The EHB system utilises the independent in-wheel traction motor's regenerative brake torque and the vehicle's hydraulic braking system to generate τ_B. The traction motors and hydraulic braking systems are modelled using first order filters with time constants B_M and B_H respectively [245]. The traction motor's time constant is lower than the hydraulic system because they are able to modulate the brake torque at a much higher frequency. These time constants offer a good representation of the brake torque responsiveness of a typical EHB system. If the command τ_{Bwh} from the FL wheel slip controller is larger than the brake torque of the traction motor for a given motor speed ω_{mwh}, then the excess brake torque is

compensated by the hydraulic braking system [329]. The control flowchart for the EHB system is shown in Figure 7.3.

7.3 FL-VSC Performance Evaluation

7.3.1 Simulation Setup and Evaluation Criteria

A vehicle containing the new FL-VSC system is compared against identical vehicles using other VSC systems during numerous different braking maneuvers. A vehicle using $G^* = 0$ on all four wheels is labelled Z-GR (Zero-Gradient) and one which uses a Conventional-ABS is labelled C-ABS. The C-ABS vehicle applies full brake torque when the wheel slip is 0.09 or lower and releases the brake torque at a wheel slip of 0.15. To show how the controllers are affected by hardware limitations and compiler errors, a series of PIL simulations are conducted alongside the main investigation. Since only one controller can operate in PIL mode at a single time, multiple PIL simulations are required for each braking scenario. Simulations where the gradient command controller is implemented in hardware are labelled FL-VSC-GR. Simulations where the front right and real left wheel slip controllers are implemented in hardware are labeled FL-VSC-FR and FL-VSC-RL respectively. During these PIL, the remaining controllers in the FL-VSC system operate in software in MIL mode.

All three vehicles use identical vehicle parameters in Table 7.4. The vehicle model uses four independent 35 kW traction motors with torque-speed characteristics given in Table 7.4. The traction motors are simulated using 2D lookup tables as described in Section 3.2.5.1.

Table 7.4 Vehicle parameters for CarSim vehicle model [234, 235]

Symbol	Value	Symbol	Value
M_{Veh}	1412 kg	k_{1r}	30 kN/m
m_s	1270 kg	k_{2f}	240 kN/m
m_{uf}	36 kg	k_{2r}	240 kN/m
m_{ur}	36 kg	c_{1f}	0.96 kNs/m
T_f	1.675 m	c_{1r}	0.8 kNs/m
T_r	1.675 m	c_{2f}	5 kNs/m
L	2.91 m	c_{2r}	5 kNs/m
a	1.01 m	K_{af}	6.7 kNm/rad
b	1.9 m	K_{ar}	6.7 kNm/rad
h_{COG}	0.54 m	K_{φ}	6.6 kNm/rad
e_s	0.45 m	C_{φ}	3.5 kNs/rad/s
I_{yaw}	1536 kg.m^2	N_{fd}	8
I_{pitch}	1540 kg.m^2	P_m	35 kW
I_{roll}	490 kg.m^2	ω_B	1675 rpm
A	0.01	ω_{MAX}	6000 rpm
I_{wh}	2 kg.m^2	B_M	0.01
R	0.3 m	B_H	0.05
k_{1f}	27 kN/m		

7.3.2 Scenario 1 – Straight Line Braking

The first braking scenario simulates a straight-line braking manoeuvre from 120 km/h on a surface with peak COF $\mu = 1$. The brake pedal is applied at time $t_1 = 1s$ ($\gamma_{brk} = 1$). Figure 7.7 shows the braking force on all four wheels for the three vehicles. Figure 7.8(a)-(b) shows the longitudinal velocity and the total distance travelled X_g for the three vehicles respectively.

The Z-GR and FL-VSC vehicles operate identically to one another. Because the vehicle travels in a straight line on an even COF surface, no steering intervention or YMC is required. The target operating gradient for all the wheels of FL-VSC vehicle is zero. All four wheels generate maximum braking force and are balanced on either side of the vehicle. Table 7.5 shows that the Z-GR and FL-VSC vehicles are able to reduce the stopping distance by 10% and braking time by 11% down from the C-ABS vehicle.

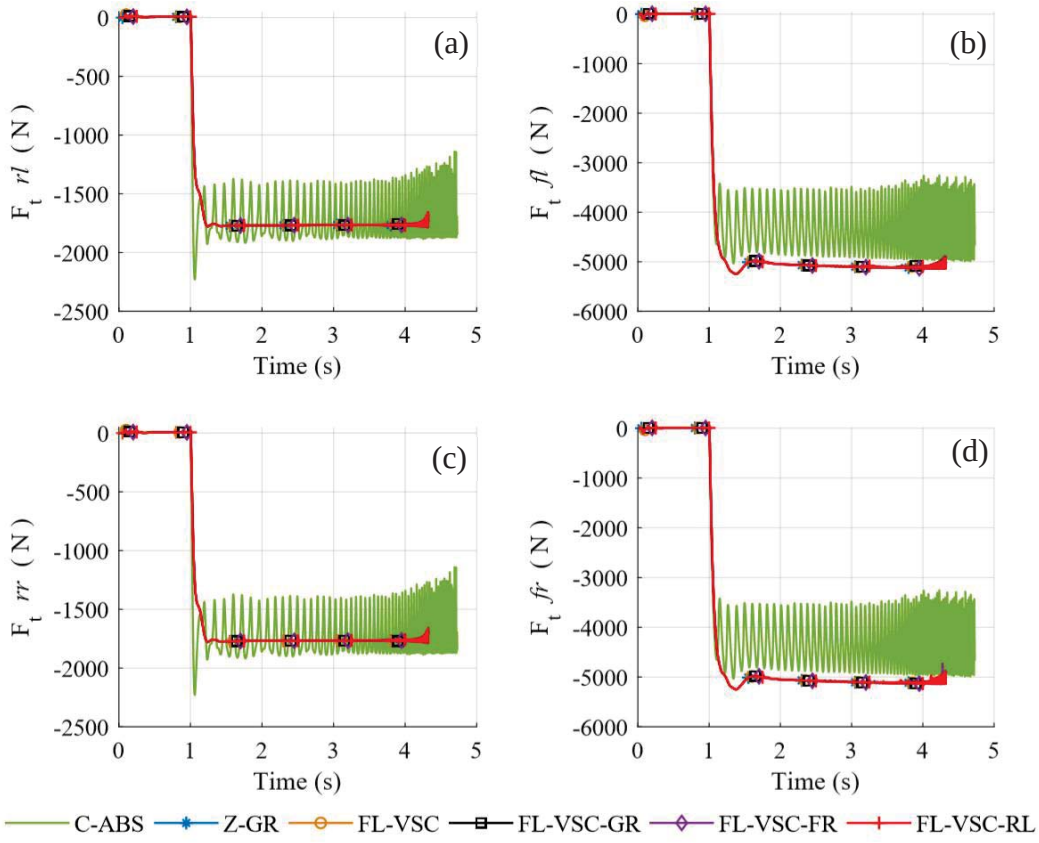

Figure 7.7 Longitudinal braking forces for scenario 1, **(a)** *rl*, **(b)** *fl*, **(c)** *rr*, **(d)** *fr*

The PIL simulations in Figure 7.7-Figure 7.8 produce numerically identical control signals to their simulated MIL counterparts, this shows that the controllers have been unaffected by the code compiler and the FL-VSC system is ready for HIL experimentation in a straight-line braking scenarios. In addition, the braking forces in Figure 7.7 for the C-ABS vehicle pulsate at a much higher frequency and magnitude than the other two vehicles, this may induce a panic release response from drivers who do not know that the juddering pedal feedback is from the ABS activating.

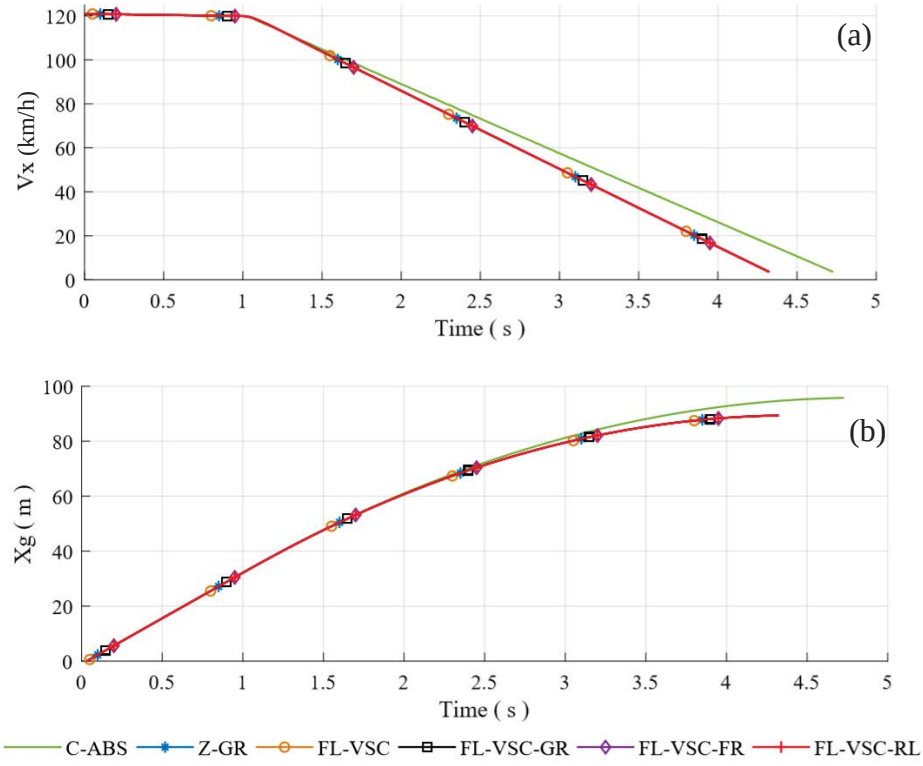

Figure 7.8 Vehicle dynamics for scenario 1, **(a)** V_x, **(b)** X_g

Table 7.5 Performance Indices comparison for braking scenario 1. Units in brackets represent percentage change from the C-ABS vehicle.

Index	C-ABS	Z-GR	FL-VSC
t_{bk}	3.73	3.32 **(-10.99%)**	3.32 **(-10.99%)**
X_{bk}	63.6	57.2 **(-10.06%)**	57.2 **(-10.06%)**

The animation screenshots from CarSim for this braking scenario are shown in Figure 7.9 and offers a representation of how the braking distances are reduced in proportion to the vehilce's scale. The Z-GR (Blue vehicle) and FL-VSC (Red Vehicle) vehicles come to a complete stop ~1.5 car lengths shorter than the C-ABS (Green Vehcile) .

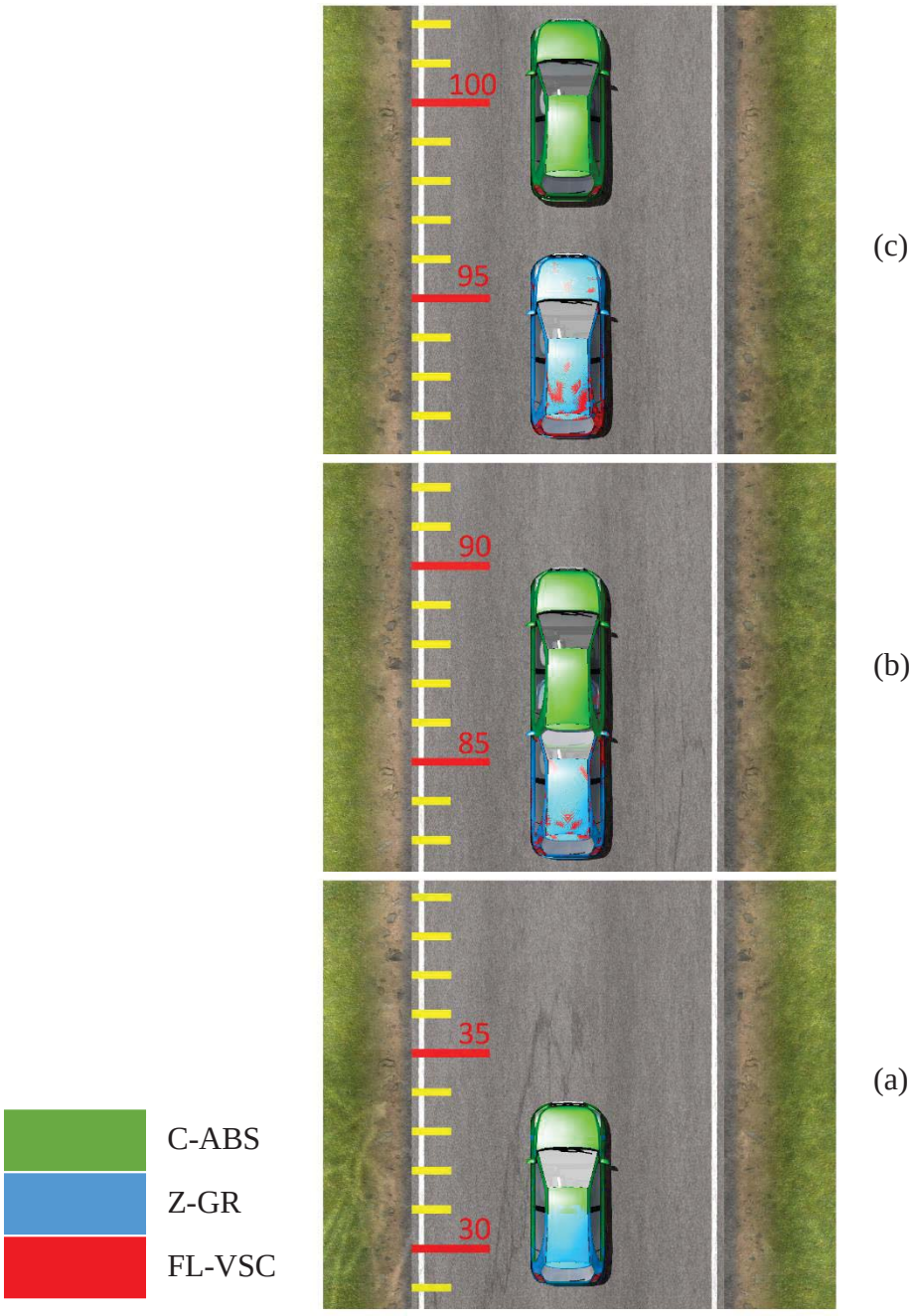

Figure 7.9 Animation preview for the accident avoidance braking manoeuvre scenario 4, **(a)** $t = 1\ s$ (start), **(b)** $t = 3.5\ s$, **(c)** $t = 4.7\ s$ final resting position

7.3.3 Scenario 2 – Split μ Braking

The vehicle initially travelling at 120 km/h fully activates the brake pedal at time $t_1 = 1s$ ($\gamma_{brk} = 1$) on a split μ surface. The roads peak COF is 0.5 and 1 on the left and right hand side of the vehicle respectively. Ideally, the FL-VSC system would enable the FL-VSC vehicle to travel straight with no yaw and minimal driving steering intervention.

The individual wheel gradient control in Figure 7.10 shows that the FL wheel slip controllers are able to control the wheel slip around positive operating gradients. The wheels on the right of the vehicle in Figure 7.10(c)-(d) have a positive operating gradient where wheels on the left in Figure 7.10(a)-(b) have a zero target operating gradient. The FL and RL wheels are thus operating at the maximum brake force available to them on their respective surface (the low COF surface).

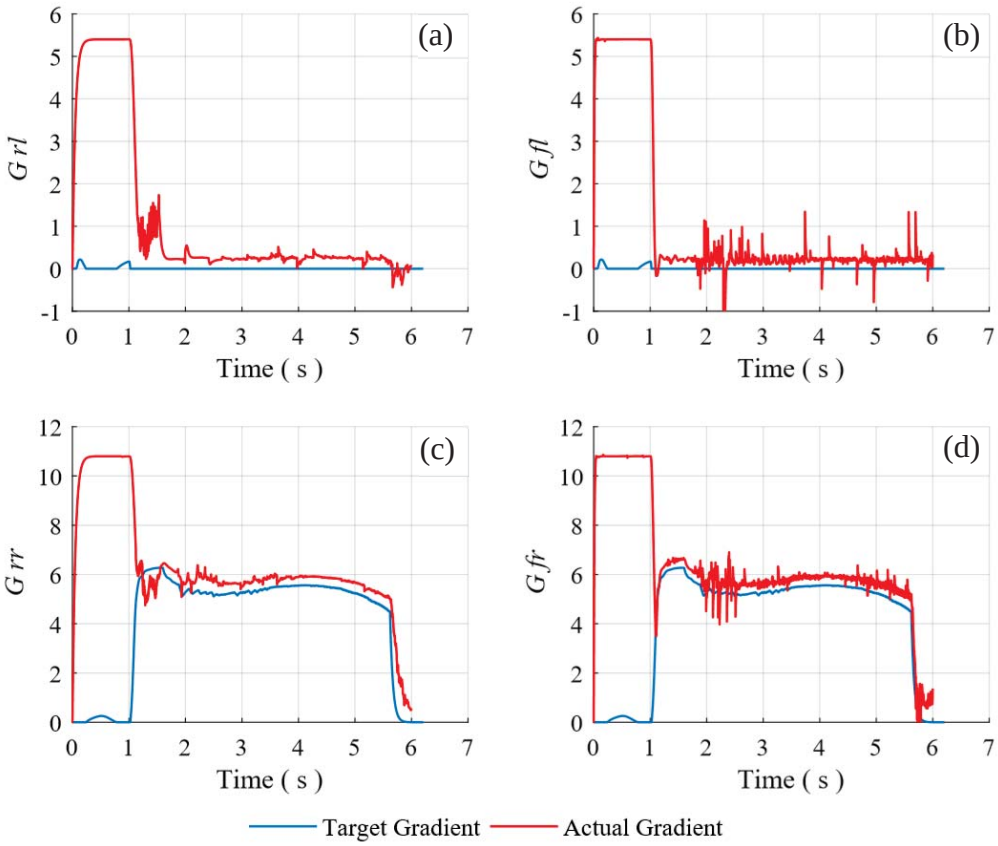

Figure 7.10 Independent gradient control for the FL-VSC vehicle during braking scenario 2, **(a)** *rl*, **(b)** *fl*, **(c)** *rr*, **(d)** *fr*

Although the *fr* and *rr* wheels on the high COF surface are able to generate higher brake forces, the FL-VSC reduces the operating wheel slip to produce a lower brake force and match the braking forces on the other side of the vehicle. This reduces the additional yaw moment generated from asymmetrical brake forces. Figure 7.11 shows that the Z-GR vehicle overall achieves higher brake forces than the FL-VSC vehicle because it attempts to operate around maximum brake for the duration of the braking manoeuvre.

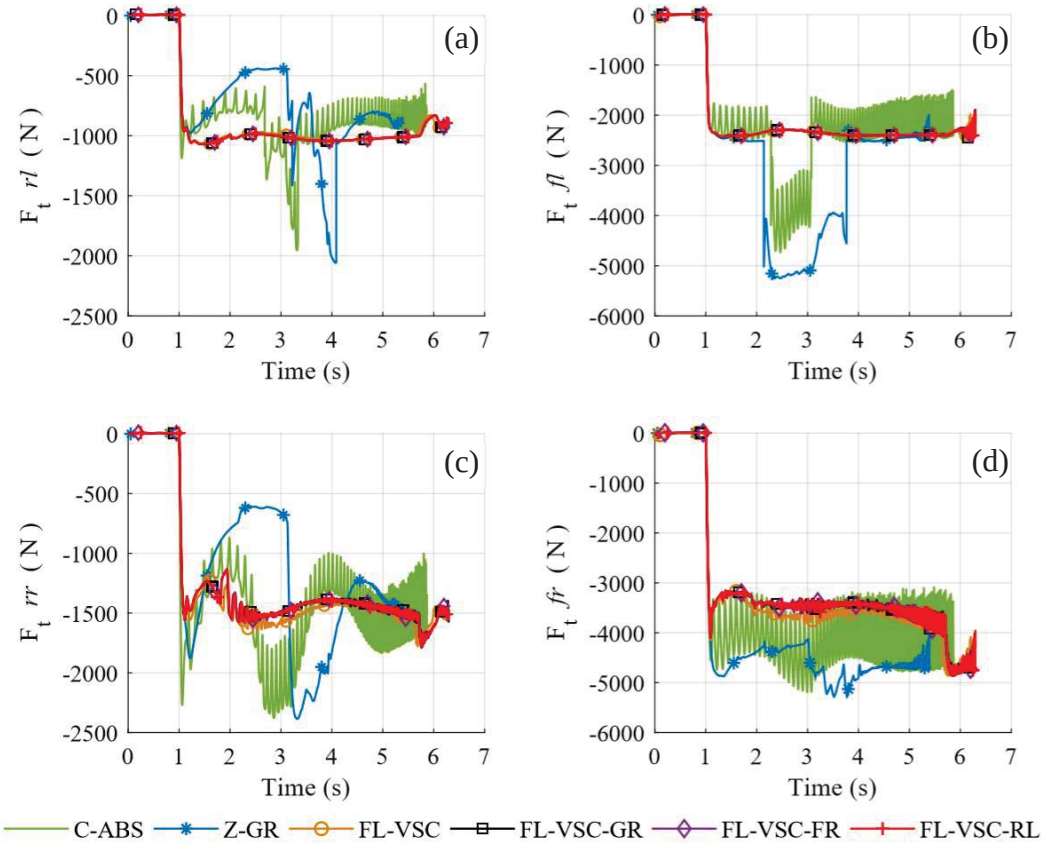

Figure 7.11 Longitudinal braking forces for scenario 2, **(a)** *rl*, **(b)** *fl*, **(c)** *rr*, **(d)** *fr*

The vehicle dynamics in Figure 7.12 and the performance indices in Table 7.6 show that the X_{bk} and t_{bk} are 6.7% and 9.8 % higher respectively for the FL-VSC vehicle over the C-ABS vehicle. However, the IYRE, ISSE and ISC indices are 43%, 53% and 39% lower

respectively. The performance index J for the FL-VSC vehicle is 36% lower over the C-ABS vehicle. These indices show that the additional braking distance of the FL-VSC vehicle is justified because there is a greater trade-off for vehicle stability and controllability. The C-ABS and Z-GR vehicles both have a much higher sideslip angle and much more driver steering intervention as seen in Figure 7.12(c)-(d). The PIL simulations in Figure 7.11-Figure 7.12 show comparable control and stability after code compiling to their software counterparts.

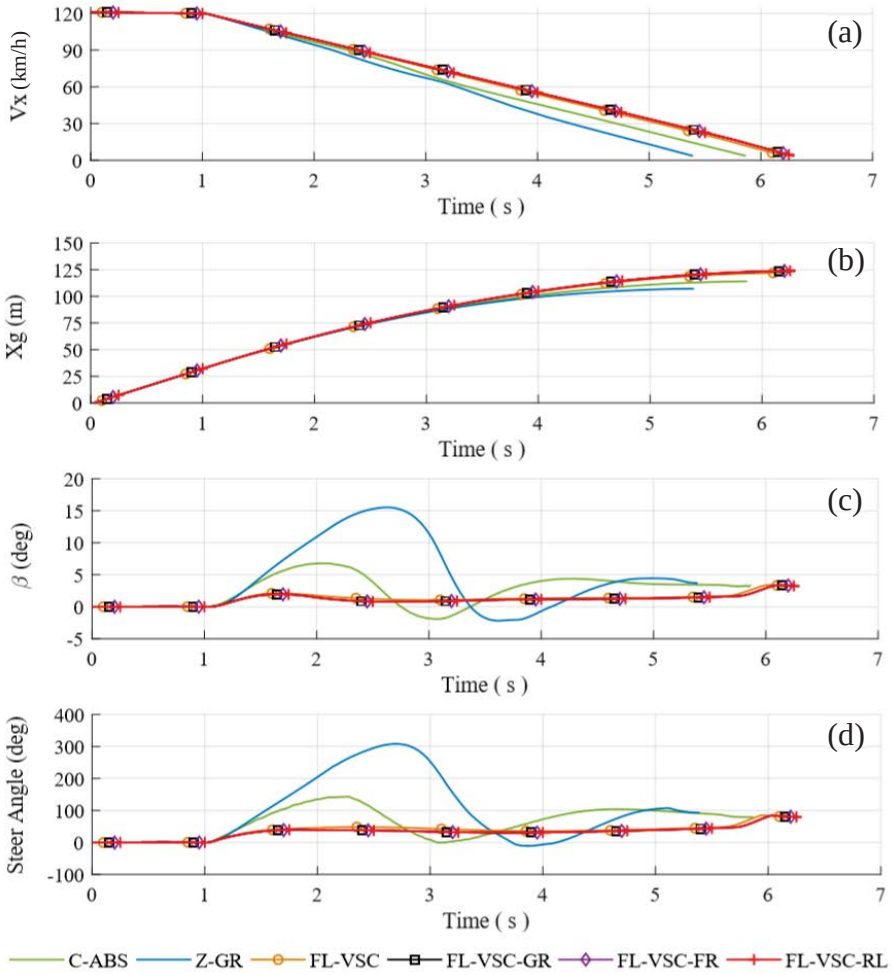

Figure 7.12 Vehicle Dynamics comparison for braking scenario 2, **(a)** V_x, **(b)** X_g, **(c)** β_{ss}, **(d)** Steering wheel angle

The animation screenshots from CarSim for this braking scenario are shown in Figure 7.13. The FL-VSC vehicle has a consistanly straight heading throughout the simulation. The FL-VSC vehicle comes to a complete stop $\sim 3-4$ car lengths more than the Z-GR vehicle, this might be perceived as having poor braking perfomance. However, it's unlikely that an average driver in the C-ABS or Z-GR vehicle is able to control the vehicle's heading, but instead more likely to spin out of control as shown by the ISC values in Table 7.6 and the steer angle in Figure 7.12(d). For the results shown, there was no limit to the steering wheel angle in this braking scenario. Previous simulations which included a steer limit of $\pm 100°$ - investigated during the development of this control system - showed the C-ABS vehicle and Z-GR vehicles spinning out of control during this braking scenario.

Table 7.6 Performance Indices comparison for braking scenario 2. Units in brackets represent percentage change from the C-ABS vehicle.

Index	C-ABS	Z-GR	FL-VSC
t_{bk}	4.87	4.39 **(-9.85%)**	5.20 **(6.77%)**
X_{bk}	81.90	75.05 **(-8.36%)**	89.97 **(9.85%)**
J	0.574	0.506 **(-11.84%)**	0.364 **(-36.6%)**
IYRE	0.89	1.33 **(49.4%)**	0.51 **(-42.7%)**
ISC	367.19	536.34 **(46.1%)**	224.2 **(-38.9%)**
ISSE	16.42	26.12 **(59.1%)**	7.76 **(-52.74%)**

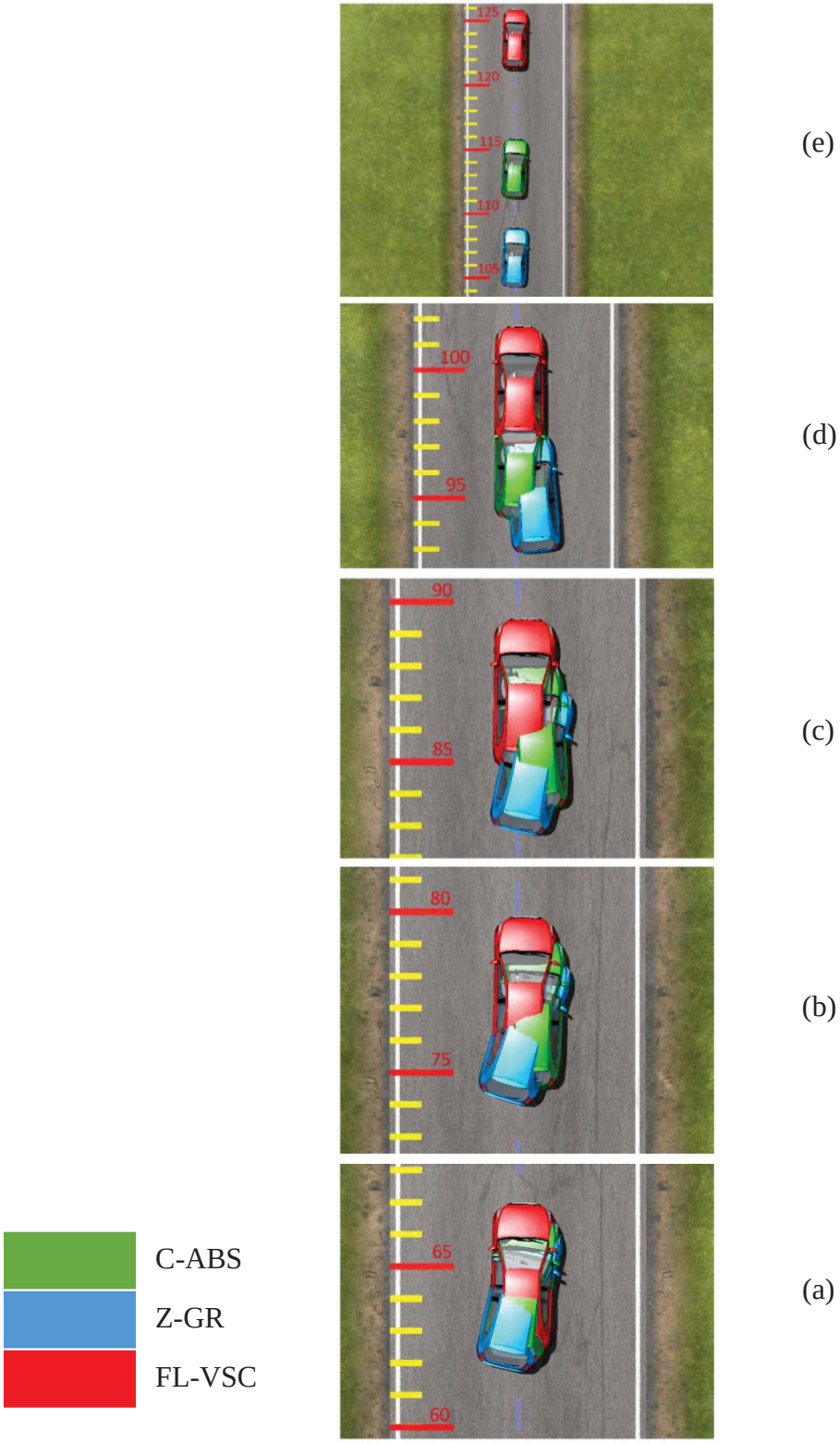

Figure 7.13 Animation preview for the accident avoidance braking manoeuvre scenario 2, **(a)** $t = 2\ s$ C-ABS greatest positive sideslip, **(b)** $t = 2.7\ s$ Z-GR greatest positive sideslip, **(c)** $t = 3\ s$ C-ABS greatest negative sideslip, **(d)** $t = 3.6\ s$ Z-GR greatest negative sideslip, **(e)** $t = 6.2\ s$ final resting position

7.3.4 Scenario 3 – Double Lane Change on a Low μ Surface

At time $t_1 = 1s$, the vehicle applies the brake pedal ($\gamma_{brk} = 1$) and begins following the target path of a Double Lane Change (DLC) manoeuvre. The vehicle has an initial velocity of 80 km/h and the test track has an average peak COF of 0.5 to replicate wet driving conditions. This scenario replicates a driver attempting to avoid a head-on collision by manoeuvring around an obstacle. It would be unlikely that the driver in this scenario would use extreme steering angles, therefore the steering wheel angle is limited to ±100°.

The gradient control for the four wheels in Figure 7.14 show that the FL gradient command controller is able to change the target operating gradient between the wheels on the left and right hand side of the vehicle during a braking manoeuvre. Figure 7.15 shows the corresponding brake forces generated by the four wheels.

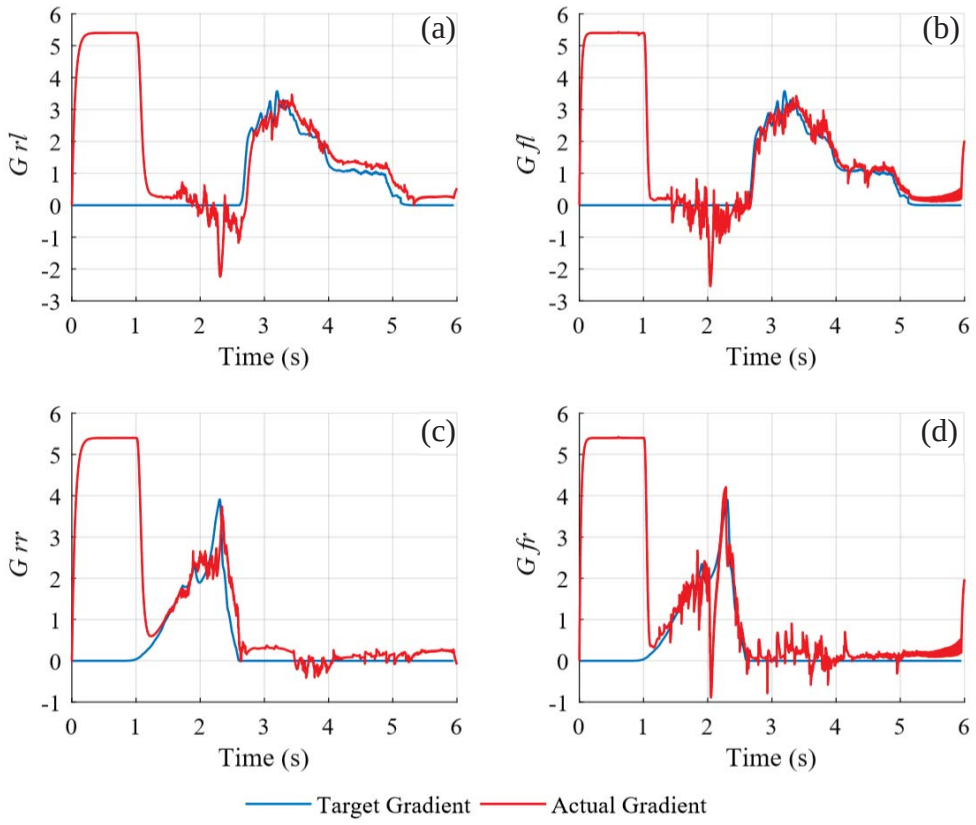

Figure 7.14 Independent wheel gradient control for FL-VSC vehicle during scenario 3, **(a)** *rl*, **(b)** *fl*, **(c)** *rr*, **(d)** *fr*

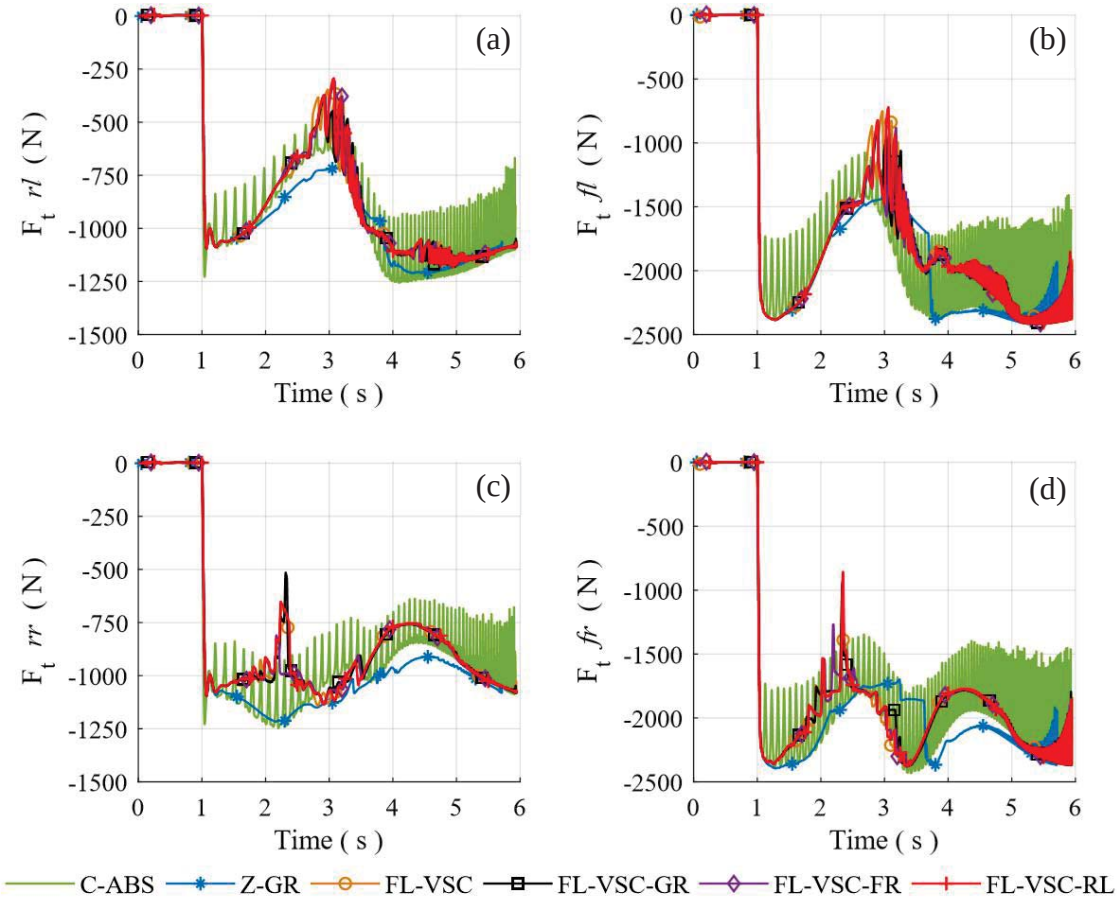

Figure 7.15 Longitudinal braking forces for scenario 3, **(a)** *rl*, **(b)** *fl*, **(c)** *rr*, **(d)** *fr*

The vehicle's yaw rate and sideslip angle for the three vehicles is given in Figure 7.17(a)-(b) respectively, it shows that the FL-VSC vehicle follows its respective target yaw rate (dotted line) closer than the C-ABS or Z-GR vehicles. It must be noted that Z-GR has the lowest sideslip angle over the entire manoeuvre, but this is a by-product from its poor yaw rate control. Figure 7.16(a)-(c) shows the global co-ordinates, steering wheel input and longitudinal velocity respectively for all three vehicles. The global co-ordinates in Figure 7.16(a) show that the FL-VSC vehicle follows the target path closer than C-ABS or the Z-GR vehicle.

Table 7.7 shows that X_{bk} and t_{bk} are similar for all three vehicles with the Z-GR vehicle having the lowest braking distance. However, the way these values are achieved are different for each vehicle system. The IYRE and ISSE for the FL-VSC vehicle are 48% and 22% lower

respectively over the C-ABS vehicle, this is achieved with 7% less steering intervention. The advantage of the FL-VSC vehicle in this scenario being that not only does it follow the DLC test track with the greatest accuracy, stability and controllability, but it also requires the least amount of steering control to do so.

Table 7.7 Performance indices comparison for braking scenario 3. Units in brackets represent percentage change from the C-ABS vehicle.

Index	C-ABS	Z-GR	FL-VSC
t_{bk}	4.931	4.716 **(-4.36%)**	4.852 **(-1.6%)**
X_{bk}	56.97	54.75 **(-3.89%)**	56.44 **(-0.93%)**
Y_{max}	4.08	3.72 **(-8.82%)**	3.67 **(-10.05%)**
J	0.087	0.07 **(-12.5%)**	0.017 **(-85%)**
IYRE	0.151	0.31 **(105.3%)**	0.078 **(-48.3%)**
ISC	299.8	284.4 **(-5.1%)**	278.1 **(-7.2%)**
ISSE	8.46	7.27 **(-14.1%)**	6.54 **(-22.7%)**

The FL-VSC vehicle has a better trade-off between braking and steering control by reducing the J index by 85%. In addition, the FL-VSC vehicle also reduces the peak global Y-coordinates (Y_{max}) by 10% which shows the FL-VSC vehicle's ability to regain control after the initial steering input and doesn't overshoot the target path. This might avoid collision with a barrier or another obsticle outside of the target trajectory.

The high IYRE for the Z-GR in Table 7.7 shows poor yaw rate control. Although the ISC for the Z-GR and FL-VSC vehicles are similar, examination of Figure 7.16(b) shows that the

FL-VSC vehicle responds quicker to the steering input and begins applying a counter steering angle sooner than the Z-GR vehicle. The shorter braking distance of the Z-GR vehicle is a by-product of poor steering controllabilty which cannot be relied on for every braking scenario.

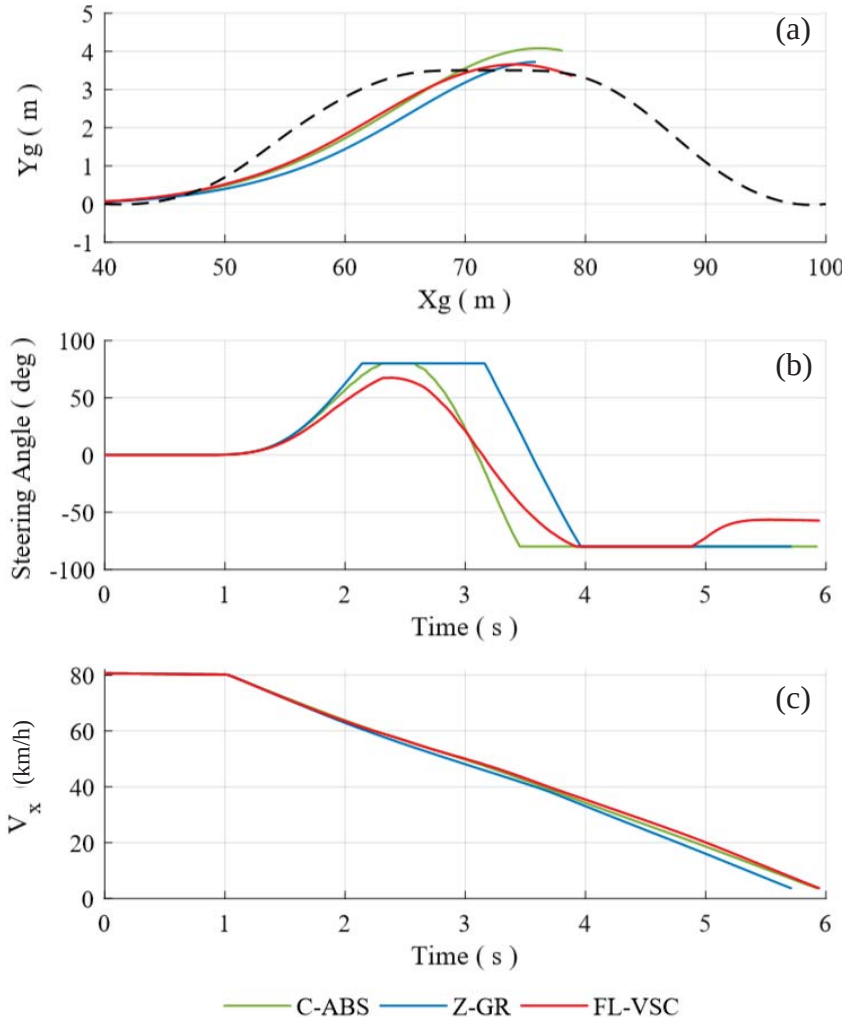

Figure 7.16 Vehicle dynamics comparison for braking scenario 3, **(a)** Global co-ordinates, **(b)** Steering wheel angle, **(c)** V_x

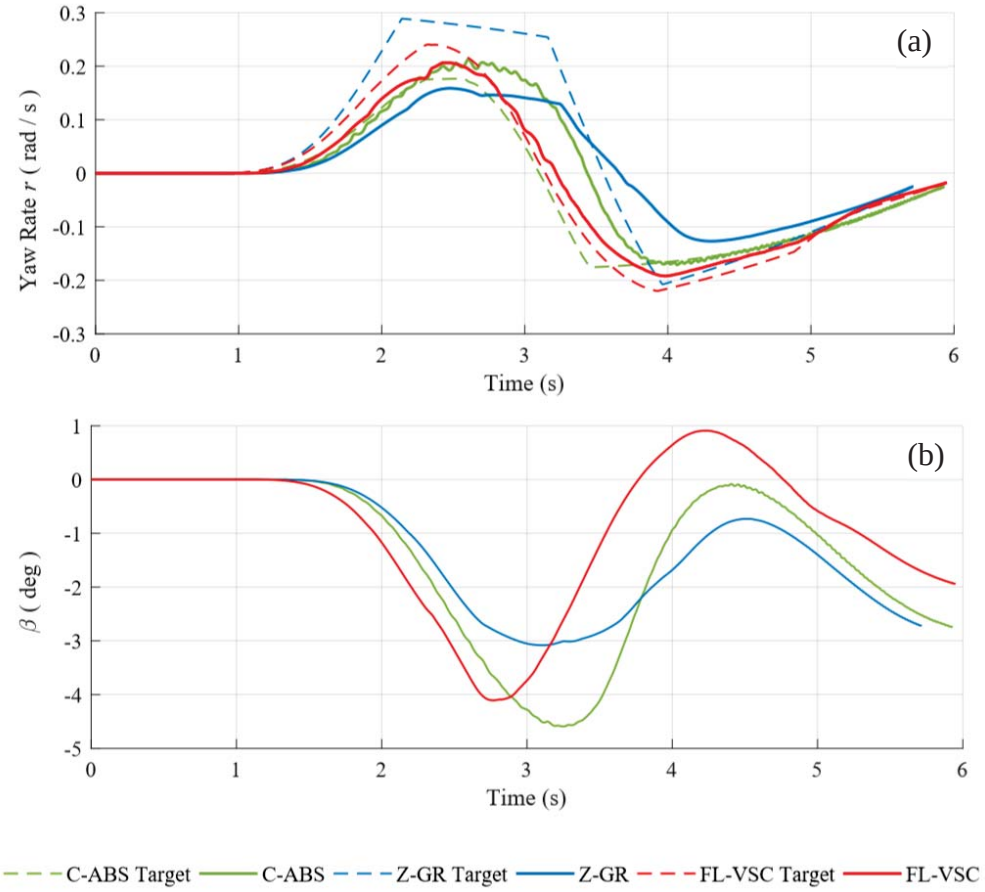

Figure 7.17 Vehicle yaw and stability control variables for braking scenario 3, **(a)** r, **(b)** β_{ss}

The animation screenshots from CarSim for this braking scenario are shown in Figure 7.18. It appears that all three vehicles follow similar global trajectories with the Z-GR vehicle having the shortest braking distance. However, a major part of this braking scenario is the manoeuvre around an obstacle and the vehicles responsiveness to steering control.

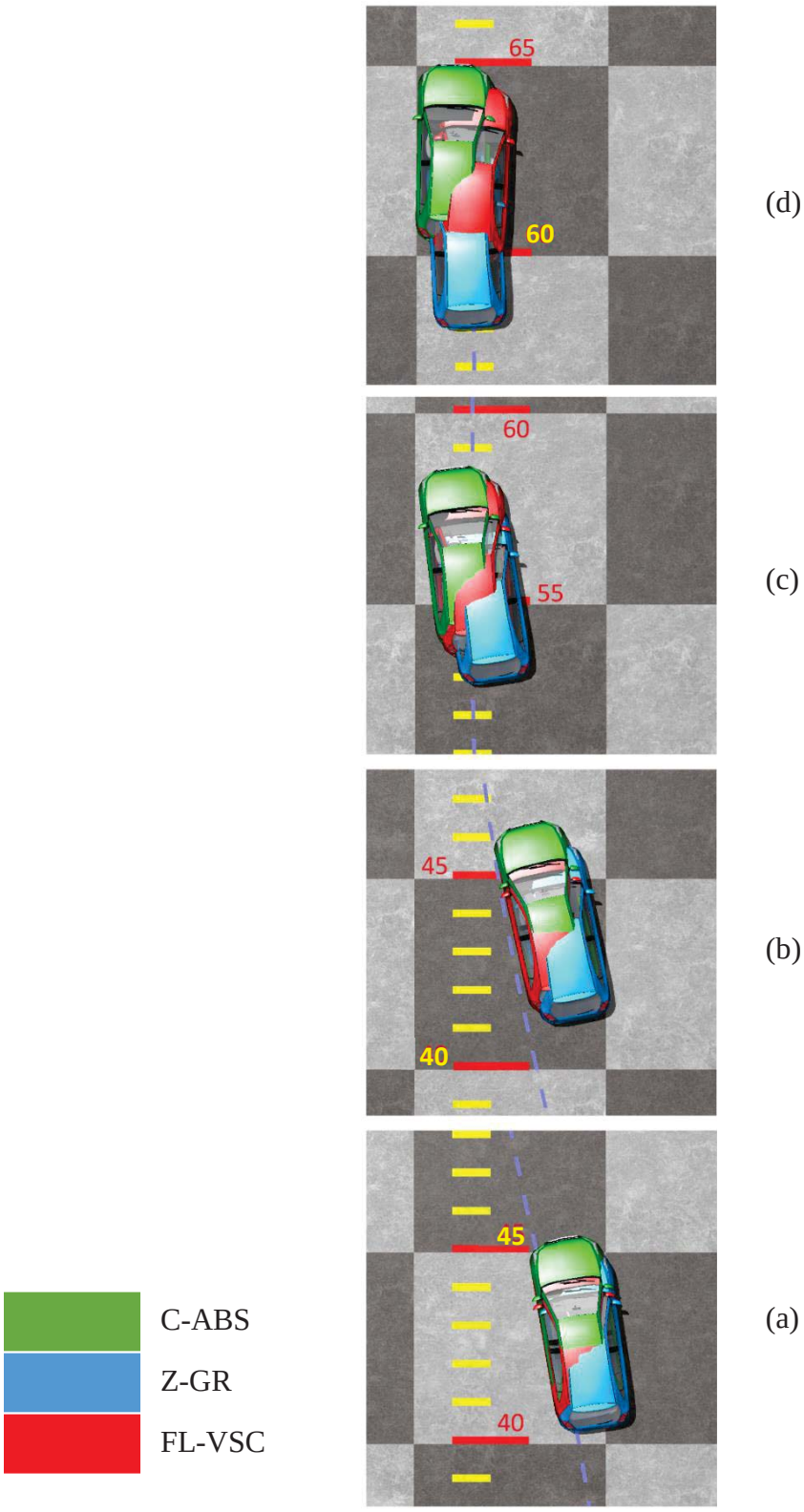

Figure 7.18 Animation preview for the accident avoidance braking manoeuvre scenario 3, **(a)** $t = 2.7\ s$ FL-VSC greatest negative sideslip, **(b)** $t = 3.2\ s$ C-ABS greatest negative sideslip, **(c)** $t = 4.3\ s$ C-ABS and FL-VSC greatest corrective sideslip, **(d)** $t = 5.9\ s$ final resting position

7.3.5 Scenario 4 – Distracted Driver Accident Avoidance

The final braking scenario is an accident avoidance manoeuvre where the driver tries to exit a 6 m danger zone on a road with an even COF of 1. This scenario may occur in the real-world if a driver is distracted from the road and quickly turns the steering wheel in a panic to avoid an obstacle. The vehicle with an initial velocity of 120 km/h begins steering at time $t = 0.5s$ and applies the brake pedal at $t_1 = 1s$ ($\gamma_{brk} = 1$). The steering wheel input is limited to ±100°. Once the vehicle has exited the 6 m danger zone, the driver attempts to regain steering control and position the vehicle on the 6 m target line. Ideally, the vehicle would exit the danger zone quickly with minimal overshoot. This would not only avoid the head-on collision inside the danger zone but also avoids a collision with a road barrier or other vehicles once it has exited the 6 m area.

The yaw rate and sideslip angle for the three vehicles are given in Figure 7.19(a)-(b) respectivley and show that only the C-ABS vehicle is unable to regain control after the intial steering input. The varying braking forces across the vehicle using the FL-VSC is shown in Figure 7.20. The global co-ordinates, steering wheel input and longitudinal velocity for the three vehicles in Figure 7.21(a)-(c) respectivley show that for similar steering wheel inputs, the FL-VSC vehicle has a superior path tracking ability than the Z-GR vehicle. Since the C-ABS vehicle did not complete the manoeuvre, its performance indices were negated from this comparison.

Table 7.8 shows that the for similar ISC, the FL-VSC vehicle reduces IYRE, ISSE and J indicies by 65%, 33% and 46% respectivly over the Z-GR vehicle. In addition, from Figure 7.21(c) and the Y_{max} in Table 7.8, the FL-VSC reduces lateral overshoot over the Z-GR vehicle by 28%. This may see the Z-GR vehicle colliding with either a road barrier or other vehicles

outside the 6 m danger zone, whereas the FL-VSC vehicle is able to quickly regain yaw control and maneouver the vehicle back towards its target path.

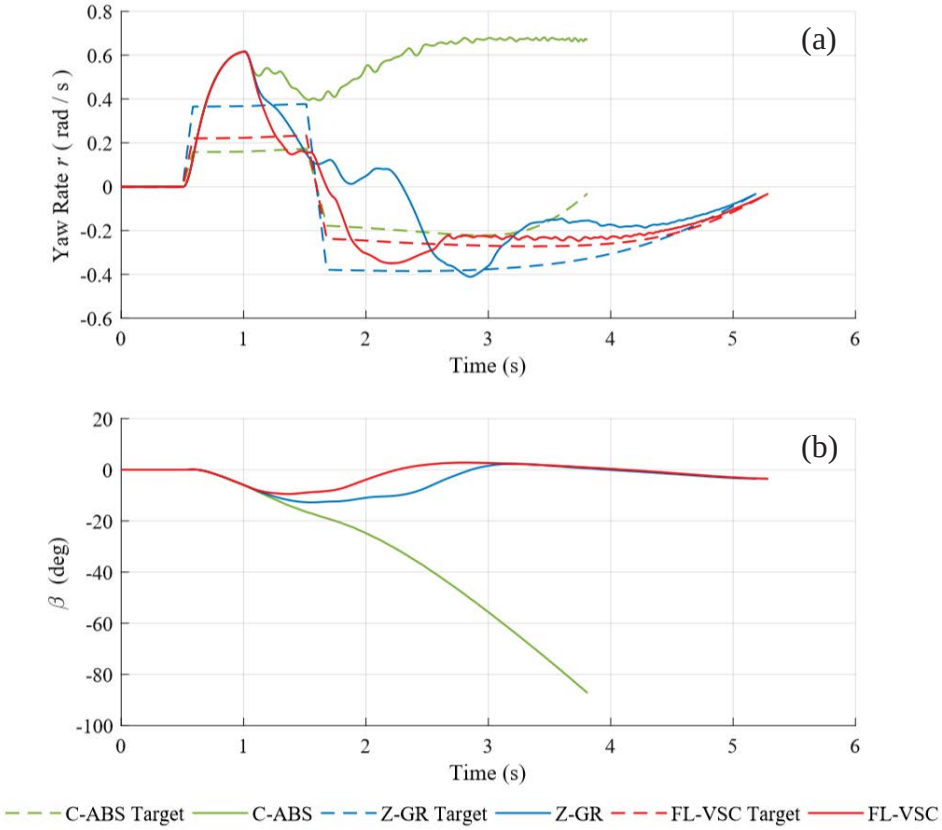

Figure 7.19 Vehicle controllability and stability variables for braking scenario 4, **(a)** r, **(b)** β_{ss}

The yaw rate error in Figure 7.19(a) is large for all three vehicles in the time between the initial steering input and the brakes being applied. The FL-VSC is not operating during this time period as it relies on the braking pedal activation level. It may be possible for future iterations of the FL-VSC to consider both constant velocity and braking scenarios.

The animation screenshots from CarSim for this braking scenario are shown in Figure 7.22. The scale of how much the FL-VSC vehicle improves upon the Z-GR vehicle clearly shows that there is a high likelyhood that the Z-GR vehicle might collide with either a barrier or another obsticle. The final resting positions of the FL-VSC vehilce is $\sim 3-4$ car widths closer to target path than the Z-GR vehilce.

Table 7.8 Performance indices comparison for braking scenario 4. Units in brackets represent percentage change from the Z-GR vehicle.

Index	C-ABS	Z-GR	FL-VSC
t_{bk}	2.81	4.189	4.287 **(2.34%)**
X_{bk}	70.3	75.379	76.49 **(1.47%)**
Y_{max}	18.77	14.598	10.54 **(-27.79%)**
J	-	0.205	0.11 **(-46.34%)**
IYRE	-	0.652	0.229 **(-64.9%)**
ISC	-	410.7	411.2 **(0.12%)**
ISSE	-	20.89	13.89 **(-33.5%)**

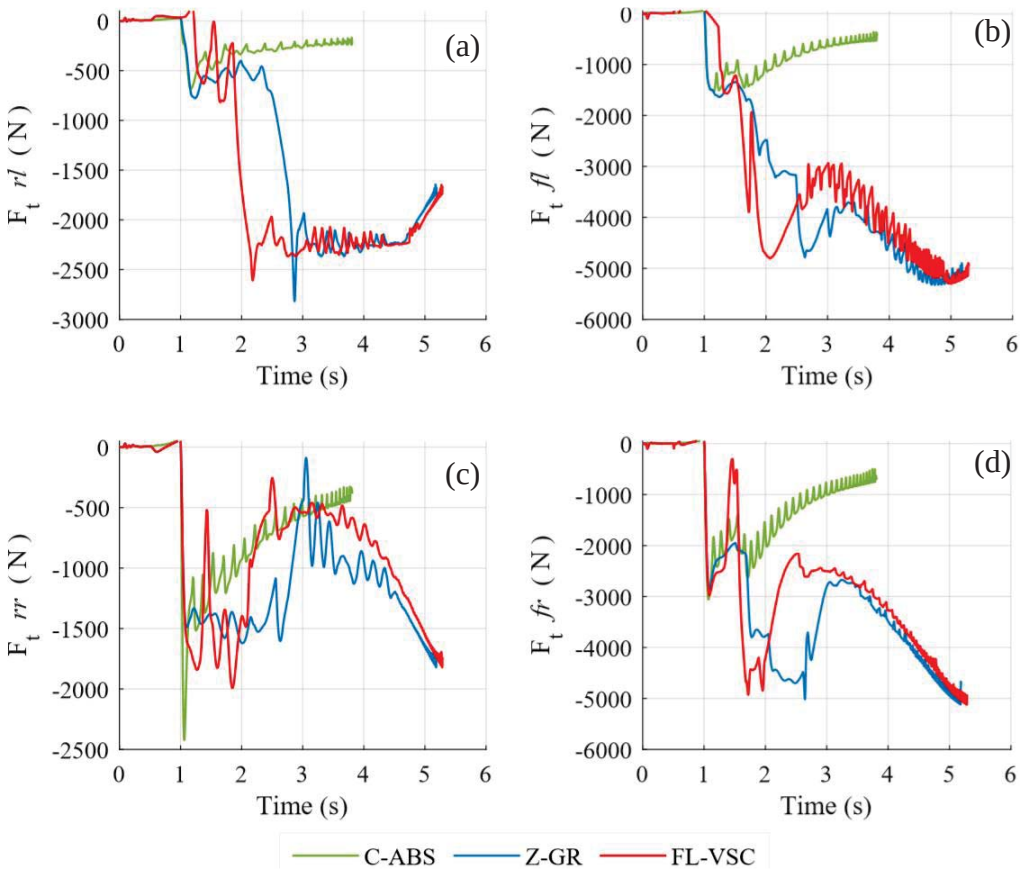

Figure 7.20 Longitudinal braking forces for scenario 4, **(a)** *rl*, **(b)** *fl*, **(c)** *rr*, **(d)** *fr*

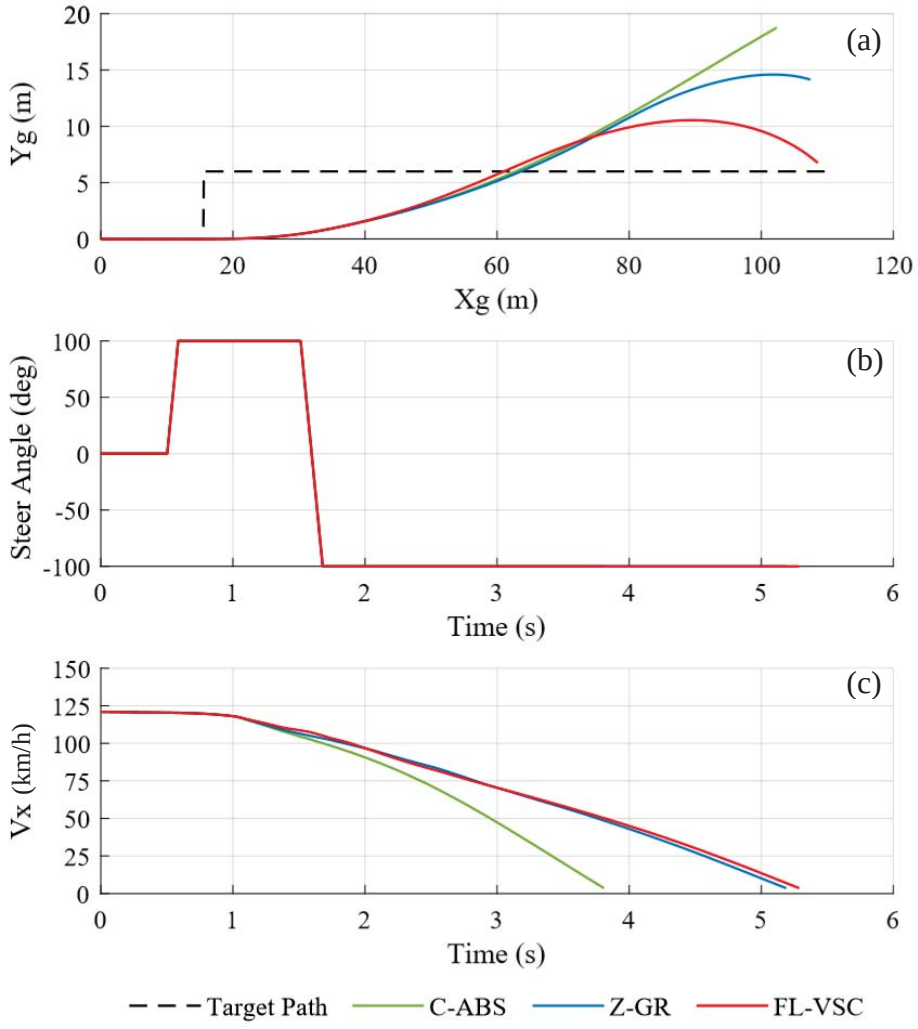

Figure 7.21 Vehicle dynamics comparison for braking scenario 4, **(a)** Global co-ordinates, **(b)** Steering wheel angle, **(c)** V_x

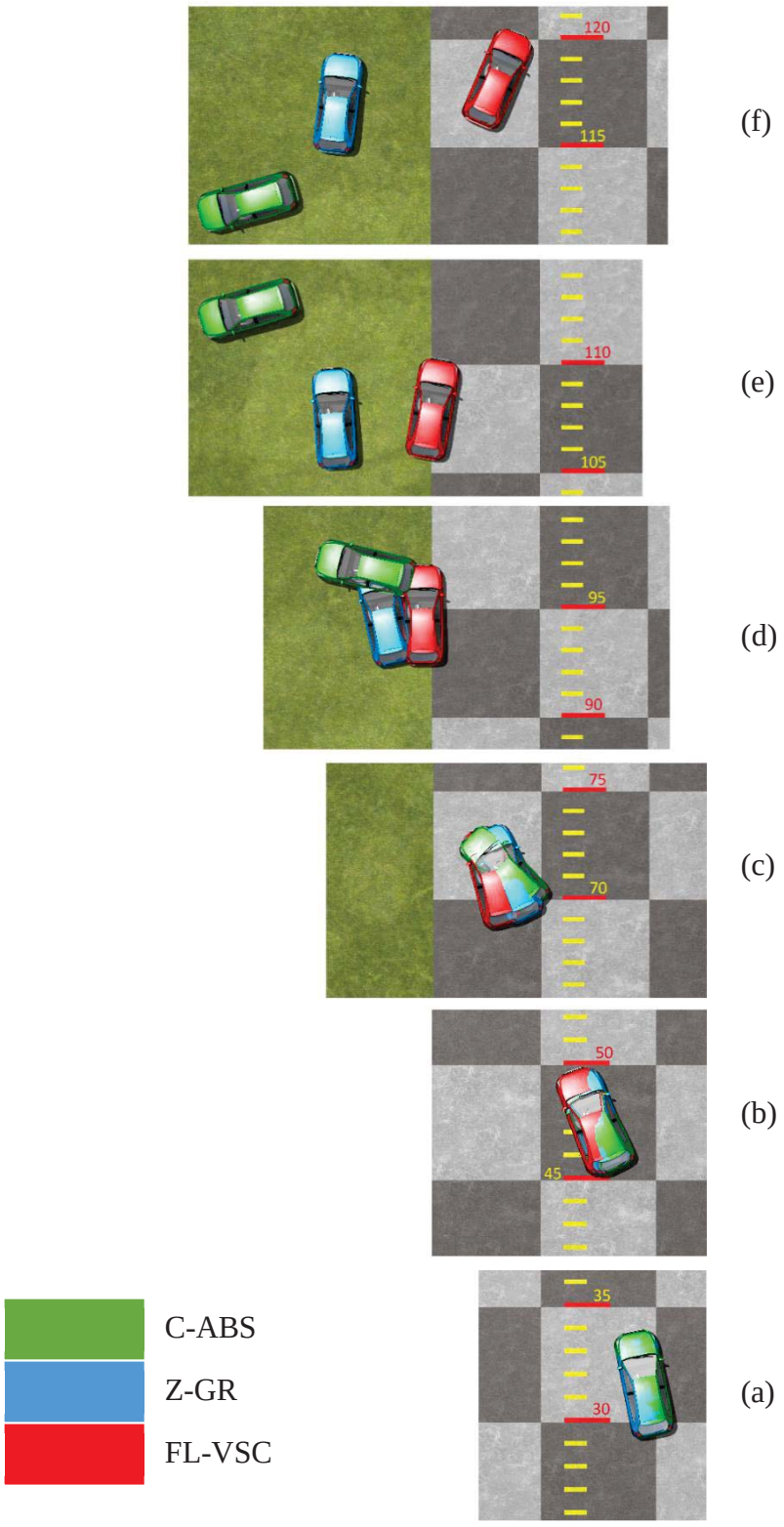

Figure 7.22 Animation preview for the accident avoidance braking manoeuvre scenario 4, **(a)** $t = 1\ s$ Brake pedal activation, **(b)** $t = 1.7\ s$ FL-VSC crosses the target lateral position, **(c)** $t = 2.3\ s$, **(d)** $t = 3\ s$ greatest FL-VSC lateral position, **(e)** $t = 3.8\ s$ Greatest Z-GR lateral position, **(f)** $t = 5.28\ s$ final resting position

7.4 Summary

A FL based VSC (FL-VSC) system was developed to improve the controllability and stability of an HEV/EV during an emergency braking manoeuvre. A FL YMC controller produced a target additional yaw moment which would reduce the yaw rate error and vehicle sideslip angle. This additional moment was sent to a new FL gradient command controller which assigned target operating gradients to the wheels on either side of the vehicle. A FL gradient based wheel slip controller regulated the wheels operating gradient via a combined Electrohydraulic Braking (EHB) system.

The FL-VSC scheme requires minimal vehicle parameters to be used within the control system, is insensitive to variable parameters or changing vehicle-road conditions and is able to be tuned to meet a vehicle's target dynamic objectives. A series of PIL experiments verify that the FLCs within this control system are unaffected by the code compiler and therefore ready to move onto the next stage of HIL validation.

In comparison to a conventional vehicle ABS system, the FL-VSC system; reduces the straight-line braking distance by 10%; requires little driver steering intervention when braking on split μ surfaces; increases stability for double lane change braking manoeuvres; and recovers control of the vehicle during an accident avoidance manoeuvre.

Chapter Eight

Summary and Conclusions

This chapter summarizes the major outcomes of the research presented in chapters four-seven in Section 8.1, plans for future research are then given in Section 8.2.

8.1 Summary of the Main Outcomes

8.1.1 Summary of Chapter Four

The research conducted within Chapter Four satisfies the first research objective set out in Section 2.5 by investigating a single FOC algorithm that is able to control multiple vehicle systems without the need for re-tuning with a further investigation into the effects of variable motor parameters on HEV/EV applications. A Fuzzy Logic (FL) based Field-Oriented Control (FOC) scheme for the traction motor/s of an HEV/EV was developed which consists of independent vehicle speed, traction motor q-axis current, d-axis current and magnetic flux (for IM) FL controllers. Developed in MATLAB/Simulink in conjunction with CarSim vehicle models, the FL based FOC (FL-FOC) scheme showed that it would be a useful tool during the development of an HEV/EV where multiple vehicle designs are under consideration, but its insensitivity to real-world variable motor parameters would make it a viable option for continuous control of the traction motors in the final production vehicle. The main outcomes from the FL-FOC scheme are as follows:

1) The FLC's showed to be unaffected by the code compiling via a series of PIL simulations which produced comparable performance to their software-based counterparts and ready to move onto the HIL validation.

2) The FL-FOC system is able to maintain the control objectives within acceptable error tolerances for multiple vehicle systems and traction motor topologies without the need for re-tuning.
3) The FL-FOC system has greater robustness over a PI controller based FOC system, not only through continual control of the various vehicle systems, but also with the inclusion of variable stator resistances.
4) The FL-FOC system is able to control the vehicle's velocity closer to how a real driver would control the vehicle over a PI based FOC scheme. This offers a better representation of how the physical vehicle would perform in the real world.

Not only would the FL-FOC scheme act as a useful control technique during the development of an HEV/EV where multiple vehicle designs are under consideration, but its insensitivity to real-world variable motor parameters would make it a viable option for continuous control of the traction motors in the final production vehicle.

8.1.2 Summary of Chapter Five

The research conducted within Chapter Five satisfies the second research objective set out in Section 2.5 by creating an empirical data based traction motor model to characterise the dynamic and thermal constraints of a motor operating in the overcurrent region. The model was able to narrow down the choice of prospective traction motors and optimise the choice of powertrain components as explained using a case study. A new traction motor sizing strategy for HEV/EVs based on an overcurrent-tolerant prediction model was developed. Using the motor's overcurrent torque-speed curve time constraints, the motor's temperature was estimated between safe upper and lower working boundaries. The rate of change in temperature is dependent on the position of the motor's output torque between the continuous and

overcurrent torque-speed curves to represent the supply current magnitude. The main outcomes of this chapter are summarised as followed:

1) The overcurrent-tolerant prediction model is able to estimate the dynamic and thermal characteristics of a motor operating in the overcurrent region requiring minimal detailed motor parameters.
2) A case study was explored where an aeroplane pushback vehicle was converted into a series HEV using this sizing strategy. Two possible HEV configurations using different traction motors and powertrain configurations were then analysed.
3) The advantages of operating in the overcurrent region and its effect on the HEV/EVs driving range, fuel consumption and emissions is revealed. The HEV using traction motors operating in the overcurrent region shows a reduction in fuel consumption by 5.7% and a reduction in electrical energy consumption of nearly 7% over a large motor confined to the continuous torque region.

This modelling technique would be more applicable during the early development stages where a wide range of traction motors are under consideration. The FL-FOC scheme of Chapter Five could then be used for control of the real model or once more detailed motor parameters become available.

8.1.3 Summary of Chapter Six

The research conducted within Chapter Six satisfies the third research objective set out in Section 2.5 to develop an on-line SVPWM scheme without impeding upon computational burden and examination of the control scheme over the full operating region applicable to HEV/EV applications. An on-line Reduced Intermediate Switching Space Vector Pulse Width Modulation (RIS-SVPWM) scheme for multilevel DC-AC inverters for HEV/EV applications

was developed. This was achieved by extending the mapping process to calculate alternative switching patterns enclosing the reference voltage vector. The switching vector which required a lower number of intermediate switching from the previous SVPWM cycle was chosen to reduce the total switching losses and increase the inverters efficiency. The main outcomes of this chapter are summarised as followed:

1) The RIS-SVPWM method operates on-line for any inverter level or topology without the need for large look-up tables.
2) The new RIS-SVPWM scheme managed to reduce the intermediate switching by 90% over the previous on-line modulation method.
3) The new RIS-SVPWM scheme managed to reduce the total number of switching by 32% for an output waveform of 150 Hz over the previous on-line modulation method. The switching losses are therefore reduced proportionally.
4) The line current THD and phase voltage WTHD for the RIS-SVPWM method are well within acceptable tolerances for the sinusoidal operating region over the full range of modulation indices and output waveform frequencies.
5) The RIS-SVPWM shows a similar linear growth in time-complexity with increasing inverter voltage levels to previous on-line SVPWM methods.
6) The RIS-SVPWM method is able to generate voltage waveforms in the sinusoidal and overmodulation regions of the inverter.

8.1.4 Summary of Chapter Seven

The research conducted within Chapter Seven satisfies the fourth research objective set out in Section 2.5 by developing a gradient based wheel slip controller which incorporates yaw control in order to improve the safety of an HEV/EV during an emergency manoeuvre.

Furthermore, the system developed required little information about the vehicle system it was implemented into that could not be estimated. A FL based Vehicle Stability Control (VSC) system (FL-VSC) was developed to improve the controllability and stability of an HEV/EV during an emergency braking manoeuvre. A FL YMC controller produced a target additional yaw moment which would reduce the yaw rate error and vehicle sideslip angle. This additional moment was sent to a new FL gradient command controller which assigned target operating gradients to the wheels on either side of the vehicle. A FL gradient based wheel slip controller regulated the wheels operating gradient via a combined Electrohydraulic Braking (EHB) system. The outcomes of this chapter are summarised as followed:

1) The FL-VSC requires minimal vehicle information as part of the control algorithm and whose robustness make it insensitive to time varying parameters.
2) The sensitivity of the control scheme is able to be tuned to meet the target dynamic objectives of a vehicle.
3) A series of PIL simulations showed that the FLCs were unaffected by the code compiler verifying that the control system is ready for HIL validation.
4) For straight line braking scenarios, the FL-VSC system reduced the braking distance by 10% over a conventional Anti-Lock Braking System (C-ABS).
5) For straight line split μ braking scenarios, the FL-VSC showed a 36% improved trade-off between braking distance and yaw rate control. The FL-VSC system also reduced the yaw rate error (IYRE) by 42%, driver steering intervention (ISC) by 39% and sideslip angle (ISSE) by 52% over this braking scenario.
6) For a double-lane change manoeuvre on a wet surface, the FL-VSC system showed an 85% greater trade-off between braking distance and yaw rate control. The FL-VSC system also reduced the IYRE by 48% and the ISSE by 23% with 7.2% less ISC.

7) For a distracted driver accident avoidance manoeuvre, the FL-VSC system showed a 28% greater trade-off between braking distance and yaw rate control over a vehicle which achieved peak longitudinal coefficient of friction (Z-GR). The FL-VSC system also reduced the IYRE by 64% and the ISSE by 33% over this braking scenario. The C-ABS vehicle could not regain control during this manoeuvre whereas the FL-VSC remained in control at all times.

8.2 Further Discussion and Future Work

8.2.1 Further Discussion for Chapter Four

Even though the SMAPE values using the FL-FOC system are within acceptable error tolerances, the SMAPE values for the PI-FOC system are still lower. The PI controllers continually integrate the input error which gives them the advantage during steady-state conditions. The input-output ranges of the FL controllers used within this work were all chosen as they offered the greatest trade-off between control stability and relatively low steady-state error. Future investigation of the FL-FOC system would involve improving the steady-state error performance of these controllers. One way to do this would be to construct an optimisation problem out of the FL-FOC scheme to tune the membership function shapes and input-output ranges in a similar manner to Hannan [85]. This may produce a FOC system that is not only more robust than a PI based FOC system, but also have comparably low steady-state error.

To fully validate the FL-FOC system, further research into how the system performs experimentally with real motors is required. The FL-FOC system has shown to work with physical hardware on a microcontroller, but any further physical limitations imposed by the motor, inverter or sensors may cause further problems. It is the intent of the author to investigate these problems in the future when more data, infrastructure, and equipment become available.

8.2.2 Further Discussion for Chapter Five

The overcurrent tolerant prediction model currently only utilises the time limits imposed by the overcurrent torque-speed curves which is ideal for when only these time limits are available from a motor manufacturer. However, it may be possible for the prediction model to incorporate the motor's efficiency map into how the temperature increases and decreases over time. Which observes the overall heat dissipation of the motor over the entire torque-speed curve. If the motor operates within an inefficient region of the continuous torque speed curve ($\sim$50% efficiency), it might decrease the total time allowed in the overcurrent region before overheating than if the motor operated in a more efficient region of the continuous torque speed curve ($\sim$90% efficiency). This would increase the accuracy of the prediction model and offer a greater representation of the motors thermal and torque characteristics.

8.2.3 Further Discussion for Chapter Six

At the current time of this research, the hardware (switching devices, DC sources, etc.) required to construct a working inverter was unavailable. It is the intent of future research to conduct a full hardware investigation into the RIS-SVPWM method to fully validate the scheme. In addition, a wider comparison into other on-line SVPWM methods and even offline methods which seek to reduce switching losses, harmonic distortion, audible noise and DC voltage balancing will be undertaken to offer a greater understanding and comparison into the current state-of-the-art SVPWM techniques.

A future Reduced Switching Loss SVPWM method is planned which directly calculates the appropriate switching pattern to reduce switching losses using switching loss equations [181]. In contrast to the RIS-SVPWM method, the Reduced Switching Loss SVPWM scheme may

not reduce the intermediate switching losses but might reduce the overall switching losses and increase the efficiency further.

8.2.4 Further Discussion for Chapter Seven

To fully validate the FL-VSC system, a complete experimental investigation is required. This would be carried out in various levels which aim to validate the various parts of the FL-VSC system:

1) The FL-VSC system is reliant on accurate estimation of the wheel slip ratio and longitudinal coefficient of friction. Finding a method which works well within this control scheme must be found and implemented into the control system.
2) Small scale bench top experimental tests to validate the estimation methods and EHB systems ability to control the wheel gradient around different operating gradients.
3) Full scale validation – A full experimental investigation with a physical vehicle, traction motors and braking system to fully validate the controller's performance.

It is the intention of the author to conduct these experimental validations in the future when the infrastructure and equipment becomes available.

Appendix: Nomenclature

Simulation setup

t	Time
t_0	Initial time

Motor Parameters

P_{max}	Maximum motor power
ω_e	Synchronous speed
θ_e	Electrical angle
v_{ds}	d-axis supply voltage (flux)
v_{qs}	q-axis supply voltage (torque)
V_s	Rated supply voltage
v_{d0}	d-axis supply voltage unit value (flux)
v_{q0}	q-axis supply voltage unit value (torque)
$v_{qs\,max}$	Maximum q-axis voltage
I_s	Rated supply current
i_{qs}	q-axis current (torque)
$i^*_{qs\,max}$	Maximum target q-axis current
i_{ds}	d-axis current (flux)
i_{dr}	d-axis rotor current
i_{qr}	q-axis rotor current
i_{ds}	d-axis stator current
i_{qs}	q-axis stator current
r_s	Stator winding resistance
r_r	Rotor winding resistance
P	Number of motor magnetic poles
λ	Magnetic flux linkage
λ_{ds}	d-axis stator magnetic flux linkage
λ_{qs}	q-axis stator magnetic flux linkage
λ_{dr}	d-axis rotor magnetic flux linkage
λ_{qr}	q-axis rotor magnetic flux linkage
ω_r	Rotor electrical rotational velocity
L_{ls}	Stator leakage inductance
L_{lr}	Rotor leakage inductance
L_m	Magnetising inductance
L_s	Stator inductance
L_r	Rotor inductance
L_q	q-axis inductance
L_d	d-axis inductance
ε	Saliency ratio
φ_r	Rotor magnetic flux wave magnitude
φ_m	Permanent magnet flux magnitude
f	Supply voltage waveform frequency
f_b	Base speed voltage supply frequency

ω_b	Motor base speed
ω_c	Critical speed
ω_{MAX}	Maximum motor rotational velocity
ω_m	Rotational velocity of prime mover
ω_f	Dropped motor speed
ρ	Rate of d-axis current decline
T	Temperature
T_F	Temperature factor
δ_τ	Relative output torque position
t_{Lim}	Peak overcurrent time curve time limit
t_{Stop}	Cool down time limit
T_{High}	Maximum motor temperature
T_{Low}	Cool down motor temperature lower limit
τ_e	Traction motor output torque
τ_O	Overcurrent torque curve
τ_C	Continuous torque curve
J_r	Rotor inertia
η_e	Motor efficiency

Vehicle Parameters

γ_{acc}	Accelerator pedal activation level
γ_{brk}	Brake pedal activation level
V_x	Longitudinal vehicle velocity
V_y	Vehicle lateral velocity
a_x	Longitudinal acceleration
r	Sprung mass yaw rate
β_{ss}	Vehicle Side-slip angle
Y_{max}	Maximum global lateral distance
$\sigma_{wh=fl,fr,rl,rr}$	Wheel slip ratio
$u_{wh=fl,fr,rl,rr}$	Velocity at road-wheel contact patch
$\omega_{wh=fl,fr,rl,rr}$	Rotational velocity of wheel
$\omega_{mwh=fl,fr,rl,rr}$	Rotational velocity of the motor
$\alpha_{wh=fl,fr,rl,rr}$	Sideslip angle of wheel
$\tau_{B\ wh=fl,fr,rl,rr}$	Brake torque at wheel
$\tau_{D\ wh=fl,fr,rl,rr}$	Drive torque at wheel
τ_L	Load torque
τ_{PM}	Torque from prime mover
τ_{ICE}	ICE output torque
F_{Aero}	Aerodynamic drag
$F_{Rolling}$	Wheel rolling resistance
$F_{Traction}$	Combined Tractive force
$F_{z\ wh=fl,fr,rl,rr}$	Tyre-road reaction force
$F_{B-Pedal}$	Brake pedal applied force
F_{Brake}	Brake force
R	Wheel rolling radius
M_{Veh}	Total vehicle mass

M_{Aero}	Total aeroplane mass
L	Wheelbase
b	Centre of gravity to rear axle
a	Centre of gravity to front axle
h_{COG}	Centre of gravity height
m_s	Sprung mass
$m_{ur(l,r)}$	Rear axle unsprung mass
$m_{uf(l,r)}$	Front axle unsprung mass
ψ_s	Sprung mass yaw angle
φ_s	Sprung mass roll angle
e_s	Centre of gravity to roll axis
Y_s	Centre of gravity Lateral position
Z_s	Centre of gravity vertical position
X_s	Centre of gravity longitudinal position
θ_s	Sprung mass pitch angle
$\delta_{fl,fr,rl,rr}$	Wheel steer angle
T_r	Rear track width
T_f	Front track width
$c_{1\ f(l,r),r(l,r)}$	Suspension damping coefficient
$c_{2\ f(l,r),r(l,r)}$	Tyre damping coefficient
$k_{1\ f(l,r),r(l,r)}$	Suspension spring coefficient
$k_{2\ f(l,r),r(l,r)}$	Tyre spring coefficient
$Z_{s\ f,r}$	Vertical height of sprung mass
$Z_{u\ f,r}$	Vertical height of unsprung mass
$Z_{r\ f,r}$	Vertical height of road
I_{roll}	Sprung mass roll inertia
I_{pitch}	Sprung mass pitch inertia
I_{yaw}	Sprung mass yaw inertia
I_{PM}	Rotational inertia of prime mover
I_T	Rotational inertia of transmission
I_{Fd}	Rotational inertia of final drive
I_{Wh}	Rotational inertia of wheel
N_{fd}	Final drive gear ratio
N_T	Transmission gear ratio
$N_{T-fd\ 1,2}$	Combined transmission final drive gear ratio
η_{fd}	Final drive efficiency
f_r	Tyre rolling resistance coefficient
C_D	Coefficient of aerodynamic drag
ρ_{air}	Density of air
A_f	Vehicle frontal area
M_r	Effective additional vehicle mass
$F_{t\ fl,fr,rl,rr}$	Wheel tractive force
$F_{s\ fl,fr,rl,rr}$	Wheel side force
D_X	Tyre magic formula peak value
C_X	Tyre magic formula shape factor

B_X	Tyre magic formula stiffness factor
E_X	Tyre magic formula curvature factor
C_α	Tyre magic formula shape factor modifier
B_α	Tyre magic formula stiffness factor modifier
G	Wheel operating gradient
$G_{wh=fl,fr,rl,rr}$	Independent wheel operating gradient
S_G	Wheel operating gradient scale function
B_M	Traction motor braking time constant
B_H	Hydraulic braking system time constant
B_{gf}	Braking force scale function
A	Stability factor
μ	Road coefficient of friction
$\mu_{X\ wh=fl,fr,rl,rr}$	Longitudinal coefficient of friction
$\mu_{Y\ wh=fl,fr,rl,rr}$	Lateral coefficient of friction
K_{af}	Front anti-roll bar stiffness
K_{ar}	Rear anti-roll bar stiffness
K_φ	Roll axis torsional stiffness
C_φ	Roll axis torsional damping
g	Acceleration of gravity
P_m	Output motor power
P_{Aux}	Auxiliary power load
P_{Gen}	Generator output power
J_{Batt}	Battery pack energy
$J_{Batt-max}$	Maximum battery pack energy

Inverter and electric circuit parameters

V_{DC}	DC source voltage
v_{ab}, v_{bc} and v_{ca}	Line voltages
v_{aO}, v_{bO} and v_{cO}	Pole voltages
v_{aN}, v_{bN} and v_{cN} or v_a, v_b andv_c	Phase voltages
i_{ab}, i_{bc} and i_{ca}	Line currents
v_α	Alpha axis voltage
v_β	Beta axis voltage
α	Alpha axis
β	Beta axis
$V_{ref-initial}$	Initial reference voltage vector
V_{ref}	Reference rotating voltage on alpha -beta axis
$V_{n\mathrm{L-SVM}}$	Voltage vector of nL-SVM diagram
V_{ref-2L}	2-Level reference voltage vector
V_{2LTS}	2-Level enclosing voltage vector
V_{step}	6 step waveform fundamental
V_0	Optimal null voltage vector
S	Inverter phase switching state
A, B and C	3-Phase AC voltage axis
E	Maximum inverter potential difference

m	Modulation index
V_m^*	Extended reference voltage magnitude
α_m^*	Modified reference voltage angle
α_h	Reference voltage holding angle
θ_c	Crossover angle
nL	Inverter voltage level
H	SVM hexagon number
h	Mapping iteration
Q_{hq}	Inner sector voltage vector
q	SVM hexagon sector
$2LTS$	2-level triangular sector
U, V and W	Inverter phase on-time pulses
m_2	2-level modulation index
$T_{0,1,2}$	Inverter voltage vector on-times
T_s	Inverter SVPWM cycle time
f_s	Inverter SVPWM switching cycle frequency
φ_{2lts}	2LTS reference voltage vector angle
ϑ_α	Initial alpha axis reference voltage angle
N	Neutral point
V_G, V_J and V_K	Example voltage vectors
$V_{ref\ G}, V_{ref\ J}$ or $V_{ref\ K}$	Example 2LTS reference voltage vectors
$\lvert V\rvert_{fund}$	Fundamental component
Hf	Harmonic component
$\lvert V\rvert_{Hf}$	Harmonic fundamental component
Hf_max	Maximum harmonic component
$\zeta_{k=d,q}$	Change in current error since last time step

Analysis tools and operators

n_max	Maximum data points
n	Data point
A_n	Actual value at data point
F_n	Forecast value at data point
t_{bk}	Total braking time
$t_{1,2}$	Start and end braking times
X_{bk}	Total braking longitudinal distance
V_{x0}	Initial velocity at the start of braking
ρ_w	Braking distance to yaw rate weighting value
J	Braking distance-yaw rate trade-off value
Δ	Error
$\frac{d}{dt}$	Time derivative
$\widehat{\ }$	Peak value
$\bar{\ }$	Complimentary switch position
*	Target value
$\lvert\ \rvert$	Magnitude

List of References

[1] C. Sabine and R. Feely, "Encyclopedia of Atmospheric Sciences (2nd Edition)," in *CLIMATE AND CLIMATE CHANGE | Carbon Dioxide*, Elsevier Ltd, 2015, pp. 10-17.

[2] W. J. Requia, M. Mohamed, C. D. Higgins, A. Arain and M. Ferguson, "How clean are electric vehicles? Evidence-based review of the effects of electric mobility on air pollutants, greenhouse gas emissions and human health," *Atmospheric Environment*, vol. 185, no. 1, pp. 64-77, 2018.

[3] E. A. Nanaki and C. J. Koroneos, "Climate change mitigation and deployment of electric vehicles in urban areas," *Renewable Energy*, vol. 99, no. 1, pp. 1153-1160, 2016.

[4] M. Ehsani, A. Ahmadi and D. Fadai, "Modeling of vehicle fuel consumption and carbon dioxide emission in road transport," *Renewable and Sustainable Energy Reviews*, vol. 53, no. 1, pp. 1638-1648, 2016.

[5] International Energy Agency, "CO2 emissions from fuel combustion," Paris, 2017.

[6] N. Hu, S. Liu, Y. Gao and J. Xu, "Large methane emissions from natural gas vehicles in Chinese cities," *Atmospheric Environment,* vol. 187, no. 1, pp. 374-380, 2018.

[7] A. R. Gopal, W. Y. Park, M. Witt and A. Phadke, "Hybrid- and battery-electric vehicles offer low-cost climate benefits in China," *Transportation Research Part D*, vol. 62, no. 1, pp. 362-371, 2018.

[8] P. Campbell, Y. Zhang, F. Yan, Z. Lu and D. Streets, "Impacts of transportation sector emissions on future U.S. air quality in a changing climate. Part II: Air quality

projections and the interplay between emissions and climate change," *Environmental Pollution,* vol. 238, no. 1, pp. 918-930, 2018.

[9] K. Palmera, J. Tate, Z. Wadud and J. Nellthorp, "Total cost of ownership and market share for hybrid and electric vehicles in," *Applied Energy,* vol. 209, no. 1, pp. 108-119, 2018.

[10] S. Jain, "Exposure to in-vehicle respirable particulate matter in passenger vehicles under different ventilation conditions and seasons," *Sustainable Environment Research,* vol. 27, no. 2, pp. 87-94, 2017.

[11] Public Health England, "The Mortality Effects of Long-Term Exposure to Particulate Air Pollution in the United Kingdom," Public Health England, London, 2010.

[12] W. J. Requia, M. D. Adams, A. Arain, P. Koutrakis and M. Ferguson, "Carbon dioxide emissions of plug-in hybrid electric vehicles: A life-cycle analysis in eight Canadian cities," *Renewable and Sustainable Energy Reviews,* vol. 78, no. 1, pp. 1390-1396, 2017.

[13] I. Kheirbek, J. Haney, S. Douglas, K. Ito and T. Matte, "The contribution of motor vehicle emissions to ambient fine particulate matter public health impacts in New York City: a health burden assessment," *Enviromental Health,* vol. 89, no. 15, pp. 1-14, 2016.

[14] J. Buekers, M. V. Holderbeke, J. Bierkens and L. I. Panis, "Health and environmental benefits related to electric vehicle introduction in EU countries," *Transportation Research Part D: Transport and Environment,* vol. 33, no. 1, pp. 26-38, 2014.

[15] R. Capata, "Urban and Extra-Urban Hybrid Vehicles: A Technological Review," *Energies,* vol. 11, no. 1, pp. 1-38, 2018.

[16] M. Steiner and J. Scholten, "Improving Overall Energy Efficiency of Traction Vehicles," Bombardier Transportation, Mannheim, 2006.

[17] M. Pourabdollah, E. Silvas, N. Murgovski, M. Steinbuch and B. Egardt, "Optimal Sizing of a Series PHEV: Comparison between Convex Optimization and Particle Swarm Optimization," in *IFAC Workshop on Engine and Powertrain Control, Simulation and Modeling* , Columbus, 2015.

[18] R. Xiong, H. He and F. Sun, "Methodology for Optimal Sizing of Hybrid Power System Usingparticle Swarm Optimization and Dynamic Programming," *Methodology for Optimal Sizing of Hybrid Power System Usingparticle Swarm Optimization and Dynamic Programming*, vol. 75, no. 1, pp. 1895-1900, 2015.

[19] International Energy Agency, "World Energy Outlook," 13 08 2018. [Online]. Available: https://www.iea.org/weo/. [Accessed 04 August 2018].

[20] U.S. Energy Information Administration, "International Energy Outlook 2017," Independant Statistics & Analysis, Washington, DC, 2017.

[21] A. Dhani, "Department for Transport: Reported road casualties in Great Britain: quarterly provisional estimates year ending June 2017," National Statistics, London, 2017.

[22] S. Reynolds, "Reported Road Casualties Great Britain: Annual Report 2016," Department for Transport, 2017.

[23] H. Sado, S. Sakai and Y. Hori, "Road condition estimation for traction control in electric vehicle," in *ISIE Proceedings of the IEEE International Symposium on Industrial Electronics*, Bled, 1999.

[24] J. Chen, J. Yu, K. Zhang and Y. Ma, "Control of regenerative braking systems for four-wheel-independently-actuated electric vehicles," *Mechatronics,* vol. 50, no. 1, pp. 394-401, 2018.

[25] Y. Hori, "Future vehicle driven by electricity and Control-research on four-wheel-motored "UOT electric march II"," *IEEE Transactions on Industrial Electronics,* vol. 51, no. 5, pp. 954 - 962, 2004.

[26] E.Esmailzadeh, A.Goodarzi and G. Vossoughi, "Optimal yaw moment control law for improved vehicle handling," *Mechatronics,* vol. 13, no. 7, pp. 659-675, 2003.

[27] B. Chen and C. Kuo, "Electronic stability control for electric vehicle with four in-wheel motors," *International Journal of Automotive Technology,* vol. 15, no. 4, pp. 573-580, 2014.

[28] M. Vignati, E. Sabbioni, D. Tarsitano and F. Cheli, "Electric powertrain layouts analysis for controlling vehicle lateral dynamics with torque vectoring," in *International Conference of Electrical and Electronic Technologies for Automotive*, Torino, 2017.

[29] J. Woo, H. Choi and JoonghaAhn, "Well-to-wheel analysis of greenhouse gas emissions for electric vehicles based on electricity generation mix: A global perspective," *Transportation Research Part D: Transport and Environment,* vol. 51, no. 1, pp. 340-350, 2017.

[30] A. Andwari, A. Pesiridis, S. Rajoo, R. Martinez-Botas and V. Esfahanian, "A review of Battery Electric Vehicle technology and readiness levels," *Renewable and Sustainable Energy Reviews,* vol. 78, no. 1, pp. 414-430, 2017.

[31] S. Morsy, "Electric Vehicle Outlook 2018," Bloomberg New Energy Finance, 2018.

[32] D. Liu and B. Xiao, "Exploring the development of electric vehicles under policy incentives: A scenario-based system dynamics model," *Energy Policy,* vol. 120, no. 1, pp. 8-23, 2018.

[33] C. G. Hoehne and M. V. Chester, "Optimizing plug-in electric vehicle and vehicle-to-grid charge scheduling to minimize carbon emissions," *Energy,* vol. 115, no. 1, pp. 646-657, 2016.

[34] S. Manzetti and F. Mariasiu, "Electric vehicle battery technologies: From present state to future systems," *Renewable and Sustainable Energy Reviews,* vol. 51, no. 1, pp. 1004-1012, 2015.

[35] Q. Zhang, C. Li and Y. Wu, "Analysis of Research and Development Trend of the Battery Technology in Electric Vehicle with the Perspective of Patent," *Energy Procedia,* vol. 105, no. 1, pp. 4274-4280, 2017.

[36] B. W. Lane, J. Dumortier, S. Carley, S. Siddiki, K. Clark-Sutton and J. D. Graham, "All plug-in electric vehicles are not the same: Predictors of preference for a plug-in hybrid versus a battery-electric vehicle," *Transportation Research Part D: Transport and Environment,* vol. 65, no. 1, pp. 1-13, 2018.

[37] K. Clement-Nyns, E. Haesen and J. Driesen, "The Impact of Charging Plug-In Hybrid Electric Vehicles on a Residential Distribution Grid," *IEEE Transactions on Power Systems,* vol. 25, no. 1, pp. 371 - 380, 2010.

[38] W. Li, R. Long, H. Chen and J. Geng, "A review of factors influencing consumer intentions to adopt battery electric vehicles," *Renewable and Sustainable Energy Reviews,* vol. 78, no. 1, pp. 318-328, 2017.

[39] L. Li, F. Dababneh and J. Zhao, "Cost-effective supply chain for electric vehicle battery remanufacturing," *Applied Energy*, vol. 226, no. 1, pp. 277-286, 2018.

[40] Vehicle Technologies Office, "Annual Progress Report for Energy Storage R&D," U.S. Department of Energy, 2015.

[41] B. Sarlioglu, C. T. Morris, D. Han and S. Li, "Driving Toward Accessibility: A Review of Technological Improvements for Electric Machines, Power Electronics, and Batteries for Electric and Hybrid Vehicles," *IEEE Industry Applications Magazine*, vol. 23, no. 1, pp. 14-25, 2016.

[42] J. Todd, J. Chen and F. Clogston, "Creating the clean energy economy: Analysis of the electric vehicle industry," International Economic Development Council, 2016.

[43] M. Guarnieri, "Looking back to electric cars," in *3rd IEEE History of ELectro-technology Conference*, Pavia, 2012.

[44] G. F. Sever and R. A. Fliess, "Operating Costs of Horse and Electric Delivery Wagons in New York City," *Transactions of the American Institute of Electrical Engineers*, vol. 16, no. 1, pp. 485 - 507, 1899.

[45] B. Berman, "History of Hybrid Vehicles," hybridCARS.com, 14 June 2011. [Online]. Available: https://www.hybridcars.com/history-of-hybrid-vehicles/. [Accessed 11 August 2018].

[46] X. Hu, N. Murgovski, L. M. Johannesson and B. Egardt, "Optimal Dimensioning and Power Management of a Fuel Cell/Battery Hybrid Bus via Convex Programming," *IEEE/ASME Transactions on Mechatronics*, vol. 20, no. 1, pp. 457 - 468, 2015.

[47] D. Zhou, A. Al-Durra, I. Matraji, A. Ravey and F. Gao, "Online Energy Management Strategy of Fuel Cell Hybrid Electric Vehicles: A Fractional-Order Extremum Seeking

Method," *IEEE Transactions on Industrial Electronics,* vol. 65, no. 8, pp. 6787 - 6799, 2018.

[48] F. Odeim, J. Roes and A. Heinzel, "Power Management Optimization of a Fuel Cell/Battery/Supercapacitor Hybrid System for Transit Bus Applications," *IEEE Transactions on Vehicular Technology,* vol. 65, no. 7, pp. 5783 - 5788, 2016.

[49] D. W. Gao, C. Mi and A. Emadi, "Modeling and Simulation of Electric and Hybrid Vehicles," *Proceedings of the IEEE,* vol. 95, no. 4, pp. 729 - 745, 2007.

[50] E. A. Grunditz and T. Thiringer, "Performance Analysis of Current BEVs Based on a Comprehensive Review of Specifications," *IEEE Transactions on Transportation Electrification,* vol. 2, no. 3, pp. 270 - 289, 2016.

[51] C. C. Chan, "The State of the Art of Electric, Hybrid, and Fuel Cell Vehicles," *Proceedings of the IEEE,* vol. 95, no. 4, pp. 704 - 718, 2007.

[52] A. Emadi, K. Rajashekara, S. Williamson and S. Lukic, "Topological overview of hybrid electric and fuel cell vehicular power system architectures and configurations," *IEEE Transactions on Vehicular Technology,* vol. 54, no. 3, pp. 763 - 770, 2005.

[53] M. Ehsani, K. Rahman and H. Toliyat, "Propulsion System Design of Electric and Hybrid Vehicles," *IEEE Transactions on Industrial Electronics,* vol. 44, no. 1, pp. 19-27, 1997.

[54] E. Silvas, T. Hofman, N. Murgovski, L. F. P. Etman and M. Steinbuch, "Review of Optimization Strategies for System-Level Design in Hybrid Electric Vehicles," *IEEE Transactions on Vehicular Technology,* vol. 66, no. 1, pp. 57 - 70, 2017.

[55] B. Bilgin, P. Magne, P. Malysz, Y. Yang and V. Pantelic, "Making the Case for Electrified Transportation," *IEEE Transactions on Transportation Electrification,* vol. 1, no. 1, pp. 4 - 17, 2015.

[56] T. Hutchinson, S. Burgess and G. Herrmann, "Current hybrid-electric powertrain architectures: Applying empirical design data to life cycle assessment and whole-life cost analysis," *Applied Energy,* vol. 119, no. 1, pp. 314-329, 2014.

[57] G. Wu, X. Zhang and Z. Dong, "Powertrain architectures of electrified vehicles: Review, classification and comparison," *Journal of the Franklin Institute,* vol. 352, no. 2, pp. 425-448, 2015.

[58] E. Bianchi and H. B. S. Polinder, "Energy consumption of electric powertrain architectures: A comparative study," in *19th European Conference on Power Electronics and Applications*, Warsaw, 2017.

[59] Y. Tang, "Model S". US Patent US7739005B1, 26 02 2009.

[60] N. Tesla, "A New System of Alternate Current Motors and Transformers," *Transactions of the American Institute of Electrical Engineers,* vol. 5, no. 10, pp. 308-324, 1888.

[61] G. Neidhofer, "Early three-phase power," *IEEE Power and Energy Magazine,* vol. 5, no. 5, pp. 88-100, 2007.

[62] P. Alger and R. Arnold, "The History of Induction Motors in America," *Proceedings of the IEEE,* vol. 64, no. 9, pp. 1380-1383, 1976.

[63] D. Cahill and B. Adkins, "The permanent-magnet synchronous motor," *Journal of the Institution of Electrical Engineers,* vol. 8, no. 96, pp. 554 - 555, 1962.

[64] C. P. Steinmetz, "The Alternating Current Induction Motor," *Transactions of the American Institute of Electrical Engineers,* vol. 14, no. 1, pp. 185-217, 1897.

[65] R. Park, "Two-Reaction Theory of Synchronous Machines," *Transactions of the American Institute of Electrical Engineers,* vol. 48, no. 3, pp. 716-727, 1929.

[66] W. C. Duesterhoeft, M. W. Schulz and E. Clarke, "Determination of Instantaneous Currents and Voltages by Means of Alpha, Beta, and Zero Components," *Transactions of the American Institute of Electrical Engineers,* vol. 70, no. 2, pp. 1248 - 1255, 1951.

[67] M. Yilmaz, "Limitations/capabilities of electric machine technologies and modelling approaches for electric motor design analysis in plug-in electric vehicle applications," *Renewable and Sustainable Energy Reviews,* pp. 88-99, 2015.

[68] D. N. Vaks, Interviewee, *A closer look at torque ripple – minimizing its effects on electric machines.* [Interview]. 22 September 2015.

[69] J. d. Santiago, H. Bernhoff, B. Ekergård, S. Eriksson and S. Ferhatovic, "Electrical Motor Drivelines in Commercial All-Electric Vehicles: A Review," *IEEE Transactions on Vehicular Technology,* vol. 61, no. 2, pp. 475 - 484, 2011.

[70] G. Pellegrino, A. Vagati and P. Guglielmi, "Performance Comparison Between Surface-Mounted and Interior PM Motor Drives for Electric Vehicle Application," *IEEE Transactions on Industrial Electronics,* vol. 59, no. 2, pp. 803 - 811, 2011.

[71] G. Pellegrino, A. Vagati, B. Boazzo and P. Guglielmi, "Comparison of Induction and PM Synchronous Motor Drives for EV Application Including Design Examples," *IEEE Transactions on Industry Applications,* vol. 48, no. 6, pp. 2322 - 2332, 2012.

[72] K. Rajashekara, "Present Status and Future Trends in Electric Vehicle Propulsion Technologies," *IEEE Journal of Emerging and Selected Topics in Power Electronics*, vol. 1, no. 1, pp. 3 - 10, 2013.

[73] E. Bostanci, M. Moallem, A. Parsapour and B. Fahimi, "Opportunities and Challenges of Switched Reluctance Motor Drives for Electric Propulsion: A Comparative Study," *IEEE Transactions on Transportation Electrification*, vol. 3, no. 1, pp. 58 - 75, 2017.

[74] A. Vagati, G. Pellegrino and P. Guglielmi, "Comparison between SPM and IPM motor drives for EV application," in *XIX International Conference on Electrical Machines (ICEM)*, Rome, 2010.

[75] S. Evangelou and W. Shabbir, "Dynamic modeling platform for series hybrid electric vehicles," *IFAC-PapersOnLine*, vol. 49, no. 11, pp. 533-540, 2016.

[76] H. Fan, G. Dawson and T. Eastham, "Model of electric vehicle induction motor drive system," in *Canadian Conference on Electrical and Computer Engineering*, Vancouver, 1993.

[77] J. G. Hayes, "Simplified electric vehicle models for use in undergraduate teaching and research," in *IEEE Energy Conversion Congress and Exposition*, Pittsburgh, 2014.

[78] Q. Zhou, W. Zhang, S. Cash, O. Olatunbosun, HongmingXu and G. Lu, "Intelligent sizing of a series hybrid electric power-train system based on Chaos-enhanced accelerated particle swarm optimization," *Applied Energy*, vol. 189, no. 1, pp. 588-601, 2017.

[79] R. Gabriel, "Microprocessor control of induction motors employing field coordinates," in *International conference on electrical variable-speed drives*, London, 1979.

[80] R. Gabriel, W. Leonhard and C. J. Nordby, "Field-Oriented Control of a Standard AC Motor Using Microprocessors," *IEEE Transactions on Industry Applications,* vol. 16, no. 2, pp. 186-192, 1980.

[81] S. Sathikumar and J. Vithayathil, "Digital Simulation of Field-Oriented Control of Induction Motor," *IEEE Transactions on Industrial Electronics,* vol. 31, no. 2, pp. 141-148, 1984.

[82] F. Blaschke, "The principle of field orientation as applied to the new TRANSVECTOR closed loop control," *Siemens Rev,* vol. 34, no. 1, pp. 217-220, 1972.

[83] K. Hasse, "Zum dynamischen Verhalten der Asynchronmaschine bei Betrieb mit variabler Ständerfrequenz und Ständerspannung," *ETZ-A,* vol. 89, no. 1, pp. 387-391, 1968.

[84] D. Casadei, F. Profumo and G. Serra, "FOC and DTC: two viable schemes for induction motors torque control," *IEEE Transactions on Power Electronics,* vol. 17, no. 5, pp. 779 - 787, 2002.

[85] M. Hannan, J. A. Ali, A. Mohamed and A. Hussain, "Optimization techniques to enhance the performance of induction motor drives: A review," *Renewable and Sustainable Energy Reviews,* vol. 81, no. 2, pp. 1611-1626, 2018.

[86] J. Köhler, M. Manderla and F. Malchow, "Embedded Model Predictive Direct Switching Control for High Performance Electrical Drives - A Quantitative Comparison," *IFAC-PapersOnLine,* vol. 50, no. 1, pp. 11871-11876, 2017.

[87] Y. Zhang, B. Xia and H. Yang, "Performance Evaluation of An Improved Model Predictive Control with Field Oriented Control as a Benchmark," *IET Electric Power Applications,* vol. 11, no. 5, pp. 677 - 687, 2017.

[88] Z. Liu, Y. Li and Z. Zheng, "A Review of Drive Techniques for Multiphase Machines," *CES Transactions on Electrical Machines and Systems,* vol. 2, no. 2, pp. 243 - 251, 2018.

[89] H. Prasetyo, A. Rohman, H. Hindersah and M. Santabudi, "Implementation of Model Predictive Control (MPC) in electric vehicle testing simulator," in *4th International Conference on Electric Vehicular Technology*, Sanur, 2017.

[90] S. Bolognani, S. Bolognani, L. Peretti and M. Zigliotto, "Design and Implementation of Model Predictive Control for Electrical Motor Drives," *IEEE Transactions on Industrial Electronics,* vol. 56, no. 6, pp. 1925 - 1936, 2009.

[91] A. Mora, Á. Orellana, J. Juliet and R. Cárdenas, "Model Predictive Torque Control for Torque Ripple Compensation in Variable-Speed PMSMs," *IEEE Transactions on Industrial Electronics,* vol. 63, no. 7, pp. 4584 - 4592, 2016.

[92] S. Odhano, R. Bojoi, A. Formentini, P. Zanchetta and A. Tenconi, "Direct flux and current vector control for induction motor drives using model predictive control theory," *IET Electric Power Applications,* vol. 11, no. 8, pp. 1483 - 1491, 2017.

[93] Y. Zhang, B. Xia, H. Yang and J. Rodriguez, "Overview of model predictive control for induction motor drives," *Chinese Journal of Electrical Engineering,* vol. 2, no. 1, pp. 62 - 76, 2016.

[94] J. Li, X. Huang, F. Niu, C. You, L. Wu and Y. Fang, "Prediction Error Analysis of Finite-Control-Set Model Predictive Current Control for IPMSMs," *Energies,* vol. 11, no. 1, pp. 1-16, 2018.

[95] C. Rojas, J. Yuz, M. Aguirre and J. Rodriguez, "A comparison of discrete-time models for model predictive control of induction motor drives," in *IEEE International Conference on Industrial Technology*, Seville, 2015.

[96] L. Cavanini, G. Cimini and G. Ippoliti, "Computationally efficient model predictive control for a class of linear parameter-varying systems," *IET Control Theory & Applications*, vol. 12, no. 10, p. 1384 – 1392, 2017.

[97] T. Geyer, G. Papafotiou and M. Morari, "Model Predictive Direct Torque Control—Part I: Concept, Algorithm, and Analysis," *IEEE Transactions on Industrial Electronics*, vol. 56, no. 6, pp. 1894 - 1905, 2008.

[98] M. Preindl and S. Bolognani, "Model Predictive Direct Torque Control With Finite Control Set for PMSM Drive Systems, Part 1: Maximum Torque Per Ampere Operation," *IEEE Transactions on Industrial Informatics*, vol. 9, no. 4, pp. 1912 - 1921, 2013.

[99] F. Wang, S. Li, X. Mei, W. Xie, J. Rodríguez and R. M. Kennel, "Model-Based Predictive Direct Control Strategies for Electrical Drives: An Experimental Evaluation of PTC and PCC Methods," *IEEE Transactions on Industrial Informatics*, vol. 11, no. 3, pp. 671 - 681, 2015.

[100] S. Vazquez, J. Leon, L. Franquelo, J. Rodriguez and H. Young, "Model Predictive Control: A Review of Its Applications in Power Electronics," *IEEE Industrial Electronics Magazine*, vol. 8, no. 1, pp. 16 - 31, 2014.

[101] L. Samaranayake and S. Longo, "Degradation Control for Electric Vehicle Machines Using Nonlinear Model Predictive Control," *IEEE Transactions on Control Systems Technology*, vol. 26, no. 1, pp. 89 - 101, 2017.

[102] M. Schubert, K. Girigoudar and R. W. D. Doncker, "MPC based current sharing for maximum torque dynamics in efficiency optimized field oriented induction machine control," in *IEEE 12th International Conference on Power Electronics and Drive Systems*, Honolulu, 2017.

[103] T. M. Jahns, G. B. Kliman and T. W. Neumann, "Interior Permanent-Magnet Synchronous Motors for Adjustable-Speed Drives," *IEEE Transactions on Industry Applications*, vol. 22, no. 4, pp. 738-747, 1986.

[104] T. M. Jahns, "Flux-Weakening Regime Operation of an Interior Permanent-Magnet Synchronous Motor Drive," *IEEE Transactions on Industry Applications*, vol. 23, no. 4, pp. 681-689, 1987.

[105] S. Morimoto, M. Sanada and Y. Takeda, "Effects and Compensation of Magnetic Saturation in Flux-Weakening Controlled Permanent Magnet Synchronous Motor Drives," *IEEE Transactions on Industry Applications*, vol. 30, no. 6, pp. 1632-1637, 1994.

[106] S. Morimoto, T. Ueno, M. Sanada, Y. Takeda and T. Hirasa, "Variable speed drive system of interior permanent magnet synchronous motors for constant power operation," in *Conference Record of the Power Conversion Conference*, Yokohama, 1993.

[107] S.-H. Kim and S.-K. Sul, "Maximum torque control of an induction machine in the field weakening region," *IEEE Transactions on Industry Applications*, vol. 31, no. 4, pp. 787-794, 1995.

[108] J. Lemmens, P. Vanassche and J. Driesen, "Optimal Control of Traction Motor Drives Under Electrothermal Constraints," *IEEE Journal of Emerging and Selected Topics in Power Electronics,* vol. 2, no. 2, pp. 249 - 263, 2014.

[109] E. S. Sergaki, "Fuzzy Logic Control for motor flux reduction during steady states and for flux recovery in transient states of Indirect-FOC AC drives," in *XIX International Conference on Electrical Machines*, Rome, 2010.

[110] R. Krishnan and A. S. Bharadwaj, "A review of parameter sensitivity and adaptation in indirect vector controlled induction motor drive systems," *IEEE Transactions on Power Electronics,* vol. 6, no. 4, pp. 695-703, 1991.

[111] E. Ho and P. Sen, "Decoupling control of induction motor drives," *IEEE Transactions on Industrial Electronics,* vol. 35, no. 2, pp. 253-262, 1988.

[112] T. Matsuo and T. A. Lipo, "A Rotor Parameter Identification Scheme for Vector-Controlled Induction Motor Drives," *IEEE Transactions on Industry Applications,* vol. 21, no. 4, pp. 624-632, 1985.

[113] B. K. Bose, "A high-performance inverter-fed drive system of an interior permanent magnet synchronous machine," *IEEE Transactions on Industry Applications*, vol. 24, no. 6, pp. 987-997, 1988.

[114] J. Holtz, "Identification of the machine parameters in a vector controlled induction motor drive," in *Conference Record of the 1989 IEEE Industry Applications Society Annual Meeting*, San Diego, 1989.

[115] R. Marino, S. Peresada and P. Tomei, "On-line stator and rotor resistance estimation for induction motors," *IEEE Transactions on Control Systems Technology,* vol. 8, no. 3, pp. 570-579, 2000.

[116] A. Faqir, F. Betin, L. C. Alaoui, B. Nahid and D. Pinchon, "Varying sliding surface control of an induction machine drive," in *Proceedings of 2003 IEEE Conference on Control Applications*, Istanbul, 2003.

[117] Z. Ma, T. Zheng, F. lin and X. You, "A new sliding-mode current controller for field oriented controlled induction motor drives," in *31st Annual Conference of IEEE Industrial Electronics Society*, Raleigh, 2005.

[118] F. Patakor, M. Sulaiman and Z. Ibrahim, "Adaptive Sliding Mode For Indirect Field Oriented Controlled of Induction Motor," in *IEEE Student Conference on Research and Development*, Cyberjaya, 2011.

[119] M. Fnaiech, F. Fnaiech and F. Betin, "Comparison between fuzzy logic and sliding mode control applied to six phase induction machine positioning," in *18th International Conference on Electrical Machines*, Vilamoura, 2009.

[120] S. Suman, M. K. Gautam, R. Srivastava and V. K. Giri, "Novel approach of speed control of PMSM drive using neural network controller," in *International Conference on Electrical, Electronics, and Optimization Techniques (ICEEOT)*, Chennai, 2016.

[121] Birowo, R. Ahmad and H. Zamzuri, "Artificial neural network based controller for line starting performance synchronous motor of a conveyor system using field oriented self-controlled," in *IEEE 3rd International Conference on Smart Instrumentation, Measurement and Applications (ICSIMA)*, Kuala Lumpur, 2015.

[122] H. Mediouni, S. E. Hani, I. Ouachtouk, M. Ouadghiri and I. Aboudrar, "Artificial neural networks applied on double squirrel cage induction motor for an electric vehicle motorisation," in *International Conference on Electrical and Information Technologies*, Rabat, 2017.

[123] F. Lftisi, G. George, A. Aktaibi, C. Butt and M. A. Rahman, "Artificial Neural Network Based Speed Controller for Induction Motors," in *IECON 2016 - 42nd Annual Conference of the IEEE Industrial Electronics Society*, Florence, 2016.

[124] P. Xie, G. Li, F. Xie, C. Hu and X. Qi, "Research on field-weakening control of induction motor based on torque current component of the voltage closed-loop," in *IEEE Conference on Industrial Electronics and Applications*, Auckland, 2015.

[125] M. Chebre, A. Meroufel and Y. Bendaha, "Speed control of induction motor using Genetic Algorithm-based PI controller," *Acta Polytechnica Hungarica*, vol. 8, no. 6, pp. 141-153, 2011.

[126] A. Kelemen, "Fuzzy controller for field-oriented robot drive with induction motor," in *IEEE International Symposium on Industrial Electronics*, Budapest, 1993.

[127] A. Tewari, A. Tripathi and S. Das, "A fuzzy logic controller based indirect field-oriented induction motor drive system," in *Proceedings of IEEE International Conference on Industrial Technology*, Goa, 2000.

[128] M. Uddin, T. Radwan and M. Rahman, "Performances of fuzzy-logic-based indirect vector control for induction motor drive," *IEEE Transactions on Industry Applications*, vol. 38, no. 5, pp. 1219-1225, 2002.

[129] B. Adhavan, A. Kuppuswamy, G. Jayabaskaran and V. Jagannathan, "Field oriented control of Permanent Magnet Synchronous Motor (PMSM) using fuzzy logic controller," in *IEEE Recent Advances in Intelligent Computational Systems*, Trivandrum, 2011.

[130] H. S. Elabed, "Indirect field oriented control of induction motor (IM) drive using fuzzy logic controller (FLC)," in *8th IEEE Conference on Industrial Electronics and Applications*, Melbourne, 2013.

[131] M. H. N. Talib, Z. Ibrahim, N. A. Rahim, A. S. A. Hasim and H. Zainuddin, "Performance improvement of induction motor drive using simplified FLC method," in *16th International Power Electronics and Motion Control Conference and Exposition*, Antalya, 2014.

[132] M. Zamani, M. Karimi-Ghartemani and N. Sadati, "Design of a fractional order PID controller for an AVR using particle swarm optimization," *Control Engineering Practice,* vol. 17, no. 12, pp. 1380-1387, 2009.

[133] I. Pan, S. Das and A. Gupta, "Tuning of an optimal fuzzy PID controller with stochastic algorithms for networked control systems with random time delay," *ISA Transactions,* vol. 50, no. 1, pp. 28-36, 2011.

[134] S. Ustun and M. Demirtas, "Modeling and control of V/f controlled induction motor," *Energy Conversion and Management,* vol. 50, no. 3, p. 786–791, 2009.

[135] R.-E. Precup, A.-D. Balint, M.-B. Radac and E. M. Petriu, "Backtracking Search Optimization Algorithm-based approach to PID controller tuning for torque motor systems," in *IEEE Systems Conference (SysCon)*, Vancouver, 2015.

[136] C. Laoufi, A. Abbou and M. Akherraz, "Comparative study between different speed controller techniques applied to the indirect field-oriented control of an induction machine - performance and limitations," *Transactions on Systems and Control,* vol. 10, no. 1, pp. 360-372, 2015.

[137] B. Heber, "Fuzzy logic enhanced speed control of an indirect field oriented induction machine drive," in *26th Annual IEEE Power Electronics Specialists Conference*, Atlanta, 1997.

[138] F.-F. Cheng, "Application of fuzzy logic in the speed control of AC servo system and an intelligent inverter," *IEEE Transactions on Energy Conversion*, vol. 8, no. 2, pp. 312-318, 1993.

[139] K. Zeb, Z. Ali, K. Saleem, W. Uddin, M. Javed and N. Christofides, "Indirect field-oriented control of induction motor drive based on adaptive fuzzy logic controller," *Electrical Engineering*, vol. 99, no. 3, p. 803–815, 2017.

[140] B. Singh, C. P. Swamy, B. Singh, A. Chandra and K. Al-Haddad, "Performance analysis of fuzzy logic controlled permanent magnet synchronous motor drive," in *International Conference on Industrial Electronics, Control, and Instrumentation*, Orlando, 1995.

[141] M. Jahmeerbacus, C. Bhurtun, K. Soyjaudah and M. Oolun, "A current-regulated field-oriented induction motor drive using a fuzzy controller," in *IEEE AFRICON. 6th Africon Conference in Africa*, George, 2002.

[142] M. A. Magzoub, "An intelligent speed controller for indirect field-oriented controlled induction motor drives," in *IEEE Conference on Clean Energy and Technology*, Lankgkawi, 2013.

[143] G. Deshpande and S.S.Sankeshwari, "Speed Control of Induction Motors using Hybrid PI plus Fuzzy Controller," *International Journal of Advances in Engineering and Technology*, vol. 6, no. 5, pp. 2253-2261, 2013.

[144] A. Lokriti, "Induction motor speed drive improvement using fuzzy IP-self-tuning controller. A real time implementation," *ISA Transactions*, vol. 52, no. 3, pp. 406-417, 2013.

[145] F. Alonge, F. D'Ippolito, F. Raimondi and A. Urso, "Method for designing PI-type fuzzy controllers for induction motor drives," *IEE Proceedings - Control Theory and Applications*, vol. 148, no. 1, pp. 61-69, 2001.

[146] M. Masiala, "Fuzzy Self-Tuning Speed Control of an Indirect Field-Oriented Control Induction Motor Drive," in *IEEE Industry Applications Annual Meeting*, New Orleans, 2007.

[147] A. Rohan, F. Asghar and S. H. Kim, "Design of Fuzzy Logic Tuned PID Controller for Electric Vehicle based on IPMSM Using Flux-weakening," *Journal of Electrical Engineering and Technology*, vol. 13, no. 1, pp. 451-459, 2018.

[148] T. Lubin, "Fuzzy controller in AC servo motor drive," in *Seventh International Conference on Electrical Machines and Drives*, Durham, 1995.

[149] A. Mishra, "Fuzzy logic based speed and current control of vector controlled PMSM drive," in *2nd International Conference on Power, Control and Embedded Systems*, Allahabad, 2012.

[150] J. Azcue-Puma, A. S. Filho and E. Ruppert, "Direct-FOC with Fuzzy Current Control for asynchronous machine," in *IEEE International Conference on Industrial Technology*, Cape Town, 2013.

[151] C. Fahassa, "Improvement of the induction motor drive's indirect field oriented control performance by substituting its speed and current controllers with fuzzy logic

components," in *3rd International Renewable and Sustainable Energy Conference*, Marrakech, 2015.

[152] R. Baker, "Electric power source". USA Patent US 3899689 A, 12 August 1975.

[153] S. Jawahar, "Minimization of Switching Devices and Driver Circuits in Multilevel Inverter," *Circuits and Systems*, vol. 7, no. 1, pp. 3371-3383, 2016.

[154] J. Rodriguez, J.-S. Lai and F. Z. Peng, "Multilevel inverters: a survey of topologies, controls, and applications," *IEEE Transactions on Industrial Electronics*, vol. 49, no. 4, pp. 724 - 738, 2002.

[155] A. Nabae, I. Takahashi and H. Akagi, "A New Neutral-Point-Clamped PWM Inverter," *IEEE Transactions on Industry Applications*, vol. 17, no. 5, pp. 518 - 523, 1981.

[156] L. Tolbert, F. Z. Peng and T. Habetler, "Multilevel Converters for Large Electric Drives," *IEEE Transactions on Industry Applications*, vol. 35, no. 1, pp. 36 - 44, 1999.

[157] Z. Du, B. Ozpineci and L. M. Tolbert, "Inductorless DC-AC Cascaded H-Bridge Multilevel Boost Inverter for Electric/Hybrid Electric Vehicle Applications," in *IEEE Industry Applications Annual Meeting*, New Orleans, 2007.

[158] A. K. Verma, P. R. Thakura, K. C. Jana and G. Buja, "Cascaded multilevel inverter for Hybrid Electric Vehicles," in *India International Conference on Power Electronics*, New Delhi, 2010.

[159] H. Ye, Y. Yang and A. Emadi, "Traction inverters in hybrid electric vehicles," in *IEEE Transportation Electrification Conference and Expo*, Dearborn, 2012.

[160] P. Qashqai, A. Sheikholeslami and H. Vahedi, "A Review on Multilevel Converter Topologies for Electric Transportation Applications," in *IEEE Vehicle Power and Propulsion Conference (VPPC)*, Montreal, 2015.

[161] J.-S. Lai and F. Z. Peng, "Multilevel converters-a new breed of power converters," *IEEE Transactions on Industry Applications,* vol. 32, no. 3, pp. 509 - 517, 1996.

[162] J. Rodriguez, S. Bernet, B. Wu, J. O. Pontt and S. Kouro, "Multilevel Voltage-Source-Converter Topologies for Industrial Medium-Voltage Drives," *IEEE Transactions on Industrial Electronics,* vol. 54, no. 6, pp. 2930 - 2945, 2007.

[163] S. Kouro, M. Malinowski and K. Gopakumar, "Recent Advances and Industrial Applications of Multilevel Converters," *IEEE Transactions on Industrial Electronics,* vol. 57, no. 8, pp. 2553 - 2580, 2010.

[164] A. Emadi, Y. J. Lee and K. Rajashekara, "Power Electronics and Motor Drives in Electric, Hybrid Electric, and Plug-In Hybrid Electric Vehicles," *IEEE Transactions on Industrial Electronics,* vol. 55, no. 6, pp. 2237 - 2245, 2008.

[165] R. Menon, A. H. Kadam, N. A. Azeez and S. S. Williamson, "A comprehensive survey on permanent magnet synchronous motor drive systems for electric transportation applications," in *42nd Annual Conference of the IEEE Industrial Electronics Society,* Florence, 2016.

[166] M. Malinowski, K. Gopakumar, J. Rodriguez and M. A. Perez, "A Survey on Cascaded Multilevel Inverters," *IEEE Transactions on Industrial Electronics,* vol. 57, no. 7, pp. 2197 - 2206, 2010.

[167] B. K. Bose, Modern Power Electronics and AC Drives, Pretice-Hall, 2002.

[168] F. Wang, "Sine-triangle versus space-vector modulation for three-level PWM voltage-source inverters," *IEEE Transactions on Industry Applications,* vol. 38, no. 2, pp. 500 - 506, 2002.

[169] A. Massoud, S. Finney and B. Williams, "Control techniques for multilevel voltage source inverters," in *Power Electronics Specialist Conference*, Acapulco, 2003.

[170] S. Calligaro, F. Pasut, R. Petrella and A. Pevere, "Modulation techniques for three-phase three-level NPC inverters: A review and a novel solution for switching losses reduction and optimal neutral-point balancing in photovoltaic applications," in *IEEE Applied Power Electronics Conference and Exposition (APEC)*, Long Beach, 2013.

[171] N. S. Hasana, N. Rosmina, D. Osmana and A. Habit, "Reviews on multilevel converter and modulation techniques," *Renewable and Sustainable Energy Reviews,* vol. 80, no. 1, pp. 163-174, 2017.

[172] J. Holtz, W. Lotzkat and A. Khambadkone, "On continuous control of PWM inverters in the overmodulation range including the six-step mode," *IEEE Transactions on Power Electronics,* vol. 8, no. 4, pp. 546 - 553, 1993.

[173] D.-C. Lee and G.-M. Lee, "A novel overmodulation technique for space-vector PWM inverters," *IEEE Transactions on Power Electronics,* vol. 13, no. 6, pp. 1144 - 1151, 1998.

[174] A. K. Gupta, "A General Space Vector PWM Algorithm for Multilevel Inverters, Including Operation in Overmodulation Range," in *IEEE International Conference on Electric Machines and Drives*, San Antonio, 2005.

[175] K. Gupta and A. Khambadkone, "A General Space Vector PWM Algorithm for Multilevel Inverters, Including Operation in Overmodulation Range," *IEEE Transactions on Power Electronics,* vol. 22, no. 2, pp. 517 - 526, 2007.

[176] N. Celanovic and D. Boroyevich, "A Fast Space-Vector Modulation Algorithm for Multilevel Three-Phase Converters," *IEEE Transactions on Industry Applications,* vol. 37, no. 2, pp. 637 - 641, 2001.

[177] J. H. Seo, C. H. Choi and D. S. Hyun, "A new simplified space-vector PWM method for three-level inverters," *IEEE Transactions on Power Electronics,* vol. 16, no. 4, pp. 545 - 550, 2001.

[178] H. Zhang, A. V. Jouanne, S. Dai, A. Wallace and F. Wang, "Multilevel inverter modulation schemes to eliminate common-mode voltages," *IEEE Transactions on Industry Applications,* vol. 36, no. 6, pp. 1645 - 1653, 2000.

[179] Y. Jiao, F. C. Lee and S. Lu, "Space Vector Modulation for Three-Level NPC Converter With Neutral Point Voltage Balance and Switching Loss Reduction," *IEEE Transactions on Power Electronics,* vol. 29, no. 10, pp. 5579 - 5591, 2014.

[180] N. Prabaharan and K. Palanisamy, "A comprehensive review on reduced switch multilevel inverter topologies, modulation techniques and application," *Renewable and Sustainable Energy Reviews,* vol. 76, no. 1, pp. 1248-1282, 2016.

[181] F. L. Mapelli, D. Tarsitano and M. Mauri, "Plug-In Hybrid Electric Vehicle: Modeling, Prototype Realization, and Inverter Losses Reduction Analysis," *IEEE Transactions on Industrial Electronics,* vol. 57, no. 2, pp. 598 - 607, 2010.

[182] Q. Attique, Y. Li and K. Wang, "A survey on space-vector pulse width modulation for multilevel inverters," *CPSS Transactions on Power Electronics and Applications,* vol. 2, no. 3, pp. 226 - 236, 2017.

[183] C. Wang, Y. Zhang, X.-m. Tang and S.-z. Chen, "Rapid and generalised space vector modulation algorithm for cascaded multilevel converter based on zero-order voltage constraint," *IET Power Electronics,* vol. 9, no. 5, pp. 1755-4535, 2016.

[184] J. Wang, Y. Gao and W. Jiang, "A Carrier-Based Implementation of Virtual Space Vector Modulation for Neutral-Point-Clamped Three-Level Inverter," *IEEE Transactions on Industrial Electronics,* vol. 64, no. 12, pp. 9580 - 9586, 2017.

[185] M. A. Kumar and M. Barai, "A novel SVPWM technique for capacitor voltage balancing in modular multilevel converters (MMCs)," in *International Conference on Compatibility, Power Electronics and Power Engineering,* Cadiz, 2017.

[186] K. Ezzeddine, M. Hamouda and K. Al-Haddad, "Comparative study between different SVPWM algorithms for NPC inverters in terms of common mode voltage reduction," in *Annual Conference of the IEEE Industrial Electronics Society,* Beijing, 2017.

[187] F. Li and L. Li, "Improved SVPWM strategy based on neutral-point charge balance for three-level neutral-point-clamped converter," in *IEEE Conference on Industrial Electronics and Applications*, Wuhan, 2018.

[188] R. Goyal, B. H. Kumar and M. M. Lokhande, "Combination of switching sequences in SVPWM to reduce line current ripple for IM drives," in *International Conference on Computer Applications In Electrical Engineering-Recent Advances (CERA),* Roorkee, 2017.

[189] G. Narayanan, D. Zhao, H. K. Krishnamurthy, R. Ayyanar and V. T. Ranganathan, "Space Vector Based Hybrid PWM Techniques for Reduced Current Ripple," *IEEE Transactions on Industrial Electronics,* vol. 55, no. 4, pp. 1614 - 1627, 2008.

[190] H. Krishnamurthy, G. Narayanan, R. Ayyanar and V. Ranganathan, "Design of space vector-based hybrid PWM techniques for reduced current ripple," in *IEEE Applied Power Electronics Conference and Exposition*, Miami Beach, 2003.

[191] Y. Huang, Y. Xu, Y. Li, G. Yang and J. Zou, "PWM Frequency Voltage Noise Cancelation in Three-Phase VSI Using the Novel SVPWM Strategy," *IEEE Transactions on Power Electronics,* vol. 33, no. 10, pp. 8596 - 8606, 2018.

[192] P. Pinewski, "Understanding Space Vector Modulation," *EDN,* pp. 45-46, 1996.

[193] M. Pahlavani and Y. Khadivi, "Optimization of Space Vector Pulse Width Modulation Switching Algorithms for Two-Level Inverters Regarding Different Objective Functions," *Journal of Basic and Applied Scientific Research,* vol. 2, no. 8, pp. 7623-7644, 2012.

[194] B. P. McGrath, "A Comparison of Multicarrier PWM Strategies for Cascaded and Neutral Point Clamped Multilevel Inverters," in *IEEE 31st Annual Power Electronics Specialists Conference*, Galway, 2000.

[195] B. P. McGrath, "Optimized space vector switching sequences for multilevel inverters," *IEEE Transactions on Power Electronics,* vol. 18, no. 6, pp. 1293 - 1301, 2003.

[196] A. A. Mohamed and M. Baiju, "A Novel Space Vector PWM Scheme for Multilevel Inverters," in *Twenty-Fourth Annual IEEE Applied Power Electronics Conference and Exposition*, Washington, DC, 2009.

[197] A. Gopinath, A. M. A. S. and M. R. Baiju, "Fractal Based Space Vector PWM for Multilevel Inverters—A Novel Approach," *IEEE Transactions on Industrial Electronics,* vol. 56, no. 4, pp. 1230 - 1237, 2009.

[198] N. Susheela, P. S. Kumar and S. K. Sharma, "Generalized Algorithm of Reverse Mapping Based SVPWM Strategy for Diode-Clamped Multilevel Inverters," *IEEE Transactions on Industry Applications*, vol. 54, no. 3, pp. 2425 - 2437, 2018.

[199] J. Pinto, B. Bose, L. Silva and M. Kazmierkowski, "A neural-network-based space-vector PWM controller for voltage-fed inverter induction motor drive," *IEEE Transactions on Industry Applications*, vol. 36, no. 6, pp. 1628 - 1636, 2000.

[200] N. Filho, J. O. P. Pinto and B. Bose, "A Neural-Network-Based Space Vector PWM of a Five-Level Voltage-Fed Inverter," in *IEEE International Conference on Smart Technologies and Management for Computing, Communication, Controls, Energy and Materials*, Chennai, 2017.

[201] D. S. Wankhede and M. V. Aware, "A neoteric space vector PWM method for multilevel inverter using image processing," in *IEEE International Conference on Smart Technologies and Management for Computing, Communication, Controls, Energy and Materials*, Chennai, 2017.

[202] S. Mondal, J. Pinto and B. Bose, "A neural-network-based space-vector PWM controller for a three-level voltage-fed inverter induction motor drive," *IEEE Transactions on Industry Applications*, vol. 38, no. 3, pp. 660 - 669, 2002.

[203] Y. Deng, K. H. Teo and R. G. Harley, "A Fast and Generalized Space Vector Modulation Scheme for Multilevel Inverters," in *IEEE Applied Power Electronics Conference and Exposition*, Long Beach, 2013.

[204] Y. Deng, K. H. Teo and C. Duan, "A Fast and Generalized Space Vector Modulation Scheme for Multilevel Inverters," *IEEE Transactions on Power Electronics*, vol. 29, no. 10, pp. 5204 - 5217, 2014.

[205] Y. Sozer, D. A. Torrey, A. Saha, H. Nguyen and N. Hawes, "Fast minimum loss space vector pulse-width modulation algorithm for multilevel inverters," *IET Power Electronics* , vol. 7, no. 6, pp. 1755-4535, 2014.

[206] P. Chamarthi, P. Chhetri and V. Agarwal, "Simplified Implementation Scheme for Space Vector Pulse Width Modulation of n-LevelInverter With Online Computation of Optimal Switching Pulse Durations," *IEEE Transactions on Industrial Electronics,* vol. 63, no. 11, pp. 6695-6704, 2016.

[207] K. N. V. Prasad, P. Pradhan, B. Misra and J. Surekha, "A modified space vector algorithm for 5-level cascaded multilevel inverter," in *Innovations in Power and Advanced Computing Technologies (i-PACT),* Vellore, 2017.

[208] K. C. Jana and S. Biswas, "Generalised switching scheme for a space vector pulse-width modulation-based N-level inverter with reduced switching frequency and harmonics," *IET Power Electronics,* vol. 8, no. 12, p. 2377 – 2385, 2015.

[209] W. Bergman, "The Basic Nature of Vehicle Understeer-Oversteer," *SAE Transactions,* vol. 74, no. 1, pp. 387-422, 1965.

[210] W. Chen, H. Xiao and Q. Wang, Integrated Vehicle Dynamics and Control, John Wiley & Sons, Inc, 2016.

[211] A. Zanten, R. Erhardt and G.Pfaff, "The Vehicle Dynamics Control System of Bosch 950759," in *International Congress & Exposition,* Detroit, 1995.

[212] Y. Shibahata, K. Shimada and T. Tomari, "Improvement of Vehicle Maneuverability by Direct Yaw Moment Control," *International Journal of Vehicle Mechanics and Mobility,* vol. 22, no. 5, pp. 456-481, 1993.

[213] S. Motoyama, H. Uki and K.Isoda, "Effect of Traction Force Distribution Control on Vehicle Dynamics," *International Journal of Vehicle Mechanics and Mobility,* vol. 22, no. 5, pp. 455-464, 1993.

[214] Y. Ikushima and K. Sawase, "A Study on the Effects of the Active Yaw Moment Control," *SAE Transactions: Journal of Passenger Cars-V104-6,* vol. 104, no. 6, pp. 425-433, 1995.

[215] The Jensen Museum, "Dunlop Maxaret Anti-Lock Braking Explained," 09 03 2018. [Online]. Available: http://www.jensenmuseum.org/dunlop-maxaret/. [Accessed 03 09 2018].

[216] R. Madison and E. Riordan, "Evolution of sure-track brake system," in *International Automotive Engineering Congress and Exposition*, 1969.

[217] M. Satoh and S. Shiraishi, "Performance of Antilock Brakes with Simplified Control Technique," *SAE Transactions,* vol. 92, no. 1, pp. 442-449, 1983.

[218] W. Newton and F. Riddy, "Evaluation Criteria for Low Cost Anti-Lock Brake Systems for FWD Passenger Cars," *SAE Transactions,* vol. 93, no. 3, pp. 391-401, 1984.

[219] J. Main and P. Chambers, "Ford anti spin control," *IEE Colloquium on Total Powertrain Control,* pp. 1-3, 1986.

[220] J. H. Moran and R. A. Grimm, "MAX TRAC -WHEEL SPIN CONTROL BY COMPUTER," in *Society of Automotive Engineers*, Montreal, 1971.

[221] O. Mokhiamar and M. Abe, "Effects of model response on model following type of combined lateral force and yaw moment control performance for active vehicle handling safety," *JSAE Review,* vol. 23, no. 1, pp. 473-480, 2002.

[222] M. Abe, "Vehicle dynamics and control for improving handling and active safety: From four-wheel steering to direct yaw moment control," *Proceedings of the Institution of Mechanical Engineers, Part K: Journal of Multi-body Dynamics,* vol. 213, no. 2, pp. 87-101, 1999.

[223] M. Abe, Y. Kano and K. Suzuki, "Side-slip control to stabilize vehicle lateral motion by direct yaw moment," *JSAE Review,* vol. 22, no. 4, pp. 413-419, 2001.

[224] S. Anwar, "Yaw Stability Control of an Automotive Vehicle via Generalized Predictive Algorithm," in *American Control Conference*, Portland, 2005.

[225] T. Goggia, A. Sorniotti and L. D. Novellis, "Integral Sliding Mode for the Torque-Vectoring Control of Fully Electric Vehicles: Theoretical Design and Experimental Assessment," *IEEE Transactions on Vehicular Technology,* vol. 64, no. 5, pp. 1701 - 1715, 2015.

[226] L. D. Novellis, A. Sorniotti and P. Gruber, "Direct yaw moment control actuated through electric drivetrains and friction brakes: Theoretical design and experimental assessment," *Mechatronics,* vol. 26, no. 1, pp. 1-15, 2015.

[227] C. Fu, R. Hoseinnezhad, A. Bab-Hadiashar and R. N. Jazar, "Direct yaw moment control for electric and hybrid vehicles with independent motors," *International Journal of Vehicle Design,* vol. 69, no. 1, pp. 1-24, 2015.

[228] L. D. Novellis, A. Sorniotti and P. Gruber, "Comparison of Feedback Control Techniques for Torque-Vectoring Control of Fully Electric Vehicles," *IEEE Transactions on Vehicular Technology,* vol. 63, no. 8, pp. 3612 - 3623, 2014.

[229] Y. Zhao, W. Deng, J. Wu and R. He, "Torque control allocation based on constrained optimization with regenerative braking for electric vehicles," *International Journal of Automotive Technology*, vol. 18, no. 4, pp. 685-698, 2017.

[230] A. Kampanakis, E. Siampis and E. Velenis, "A Torque Vectoring Optimal Control Strategy for Combined Vehicle Dynamics Performance Enhancement and Electric Motor Ageing Minimisation," in *IFAC Symposium on Advances in Automotive Control AAC*, Norrköping, 2016.

[231] D. Kasinathan, A. Kasaiezadeh and A. Wong, "An Optimal Torque Vectoring Control for Vehicle Applications via Real-Time Constraints," *IEEE Transactions on Vehicular Technology*, vol. 65, no. 6, pp. 4368-4378, 2016.

[232] A. Wong, D. Kasinathan and A. Khajepour, "Integrated torque vectoring and power management framework for electric vehicles," *Control Engineering Practice*, vol. 48, no. 1, pp. 22-36, 2016.

[233] L. Zhai, T. Sun and J. Wang, "Electronic Stability Control Based on Motor Driving and Braking Torque Distribution for a Four In-Wheel Motor Drive Electric Vehicle," *IEEE Transactions on Vehicular Technology*, vol. 65, no. 6, pp. 4726-4739, 2016.

[234] B. Boada, M. Boada and V. Díaz, "Fuzzy-logic applied to yaw moment control for vehicle stability," *International Journal of Vehicle Mechanics and Mobility*, vol. 43, no. 10, pp. 753-770, 2003.

[235] M. Boada, B. Boada and A. Muñoz, "Integrated control of front-wheel steering and front braking forces on the basis of fuzzy logic," *Proceedings of the Institution of Mechanical Engineers, Part D: Journal of Automobile Engineering*, vol. 220, no. 3, pp. 253-267, 2006.

[236] B. Li and F. Yu, "Design of a vehicle lateral stability control system via a fuzzy logic control approach," *Proceedings of the Institution of Mechanical Engineers, Part D: Journal of Automobile Engineering*, vol. 224, no. 3, pp. 313-326, 2009.

[237] L. Jin, X. Xie and C. Shen, "Study on electronic stability program control strategy based on the fuzzy logical and genetic optimization method," *Advances in Mechanical Engineering*, vol. 9, no. 5, pp. 1-13, 2017.

[238] S. Ghosh, A. Deb and M. Mahala, "Active Yaw Control of a Vehicle using a Fuzzy Logic Algorithm," in *SAE 2012 World Congress & Exhibition*, Detroit, 2012.

[239] S. Krishna, S. Narayanan and S. Ashok, "Fuzzy logic based yaw stability control for active front steering of a vehicle," *Journal of Mechanical Science and Technology*, vol. 28, no. 12, pp. 5169-5174, 2014.

[240] D. Kim and H. Kim, "Vehicle stability control with regenerative braking and electronic brake force distribution for a four-wheel drive hybrid electric vehicle," *Proceedings of the Institution of Mechanical Engineers, Part D: Journal of Automobile Engineering*, vol. 220, no. 6, pp. 683-693, 2006.

[241] L. Austin and D. Morrey, "Recent advances in antilock braking systems and traction control systems," *Proceedings of the Institution of Mechanical Engineers, Part D: Journal of Automobile Engineering*, vol. 214, no. 6, pp. 625-638, 2000.

[242] A. Mirzaei, M. Moallem, B. Mirzaeian and B. Fahimi, "Design of an optimal fuzzy controller for antilock braking systems," in *IEEE Conference Vehicle Power and Propulsion*, Chicago, 2005.

[243] A. Harifi, A. Aghagolzadeh, G. Alizadeh and M. Sadeghi, "Designing a sliding mode controller for slip control of antilock brake systems," *Transportation Research Part C: Emerging Technologies,* vol. 16, no. 6, pp. 731-741, 2008.

[244] C. Mi, H. Lin and Y. Zhang, "Iterative learning control of antilock braking of electric and hybrid vehicles," *IEEE Transactions on Vehicular Technology,* vol. 54, no. 2, pp. 486 - 494, 2005.

[245] S. Kuruppu, K. Ariyur and N. Kulatunga, "Electric machine vs mechanical brakes for traction control with real time extremum seeking control," in *40th Annual Conference of the IEEE Industrial Electronics Society (IECON)*, Dallas, 2014.

[246] V. Ivanov, D. Savitski and K. Augsburg, "Electric vehicles with individually controlled on-board motors: Revisiting the ABS design," in *IEEE International Conference on Mechatronics (ICM),* Nagoya, 2015.

[247] P. Spichartz, T. Bokker and C. Sourkounis, "Comparison of electric vehicles with single drive and four wheel drive system concerning regenerative braking," in *Twelfth International Conference on Ecological Vehicles and Renewable Energies (EVER),* Monte Carlo, 2017.

[248] S. Drakunov, U. Ozguner and P. Dix, "ABS control using optimum search via sliding modes," *IEEE Transactions on Control Systems Technology,* vol. 3, no. 1, pp. 79 - 85, 1995.

[249] A. Will, S. Hui and S. Zak, "Sliding-mode wheel slip controller for an antilock braking system," *International Journal on Vehicle Design,* vol. 19, no. 4, pp. 523-539, 1998.

[250] J. Song, H. Kim and K. Boo, "A study on an anti-lock braking system controller and rear-wheel controller to enhance vehicle lateral stability," *Proceedings of the Institution*

of Mechanical Engineers, Part D: Journal of Automobile Engineering, vol. 221, no. 7, pp. 777-787, 2007.

[251] G. Lui and L. Jin, "A Study of Coordinated Vehicle Traction Control System Based on Optimal Slip Ratio Algorithm," *Mathematical Problems in Engineering*, vol. 2016, no. 1, pp. 1-10, 2016.

[252] J. Layne, K. Passino and S. Yurkovich, "Fuzzy learning control for antiskid braking systems," *IEEE Transactions on Control Systems Technology,* vol. 1, no. 2, pp. 122 - 129, 1993.

[253] P. Khatun, C. Bingham and N. Schofield, "Application of fuzzy control algorithms for electric vehicle antilock braking/traction control systems," *IEEE Transactions on Vehicular Technology,* vol. 52, no. 5, pp. 1356 - 1364, 2003.

[254] M. Bauer and M. Tomizuka, "Fuzzy Logic Traction Controllers and their Effect on Longitudinal Vehicle Platoon Systems," *International Journal of Vehicle Mechanics and Mobility,* vol. 25, no. 4, pp. 277-303, 1996.

[255] P. Koker, J. Gouws and L. Pretorius, "Fuzzy control algorithm for automotive traction control systems," in *In Proceedings of Mediterranean Electrotechnical Conference MELECON*, Bari, 1996.

[256] V. Colli, G. Tomassi and M. Scarano, "Fuzzy Longitundinal Traction Control," in *International Confernec on Advanced Intelligent Mechatronics*, Monterey, 2005.

[257] V. Colli, G. Tomassi and M. Scarano, ""Single Wheel" longitudinal traction control for electric vehicles," *IEEE Transactions on Power Electronics,* vol. 21, no. 3, pp. 799 - 808, 2006.

[258] H. Li, l. He and M. Kang, "PID plus fuzzy logic method for torque control in traction control system," *International Journal of Automotive Technology,* vol. 13, no. 3, pp. 441-450, 2012.

[259] L. Zhang, L. Yu and Z. Wang, "All-Wheel Braking Force Allocation During a Braking-in-Turn Maneuver for Vehicles With the Brake-by-Wire System Considering Braking Efficiency and Stability," *IEEE Transactions on Vehicular Technology,* vol. 65, no. 6, pp. 4752 - 4767, 2016.

[260] B. d'Andrea-Novel and M. Ellouze, "Tracking with stability for a vehicle braking in a corner," in *IEEE Conference on Decision and Control*, Orlando, FL, 2001.

[261] P. Heinzl, P. Lugner and M. Plöchl, "Stability Control of a Passenger Car by Combined Additional Steering and Unilateral Braking," *International Journal of Vehicle Mechanics and Mobility,* vol. 37, no. 1, pp. 211-233, 2002.

[262] L. Pinto, S. Aldworth and M. Watkinson, "Advanced Yaw Motion Control of a Hybrid Vehicle using Twin Rear Electric Motors," in *Advanced Vehicle Control Conference*, Loughborough, 2010.

[263] G. Kaiser, F. Holzmann and B. Chretien, "Torque Vectoring with a feedback and feed forward controller - applied to a through the road hybrid electric vehicle," in *IEEE Intelligent Vehicles Symposium (IV)*, Baden, 2011.

[264] G. Kaiser, Q. Liu and C. Hoffmann, "Torque vectoring for an electric vehicle using an LPV drive controller and a torque and slip limiter," in *IEEE 51st Annual Conference on Decision and Control (CDC)*, Maui, 2012.

[265] J. Song, "Enhanced braking and steering yaw motion controllers with a non-linear observer for improved vehicle stability," *Proceedings of the Institution of Mechanical*

Engineers, Part D: Journal of Automobile Engineering, vol. 222, no. 3, pp. 293-304, 2008.

[266] J. Song, "Comparison and evaluation of steer yaw motion controllers with an anti-lock brake system," *Proceedings of the Institution of Mechanical Engineers, Part D: Journal of Automobile Engineering,* vol. 223, no. 4, pp. 503-518, 2009.

[267] H. Mirzaeinejad, M. Mirzaei and R. Kazemi, "Enhancement of vehicle braking performance on split-k roads using optimal integrated control of steering and braking systems," *Proceedings of the Institution of Mechanical Engineers, Part K: Journal of Multi-body Dynamics,* vol. 230, no. 4, pp. 401-415, 2015.

[268] M. Mirzaei and H. Mirzaeinejad, "Fuzzy Scheduled Optimal Control of Integrated Vehicle Braking and Steering Systems," *IEEE/ASME Transactions on Mechatronics,* vol. 22, no. 5, pp. 2369 - 2379, 2017.

[269] H. Mirzaeinejad and M. Mirzaei, "Optimization of nonlinear control strategy for anti-lock braking system with improvement of vehicle directional stability on split-μ roads," *Transportation Research Part C: Emerging Technologies,* vol. 46, no. 1, pp. 1-15, 2014.

[270] P. Naderi, A. Naderipour and M. Mirsalim, "Intelligent Braking System Using Fuzzy Logic and Sliding Mode Controller," *Control and Intelligent Systems,* vol. 38, no. 4, pp. 236-244, 2010.

[271] H. Dogruğüven and T. Acarman, "Proposal of regenerative braking algorithm to maximize energy transfer and to enhance yaw stability," in *IEEE International Conference on Vehicular Electronics and Safety (ICVES),* Instanbul, 2012.

[272] E. Dincmen, B. Guvenc and T. Acarman, "Extremum-Seeking Control of ABS Braking in Road Vehicles With Lateral Force Improvement," *IEEE Transactions on Control Systems Technology*, vol. 22, no. 1, pp. 230 - 237, 2014.

[273] J. Song, "Design and Comparison of AFS Controllers with PID, Fuzzy-Logic, and Sliding-Mode Controllers," *Advances in Mechanical Engineering*, vol. 5, no. 1, pp. 1-14, 2013.

[274] F. Tahami, R. Kazemi and S. Farhanghi, "A novel driver assist stability system for all-wheel-drive electric vehicles," *IEEE Transactions on Vehicular Technology*, vol. 52, no. 3, pp. 683 - 692, 2003.

[275] F. Un-Noor, S. Padmanaban, L. Mihet-Popa, M. N. Mollah and E. Hossain, "A Comprehensive Study of Key Electric Vehicle (EV) Components, Technologies, Challenges, Impacts, and Future Direction of Development," *Energies*, vol. 10, no. 1, pp. 1-84, 2017.

[276] Y. Liu, J. Zhao and R. Wang, "Performance Improvement of Induction Motor Current Controllers in Field-Weakening Region for Electric Vehicles," *IEEE Transactions on Power Electronics*, vol. 28, no. 5, pp. 2468 - 2482, 2012.

[277] J. Osorio, P. Ponce and A. Molina, "Electric Vehicle Powertrain Control with Fuzzy Indirect Vector Control," in *11th Mexican International Conference on Artificial Intelligence*, San Luis Potosi, 2012.

[278] S. Fadul, I. Aris, N. Misron, I. Halin and A. P. Iqbal, "Modelling and simulation of electric drive vehicle based on Space Vector Modulation technique and Field Oriented Control strategy," in *International Conference on Communication, Control, Computing and Electronics Engineering (ICCCCEE)*, Khartoum, 2017.

[279] A. Leedy, "Simulink/MATLAB Dynamic Induction Motor Model for Use as A Teaching and Research Tool," *International Journal of Soft Computing and Engineering*, vol. 3, no. 4, pp. 102-107, 2013.

[280] V. Pahwa and K. S. Sandhu, "Transient anslysis of three-phase induction machine using different reference frames," *Journal of Engineering and Applied Sciences*, vol. 4, no. 8, pp. 31-38, 2009.

[281] J.-W. Park, D.-H. Koo and J.-M. Kim, "Development of interior permanent magnet synchronous motor and driver for electric vehicle," in *International Conference on Power Electronic Drives and Energy Systems for Industrial Growth*, Perth, 1998.

[282] S. Mahammadsoaib, "Vector controlled PMSM drive using SVPWM technique - A MATLAB / simulink implementation," in *International Conference on Electrical, Electronics, Signals, Communication and Optimization*, Visakhapatnam, 2015.

[283] W. Soong and T. Miller, "Theoretical limitations to the field-weakening performance of the five classes of brushless synchronous AC motor drive," in *Sixth International Conference on Electrical Machines and Drives*, London, 1993.

[284] W. Soong and N. Ertugrul, "Field-weakening performance of interior permanent-magnet motors," in *Annual Meeting and World Conference on Industrial Applications of Electrical Energy*, Rome, 2000.

[285] S. Morimoto, "Expansion of operating limits for permanent magnet motor by current vector control considering inverter capacity," *IEEE Transactions on Industry Applications*, vol. 26, no. 5, pp. 866-871, 1990.

[286] S.-Y. Jung, C. C. Mi and K. Nam, "Torque Control of IPMSM in the Field Weakening Region with Improved DC-Link Voltage Utilization," *IEEE Transactions on Industrial Electronics*, vol. 62, no. 6, pp. 3380 - 3387, 2015.

[287] X. Cao and L. Fan, "A novel flux-weakening control scheme based on the fuzzy logic of PMSM drive," in *International Conference on Mechatronics and Automation*, Changchun, 2009.

[288] B. M. Dehkordi, A. Kiyoumarsi, P. Hamedani and C. Lucas, "A comparative study of various intelligent based controllers for speed control of IPMSM drives in the field-weakening region," *Expert Systems with Applications*, vol. 38, no. 10, pp. 12643-12653, 2011.

[289] M. Haris, M. Pathak and P. Agarwal, "Comparison of SPWM multilevel inverter fed PMSM drive with two level inverter fed drive," in *Recent Advances and Innovations in Engineering*, Jaipur, 2014.

[290] L. Li, F.-Y. Wang and Q. Zhou, "Integrated longitudinal and lateral tire/road friction modeling and monitoring for vehicle motion control," *IEEE Transactions on Intelligent Transportation Systems*, vol. 7, no. 1, pp. 1 - 19, 2006.

[291] H. Pacejka and I. Besselink, "Magic Formula Tyre Model with Transient Properties," *International Journal of Vehicle Mechanics and Mobility* , vol. 27, no. 1, pp. 234-249, 1997.

[292] E. Siampis, M. Massaro and E. Velenis, "Electric rear axle torque vectoring for combined yaw stability and velocity control near the limit of handling," in *52nd IEEE Conference on Decision and Control*, Florence, 2013.

[293] R. Babau, I. Boldea, T. Miller and N. Muntean, "Complete Parameter Identification of Large Induction Machines From No-Load Acceleration–Deceleration Tests," *IEEE Transactions on Industrial Electronics,* vol. 54, no. 4, pp. 1962 - 1972, 2007.

[294] C. Grantham and D. McKinnon, "Rapid parameter determination for induction motor analysis and control," *IEEE Transactions on Industry Applications,* vol. 39, no. 4, pp. 1014 - 1020, 2003.

[295] S. Cash and O. Olatunbosun, "Fuzzy logic field-oriented control of an induction motor and a permanent magnet synchronous motor for hybrid/electric vehicle traction applications," *International Journal of Electric and Hybrid Vehicles,* vol. 9, no. 3, pp. 269-284, 2017.

[296] T. D. Gillesspie, Fundamentals of Vehicle Dynamics, Warrendale,PA: Society of Automotive Engineers, Inc, 1992.

[297] C. Tofallis, "A better measure of relative prediction accuracy for model selection and model estimation," *Journal of the Operational Research Society,* vol. 66, no. 8, p. 1352–1362, 2015.

[298] K. H. Nam, AC Motor Control and Electric Vehicle Applications, CRC Press, 2010, 2010.

[299] R. Dharmaprakash and J. Henry, "Switching table based 2-level inverter and 3-level diode clamped inverter," *Journal of Theoretical and Applied Information Technology,* vol. 60, no. 2, pp. 380-388, 2014.

[300] J. Pou, J. Zaragoza, S. Ceballos, M. Saeedifard and D. Boroyevich, "A Carrier-Based PWM Strategy With Zero-Sequence Voltage Injection for a Three-Level Neutral-Point-

Clamped Converter," *IEEE Transactions on Power Electronics,* vol. 27, no. 2, pp. 642 - 651, 2012.

[301] V. Manimala, N. Geetha and P. Renuga, "Design and simulation of five level cascaded inverter using multilevel sinusoidal pulse width modulation strategies," in *3rd International Conference on Electronics Computer Technology*, Kanyakumari, 2011.

[302] S. Motahhir, A. Ghzizal, S. Sebti and A. Derouich, "MIL and SIL and PIL tests for MPPT algorithm," *Cogent Engineering,* vol. 4, no. 1, pp. 1-18, 2017.

[303] M. Inc, "Software-in-the-Loop Simulations," MathWorks Inc, 01 01 2018. [Online]. Available: https://uk.mathworks.com/help/ecoder/software-in-the-loop-sil-simulation.html?searchHighlight=software%20in%20the%20loop&s_tid=doc_srchtitle. [Accessed 25 01 2019].

[304] J. Mina, Z. Flores, E. López, A. Pérez and J. Calleja, "Processor-in-the-loop and hardware-in-the-loop simulation of electric systems based in FPGA," in *13th International Conference on Power Electronics*, Guanajuato, 2016.

[305] Z. Jiang, R. Leonard, R. Dougal, H. Figueroa and A. Monti, "Processor-in-the-loop simulation, real-time hardware-in-the-loop testing, and hardware validation of a digitally-controlled, fuel-cell powered battery-charging station," in *35th Annual Power Electronics Specialists Conference,* Aachen, 2004.

[306] I. MathWorks, "SIL and PIL Simulations," MathWorks, 01 01 2018. [Online]. Available: https://uk.mathworks.com/help/ecoder/ug/about-sil-and-pil-simulations.html. [Accessed 25 01 2019].

[307] Arduino, "ARDUINO MEGA 2560 REV3," [Online]. Available: https://store.arduino.cc/arduino-mega-2560-rev3. [Accessed 05 09 2018].

[308] S. Cash, Q. Zhou, O. Olatunbosun and H. Xu, "A Robust Fuzzy Logic Field-Oriented Control Scheme for Hybrid and Electric Vehicles," in *4th Biennial International Conference on Powertrain Modelling and Control Testing*, Loughborough, 2018.

[309] Mechanical Simulation, "CarSim," 2018.

[310] S. Cash, Q. Zhou, O. Olatunbosun and H. Xu, "Development of a Hybrid Tug for Aircraft Pushback," in *EAEC 15th Automotive European Congress*, Madrid, 2017.

[311] X. Liu, D. Diallo and C. Marchand, "Design methodology of hybrid electric vehicle energy sources: Application to fuel cell vehicles," *International Journal of Automotive Technology*, vol. 12, no. 3, p. 433−441, 2011.

[312] F. Millo, C. Cubito, L. Rolando, E. Pautasso and E. Servetto, "Design and development of an hybrid light commercial vehicle," *Energy*, vol. 136, no. 1, pp. 90-99, 2017.

[313] K. Butler, M. Ehsani and P. Kamath, "A Matlab-Based Modeling and Simulation Package for Electric and Hybrid Electric Vehicle Design," *IEEE Transactions on vehicular technology*, vol. 48, no. 6, pp. 1770-1778, 1998.

[314] G.Offer, D.Howey, M.Contestabile, R.Clague and N.P.Brandon, "Comparative analysis of battery electric, hydrogen fuel cell and hybrid vehicles in a future sustainable road transport system," *Energy Policy*, vol. 38, no. 1, pp. 24-29, 2010.

[315] Boeing, "Beoing - Airport Compatability," 01 September 2013. [Online]. Available: http://www.boeing.com/resources/boeingdotcom/commercial/airports/acaps/737MAX.pdf. [Accessed 01 June 2018].

[316] Zytek Group Limited, "Zytek 170kW 460Nm," [Online]. Available: http://www.zytekautomotive.co.uk/products/electric-engines/170kw/. [Accessed 04 09 2018].

[317] TM4 DANA, "Sumo - Specifications," [Online]. Available: https://www.tm4.com/products/direct-drive-electric-powertrain/sumo-md/. [Accessed 04 09 2018].

[318] R. Cooper, "New hybrid aircraft push-back tractor on show at Inter Airport Europe Exhibition," Hyperdrive Innovation, 12 October 2017. [Online]. Available: https://hyperdriveinnovation.com/new-hybrid-aircraft-push-back-tractor-on-show-at-inter-airport-europe-exhibition/. [Accessed 08 August 2018].

[319] A. Choudhury, P. Pillay and S. Williamson, "Comparative Analysis Between Two-Level and Three-Level DC/AC Electric Vehicle Traction Inverters Using a Novel DC-Link Voltage Balancing Algorithm," *IEEE Journal of Emerging and Selected Topics in Power Electronics*, vol. 2, no. 3, pp. 529 - 540, 2014.

[320] A. Choudhury, P. Pillay and S. S. Williamson, "DC-Link Voltage Balancing for a Three-Level Electric Vehicle Traction Inverter Using an Innovative Switching Sequence Control Scheme," *IEEE Journal of Emerging and Selected Topics in Power Electronics*, vol. 2, no. 2, pp. 296 - 307, 2014.

[321] W. Dong, J.-Y. Choi and Y. Li, "Efficiency considerations of load side soft-switching inverters for electric vehicle applications," in *IEEE Applied Power Electronics Conference and Exposition*, New Orleans, 2000.

[322] T. Hoevenaars, K. LeDoux and M. Colosino, "Interpreting IEEE STD 519 and meeting its harmonic limits in VFD applications," in *IEEE Industry Applications Society 50th Annual Petroleum and Chemical Industry Conference*, Houston, 2003.

[323] W. G. d. Silva, M. A. A. d. Freitas and I. Kopcak, "IEEE Standard 519-92 and the harmonic currents caused by the inverter fed induction motor," in *Brazilian Power Electronics Conference*, Gramado, 2013.

[324] S. Madishetti, G. Bhuvaneswari and B. Singh, "Improved power quality converter for direct torque control-based induction motor drives," *IET Power Electronics*, vol. 6, no. 2, pp. 276 - 286, 2013.

[325] B. McGrath and D. Holmes, "A Comparison of Multicarrier PWM Strategies for Cascaded and Neutral Point Clamped Multilevel Inverters," in *IEEE 31st Annual Power Electronics Specialists Conference*, Galway, 2000.

[326] A. Tripathi, A. M. Khambadkone and S. K. Panda, "Dynamic control of torque in overmodulation and in the field weakening region," *IEEE Transactions on Power Electronics*, vol. 21, no. 4, pp. 1091 - 1098, 2006.

[327] A. Ghaderi, J. Soltani, M. Ebrahimi and A. A. F. Nassiraei, "Modification of electric drive vehicles performances using a direct torque control with over-modulation ability," in *Annual Conference of the IEEE Industrial Electronics Society*, Yokohama, 2015.

[328] A. Ghaderi, T. Umeno and M. Sugai, "An Altered PWM Scheme for Single-Mode Seamless Control of AC Traction Motors for Electric Drive Vehicles," *IEEE Transactions on Industrial Electronics*, vol. 63, no. 3, pp. 1385 - 1394, 2015.

[329] Y. Gao, L. Chu and M. Ehsani, "Design and Control Principles of Hybrid Braking System for EV, HEV and FCV," in *IEEE Vehicle Power and Propulsion Conference*, Arlington, 2007.

[330] F. Wang, Z. Zhang, X. Mei, J. Rodríguez and R. Kennel, "Advanced Control Strategies of Induction Machine: Field Oriented Control, Direct Torque Control and Model Predictive Control," *Energies,* vol. 11, no. 1, pp. 1-13, 2018.

[331] H. Jordan, "Analysis of Induction Machines in Dynamic Systems," *IEEE Transactions on Power Apparatus and Systems,* vol. 84, no. 11, pp. 1080-1088, 1965.

[332] P. C. Krause and C. H. Thomas, "Simulation of Symmetrical Induction Machinery," *IEEE Transactions on Power Apparatus and Systems,* vol. 84, no. 11, pp. 1038 - 1053, 1965.

[333] W. Peters, O. Wallscheid and J. Böcker, "Optimum efficiency control of interior permanent magnet synchronous motors in drive trains of electric and hybrid vehicles," in *17th European Conference on Power Electronics and Applications*, Geneva, 2015.

[334] Q. Guo, C. Zhang, L. Li, J. Zhang, J. Liu and T. Wang, "Efficiency Optimization Control of Permanent-Magnet Synchronous Machines for Electric Vehicle Traction Systems," in *IEEE Vehicle Power and Propulsion Conference*, Hangzhou, 2016.